Universidad del País Vasco
Euskal Herriko Unibertsitatea
The University of the Basque Country

Poly(lactic acid)-based bio-blends and nanocomposites

Jon Urkijo Elortegi

Faculty of Chemistry

Polymer Science and Technology Department

Donostia, 2015

Index

Chapter 1: Introduction 1

Chapter 2: State of the art 3
2.1 Poly(lactic acid) (PLA) 3
2.2 PLA-based blends 5
    2.2.1 PLA/PCL blends 7
    2.2.2 PLA/PBAT blends 10
2.3 Polymer nanocomposites 12
    2.3.1 Polymer/nanoclay nanocomposites 13
    2.3.2 Polymer/CNT nanocomposites 18
2.4 Nanocomposites based on polymer blends 23
    2.4.1 Location of nanoparticles in immiscible polymer blends 23
    2.4.2 Morphological changes produced by nanoparticles in polymer blends 25
    2.4.3 Nanocomposites based on biodegradable polymer blends 31

Chapter 3: Experimental part 35
3.1 Materials 35
    3.1.1 Poly(lactic acid) (PLA) 35
    3.1.2 Poly(ε-caprolactone) (PCL) 36
    3.1.3 Poly(butylene adipate-co-terephthalate) (PBAT) 37
    3.1.4 Montmorillonite (MMT) 38
    3.1.5 Carbon nanotubes (CNT) 39
3.2 Processing 40
    3.2.1 Drying 41
    3.2.2 Blending 41

3.2.3 Manufacturing 43

3.3 Characterization and testing techniques 44

3.3.1 Differential Scanning Calorimetry (DSC) 44

3.3.2 Dynamic Mechanical Thermal Analysis (DMTA) 45

3.3.3 Proton Magnetic Nuclear Resonance (^{1}H-RMN) 45

3.3.4 Contact-angle measurements 46

3.3.5 X-Ray Diffraction (XRD) 46

3.3.6 Rheological measurements 47

3.3.7 Morphology 49

3.3.8 Mechanical properties 51

3.3.9 Izod Impact tests 52

3.3.10 Measurements for oxygen permeability 53

3.3.11 Electrical conductivity measurements 53

Chapter 4: PLA-based blends 55

4.1 PLA/PCL blends 57

4.1.1 Phase structure 57

4.1.2 Morphology 60

4.1.3 Viscoelasticity 61

4.1.4 Mechanical properties 62

4.2 PLA/PBAT blends 71

4.2.1 Phase structure 71

4.2.2 Morphology 76

4.2.3 Viscoelasticity 77

4.2.4 Mechanical properties 78

Chapter 5: Nanocomposites based on PLA 83
- 5.1 PLA/oMMT nanocomposites 85
  - 5.1.1 Nanostructure and morphology 85
  - 5.1.2 Phase structure 87
  - 5.1.3 Viscoelasticity 90
  - 5.1.4 Mechanical properties 92
  - 5.1.5 Oxygen permeability 95

- 5.2 PLA/CNT nanocomposites 97
  - 5.2.1 Nanostructure and morphology 97
  - 5.2.2 Phase structure 99
  - 5.2.3 Viscoelasticity 102
  - 5.2.4 Mechanical properties 103
  - 5.2.5 Electrical conductivity 105

Chapter 6: Nanocomposites based on PLA/PCL and PLA/PBAT blends 109
- 6.1 PLA/PCL/oMMT nanocomposites 111
  - 6.1.1 Nanostructure and morphology 111
  - 6.1.2 Phase structure 117
  - 6.1.3 Viscoelasticity 119
  - 6.1.4 Mechanical properties 121
  - 6.1.5 Oxygen permeability 125

- 6.2. PLA/PCL/CNT nanocomposites 127
  - 6.2.1 Nanostructure and morphology 127
  - 6.2.2 Viscoelasticity 131
  - 6.2.3 Phase structure 132
  - 6.2.4 Mechanical properties 135

6.2.5 Electrical conductivity 139

6.3. PLA/PBAT/CNT nanocomposites 141

6.3.1 Nanostructure and morphology 141

6.3.2 Viscoelasticity 144

6.3.3 Phase structure 146

6.3.4 Mechanical properties 149

6.3.5 Electrical conductivity 153

Chapter 7: Conclusions 155

Chapter 8: Bibliography 157

Glossary 167

Chapter 1: Introduction

Chapter 1: Introduction

Two serious issues of great concern nowadays are the dwindling sources of polymers and the problem of waste residue. Biopolymers (or bioplastics) are materials synthesized from renewable sources and/or 100% biodegradable, so their study and development constitute a major field of interest, both in academia, in the area of macromolecular science, and in industry, in the packaging, automotive, construction, textile and electronics sectors, in particular. The common concern and objective is to replace conventional polymeric materials with biopolymers.

Poly (lactic acid) or PLA is a large-scale produced renewable and biodegradable thermoplastic polymer. As a result of its acceptable thermo-mechanical properties, PLA is currently used for the production of different goods and objects. However, it does present some drawbacks which have prevented it from being used for other industrial applications. The first main goal of this work was to modify PLA by melt-processing with other polymers and nanoparticles, in order to improve its performance. Taking into account the unique environmental characteristics of PLA, care was taken to preserve its biodegradability throughout the entire modification process.

Regarding mechanical properties, one of the main shortcomings of PLA is its intrinsic brittleness. Extensive literature exists on how to improve the deformability of PLA by blending with plasticizers, rubbers and other deformable polymers. In the present work, two thermoplastic polymers, poly(ε-caprolactone) (PCL) and poly(butylene adipate-co-terephthalate) (PBAT), were used. Both are deformable and tough and, despite the fact that both are petroleum derived, they are fully biodegradable. PLA/PCL and PLA/PBAT blends have already been studied, but some results concerning the compatibility of the blends remain unclear, as well as how it affects their mechanical properties.

In recent years, one of the most commonly studied methods for improving the performance of polymeric materials has been their modification with nanoparticles, as they are capable of improving the properties of the materials just as much as conventional reinforcement agents, but at much lower contents. Depending on whether the property to be improved is thermal, mechanical, barrier or electrical, different nanoparticles can be used, ranging from nanoclays (which are usually modified) to carbon nanotubes or, more recently, graphene. In the present work, the effect of the addition of organically modified montmorillonite nanoplatelets (oMMT) and carbon nanotubes (CNT) to PLA was studied. The first step was to select the most suitable nanoparticles and the most efficient processing methods in order to obtain the best dispersed PLA/oMMT and PLA/CNT nanocomposites. A full characterization of these optimized nanocomposites allowed us to compare the performance of oMMT and CNTs, particularly regarding their level of dispersion within PLA and the final mechanical properties of PLA/oMMT and PLA/CNT nanocomposites.

One of the main drawbacks associated with the addition of nanoparticles to polymeric materials is that they cause greater fragility, which is particularly acute in the case of PLA, because of its above mentioned intrinsic brittleness. This is why it would be of great interest to obtain ternary systems which combine PLA/PCL and PLA/PBAT blends with PLA/oMMT and PLA/CNT nanocomposites. The preparation of polymer/polymer/nanoparticle nanocomposites is currently a commonly used method for producing high performance materials, as they combine the technology of polymer blends with that of polymer nanocomposites. So, adding MMT nanoplatelets and CNTs to PLA/PCL and PLA/PBAT materials would appear to be a very good way of obtaining high performance biodegradable materials. In addition, it would provide greater insight into some ternary nanocomposite-related issues, such as the relationship between the dispersion level of the nanoparticles and the morphology and final properties of the nanocomposites, the effect of processing on the final properties of the nanocomposites, and the relationship between the morphological and viscoelastic properties of ternary nanocomposites.

Thus, following this Introduction (Chapter 1), Chapter 2 of this thesis summarizes the most relevant results in the literature published so far concerning the main topics under discussion in the present work. Chapter 3 presents the different materials, processing and characterization techniques used throughout the study. Chapter 4 includes the results and discussion on PLA/PCL and PLA/PBAT blends, Chapter 5 deals with PLA/oMMT and PLA/CNT nanocomposites and Chapter 6 discusses ternary PLA/PCL/oMMT, PLA/PCL/CNT and PLA/PBAT/CNT nanocomposites. The phase structure and the morphology/nanostructure were analyzed, and the macroscopic properties were measured for all the compositions studied. In all cases an attempt was made to correlate the structure and the properties of the materials, in order to discuss about the processing-structure-properties relationships therein. Chapter 7 summarizes the main conclusions obtained.

Chapter 2: State of the art

Chapter 2: State of the art

El objetivo del presente capítulo es establecer el marco del conocimiento científico y tecnológico actual en el que puede encuadrarse este trabajo de investigación. Los temas que se han abordado a lo largo del trabajo son de gran interés científico, y la bibliografía existente relacionada muy amplia; en la presente revisión bibliográfica únicamente se muestran los resultados más significativos. Asimismo, la información aquí recogida ha servido para argumentar y justificar de forma exhaustiva los resultados obtenidos, realizando las discusiones pertinentes y remarcando las aportaciones principales.

2.1. Poly(lactic acid) (PLA)

La renovabilidad del monómero constituyente[1,2], su completa biodegradabilidad[3], su naturaleza termoplástica, su sencilla procesabilidad mediante las técnicas convencionales de procesado de polímeros[4,5] y las buenas prestaciones que presenta[6] son las principales razones por las que el poli(ácido láctico) (PLA)[7] ha despertado un gran interés. En los últimos años, el PLA se ha convertido en el tercer bioplástico más producido del mundo, tan sólo por detrás de los basados en almidón y lignocelulosa, y ha empezado a sustituir diferentes polímeros convencionales en sectores industriales tales como el textil, envasado y embalaje, electrónico y automovilístico.

El procesado en fundido es el método más empleado para producir productos basados en PLA, ya que posibilita de una manera sencilla, rápida y económica la obtención de productos acabados con la forma y características requeridas para la aplicación a la que van a ser destinados[4]. Sin embargo, el PLA presenta algunos inconvenientes para su procesado en fundido tales como su baja resistencia en fundido y la posibilidad de degradación térmica y de escisión de cadena mediante degradación hidrolítica[4]. Por ello, la optimización de la temperatura de procesado, el tiempo de residencia en la maquinaria empleada y las condiciones de secado previas al procesado en fundido del material son factores fundamentales a tener en cuenta[4].

El monómero constituyente del PLA, el ácido láctico, contiene un carbono asimétrico en su cadena principal, y por lo tanto puede encontrarse en las formas enantioméricas L (+) o D (-). El control estereoquímico del ácido láctico durante el proceso de polimerización del PLA resulta, por tanto, fundamental. En el mercado existe una amplia gama de PLAs comerciales con diferentes pesos moleculares y con cadenas macromoleculares que contienen distintas proporciones de isómeros. De todos ellos, los más utilizados son copolímeros ópticos aleatorios de alto peso molecular constituidos mayoritariamente por ácido L-láctico[1,6,7]. Estos PLAs comerciales basados en copolímeros ópticos aleatorios tienen una temperatura de transición vítrea cercana a 60ºC y sus cristales se forman y funden a temperaturas que oscilan entre 110-130ºC y 150-170ºC, respectivamente. Tanto la temperatura de fusión como la cristalizabilidad del PLA dependen directamente de la relación L/D de los isómeros que conforman las cadenas poliméricas. Los conformados con altos contenidos de ácido L-láctico pueden ser utilizados para producir materiales semicristalinos, mientras que los polímeros con contenidos superiores al 15% de isómero D son completamente amorfos. Sin embargo, el PLA es un polímero que se caracteriza por tener una cinética de cristalización muy lenta, y por ello apenas suele cristalizar cuando es enfriado en tiempos muy cortos desde el fundido hasta temperatura ambiente, típicos en procesos industriales tales como el moldeo por inyección.

El PLA comercial debe procesarse a temperaturas relativamente bajas (entre 170ºC y 210ºC) en comparación con otros polímeros convencionales, lo cual supone una ventaja desde un punto de vista de consumo energético pero también supone un inconveniente -por posibilidades de degradación térmica-, ya que dificulta su mezclado con polímeros que tienen temperaturas de procesado superiores. Algunos de los ejemplos de productos comerciales procesados en fundido son cubiertos desechables moldeados por inyección, recipientes y tazas termoconformadas, botellas obtenidas por inyección-soplado, films extruidos y calandrados o fibras hiladas, entre otros.

La posibilidad de procesar PLA completamente amorfo permite confeccionar productos transparentes, muy útiles en la industria del embalaje y del envasado, entre otros. Sin embargo, existen otras aplicaciones en las cuales la transparencia del producto no supone un requerimiento imprescindible y por lo tanto, teniendo en cuenta la mejora general que conlleva la cristalización del PLA en sus propiedades[8], se han llevado a cabo diversos estudios para tratar de incrementar su cristalizabilidad[9]. Ésta es, de hecho, una de las áreas más activas de investigación en relación con el PLA.

El modo más empleado en la actualidad para la obtención de piezas semicristalinas de PLA es la aplicación de procesos de recocido a las mismas, ya sea durante el procesado -en el caso del moldeo por inyección este proceso se llevaría a cabo dejando el material acabado en el molde durante algún tiempo a temperaturas cercanas a la de cristalización del PLA- como en una etapa posterior -en un horno-. Sin embargo, ambos procedimientos requieren tiempo y energía adicionales al conformado, por lo que no son muy viables para llevarse a cabo en procesos industriales, a no ser que sean utilizados para generar materiales de altas prestaciones que tengan un alto valor añadido. Son muchos los compuestos –polímeros, microcargas, nanocargas y plastificantes, entre otros- que nuclean el PLA de una manera efectiva, lo cual se refleja tanto en descensos de la temperatura de cristalización como en incrementos de la entalpía de fusión de las estructuras cristalinas. Sin embargo, pocos son los aditivos con los que se ha logrado una disminución significativa del tiempo necesario para que el PLA cristalice durante el moldeo por inyección. Así, podemos mencionar que el talco[8], los nanotubos de carbono[10], algunos compuestos orgánicos[10,11] o plastificantes[12], y sobre todo, la adición de estos agentes combinados entre ellos[13], sí han servido para que el polímero cristalice durante el proceso de moldeo por inyección en tiempos que podrían asemejarse a los empleados en procesos industriales convencionales.

En lo que se refiere a las propiedades mecánicas, el PLA muestra un muy buen balance de propiedades de baja deformación. El PLA se caracteriza por su alta rigidez -tiene un módulo de Young cercano a 3500 MPa- y su elevada tensión en fluencia, superior a 70 MPa[6]. Sin embargo, el PLA presenta una fragilidad intrínseca frente a cargas de tracción y flexión, que imposibilita su deformación plástica. Como resultado, la fractura del material ocurre a deformaciones muy bajas y mediante un mecanismo de crazing[14,15]. Asimismo, presenta prestaciones muy limitadas frente a los impactos, sobre todo en casos desfavorables como son los ensayos con entalla. Esta carencia limita considerablemente su uso para la fabricación de piezas estructurales u otro tipo de objetos que requieren un buen comportamiento frente a los golpes[14,15]. Ambas desventajas suponen una restricción evidente del rango de aplicaciones industriales que puede tener el PLA.

2.2 PLA-based blends

Con el fin de mejorar su deformabilidad y su resistencia frente a los impactos, el PLA ha sido modificado y mezclado con una amplia gama de diferentes polímeros, plastificantes y cauchos[6,14,15]. Como resultado, se han obtenido nuevos materiales con un amplio balance de propiedades físicas, térmicas y mecánicas. Las mezclas se han efectuado tanto con polímeros convencionales, no renovables y no biodegradables, como con otros de origen renovable -dando lugar a nuevos materiales de origen renovable al 100% - y / o totalmente biodegradables.

En el primero de los casos, los polímeros convencionales pueden mejorar las prestaciones del PLA y también abaratar costes económicos, debido a que éstos suelen ser en muchos casos más económicos. Entre otras, las mezclas PLA/PBT[16], PLA/PC[17-19] y PLA/PA[20] muestran un buen balance de propiedades mecánicas. Las modificaciones más eficientes, sin embargo, han sido aquellas llevadas a cabo con diferentes cauchos y elastómeros termoplásticos[14,15], ya que han dado lugar a mejoras significativas tanto de la deformabilidad como de la resistencia al impacto. El mayor inconveniente de las mezclas PLA/caucho es su incompatibilidad (exceptuando algunos casos concretos tales como poliamidas elastoméricas (PAE)[21,22] y el copolímero etileno-glicidil metacrilato (EGMA)[23,24]), debido a que el PLA es un polímero polar y la mayoría de estos modificadores de impacto son apolares. La mejora de la compatibilidad entre ambos se ha llevado a cabo generalmente mediante la adición de un agente modificador[25-28] o mediante la modificación química del caucho[29-31].

Sin embargo, las mezclas basadas en PLA que más interés están atrayendo son aquellas preparadas con otros polímeros de origen renovable y/o biodegradable. Claro está, el principal objetivo de estas modificaciones es tratar de obtener nuevos “biomateriales” con origen 100% renovable y/o totalmente biodegradables, que podrían servir para reemplazar en el futuro, materiales que hoy en día están totalmente basados en derivados del petróleo y que no son biodegradables. El mayor inconveniente, sin embargo, es la escasa oferta de polímeros con estas características [32,33].

Se han obtenido materiales con buenas propiedades mecánicas basadas en mezclas PLA/biopolímero con almidón termoplástico[34,35], diferentes poliamidas de origen renovable[36-38] y cauchos naturales[39,40] entre otros. Las mezclas PLA/biopolímero que más atención han despertado hasta la fecha han sido, sin embargo, las basadas en PCL y PBAT. La PCL y el PBAT son dos poliésteres obtenidos a partir de fuentes no-renovables pero que, sin embargo, son 100% biodegradables. Ambos polímeros presentan una baja rigidez combinada con una alta deformabilidad y tenacidad, debido a lo cual son dos buenos candidatos para mejorar la fragilidad intrínseca que muestra el PLA. De hecho, las mezclas PLA/PCL y PLA/PBAT han dado lugar a nuevos materiales con un balance de propiedades finales muy interesante. Generalmente, las mezclas PLA/PCL y PLA/PBAT muestran una menor rigidez que el PLA combinada con una mayor deformabilidad y tenacidad. Ambas son completamente biodegradables, por lo que los materiales obtenidos pueden ser utilizados tanto para la fabricación de materiales con un corto tiempo de vida o de "usar y tirar" -envases, films y embalajes sobre todo- como también de larga durabilidad. En los siguientes apartados se detallarán los resultados más relevantes obtenidos hasta ahora en mezclas PLA/PCL y PLA/PBAT.

2.2.1 PLA/PCL blends

Las mezclas PLA/PCL tienen morfología bifásica, y a pesar de que algunos autores hayan observado una ligerísima miscibilidad parcial entre el PLA y la PCL[41,42], en la mayoría de los trabajos se ha mencionado que ambos polímeros son totalmente inmiscibles. Las propiedades de tracción y flexión de baja deformación de las mezclas PLA/PCL son intermedias entre las de los componentes puros. Respecto a las de alta deformación, únicamente se ha observado elevada ductilidad en mezclas con altos contenidos de PCL[41,43,44], a pesar de la apreciable adhesión interfacial existente entre ambos polímeros y de que incluso hayan sido catalogados como compatibles[45]. En lo que respecta a las propiedades de impacto, se han observado diferentes resultados, desde propiedades intermedias hasta mezclas supertenaces que se mencionarán más adelante.

Se han añadido diferentes agentes compatibilizadores a las mezclas PLA/PCL con el fin de mejorar la compatibilidad y como resultado, su ductilidad, a bajos contenidos de PCL. En disolución, la adición de diferentes copolímeros sintetizados a escala de laboratorio tales como PLLA-PCL-PLLA[46], PCL-PEG[47] y PLLA-PCL[48] ha servido para mejorar la compatibilidad, incluso hasta el punto de incrementar la miscibilidad entre ambos polímeros[47].

Por otro lado, la presencia de pequeños contenidos de triisocianato de L-lisina (LTI) durante el mezclado en fundido entre el PLA y la PCL provocó reacciones de intercambio de cadena y de reticulación[49,50]. Como consecuencia, el tamaño de las partículas de PCL decreció y la adhesión interfacial entre ambas fases aumentó. El efecto compatibilizador del LTI tuvo una gran influencia en las propiedades mecánicas del sistema, ya que permitió obtener materiales dúctiles a bajos contenidos de PCL y a su vez incrementar la resistencia frente a los impactos de las mezclas.

La realización de procesos de recocido sobre la mezcla compatibilizada PLA/PCL/LTI (85/15/1) sirvió además para inducir reacciones adicionales entre el PLA y la PCL, y como resultado la deformabilidad de las mezclas aumentó aún más como resultado de la supresión del proceso de cavitación[51], que provoca la rotura prematura de las mismas. Harada y col.[52] observaron que, como resultado de una mayor compatibilidad, la deformabilidad de la mezcla PLA/PCL 80/20 aumentó de 22% a 288% en presencia de 0.3% de LTI y la resistencia al impacto de 2 KJ/m^2 hasta 17.3 KJ/m^2 en presencia de 0.5% de LTI. Del mismo modo, el trabajo de fractura de las mezclas PLA/PCL 50/50[53,54] y 85/15[49,50] aumentó en presencia de la LTI.

La adición de pequeños contenidos de dicumil peróxido (DCP) durante el procesado de las mezclas también sirvió para incrementar la ductilidad y la resistencia al impacto de las mezclas PLA/PCL, ya que éste provocó que se produjeran reacciones de entrecruzamiento entre ambos polímeros. Sin embargo, a contenidos demasiado elevados de DCP, el efecto se invirtió como consecuencia del alto nivel de entrecruzamiento producido durante el mezclado[45]. Además, se observó que la adición del agente de entrecruzamiento fue más eficiente cuando se realizó durante el proceso de extrusión que al inicio del mismo[55]. Como resultado de la presencia de DCP, el módulo de Young de las mezclas compatibilizadas fue ligeramente superior al de las puras, y en la mezcla 70/30 la compatibilización dio lugar al alargamiento de las partículas de PCL y como consecuencia, se obtuvieron valores de deformabilidad superiores al 60% en presencia de 0.1% y 0.2% de DCP[56]. Con la adición de trifenil fosfito (TPP) también se obtuvieron resultados similares[57].

Cuando la PCL ha sido empleada exclusivamente como modificadora frente a los impactos del PLA[11,58], se han obtenido materiales 100% biodegradables con una alta tenacidad. En el primero de los trabajos[11] se emplearon copolímeros al azar poli(ε-caprolactona-ácido láctico) (P[CL-co-LA]) sintetizados en el laboratorio como modificadores de impacto. Se sintetizaron copolímeros con diferentes contenidos CL/LA (mol/mol) que variaron su composición de 91/9 a 51/49 y se añadieron al PLA en un 10% en todos los casos. El módulo de Young del PLA descendió un 10% tras la adición de los copolímeros, y la elongación a rotura aumentó del 4% al 20%. La tenacidad del PLA, medida mediante ensayos de impacto Izod con entalla y con un valor de 2.7±0.1 KJ/m^2 en el polímero puro, aumentó tras la adición de todos los copolímeros, obteniéndose los valores más elevados en la mezcla con el copolímero 72/28, cuya resistencia al impacto fue de 11.4 KJ/m^2. En todos los demás casos los valores obtenidos fueron menores de 8.5 KJ/m^2. Como resultado positivo adicional, la transparencia del PLA también se mantuvo en las mezclas. Las imágenes de SEM de las diferentes mezclas compatibilizadas revelaron que las partículas de la fase dispersa, de morfología esférica, tenían un tamaño muy parecido entre ellas, entre 0.70 y 0.90 µm. El mayor tamaño de partícula se midió en la mezcla más tenaz. La morfología de las mezclas también fue analizada mediante TEM y AFM - que tienen mayor resolución- y se observó en todos los casos una población minoritaria adicional de partículas de mucho menor tamaño, del orden de 100-200 nm, prácticamente inapreciables mediante SEM. La forma de estas partículas varía con la relación LA/CL del copolímero, y se observó que en el caso de la 72/28 fue fibrilar mientras que en todas las demás fue esférica. Esta morfología, también observada en otras mezclas PLA/PCL[59] se relacionó con la afinidad y miscibilidad entre el PLA y el copolímero, y pudo ser la causante de la mayor tenacidad de la mezcla.

En el segundo de los trabajos[58] se obtuvieron mezclas PLA/PCL supertenaces con alta resistencia térmica (medida mediante HDT). Además, se analizó el efecto que ejerce la cristalinidad del PLA en la tenacidad de las mezclas, y los resultados obtenidos indicaron la existencia de una relación directa entre la resistencia al impacto de las mezclas, el grado de cristalinidad del PLA y el tamaño de las partículas de PCL. El estudio se llevó a cabo sobre la composición PLA/PCL 80/20, mezclada en una extrusora bi-tornillo a diferentes velocidades de giro de los husillos (50-400 rpm) y posteriormente moldeada por inyección a dos temperaturas diferentes de molde (50ºC y 130ºC), y sometida a diferentes procesos de recocido por tiempos entre 1 y 6 min en el molde a 130ºC. Para incrementar el grado de cristalinidad del PLA se añadió un agente de nucleación –N, N’, N’’-tricicloexil-1, 3,5-benceno-tricarboxiamida o (TMC-328)- durante el mezclado. Las distintas velocidades de giro de los husillos de la extrusora se utilizaron para controlar el tamaño de las partículas de PCL, y la adición de TMC-328 y las diferentes temperaturas del molde durante el proceso de inyección para controlar el grado de cristalinidad del PLA. Los resultados obtenidos en el trabajo muestran que el tamaño óptimo de partícula de PCL para obtener supertenacidad depende directamente del grado de cristalinidad del PLA.

En el caso de mezclas con matriz semicristalina el tamaño de partícula de caucho efectiva para incrementar la tenacidad es menor (0.3-0.5 µm) que en el caso de mezclas que contienen una matriz totalmente amorfa (0.7-1.1 µm). Este hecho está relacionado con el mecanismo de fractura de cada tipo de material, el cual ocurre mediante “shear yielding” en el primero de los casos y mediante “crazing” en el segundo de ellos. Por ello, la resistencia al impacto máxima que se obtuvo con matriz semicristalina, superior a 30 KJ/m^2, fue mayor que la obtenida con matriz amorfa, inferior a 16 KJ/m^2 [60]. Estos resultados podrían servir para explicar los incrementos en la resistencia al impacto de mezclas PLA/caucho estudiadas previamente, en las que se observó que la tenacidad variaba con el grado de cristalinidad de la matriz[23,25,61].

2.2.2 PLA/PBAT blends

Los resultados obtenidos en lo que respecta a la estructura de las mezclas PLA/PBAT no son concluyentes. Algunos autores afirman que el PLA y el PBAT son totalmente inmiscibles[62-66], aunque se han observado tamaños de partícula muy pequeños[63] e interacciones entre ambos polímeros[64]. Otros autores han observado descensos en la Tg del PLA, típicos de mezclas parcialmente miscibles, en presencia de PBAT[65,67,68], y sin embargo, la miscibilidad parcial no ha dado lugar a mezclas compatibles[67]. Incluso, las mezclas mostraron miscibilidad total entre el PLA y el PBAT a muy bajos contenidos del último, 2.5%, y miscibilidad parcial a mayores contenidos de PBAT[69]. También existen diferencias en cuanto al tamaño de las partículas de PBAT que, como es conocido, depende de la relación entre las viscosidades de ambas fases y de la tensión interfacial entre ambos polímeros[64]. Por ejemplo, mientras que en uno de los trabajos se observó que el tamaño de partícula aumenta de 1 μm a 5 μm al pasar de la mezcla 95/5 a la 80/20[62], en otro se mantuvo constante, cerca de 300 nm, independientemente del contenido de PBAT[63].

La adición de PBAT da lugar a un incremento de la elasticidad en fundido[63] y de la viscosidad del PLA[63,66]. Además, disminuye el módulo de Young, así como la tensión de fluencia y la de rotura del PLA. Por el contrario, la deformabilidad y la resistencia al impacto del PLA aumentan en general en presencia de PBAT, en mayor o menor medida dependiendo de la compatibilidad del sistema.

En lo que respecta las propiedades de las mezclas PLA/PBAT, Farsetti y col.[62] observaron que el módulo de Young y la tensión en fluencia del PLA decrecen de 3680 MPa y 65 MPa a 2520 MPa y 46 MPa, respectivamente, con 20% de PBAT añadido, y que la deformabilidad aumenta de 3.6% hasta 44.6%. Con la adición del mismo contenido de PBAT, Yeh y col.[69] obtuvieron mezclas de mucha mayor ductilidad, deformables hasta 266%, aunque este incremento estuvo acompañado de un descenso muy pronunciado de la resistencia a la rotura del PLA, de aproximadamente 60 MPa a 10 MPa. En otro de los trabajos[63], se obtuvieron descensos del módulo y de la resistencia a la tracción de 3400 MPa a 2600 MPa y de 63 MPa a 47 MPa, respectivamente, con 20% de PBAT. La deformabilidad de las mezclas fue superior a 100% con 10% de PBAT y todavía mayor a contenidos más elevados, mientras que la resistencia al impacto, medida mediante ensayos Izod, se incrementó de 2.6 KJ/m^2 a 4.4 KJ/m^2 con 20% de PBAT.

Algunos autores han estudiado el efecto de la adición de diferentes compatibilizadores acrílicos[65,67,70,71] y de DCP en las propiedades mecánicas de diferentes mezclas PLA/PBAT. Kumar y col.[67] añadieron 3% y 5% de glicidil metacrilato (GMA) a la mezcla PLA/PBAT 75/25. La adición del compatibilizador provocó un incremento del módulo de Young de la mezcla, y así, con 5% de GMA añadido, su valor aumentó hasta llegar a ser incluso un 40% mayor que el del PLA puro. El mecanismo de rotura de los materiales en ensayos de tracción cambió en presencia del compatibilizador, pero este hecho no se plasmó en la ductilidad. Así, la deformación a rotura de la mezcla 75/25, 6.75%, no varió en presencia de 3% y 5% de GMA. También se observó un cambio en el mecanismo de rotura en impacto de la mezcla 75/25, de frágil a tenaz, y la resistencia al impacto Izod del PLA aumentó de 21 J/m a 50 J/m con 25% de PBAT y hasta 76 J/m con 5% de GMA añadido.

En otro de los trabajos[65] se estudió el efecto que tiene la adición de T-GMA, de 0% a 10%, en diferentes mezclas PLA/PBAT. Tanto la resistencia a la tracción como la ductilidad de las mezclas aumentaron en presencia de T-GMA. Por ejemplo, la ductilidad de la mezcla 90/10 aumentó de 50% a 180% con un 5% de compatibilizador añadido. Por otro lado, el mecanismo de fractura de las mezclas PLA/PBAT cambió tras la adición de T-GMA, pasándose a observar estricción en el ensayo de tracción. Para cada mezcla PLA/PBAT se determinó un contenido óptimo de contenido de compatibilizador, llegándose a obtener valores máximos de resistencia al impacto de 15 KJ/m^2, 28 KJ/m^2 y 32 KJ/m^2 en las mezclas 90/10/4%, 80/20/2% y 70/30/3%, respectivamente. Del mismo modo, la adición de 0.3%, 0.5%, 1% y 2% de un copolímero funcionalizado con grupos epoxi de nombre comercial JONCRYL a mezclas PLA/PBAT 95/5, 85/15 y 70/30[70] dio lugar a un aumento considerable de su resistencia al impacto, medida mediante ensayos Charpy. Los valores máximos obtenidos fueron 26 KJ/m^2 y 28 KJ/m^2 en las mezclas 85/15/0.5% y 70/30/0.2%, respectivamente. El mecanismo de fractura de los materiales se analizó mediante SEM tomando como ejemplo la composición 85/15. En la mezcla pura se observó despegue y cavitación de las partículas de PBAT, mientras que en la mezcla compatibilizada con 0.5%, además del despegue y cavitación de las partículas dispersas, se observó que la matriz de PLA sufrió deformación plástica y, como consecuencia, fue capaz de disipar la energía recibida en el impacto.

Al-Itry y col. estudiaron el efecto de la adición de diferentes contenidos de una resina epoxi multifuncional comercial en la mezcla PLA/PBAT 80/20[71]. La adición del compatibilizador sirvió, por un lado, para contrarrestar la degradación térmica padecida por el PLA durante el procesado en fundido de la mezcla, ya que las reacciones de ramificación inducidas en su presencia compensaron el descenso del peso molecular de las cadenas. Por otro lado, el módulo del PLA descendió en presencia de PBAT, pero la presencia del compatibilizador sirvió para contrarrestar parcialmente este descenso. Además, la ductilidad del PLA aumentó de 14% a 50% con la adición de PBAT, y hasta 135% tras añadir 0.5% de compatibilizador a la mezcla. Por último, la adición de diferentes contenidos de DCP provocó un incremento en la compatibilidad de la mezcla PLA/PBAT 80/20, ya que los radicales de PLA y PBAT formados en la mezcladora tras la adición del peróxido reaccionaron entre sí dando lugar a ramificaciones/entrecruzamientos PLA/PLA, ramificaciones/entrecruzamientos PBAT/PBAT, copolímeros PLA-g-PBAT y redes PLA-PBAT entrecruzadas. Todo ello provocó un descenso de la tensión interfacial y del tamaño de las partículas de PBAT. La mezcla PLA/PBAT 80/20, aunque deformable en tracción, mostró una baja resistencia al impacto. La adición de pequeños contenidos de DCP dio lugar a un incremento de la ductilidad de la mezcla hasta más de 300%, aunque a contenidos superiores esta propiedad decreció. Por su parte, la resistencia al impacto Izod con entalla aumentó hasta el valor máximo de 110 J/m con 0.5% de DCP añadido. Ambos incrementos se atribuyeron a cambios en los mecanismos de fractura de la mezcla.

2.3 Polymer nanocomposites

La adición de pequeños contenidos de nanopartículas orgánicas o inorgánicas ha resultado ser una manera muy simple, pero eficiente, de mejorar las prestaciones de los polímeros, y también de dotarles de propiedades únicas para que éstos puedan ser empleados en aplicaciones más específicas hasta ahora cubiertas por otro tipo de materiales.

La eficiencia de las nanopartículas suele depender de su grado de dispersión en la matriz polimérica. Generalmente, las propiedades mecánicas de baja deformación y las propiedades de barrera mejoran cuanto mayor es el grado de dispersión y lo contrario sucede con la deformabilidad y la resistencia al impacto. Para obtener buenos niveles de dispersión, la superficie de las nanopartículas se encuentra habitualmente parcialmente modificada con grupos o agentes químicos que son compatibles con el polímero en el que deben dispersarse. Sin embargo, el método y las condiciones empleadas para la obtención y producción de nanocompuestos también juegan un rol muy importante. En el caso concreto de los nanocompuestos poliméricos preparados en estado fundido, el tiempo, la temperatura y el esfuerzo de cizalla empleados durante el mezclado son parámetros que pueden influir drásticamente en el nivel de dispersión final.

El PLA ha sido modificado con diferentes nanocargas orgánicas y minerales tales como nanotubos de carbono, grafeno, diferentes nanoarcillas o nanopartículas de sílice[72]. Se han obtenido nanocompuestos basados en PLA con propiedades mecánicas mejoradas y se ha dotado al polímero de características específicas para que pueda ser utilizado en diversas aplicaciones ingenieriles. Estas han sido, entre otras, una mayor temperatura de reblandecimiento HDT[8], retardo a la llama[73], semiconductividad[74] o propiedades barrera frente al paso de gases y vapores[75].

2.3.1 Polymer/nanoclay nanocomposites

Los nanocompuestos polímero/arcilla son materiales multicomponente que contienen una matriz polimérica y partículas inorgánicas de arcilla laminar. Son materiales de gran interés porque presentan propiedades mecánicas y térmicas mejoradas, unidas a una alta resistencia al fuego y una menor permeabilidad a los gases y vapores en comparación con el polímero puro preparado en las mismas condiciones.

Las montmorillonitas (MMT)[76] son las arcillas más empleadas en estos nanocompuestos debido a su abundancia, al bajo coste para su obtención y la facilidad para su modificación química. La montmorillonita pura suele ser en general incompatible con los polímeros debido a su alta hidrofilia y por lo tanto es habitual su modificación química con diferentes cationes orgánicos, por ejemplo de tipo amonio, denominados surfactantes, para aumentar las interacciones entre ambos y así mejorar el nivel de dispersión. En el mercado existen diferentes montmorillonitas modificadas orgánicamente (oMMT) con diferentes surfactantes.

La técnica más utilizada en la actualidad para la fabricación de nanocompuestos polímero/arcilla es la intercalación en fundido[77]. Durante el procesado en fundido, el polímero y la arcilla se mezclan a una temperatura adecuada en presencia de esfuerzos de cizalla, y se obtienen nanocompuestos intercalados o exfoliados dependiendo del grado de difusión de las cadenas poliméricas entre las láminas de arcilla.

2.3.1.1 PLA/oMMT nanocomposites

Ray, Okamoto y col. llevaron a cabo una pionera y exhaustiva investigación relativa a nanocompuestos PLA/arcilla procesados en fundido[78-85]. En los diferentes trabajos se utilizaron diferentes tipos de arcillas modificadas a escala de laboratorio con una larga serie de surfactantes. Los nanocompuestos se obtuvieron en todos los casos en una extrusora de doble husillo a 210ºC y después se procesaron láminas mediante moldeo por compresión, que fueron cristalizadas tras un proceso de recocido para efectuar las medidas de difracción de rayos-X (WAXD), microscopía electrónica de transmisión (TEM) y análisis mecánico dinámico (DMTA).

Los nanocompuestos basados en PLA y MMT modificada con dimetiloctadecilamina (DMODA)[84] y trimetiloctadecilamina (TMODA)[80] mostraron buenas propiedades generales, a pesar de que, independientemente del contenido añadido, en ambos casos se observó intercalación del polímero entre las láminas de arcilla, pero no completa exfoliación. Con DMODA-MMT el módulo de flexión del PLA aumentó un 12% con 4% añadido y el máximo valor de la resistencia a la flexión fue 24% mayor que el del PLA puro, con 5% añadido. El máximo aumento de la temperatura HDT (de 76ºC a 108ºC) y el mayor descenso de la permeabilidad al oxígeno (25%) se observaron con 7% de arcilla. En los nanocompuestos preparados con TMODA-MMT los mejores resultados se obtuvieron con 7% de arcilla, que dio lugar a un aumento en el módulo de flexión de un 20%, en la tempertura HDT de 76ºC a 111ºC y a un descenso de un 19% de la permeabilidad al oxígeno del PLA.

En lo que respecta a trabajos llevados a cabo exclusivamente con montmorillonitas comerciales, tanto en nanocompuestos obtenidos en disolución[86] como en fundido[87,88], el mayor grado de dispersión se ha obtenido con arcillas modificadas con cadenas hidrogenadas de metil dihidroxietil amonio (comercialmente conocida, entre otras denominaciones, como Cloisite30B). Esta arcilla fue la que mostró mayor afinidad con el PLA, como resultado de las interacciones entre los grupos hidroxilo del modificador orgánico y los grupos carbonilo de las cadenas macromoleculares[86]. Krishnamachari y col. analizaron el nivel de dispersión de montmorillonitas modificadas de la casa Southern Clay[87,88] en nanocompuestos procesados en fundido en un mezclador interno. La Cloisite30B fue la única de las diferentes arcillas que se exfolió por completo en la matriz de PLA. La secuencia del nivel de intercalación de las cadenas de PLA entre las láminas de las demás arcillas fue $Na^+ < 25A < 20A < 93A < 15A$.

A pesar de la buena afinidad existente entre el PLA y la Cloisite30B, su mezclado ha dado lugar, en general, a nanocompuestos intercalados, independientemente del contenido de arcilla. En algunos casos también se han obtenido nanocompuestos totalmente exfoliados[87-93], y en otros las láminas de oMMT se encuentran totalmente exfoliadas a bajos contenidos e intercaladas a contenidos superiores[94]. También se ha conseguido convertir nanocompuestos intercalados en nanocompuestos totalmente exfoliados incrementando el tiempo de mezclado[95]. Merece la pena mencionar el denominado "d-spacing collapse", proceso observado por primera vez por Filippi y col.[96] y que está relacionado con la dispersión de la arcilla Cloisite30B. Se produce cuando en nanocompuestos polímero/Cloisite30B procesados en fundido a temperaturas cercanas o inferiores a 200º los modificadores orgánicos de la Cloisite30B son capaces de cambiar su disposición espacial y compactarse, provocando que la distancia interlaminar entre las láminas de oMMT disminuya y dando lugar a un empeoramiento del nivel de dispersión.

Las láminas de oMMT actúan como agentes de nucleación del PLA, y su poder nucleante suele estar directamente relacionado con su dispersión dentro de la matriz de PLA. Generalmente, la densidad de nucleación del PLA y la cristalinidad son superiores en nanocompuestos intercalados que en nanocompuestos totalmente exfoliados[83,90,94]. Para explicar este comportamiento se mencionó que las láminas de arcilla completamente exfoliadas dificultan las interacciones intermoleculares entre las diferentes cadenas de PLA, que son vitales para la formación de los núcleos cristalinos[90].

La adición de oMMT ha servido generalmente para incrementar la estabilidad térmica del PLA[88,89,95,97], aunque también se han visto descensos de 25ºC en la temperatura de degradación (medida como $T_{5\%wt}$) a altos contenidos de arcilla (8%)[98]. Por otro lado, la presencia de oMMT incrementa la velocidad de degradación foto-oxidativa del polímero [99,100]. La presencia de oMMT también puede modificar la velocidad de degradación del polímero en condiciones de biodegradación bajo compost o enzimática[80,101-103], aunque existe controversia respecto al efecto real que ejercen las láminas de la arcilla.

Se han medido las propiedades mecánicas de nanocompuestos PLA/oMMT en diversos trabajos. En algunos de ellos, las propiedades se midieron mediante ensayos mecánico-dinámicos, en los cuales se observó que el módulo de almacenamiento del PLA aumenta con el contenido de arcilla[97,104,105], y de forma más pronunciada cuanto mayor es la temperatura de ensayo[97].

Las láminas de arcilla pueden ejercer un doble papel en la deformación micro-mecánica de los nanocompuestos: por una parte pueden proporcionar zonas de nucleación en sus superficies capaces de facilitar la rendición por cortadura del material, mientras que a altos contenidos impiden la coalescencia de estas zonas, por lo que se favorecería la rotura mediante "crazing"[106].

Como resultado, los nanocompuestos con bajos contenidos de arcilla (2.5%) son más deformables que el PLA puro. A mayores contenidos sin embargo (5% y 7.5%) las láminas de arcilla forman una red de percolación dentro de la matriz, lo que restringe la movilidad de las cadenas de PLA durante el proceso de tracción. Además, la cantidad de aglomerados que se forman a altos contenidos es mayor, lo que facilita la fractura prematura de los nanocompuestos[106]. Resultados similares se obtuvieron en el trabajo de Lai y col.[94]. Estos autores observaron un efecto plastificante producido por láminas de arcilla exfoliadas cuando el contenido fue del 1%, que desapareció a mayores contenidos, 3% y 5%. Debido a la plastificación, el módulo de Young del PLA decreció un 30% y la deformabilidad aumentó de 5% a 208%. El efecto observado se relacionó con el alto nivel de exfoliación de oMMT, debido al cual se creó una amplia área de contacto entre ambas fases, y como consecuencia una región interfacial muy plastificada. Estas zonas del material son muy deformables bajo esfuerzos de tracción, y son capaces de cambiar el mecanismo de deformación del nanocompuesto, dando lugar así a ductilidades superiores al 200%.

Zaidi y col. por su parte estudiaron las propiedades de tracción de nanocompuestos PLA/oMMT con 1, 3 y 5% de arcilla[89,100]. La adición de contenidos crecientes de arcilla dio lugar a un incremento progresivo del módulo de Young del PLA, acompañado de un descenso de la deformabilidad y de la resistencia a la tracción. Con el máximo contenido, los valores correspondientes de dichas propiedades fueron 5577 MPa, 28.8 MPa y 0.7% respectivamente. El descenso de la resistencia a la tracción se relacionó con el descenso de la deformabilidad, ya que la fractura de los nanocompuestos se produjo antes del punto de fluencia. En cuanto a las propiedades de nanoindentación, medidas con dos penetradores diferentes, también se observo un incremento progresivo del módulo y una mayor dureza a mayores contenidos de oMMT. La dureza máxima de los nanocompuestos fue dependiente del tipo de penetrador utilizado, 36% y 19% superior a la del PLA puro. Jiang y col.[106] también observaron que el módulo de Young del PLA aumenta progresivamente con el contenido de una oMMT que contiene el mismo surfactante que la Cloisite30B.

2.3.1.2 PCL/oMMT nanocomposites

Los nanocompuestos PCL/MMT fueron, en 1993, los primeros nanocompuestos biopolímero/arcilla investigados, procesados mediante polimerización in situ[107]. Los modos más empleados para preparar nanocompuestos PCL/oMMT han sido el anteriormente mencionado y en disolución[108-110], aunque también existen trabajos relativos a nanocompuestos preparados en estado fundido[111-116].

Pantoustier y col.[111] prepararon nanocompuestos PCL/oMMT con 3% de las arcillas CloisiteNa, Cloisite25A (modificada con una cadena hidrocarbonada), Cloisite30B y nanofil820 (modificada con grupos reactivos ácido) tanto en fundido como por polimerización in-situ. A pesar de que los niveles de dispersión más elevados se obtuvieron mediante la polimerización in-situ, el mezclado en fundido también sirvió para dispersar adecuadamente las láminas de arcilla en la matriz de PCL. Los nanocompuestos con las arcillas 25A y 30B mostraron estructuras intercaladas/exfoliadas, con un mayor nivel de intercalación en el caso de la 30B.

Del mismo modo que otros autores hicieron con el PLA[86-88], se ha estudiado el nivel de dispersión de seis diferentes arcillas tipo Cloisite y las propiedades mecánicas de los nanocompuestos basados en PCL con 5% de cada una de ellas[115,116]. La arcilla Cloisite20A se exfolió completamente en la PCL, y las demás mostraron estructuras intercaladas con un nivel de intercalación en el orden 30B>25A>10A>93A>Na. El módulo de Young de la PCL aumentó tras la adición de las arcillas, y se obtuvieron valores directamente relacionados con el grado de dispersión de cada una de ellas. Los incrementos con la 20A y la 30B fueron 42% y 30%, respectivamente. La resistencia a la tracción se mantuvo cercana a 15 MPa en todos los casos y la deformabilidad de la PCL disminuyó hasta un 36% respecto al material puro, aunque aún manteniendo valores superiores a 1200% en todos los casos.

El grado de dispersión de los nanocompuestos PCL/oMMT está relacionado con la temperatura del fundido polimérico durante el mezclado, siendo mayor cuando el mezclado se lleva a cabo a 100ºC que a 180ºC, debido a las mayores fuerzas de cizalla consecuencia de la mayor viscosidad de la matriz[112]. Se obtuvieron conclusiones similares en otro trabajo[114], en el que se prepararon diferentes nanocompuestos PCL/oMMT en condiciones de alta cizalla y cortos tiempos de residencia (velocidad de giro de tornillo 250 rpm) a partir de masterbatches con 30% de arcilla preparados anteriormente en un mezclador interno.

Estos últimos nanocompuestos se moldearon posteriormente por inyección. El módulo de Young de la PCL aumentó con el contenido de las tres arcillas casi de igual manera, y con un 5% añadido su valor se duplicó de ≈400 MPa a ≈800 MPa. En el caso de nanocompuestos con estructuras intercaladas (Δd_{001}=0.84 nm o Δd_{001}=1.26 nm para las arcillas 25A y 30B, respectivamente), los valores de módulo más elevados fueron 28-33% superiores al de la PCL pura y su ductilidad se mantuvo por encima de 500%[111].

Las propiedades barrera de los nanocompuestos PCL/oMMT dependen del nivel de dispersión de las arcillas, que puede ser controlado durante el procesado. La permeabilidad de los nanocompuestos procesados en fundido con 3% de Cloisite30B fue 47%, 48% y 56% menor que la de la PCL pura frente al helio, al hidrógeno y al dióxido de carbono, respectivamente[113]. Por otro lado, la oMMT actúa como agente nucleante para la cristalización de la PCL a bajos contenidos (2% y 5%), mientras que a contenidos superiores (10%), la inmovilización de las cadenas de PCL producida por la presencia de las láminas de arcilla dificulta el proceso[112].

2.3.2 Polymer/CNT nanocomposites

Los nanotubos de carbono conforman, al igual que el grafito o diamante, una forma alotrópica del carbono. Morfológicamente son láminas de grafito enrolladas sobre sí mismas con diámetros que pueden oscilar de 1 nm a 5 nm y que, dependiendo de si están formados por una o varias láminas concéntricas se denominan nanotubos de pared simple (SWCNT) o de pared múltiple (MWCNT), respectivamente. Poseen una rigidez y una conductividad eléctrica muy elevadas y, cuando se añaden a los materiales poliméricos, incluso en muy pequeñas cantidades, permiten obtener materiales con propiedades específicas de gran interés. Esto convierte a los nanocompuestos polímero/CNT en materiales de gran atractivo, ya que presentan propiedades mecánicas y térmicas mejoradas, muy bajo peso específico, y en las condiciones adecuadas, semiconductividad[117-120], lo que permitiría su posible aplicación en dispositivos eléctricos y electrónicos, en sustitución de materiales semiconductores convencionales tales como el silicio y/o el germanio entre otras posibles aplicaciones.

Se pueden obtener nanocompuestos polímero/CNT con altos niveles de dispersión de los nanotubos tanto en disolución como en estado fundido[119,121], aunque desde un punto de vista industrial el procesado en fundido resulta mucho más interesante. Existen dos vías principales para optimizar el mezclado en fundido entre los polímeros y los nanotubos de carbono y obtener así diferentes grados de dispersión y, como consecuencia de ello, diferentes propiedades. Por un lado, la modificación de los parámetros de procesado de los nanocompuestos[121,122] y, por otro, la modificación química de la superficie de los nanotubos mediante el injerto de grupos afines al polímero en el que se pretenden dispersar[123,124].

La condición necesaria para obtener nanocompuestos que presenten semiconductividad es la formación de una red tridimensional conductora de los nanotubos en el seno de la matriz polimérica. La concentración crítica de nanotubos a partir de la cual ocurre un incremento drástico en la conductividad eléctrica de los nanocompuestos polímero/CNT se conoce como percolación eléctrica (p:)[125,126]. Los valores típicos de p: suelen encontrarse entre el 1% y el 5% de contenido de nanotubos, aunque en bibliografía se han mencionado valores superiores[127] e inferiores[128-130].

2.3.2.1 PLA/CNT nanocomposites

Los nanocompuestos PLA/CNT se han obtenido en disolución, en estado fundido, e incluso mediante la combinación de ambos[10,131]. La gran mayoría de los estudios se han llevado a cabo utilizando nanotubos comerciales no modificados (llamados “pristine” o purificados, pCNT)[74,131-136] y modificados con grupos carboxilo[133-137] o hidroxilo[136,138,139]. Asimismo, también se han preparado nanocompuestos con nanotubos modificados en el laboratorio, entre los que destacan los realizados con CNT-g-PLA[139-143], CNT-g-HDA[144,145], CNT-g-DDA[146] y CNT-g-MA[147].

Se ha comprobado que el nivel de dispersión de los nanotubos en el PLA depende íntimamente de la funcionalización de los mismos y, de acuerdo con resultados obtenidos mediante caracterización viscoelástica, los modificados con grupos carboxilo se dispersan mejor que los no-modificados y que los modificados con grupos hidroxilo[136]. Sin embargo, el nivel de dispersión de los pCNTs puede mejorarse considerablemente optimizando las condiciones de procesado en fundido[74]. La velocidad de giro de los husillos (y por tanto, la fuerza de cizalla empleada) es el parámetro más importante para obtener altos niveles de dispersión, y la mejora que supone incrementar la velocidad de 100 rpm a 500 rpm es muy notable. Optimizando las condiciones de procesado se logró obtener nanocompuestos en los que un 99.8% de los nanotubos se encontraban monodispersos, y cuya percolación eléctrica tuvo lugar a contenidos de 0.5% de nanotubo.

La incorporación de nanotubos de carbono al PLA suele conllevar cambios en la capacidad de cristalización del polímero debido al pequeño tamaño y alto factor de forma que éstos presentan[9]. Todos los autores subrayan que debido a la nucleación heterogénea promovida por los nanotubos, la cantidad de esferulitas de PLA aumenta y su tamaño decrece en los nanocompuestos[10,132,144,145,148]. La eficiencia nucleante de los nanotubos está directamente relacionada con la dispersión de los mismos[74], y es mayor cuanto mejor dispersos están. Por ello, algunos autores dudan del verdadero carácter nucleante de los nanotubos en nanocompuestos preparados en fundido[9], en los cuales se obtienen generalmente peores dispersiones que en los nanocompuestos preparados en disolución[119].

Sin embargo, algunos trabajos basados en nanocompuestos PLA/CNT procesados en fundido muestran claramente que los nanotubos aceleran la velocidad de cristalización del PLA, tanto en condiciones isotérmicas como no-isotérmicas. Esta mayor velocidad se debe a un diferente mecanismo de crecimiento de los cristales promovido por la elevada densidad de puntos de nucleación en el área superficial de los nanotubos[132]. Por otro lado, los nanotubos pueden provocar comportamientos contrarios en el proceso de cristalización en frío del PLA cuando se somete a éste a un barrido de calentamiento, ya que por un lado promueven la nucleación (factor termodinámico) pero por otro lado impiden el crecimiento de los cristales (factor dinámico)[148].

En lo que respecta al grado de cristalinidad del PLA, se han observado resultados contrapuestos, incluso utilizando los mismos nanotubos de carbono[144,145]. A bajos contenidos (0.5%) el grado de cristalinidad decrece[138] y a contenidos superiores (1.5%) aumenta[139]. Tanto el tipo de nanotubos como el método de procesado empleados en ambos trabajos son idénticos, por lo que la diferencia debería estar únicamente relacionada con el contenido de nanotubos. La combinación del efecto nucleante de los nanotubos y la orientación de las cadenas de PLA pueden tener un efecto sinergístico, lo que da lugar a un incremento en la velocidad de crecimiento de los cristales de PLA alrededor de los nanotubos[10]. Este efecto fue incluso aprovechado para obtener nanocompuestos semicristalinos por moldeo por inyección, lo que, teniendo en cuenta la rápida velocidad de enfriamiento típico de ésta técnica de procesado y la lenta cinética de cristalización del PLA, es un resultado notable.

Es habitual observar que las propiedades de tracción del PLA mejoran en presencia de diferentes tipos de nanotubos. Los nanotubos no modificados son capaces de aumentar significativamente el módulo de Young, ~7.5%, y la resistencia a la tracción del PLA, ~19%, incluso a bajos contenidos añadidos[132]. Las propiedades mecánicas de los nanocompuestos PLA/COOH-CNT dependen del factor de forma de los nanotubos[137]. Los nanocompuestos preparados con nanotubos de alto factor de forma (HAR-CNT) poseen mayor rigidez que los preparados con nanotubos de bajo factor de forma (LAR-CNT), sobre todo a altos contenidos. Este efecto se debe a que, a bajos contenidos, los LAR-CNT se dispersan como fibras flexionadas de nanotubos y los HAR-CNT como pequeños conjuntos enmarañados, mientras que a altos contenidos ambos se enmarañan en la matriz. Así, a altos contenidos de nanotubos los nanocompuestos con HAR-CNT forman una red percolada mucho más compacta, lo cual produce una mayor rigidez en comparación con los nanocompuestos preparados con LAR-CNT.

Un resultado inesperado fue el obtenido en nanocompuestos recocidos PLA/CNT-HDA[145]. A pesar de la buena afinidad entre ambos componentes y, por tanto, la buena dispersión de los nanotubos en la matriz PLA, el módulo de Young decreció sorprendentemente de 6100 MPa a 4700 MPa, mientras que la resistencia a la tracción y la deformabilidad del PLA aumentaron con un contenido de 1.5%, de 61.0 MPa a 61.6 MPa y de 1.5% a 2.7%, respectivamente. No se presentaron razones para justificar estos resultados.

En cuanto a la conductividad eléctrica de los nanocompuestos se refiere, tanto con CNT-COOH como con HAR-CNTs se obtuvieron materiales semiconductores, aunque el contenido necesario para lograrlo fue diferente en cada caso[135]. La percolación eléctrica de los nanocompuestos PLA/CNT-COOH y PLA/HAR-CNT se observó con 3% y 1% de nanotubos, respectivamente. Por otro lado, la adición de 1.5% de MWCNT-g-HDA no tuvo ningún efecto en la conductividad del PLA, debido seguramente a que los grupos alquilo que tiene el HDA injertados en la superficie de los nanotubos dificultan el paso de los electrones[145]. Por último, en condiciones de procesado en fundido optimizadas se obtuvieron nanocompuestos PLA/pCNT semiconductores a partir de 0.5% de contenido de nanotubos[74].

La adición de los nanotubos también provoca un aumento en la estabilidad térmica del PLA[132,136,148] debido a su mayor estabilidad térmica respecto al propio PLA y también porque crean una barrera física dentro del material, que retrasa la descomposición de los nanocompuestos en comparación con el PLA puro. Por otro lado, la velocidad de biodegradación del PLA se retarda en presencia de los nanotubos debido al efecto inhibidor de los mismos[148].

2.3.2.2 PCL/CNT nanocomposites

Se ha observado que las condiciones óptimas para dispersar pCNTs en la PCL en una extrusora de doble husillo son altas velocidades de husillo (500 rpm)[149], mientras que en un mezclador interno parecen más eficaces bajas velocidades (75 rpm)[149]. La cizalla que favorece la dispersión en el extrusor provoca la degradación del polímero en el mezclador. La red de percolación eléctrica en el primero de los casos se formó con un contenido en nanotubos de 0.37%.

En otros dos trabajos relativos a PCL/pCNT mezclados en una extrusora, la semiconductividad también se observó con contenidos de nanotubos similares, cercanos a 0.3%[150,151]. En ambos casos se observó un muy buen nivel de dispersión de los nanotubos, lo que provocó, además, cambios importantes en la cinética de cristalización de la matriz. En ambos casos la temperatura de cristalización de la PCL aumentó considerablemente, 14ºC y 17ºC respectivamente. De hecho, el primero de los trabajos habla de supernucleación de la PCL[150], definida como un mayor poder de nucleación que el proporcionado por los propios cristales del mismo polímero. En el segundo de los trabajos, la nucleación provocada por la presencia de los nanotubos hizo que el grado de cristalinidad de la PCL aumentase un 65%, lo que, a su vez, dio lugar a una mejora sustancial en sus propiedades mecánicas[151].

La modificación simultánea de los nanotubos con grupos hidroxilo (CNT-OH) y de la PCL con ácido acrílico (PCL-g-AA) permitió obtener un mayor grado de dispersión debido a la formación de enlaces covalentes entres los grupos carboxilo de PCL-g-AA y los hidroxilos de CNT-OH[152]. La compatibilización incrementó la resistencia a la tracción y la estabilidad térmica de los nanocompuestos PCL/CNT. El mejor balance de propiedades fue el mostrado por el nanocompuesto con 5% de nanotubos, cuya resistencia a la tracción fue cercana a 55 MPa y la temperatura inicial de descomposición 77ºC superior a la de la PCL pura.

2.3.2.3 PBAT/CNT nanocomposites

La bibliografía sobre PBAT/CNT procesados en fundido es muy escasa. En nanocompuestos PBAT/pCNTs la resistencia a la tracción del PBAT (19 MPa) aumentó con el contenido de pCNTs, llegando a obtenerse un valor máximo de 25 MPa con 2% de pCNT[153]. Por el contrario, la ductilidad disminuyó considerablemente, aunque siempre se mantuvo en valores superiores a 600%.

La modificación de PBAT con ácido acrílico (PBAT-g-AA) y la de los nanotubos con grupos hidroxilo (CNT-OH) dio lugar a una mejora en el nivel de dispersión de los nanotubos[154], aunque con un contenido de 5% se formaron agregados. La resistividad de los nanocompuestos PBAT/CNT sin modificación y la de los PBAT-g-AA/CNT-OH disminuyó con el contenido de nanotubos. A iguales contenidos se observó una menor resistividad, y por lo tanto una mayor conductividad, en el caso de los nanocompuestos modificados.

2.4. Nanocomposites based on polymer blends

Los nanocompuestos ternarios polímero/polímero/nanopartícula son materiales híbridos que combinan las tecnologías de las mezclas poliméricas y de los nanocompuestos poliméricos, y por lo tanto, suponen la adición de nanopartículas a mezclas poliméricas o la adición de un segundo polímero a nanocompuestos binarios. Su estudio y desarrollo está permitiendo obtener nuevos materiales con altas prestaciones combinando propiedades térmicas-mecánicas mejoradas con propiedades específicas relacionadas con el tipo de nanopartícula empleada[155-157].

Evidentemente, las propiedades finales de los nanocompuestos ternarios están relacionadas principalmente con las características y propiedades de los polímeros y de las nanopartículas constituyentes. En general, se suele emplear un par de polímeros que muestran un buen balance inicial de propiedades, a los cuales se les pueden añadir diferentes nanopartículas en función de las características que se persiguen. La morfología que muestran las fases poliméricas suele estar relacionada con la localización y con el nivel de dispersión de las nanopartículas en las mismas.

El procesado en fundido de los nanocompuestos ternarios es un proceso muy complejo en el cual las nanopartículas se distribuyen en uno de los polímeros, en ambos, en las interfases, y/o migran de uno a otro, a la vez que se va estructurando la morfología. Ambos procesos dependen de diversos factores, que serán los que establecerán la localización y dispersión de las nanopartículas, y la morfología de los polímeros en los nanocompuestos ternarios.

2.4.1 Location of nanoparticles in immiscible polymer blends

La localización y distribución de las nanoparticulas en mezclas poliméricas inmiscibles suele estar generalmente establecida por la afinidad química existente entre ambos polímeros y las nanoparticulas[158,159]. Normalmente esta afinidad o compatibilidad suele cuantificarse mediante la tensión interfacial existente entre los constituyentes, y esta puede calcularse de modo sencillo mediante diferentes técnicas y modelos[160-162]. A pesar de que existen divergencias en cuanto a la validez de estos modelos (la tensión interfacial se determina normalmente en estado sólido y a temperatura ambiente), en muchos trabajos relativos a nanocompuestos ternarios han servido para predecir adecuadamente la localización de las nanoparticulas. Sin embargo, la utilización de la tensión interfacial para predecir la localización de las nanoparticulas se limita a procesos de mezclado en los que, hipotéticamente, se ha trabajado en condiciones de equilibrio termodinámico, estado que raramente se alcanza en procesos industriales y que, por otra parte, resulta difícil de comprobar. Así pues, existen parámetros a tener en cuenta, relacionados con el proceso de mezclado, que pueden establecer o inducir una localización de las nanoparticulas diferente a la prevista en base a la afinidad química entre los diferentes constituyentes de los nanocompuestos.

Cuando la preparación de los nanocompuestos ternarios se realiza en fundido, son posibles tres rutas alternativas de mezclado; (1) adición los tres componentes simultáneamente, (2) premezclado de los polímeros y, en un segundo paso, adición de las nanopartículas a la mezcla polimérica y (3) pre-mezclado de uno de los polímeros con las nanoparticulas y adición del otro polímero en una segunda etapa al nanocompuesto binario inicial. El mezclado se suele llevar a cabo en los tres casos a temperaturas suficientemente elevadas para asegurar una viscosidad suficientemente baja de los materiales poliméricos, de modo que las nanopartículas puedan dispersarse adecuadamente en función de su afinidad. En cualquier caso, la secuencia de mezclado empleada puede tener una gran importancia en la localización final de las nanopartículas.

En el caso concreto de nanocompuestos preparados mediante las rutas 1 y 2 con polímeros cuyas temperaturas de procesado son muy diferentes, en los primeros momentos del mezclado, las nanopartículas se localizarán generalmente en el polímero de temperatura de procesado más baja, debido a que el de temperatura de procesado más elevada se encontrará todavía en estado sólido o altamente viscoso, independientemente de las interacciones existentes entre ellos. Si este polímero de temperatura de procesado inferior es el más afín con las nanopartículas, éstas se mantendrán en él, pero si no es el caso, la localización de las nanopartículas dependerá de que las condiciones de mezclado empleadas faciliten o dificulten la migración de las mismas hacia el otro polímero más afín. Lo mismo ocurre si se emplea la ruta 3 premezclando las nanopartículas con el polímero más afín o menos afín, respectivamente. Si los tiempos de mezclado son demasiado cortos, y la viscosidad del polímero con mayor afinidad es demasiado elevada y/o si concurren otros factores que puedan dificultar la migración de las nanopartículas, tales como su morfología[163,164] o un bajo nivel de cizalla[158,165], éstas se podrán localizar en el polímero menos compatible o en la interfase entre ambos polímeros al final del proceso de mezclado.

La localización de las nanopartículas tiene una transcendental importancia en las propiedades finales de los nanocompuestos ternarios. En cuanto a las propiedades mecánicas se refiere, la localización en cualquiera de las fases poliméricas resulta más eficiente que la localización interfacial para rigidificar la mezcla polimérica[166,167]. Del mismo modo, se ha observado que la localización de las nanopartículas en la interfase puede impedir la transmisión de esfuerzos entre ambas fases, y por lo tanto, hacer descender considerablemente la deformabilidad de la mezcla cuando la interfase se satura por completo[166]. Por su parte, la localización interfacial de los nanotubos de carbono en mezclas con morfología continua ha sido la más efectiva para obtener materiales semiconductores, ya que de este modo se han obtenido los valores de percolación más bajos[168,169].

Sin embargo, un aspecto fundamental relacionado con la localización de las nanopartículas en mezclas poliméricas es su gran capacidad para modificar la morfología de éstas, efecto que, evidentemente, repercutirá directamente en las propiedades finales de los nanocompuestos. Por lo tanto, el efecto de las nanopartículas en las propiedades de las mezclas poliméricas es doble; por un lado está el efecto de las nanopartículas mismas, y por otro el relacionado con el cambio morfológico que éstas pueden llegar a producir en las fases poliméricas. Este último efecto se analiza en profundidad en el apartado siguiente.

2.4.2 Morphological changes produced by nanoparticles in polymer blends

Como se ha comentado, es habitual que la presencia de nanopartículas en cualquiera de las fases que constituyen una mezcla polimérica bifásica o en la interfase entre ambas modifique la morfología de la mezcla de partida[158,159,170]. Es por ello que, a la modificación de las propiedades de la mezcla polimérica atribuible intrínsecamente a la propia presencia de las nanopartículas, hay que añadir la derivada de los cambios morfológicos producidos por éstas[171-175]. Asimismo, estos cambios morfológicos inducidos por la presencia de nanopartículas se han demostrado cruciales para que el material híbrido resultante muestre alguna propiedad específica concreta, como es el caso de la semiconductividad eléctrica en sistemas que contienen nanotubos de carbono[176,177].

Las razones que se recogen en bibliografía para justificar los cambios morfológicos inducidos por la presencia de nanopartículas son diversas y serán discutidas a lo largo de la presente exposición. Sin embargo, en aras de que ésta sea lo más clara posible, distinguiremos los casos en los que las nanopartículas se localizan preferentemente: 1) en la fase polimérica continua, 2) en la interfase y 3) en la fase polimérica dispersa.

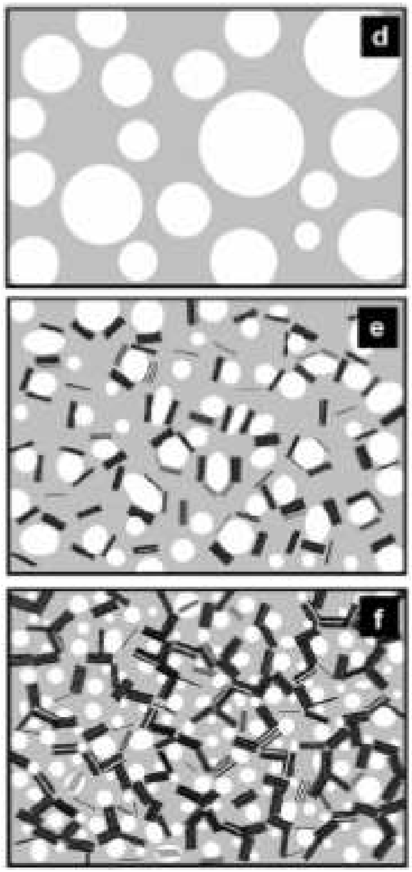

Figura 2.4.1: Evolución esquemática de la morfología de la mezcla PA6/HDPE 75/25 con el contenido de oMMT. Imagen obtenida de la referencia 184.

En el primer caso, cuando las nanopartículas se localizan en la fase continua, es habitual observar un descenso del tamaño de las partículas de la fase dispersa, aunque se han observado excepciones[178]. Estos descensos suelen estar relacionados con el incremento de la viscosidad de la matriz[179-181] como consecuencia de la presencia de las nanopartículas, que da lugar a un mayor efecto de masticación sobre la fase minoritaria, y/o con la mayor dificultad que tiene la fase dispersa para coalescer durante el mezclado en fundido debido al efecto de barrera física que ejercen las nanopartículas[182-184]. Este último efecto se representa esquemáticamente en la figura 2.4.1. Los descensos en el tamaño de las partículas de la fase dispersa han sido especialmente ventajosos en nanocompuestos ternarios tenaces, en los cuales el menor tamaño de las partículas elastoméricas dispersas ha dado lugar a un incremento de la resistencia al impacto de la mezcla inicial[172,174].

En el caso de que las nanopartículas se localicen en la interfase de la mezcla polimérica, también suele observarse un descenso en el tamaño de las partículas de la fase dispersa, aunque en determinados casos se ha observado, en cambio, una transición a la co-continudad[171,185]. En analogía con lo observado para nanopartículas localizadas en la matriz, en este caso también tiene lugar un efecto barrera que impide la coalescencia de las partículas de la fase dispersa. La morfología de las nanopartículas no parece ser determinante, ya que este efecto sucede independientemente de que sean tubulares como los nanotubos[186,187], laminares como las nanoarcillas[180,188] o esféricas como las nanopartículas de sílice[189,190]. Las nanopartículas localizadas en la interfase también pueden compatibilizar la mezcla termodinámicamente. De hecho, varios autores han observado que las nanopartículas pueden actuar como agente emulsificante, ya que su presencia conlleva un descenso en la tensión interfacial entre la matriz y la fase dispersa[191-195]. Por otro lado, y exclusivamente con láminas de arcilla, se ha observado que cadenas de ambos componentes poliméricos pueden intercalarse simultáneamente entre ellas, y como consecuencia, la estructura entera actúa como si fuese un copolímero de bloque[167].

El efecto compatibilizador de las nanopartículas localizadas en la interfase ha servido en algunos casos para incrementar la transferencia de esfuerzos entre ambas fases y, como resultado, para incrementar la resistencia a la tracción[193,196] y/o la deformación a la rotura[196] de las mezclas de partida. La transición de la morfología de matriz/fase dispersa a co-continua también ha servido para facilitar la transmisión de esfuerzos entre dos polímeros, lo cual ha propiciado incrementos en la resistencia al impacto[171].

En el último de los casos, cuando las nanopartículas se localizan preferentemente en la fase dispersa minoritaria, es habitual observar un cambio de la morfología de las mezclas del tipo matriz/fase dispersa a co-contínua[177,184,197-211], con alguna excepción en la que la compatibilidad entre los dos polímeros se ha visto incrementada provocando un descenso del tamaño de las partículas dispersas[195]. En el caso habitual, el efecto observado supone que la presencia de nanopartículas en la fase dispersa puede ampliar el rango de co-continuidad de la mezcla de partida incluso en composiciones muy ricas en una de las dos fases, tal como se observó por ejemplo en mezclas PLA/PA11[177] y ABS/PA6[211]. Los factores que contribuyen a estos cambios morfológicos son conocidos, pero algunos aspectos relacionados son todavía objeto de investigación. Por ejemplo, la presencia de nanopartículas en la fase polimérica minoritaria da lugar a un incremento de su viscosidad y su elasticidad en fundido, tal y como ocurre en la otra fase cuando están localizadas en la matriz. El efecto que produce este aumento de la viscosidad de la fase dispersa es contrario al explicado para la matriz, ya que en este caso, el proceso de fractura de las partículas poliméricas minoritarias durante el procesado en fundido de los nanocompuestos se ve dificultado. Esto da lugar a la formación de dominios poliméricos estables más grandes y elongados, y que podrían llegar a resultar en estructuras totalmente contínuas[202-204].

Tanto Kontopoulou y col.[204] como Filippone y col.[184] analizaron el efecto de la presencia de nanopartículas de oMMT en una u otra fase, mediante el estudio de distintas composiciones de mezclas poliméricas bifásicas con morfología matriz/fase dispersa. En ambos casos, la arcilla localizada en la fase mayoritaria produjo un descenso en el tamaño de las partículas dispersas, mientras que la morfología de la mezcla se transformó en co-continua con la arcilla localizada en la fase minoritaria.

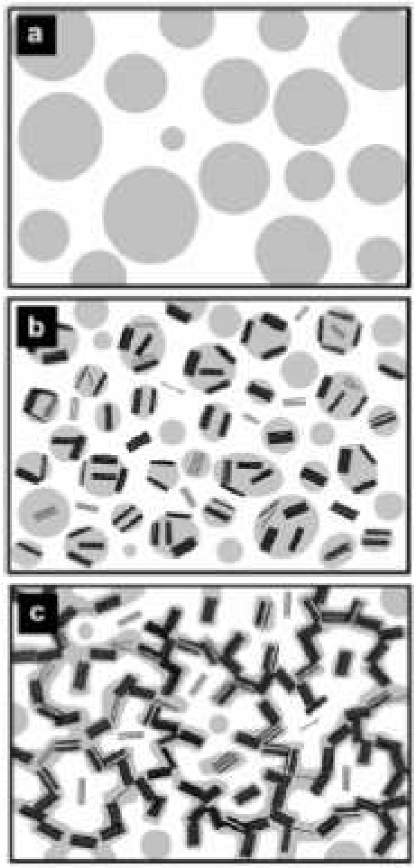

Figura 2.4.2: Evolución esquemática de la morfología de la mezcla HDPE/PA6 75/25 con el contenido de oMMT. Imagen obtenida de la referencia 184.

También es el caso, por ejemplo, de una mezcla PS/PA6, en la que se observó una mayor dificultad para la formación de gotas de poliamida dispersas en una matriz de PS tras la adición de sílice[203] debido a la presencia preferencial de las nanopartículas de sílice en la PA6. Los autores analizaron tanto los efectos sobre la tensión interfacial como los viscoelásticos, y llegaron a la conclusión de que el incremento de la viscosidad de la fase dispersa cargada fue el factor dominante en este caso. Asimismo, la morfología de la mezcla PP/PA66 70/30 puede variar controlando el contenido de arcilla localizado en la fase minoritaria de poliamida, cuya viscosidad varía en función de dicho contenido[202]. La mezcla de partida tiene una morfología matriz/fase dispersa, con una fracción de co-continuidad en las proximidades del 40%. A bajos contenidos de oMMT este valor apenas varía, pero a partir de 5% de oMMT aumenta considerablemente hasta llegar a un 90% con 10% de oMMT. En el mismo trabajo se observó que la compatibilización de la mezcla PP/PA66 contrarresta el efecto de la adición de arcilla, ya que, incluso a altos contenidos de ésta, el rango de co-continuidad del sistema sólo alcanza el 50%. Estos resultados indican, por tanto, que la capacidad de las nanopartículas para modificar la morfología de las mezclas depende de la compatibilidad entre los componentes poliméricos, siendo esta capacidad mayor cuanto menos compatible es el sistema.

Además de los cambios en la viscosidad con la adición de nanocarga, se han observado otros factores que también parecen influir en la formación de morfologías co-continuas. Por ejemplo, la capacidad que tienen las nanopartículas para formar redes dentro de la fase polimérica parece ser un factor determinante para fomentar la creación de este tipo de morfologías[207,208,211]. Adicionalmente, las nanopartículas dispersas en la fase minoritaria pueden inmovilizarla cinéticamente, dificultando así la fractura de las partículas durante el procesado en fundido de los nanocompuestos[184,205,206].

Por ejemplo, la morfología de la mezcla HDPE/PA6 75/25 evolucionó a co-continua con nanoarcilla dispersa en la fase minoritaria de poliamida sin que los cambios producidos en las propiedades viscoelásticas de las fases afectasen a este proceso[184]. La concentración de oMMT que posibilitó la morfología co-continua en el sistema coincidió con la concentración de percolación reológica del mismo, es decir, la continuidad de la fase de oMMT a través del sistema resultó en la continuidad de la PA6 a través del HDPE. Estos resultados indican que la morfología co-continua del sistema estuvo gobernada por la dispersión de las láminas de arcilla a través de la mezcla polimérica. Incluso a contenidos de arcilla inferiores al necesario para la percolación reológica, la propia dispersión de las nanopartículas fue la que provocó una morfología matriz/fase dispersa más fina. La figura 2.4.2 representa esquemáticamente este proceso.

En otro estudio[207], se analizó el efecto de la adición de nanotubos de carbono al mismo sistema HDPE/PA6, si bien en este caso la composición analizada fue 50/50. Los resultados obtenidos fueron similares a los anteriormente descritos, ya que, a bajos contenidos, el efecto de las nanopartículas en la morfología de la mezcla fue despreciable, y la morfología inicial, compuesta por una matriz de poliamida y partículas dispersas de polietileno, se mantuvo. Sin embargo, mayores contenidos de nanotubos promovieron la inversión de las fases, y una morfología en la cual la estructura de la fase de poliamida se rigió por la dispersión de los nanotubos de carbono en el seno de la misma. Incluso se han propuesto[212] modelos matemáticos para reproducir la capacidad que tienen las nanopartículas cilíndricas para modificar la morfología esférica de la fase minoritaria a dominios alargados e interconectados entre sí.

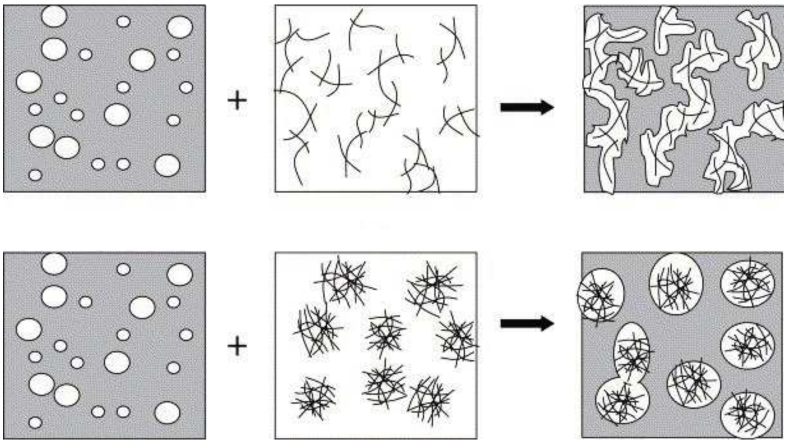

Figure 2.4.3: Efecto de la dispersión de las nanopartículas en la morfología final de la mezcla PPS/PA66 60/40. Imagen obtenida de la referencia 210.

El efecto de la dispersión de las nanopartículas en la morfología final fue analizado por Zou y col. en nanocompuestos PPS/PA66/CNT[210]. Los nanotubos se localizaron en la fase de poliamida, y se dispersaron en función de su contenido. A bajos contenidos, los nanotubos tendieron a dispersarse homogéneamente en la fase poliamida, y la morfología de la fase de PA66 dispersa en la matriz de PPS tuvo que variar para mantener la buena dispersión de los nanotubos. Como resultado, la fase de PA66 formó una estructura interconectada y continua dentro de la fase mayoritaria de PPS. Por el contrario, a altos contenidos de nanotubos, éstos dieron lugar a agregados de morfología esférica, lo que provocó la aparición de una morfología de tipo “sea-island”. La figura 2.4.3 representa esquemáticamente estos procesos.

Asimismo, Li y col.[206] estudiaron el efecto que ejerce la morfología de las nanopartículas en la formación de la estructura co-continua en mezclas PS/PVME. Compararon la eficiencia de nanoesferas y de nanotubos de CdS, y observaron que la morfología tubular de las nanopartículas es más eficiente que la morfología esférica[206]. La mayor facilidad que tienen los nanotubos para formar estructuras percoladas en los polímeros fue la razón esgrimida para explicar este efecto.

En un reciente y ambicioso trabajo, Nuzzo y col.[177] investigaron distintos factores que inducen la obtención de una morfología co-continua a partir de de una tipo matriz/fase dispersa, comparando el efecto de la adición de dos arcillas diferentes (sepiolita y montmorillonita) y nanotubos de carbono a una mezcla PLA/PA11 de composición 70/30. Puesto que los tres tipos de nanopartículas se localizaron preferentemente en la fase dispersa de PA11, en todos los casos se observó la transición de la morfología a co-continua a partir de un determinado contenido crítico de nanorefuerzo. Sin embargo, dicha transición solo coincidió con el punto de percolación reológica en el caso de las arcillas, mientras que en el caso de los nanotubos fue necesario un contenido superior al de la percolación eléctrica para lograr la percolación reológica. Además, las arcillas mostraron una mayor capacidad para producir el cambio morfológico que los nanotubos de carbono, a pesar de que éstos formaron estructuras completamente percoladas con mayor facilidad. Estos resultados indican que hay más factores implicados en estos cambios morfológicos derivados de la presencia de nanopartículas; se han propuesto la modificación de la tensión interfacial entre los componentes poliméricos por la presencia del nanorefuerzo o las características mecánicas (rigidez-deformabilidad) de las propias nanopartículas.

Como ya se comentó al principio de la presente sección, la capacidad que tienen las nanopartículas para modificar la morfología de las mezclas es fundamental, ya que puede conllevar mejoras adicionales a las prestaciones propias de los nanocompuestos. Por un lado, las estructuras co-continuas pueden mostrar una mayor rigidez[198,200,201] o una mayor tenacidad[171,175,209] que las de matriz/fase dispersa, y por otro lado pueden dotar a los materiales de una mayor estabilidad térmica[184,213] y semiconductividad eléctrica con efecto de doble percolación[177,209]. Uno de los objetivos del presente trabajo de investigación es contribuir a un mejor conocimiento de estos efectos.

2.4.3 Nanocomposites based on biodegradable polymer blends

Siendo aplicable a los polímeros biodegradables todo lo anteriormente mencionado para nanocompuestos basados en polímeros convencionales, es importante señalar que la adición de nanocargas a mezclas basadas en estos últimos puede modificar su velocidad de degradación, tal como lo hace con los polímeros puros, pero los materiales resultantes mantienen la biodegradabilidad total de las mezclas de partida. Por lo tanto, la preparación de nanocompuestos basados en mezclas poliméricas biodegradables permite obtener materiales 100% biodegradables con un buen balance de propiedades mecánicas y con propiedades específicas relacionadas con las nanopartículas que han sido empleadas para su preparación.

2.4.3.1 PLA/PCL/oMMT nanocomposites

Se han estudiado nanocompuestos PLA/PCL/oMMT procesados en fundido[214-218] y en disolución[216] utilizando varios tipos de arcillas y diferentes relaciones PLA/PCL. Los nanocompuestos preparados en estado fundido muestran un mejor balance de propiedades que los preparados por disolución[216]. Independientemente de la proporción PLA/PCL y de la secuencia de mezclado utilizada para efectuar el mezclado de los nanocompuestos, las láminas de arcilla se han localizado preferencialmente en la fase PLA[214-216], o en la fase de PLA y en la interfase al mismo tiempo[217]. En uno de los trabajos[218] no se especificó cuál fue la localización exacta. La localización mayoritaria de las láminas de arcilla en la fase PLA se atribuyó a la mayor afinidad entre ambos componentes, deducida por medidas de ángulos de contacto[217].

Las láminas de arcilla han mostrado en general una nanoestructura intercalada[214-218], aunque se ha observado que las pocas localizadas en la interfase entre el PLA y la PCL están completamente exfoliadas[217]. También se ha observado que la adición de 5% de oligocaprolactona (o-PCL) a nanocompuestos PLA/oMMT puede producir una estructuración más regular de las láminas intercaladas de arcilla, y como resultado un incremento del grado de cristalinidad del PLA[79].

Tal como se mencionó en el apartado anterior, la presencia de las láminas de arcilla ha dado lugar a cambios en la morfología de la mezcla PLA/PCL de partida. La localización de la oMMT en la matriz de PLA ha resultado en un descenso del tamaño de las partículas dispersas de PCL[214,216,217], mientras que la localización de las láminas en la fase dispersa de PLA ha conllevado una transición hacia la co-continuidad[217].

La adición de oMMT ha servido para mejorar las propiedades mecánicas de las mezclas PLA/PCL[214,216,218]. En uno de los trabajos se observó un rango de contenido óptimo de arcilla (1-3%) para mejorar las propiedades de la mezcla PLA/PCL, ya que a mayores contenidos, las propiedades de tracción empeoraron[214]. Por ejemplo, el módulo de Young de los nanocompuestos con 1 y 3% de oMMT es 20% y 23% superior que el de la mezcla de partida, respectivamente. Sin embargo, en un trabajo de Li y col.[218] se observó que la rigidez de la mezcla PLA/PCL se incrementa linealmente con el contenido de oMMT, 15%, 40% y 70% con 2%, 5% y 10%, respectivamente, sin que se observe un contenido óptimo a partir del cual ésta disminuya. La presencia de oMMT también dio lugar a una mayor estabilidad térmica y velocidad de biodegradación de las mezclas[214,218].

2.4.3.2 PLA/PCL/CNT nanocomposites

Hasta ahora, los nanocompuestos PLA/PCL/CNT siempre se han preparado empleando nanotubos modificados con grupos carboxilo (COOH-CNT) [169,193,217,219,220], debido a que éstos se dispersan mejor en las mezclas PLA/PCL que los nanotubos no modificados (p-CNT)[193].

La afinidad entre los nanotubos y las fases poliméricas se cuantificó por medio de medidas de ángulos de contacto, y se observó que ésta es mayor con el PLA que con la PCL[217]. Sin embargo, en la mayoría de los trabajos los nanotubos se han localizado preferencialmente en la fase de PCL y en la interfase entre ambas[193,217,219]. Ésta localización se atribuyó al empleo en todos estos trabajos de un sistema PLA/PCL que presentaba una gran diferencia de viscosidades ($\eta_{PLA}/\eta_{PCL} = 16$), lo cual impidió la difusión de los nanotubos en el PLA. Con el fin de constatar la validez de esta justificación[217] se empleó otra PCL de viscosidad similar a la del PLA, observándose, efectivamente, que los nanotubos se localizaron en este caso en la fase más afín de PLA.

La presencia de nanotubos en la fase PCL de la mezcla PCL/PLA 70/30 dio lugar a una disminución del tamaño de las partículas dispersas de PLA. Los nanotubos incrementaron la viscosidad de la matriz, pero curiosamente fueron los pocos nanotubos localizados en la interfase los principales causantes del descenso observado en el tamaño de partícula, debido al efecto emulsificador que provocaron[193]. El consiguiente descenso de la tensión interfacial entre el PLA y la PCL y, por tanto, la mejor transmisión de esfuerzos entre ambos, provocó un incremento de la resistencia a la tracción de la mezcla de mayor importancia que el debido al efecto reforzante de los nanotubos. Por otro lado, la localización simultánea de los nanotubos en la matriz y en la interfase provocó que tanto la percolación reológica y como la eléctrica se produjeran a contenidos menores de nanotubos en comparación con las de los nanocompuestos PLA/CNT y PCL/CNT de partida (la percolación eléctrica se estableció en un 0.98% de contenido de nanotubos)[193,219].

En otro de los trabajos[220] se estudió el efecto de la composición de la mezcla PLA/PCL en las propiedades eléctricas de los nanocompuestos ternarios PLA/PCL/COOH-CNT con un contenido fijo de 1% de nanotubos. Los nanotubos se localizaron exclusivamente en la PCL, aunque los autores no justificaron esta localización por medio de ninguna medida experimental. La composición PLA/PCL 60/40 fue la que exhibió una mayor conductividad, que se relacionó con el mayor nivel de co-continuidad que mostró ésta entre todas las estudiadas.

Por último, se obtuvieron valores de percolación eléctrica a contenidos extraordinariamente bajos de CNT (0.025%) en una mezcla intermedia y co-continua PLA/PCL 50/50[169]. Este resultado se relacionó con la localización interfacial de los nanotubos, la cual se consiguió gracias al protocolo utilizado para procesar los nanocompuestos. Los nanotubos se mezclaron en una primera etapa con el PLA y en una segunda se añadió la PCL a los nanocompuestos PLA/CNT. Contrariamente a lo observado por Wu y col.[193,217,219], en éste trabajó se mencionó una mayor afinidad de los nanotubos con la fase de PCL, aunque tampoco se llevaron a cabo medidas para justificarla. Al ser los nanotubos más compatibles con la PCL, éstos migraron a esta fase desde el PLA durante la segunda etapa de mezclado. Optimizando las condiciones de procesado, fundamentalmente el tiempo, se consiguió controlar el proceso de migración y, como consecuencia, la localización exclusivamente interfacial de los nanotubos.

2.4.3.3 PLA/PBAT/CNT nanocomposites

Los nanocompuestos PLA/PBAT/CNT apenas han sido estudiados hasta el momento, y en bibliografía se han encontrado únicamente dos trabajos, ambos de los mismos autores[221,222]. En ambos se trabajó con pCNTs y se añadieron pequeños contenidos de antioxidante para minimizar la degradación de los polímeros durante el procesado en fundido. Se estudiaron nanocompuestos con diferentes proporciones PLA/PBAT y contenidos de nanotubos. Debido a la mayor afinidad química y también a la menor viscosidad del PBAT, los nanotubos se localizaron preferencialmente en esta fase, independientemente de la relación PLA/PBAT[221,222]. La morfología de las mezclas de partida no se vio alterada tras la adición de nanotubos. Tanto la estabilidad térmica, medida por ensayos termogravimétricos, como las propiedades viscoelásticas de las mezclas, mejoraron tras la adición de los nanotubos a las mezclas. Las propiedades mecánicas y eléctricas de los nanocompuestos no fueron analizadas.

Chapter 3: Experimental part

Chapter 3: Experimental part

3.1 Materials

3.1.1 Poly(lactic acid) (PLA)

PLA is a linear aliphatic and thermoplastic polyester which is synthesized by polycondensation from lactic acid and which is completely biodegradable and biocompatible. Figure 3.1 shows its chemical structure. While PLA was firstly synthesized in the 1930's, it was not until the 1980's that PLA began to be large-scale produced, mainly thanks to the advances made in the fermentation process which enabled the production of lactic acid. However, the first industrial PLA synthesizing plant opened in 2002 in Minnesota (USA). Nowadays, PLA is the third more widely produced bioplastic in the world behind starch and lignocelluloses derivates, and it has begun to replace conventional polymers in textile and packaging industries, among others.

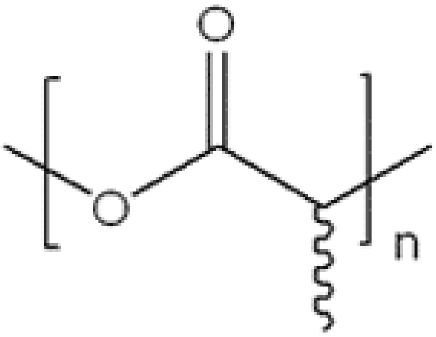

Figure 3.1: Chemical structure of PLA.

High molecular weight PLA combines high stiffness and strength, but also an intrinsic fragility that usually forces to additivate the polymer. PLA can be processed in many different ways, so multiple industrial applications for PLA exist; injection molded objects, bottles, fibres or films for packaging industry, and so on. In the present work the injection-molding PLA Natureworks 3052D grade has been used, purchased from Dow Chemical and with a 96% L-lactic acid content. Table 3.1 shows its main properties, according to the supplier.

Table 3.1: Main properties of PLA Natureworks 3052D.

Property (units)	**Standard**	**Value**
Physical properties		
Appearance	-	Transparent
L-isomer contents (% wt.)	-	~ 96
Density (g/cm^3)	ASTM D792	1.24
Melt Flow Ratio (MFR) (g/10 min)	ASTM D1238	14
Thermal properties		
Glass-transition temperature (ºC)	ASTM D3418	55-60
Melting temperature (ºC)	ASTM D3418	145-160
Mechanical properties		
Yield strength (MPa)	ASTM D638	62
Elongation at break (%)	ASTM D638	3.5
Izod impact strength (J/m)	ASTM D256	16.0
Bending strength (MPa)	ASTM D790	108
Bending modulus (MPa)	ASTM D790	3600

3.1.2 Poly(ε-caprolactone) (PCL)

PCL is an aliphatic and thermoplastic polyester synthesized from the polycondensation of the cyclic ε-caprolactone monomer. Although it is produced from non-renewable sources, PCL is fully biodegradable and also biocompatible. Figure 3.2 shows the chemical structure of PCL. PCL is semicrystalline, tough, flexible and soluble in many solvents, but very resistant to water. The PCL used in the present work was purchased from Perstorp under the trade name of CAPA®6800. Table 3.2 shows the main characteristics of this polymer.

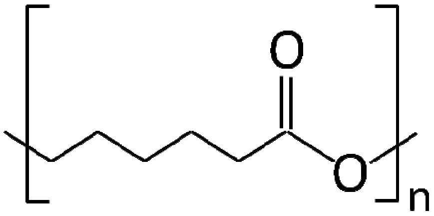

Figure 3.2: Chemical structure of PCL.

As a result of the low melting temperature of PCL, it can be easily processed using different conventional techniques even at relatively low temperatures. Additionally, it is a polymer which shows a high capability to be melt-blended with many amorphous or crystalline polymers, even at high temperatures. As an example, PCL is currently used as an adhesive, as an impact modifier and as a biodegradable packaging for food.

Table 3.2: Main properties of PCL CAPA 6800.

Property (units)	**Standard**	**Value**
Molecular Weight (g/mol)	-	80000
Melting temperature (ºC)	-	58-60
Melt Flow Index (MFI) (g/10 min)	ASTM D-1238	7.3
Elongation at break (%)	-	800

3.1.3 Poly(butylene adipate-co-terephthalate) (PBAT)

PBAT is a thermoplastic block co-polyester obtained from the polycondensation between 1, 4-butylene glycol, adipic acid and terephthalic acid and therefore obtained from non-renewable resources. However, it is a fully biodegradable polymer. Figure 3.3 shows its chemical structure.

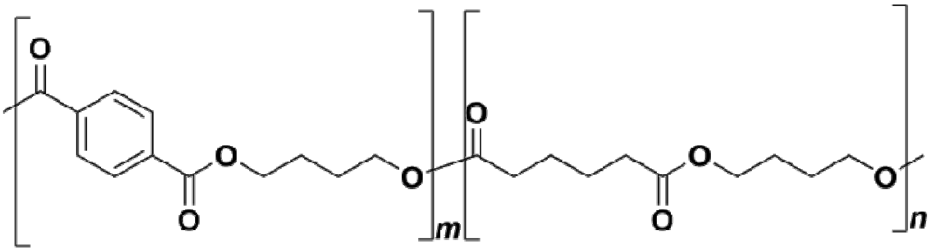

Figure 3.3: Chemical structure of PBAT.

PBAT is semicrystalline and shows an acceptable balance of mechanical properties, high toughness and good thermal and thermodimensional stabilities. PBAT employed in the present work was ECOFLEX F BLEND 1200 grade, purchased from BASF. Table 3.3 shows its main characteristics.

PBAT can be easily processed by injection molding, extrusion, compression-molding, blowing, and so on. In addition, it admits a very wide range of processing temperatures. PBAT is usually commercialized after been melt blended with other biopolymers or fillers such as wood powder.

Table 3.3: Main properties of PBAT Ecoflex F BLEND 1200.

Property (units)	**Standard**	**Value**
Physical properties		
Level of transparency (%)	-	82
Density (g/cm^3)	-	0.924
Melt Flow Ratio (MFR) (g/10 min)	ASTM D-1238	2.7-4.9
Thermal properties		
Melting temperature (ºC)	ASTM D-3418	110-120
Vicat softening temperature (ºC)	-	91
Mechanical properties		
Yield strength (MPa)	ASTM D-638	35-44
Tensile strength (MPa)	-	36-45
Elongation at break (%)	-	560-710
Shore hardness (D)	-	32

3.1.4 Montmorillonite (MMT)

MMT is a mineral clay belonging to the family of philosilicates. The chemical formula of MMT is $(Al_{1.67}\ Mg_{0.33})\ [(OH)_2\ Si_4O_{10}]_{0.33}\text{-}Na_{0.33}(H_2O)$ and it is structured as laminar parallel sheets. The very high cation-exchange capacity of the surface of MMT (between 80 and 150 meq/100 g) and the expansive behavior of the network make MMT the most popular nanofiller for the preparation of polymer/clay nanocomposites.

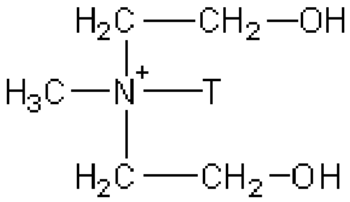

Figure 3.4: Chemical structure of the organic modifier of the Cloisite30B nanoclay.

Before being combined with polymers, MMT is usually organically modified to enhance its compatibility. The organically modified MMT (oMMT) employed in the present work has been Cloisite30B, purchased from Southern Clay Products. The organic modifier (surfactant) of this oMMT is a methyl, tallow, bis-2 *hydroxyethyl*, quaternary ammonium. Figure 3.4 shows its chemical structure, and Table 3.4 shows the main characteristics of Cloisite30B.

Table 3.4: Main properties of the Cloisite30B nanoclay.

Property (units)	**Value**
Physical properties	
Density (g/cm^3)	1.98
Amount of surfactant (% wt.)	30
Interlaminar distance (nm)	1.85
Mechanical properties	
Young’s modulus (GPa)	4657
Tensile strength (MPa)	101
Elongation at break (%)	8
Notched impact strength (J/m)	27
Shore hardness (D)	83

3.1.5 Carbon nanotubes (CNT)

Carbon nanotubes are, together with graphite, diamond and fullerenes, one of the allotropic forms of carbon. Their structure consists of graphite sheets coiled onto themselves, forming one or several concentric long tubes or walls.

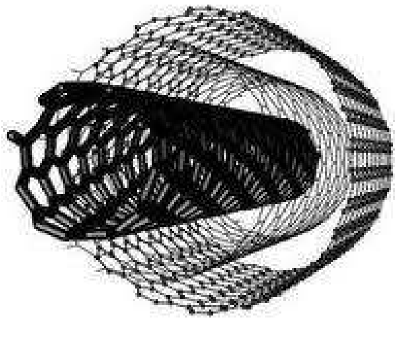

Figure 3.5: Chemical structure of p-MWCNTs.

CNTs present a very high length/diameter ratio, and therefore surface/volume ratio. Their excellent mechanical, thermal and electrical properties of CNTs are due to the very high physic-chemical stability and strength of the sp^2 hybridized covalent bonds between carbon atoms. CNTs are the toughest manufacturable fiber today and additionally they can be notably deformed in the elastic regime.

In the present work pristine multi walled carbon nanotubes (p-MWCNT) were employed, purchased from CHEAPTUBES. Figure 3.5 and Table 3.5 show their chemical structure and main characteristics, respectively.

In the early years after being discovered, the application of CNTs was merely academic. However, since the beginning of the 21st century their application has spread to industry, and nowadays they are used in the chemical industry, in the fabrication of super-condensers or solar cells, as hydrogen storage devices, in electronics, in the automobile and aerospace industries and in biomedicine, among others.

Table 3.5: Main properties of p-MWCNTs CHEAPTUBES.

Property (units)	Value
External diameter (nm)	10-20
Internal diameter (nm)	3-5
Length (µm)	10-30
Carbonaceous residue (% wt.)	< 1.5
Purity (% wt.)	> 95
Specific area (m^2/g)	233
Electrical conductivity (S/cm)	> 100

3.2 Processing

The objective of polymer processing is to obtain durable materials and objects, in specific shapes and sizes with the right characteristics for their end application. The main advantages of polymeric materials are mainly the ease and the low cost of production, their considerable versatility and the fact that they are easily modified using a wide range of other polymers, pigments, fillers and additives. As a result, the production and use of polymers and polymer based materials is currently enormously popular.

All blends and nanocomposites characterized in the present work were processed in the melt state, by which polymeric products can be large scale produced in a simple, short, solvent-free and economical way. Blending was carried out by extrusion, and all materials were manufactured by injection molding and/or compression molding.

3.2.1 Drying

All polymers materials absorb moisture. The presence of even very low water contents in polymers obtained by polycondensation may result in their hydrolytic degradation during the melt processing and/or may cause defects such as bubbles in the final manufactured product. Therefore, polymer pellets and the oMMT powder used were dried before blending, as well as all the extruded pellets before manufacturing. Table 3.6 shows the drying conditions used for different materials used in this work.

Table 3.6: Drying conditions of the materials employed.

Material	Drying conditions
PLA	Overnight at 80ºC in a dehumidifier
PCL	Overnight at room temperature in a vacuum-oven
PBAT	Overnight at 80ºC in a vacuum-oven
oMMT	Overnight at 60ºC in a forced air oven
CNT	Not dried
All extruded pellets	Overnight at 80ºC in a dehumidifier

3.2.2 Blending

Before being melt-blended or manufactured, the different solid pellets and powders were manually premixed to obtain pre-blends with a good starting distribution of the different components.

Together with internal mixing, extrusion is the most common technique for melt-blending thermoplastic polymers. Extrusion processing can be very useful to efficiently mix different thermoplastic polymers, but also to additivate or reinforce them. The main advantages of extrusion processing are good mixing related to the high shear rate, simplicity of use, high productivity and low cost of implementation.

Table 3.7: Blending conditions of all compositions in the twin-screw extruder.

Composition	Temperature (ºC)	Screw-speed (rpm)
PLA+PCL*	180	80
PLA+PBAT	180	80
PLA+oMMT	180	320
PLA+CNT	180	320
(PLA/CNT)+PCL	180	80
(PLA/PCL)+oMMT	180	320
(PLA/CNT)+PBAT	180	80

*Mixed in two extrusion machines at the same temperature and screw-speed.

Blending of all polymer blends and nanocomposites prepared in the present work was carried out in a Collin ZK 25 twin screw-extruder kneader (L/D ratio 30, screw diameter 25 mm). The kneading extruder was equipped by two co-rotating and engaged screws. The screws had specific kneading zones, which enhance the blending and the dispersion of nanoparticles in melted polymers. The dosage of pellets or powder to the machine was carried out using a dosage unit made up of a feed hopper and two metering screws. The nozzle section used was circular. Table 3.7 shows temperatures and screw-speeds used for the preparation of the different compositions.

For comparison purposes, some of the PLA/PCL blends studied in Chapter 4.1 were also blended in a Collin Teachline twin-screw extruder (L/D ratio 18, screw diameter 25 mm), which has a lower blending and dispersing capacity than the Collin ZK 25 previously mentioned. However, all other features were the same.

All obtained extrudates were cooled in a water bath and subsequently pelletized in a COLLIN CSG-171 pelletizer unit.

3.2.3 Manufacturing

3.2.3.1 Injection molding

Injection molding ranks as one of the prime processes for manufacturing polymer materials. Injection molding consists of a process in which many identical items, from high precision engineering components to disposable consumer goods, are produced relatively quickly, using a hollow mold.

The injection molding machine consists of a heated barrel equipped with a reciprocating screw (driven by a hydraulic or electric motor), which feeds the molten polymer into a temperature controlled split mold via a channel system of gates and runners. The screw plasticizes the polymer, and also acts as a ram during the injection phase. The screw action also provides additional heating to the molten polymer as a result of the shearing action. The polymer is injected into a mold that defines the shape of the molded part.

Injection molding of all compositions studied in this work was carried out in a reciprocating screw BATTENFELD BA-230-E injection-molding machine, which was equipped with a plasticization screw with 18 mm diameter, L/D 17.8 and a clamping force of 23 tons. Injection molding was carried out at 180ºC using an injection speed of 10.2 cm^3/s. The mold temperature was fixed at 20ºC in all cases. Normalized tensile and impact specimens with dimensions according to ASTM D-638 type IV and ASTM D-256 standards, respectively, were obtained for all compositions.

3.2.3.2 Compression molding

Compression molding is a technique which is characterized by a short and multidirectional flow during filling of the mold cavity, and so, molded products are obtained with very low levels of molecular orientation. In the present work, compression molding was carried out to obtain films for the determination of barrier properties and sheets for the determination of volume conductivities and viscoelastic properties. Normalized tensile specimens of some PLA/PCL blends of Chapter 4.1 were also obtained as an alternative processing method. Dry pellets were subjected to crushing flow between two sheets of stainless steel in order to obtain the aforementioned specimens.

The machine used was a hydraulic Collin P200E press, equipped with a cooling system based on circulating water. The molding process was developed in three stages: preheating, or plasticising (closure without pressure) (3 min), compression (closure under pressure to 200 bar) (2 minutes) and cooling (7 min). The temperature employed was 180 °C to obtain PLA/PCL tensile specimens and 300ºC to obtain the different films and sheets.

3.3 Characterization and testing techniques

Experimental techniques presented in this section were used to determine the most important macroscopic characteristics, such as the thermal, physical, rheological and mechanical properties of processed materials, and also to analyse their morphology, micro and nanostructure. As additional measurements, the oxygen permeability and the electrical conductivity of some of the compositions were determined.

3.3.1 Differential Scanning Calorimetry (DSC)

DSC is the most used technique to analyse the main thermal properties of polymeric materials. By simple scans performed at a constant rate of heating or cooling, glass transition (Tg), melting (Tm) and crystallization (Tc) temperatures of polymers, and the enthalpies involved in the melting and crystallization processes of semicrystalline polymers can be easily determined. This technique requires small amounts of sample (~ 10 mg), and allows to study thermally sensitive systems to be studied in a short time. The major drawback of DSC is its low sensitivity to determine the Tg-s of highly crystalline polymers, whose transitions are very difficult to detect.

Calorimetric analyses were performed on a Perkin Elmer DSC-7 differential scanning calorimeter. The apparatus was calibrated with reference to an indium standard and a constant nitrogen flow was maintained through the sample and reference chambers. All scans were performed at constant heating or cooling rates of 20ºC/min. Melting and crystallization temperatures were determined at the maxima and minima of the corresponding peaks, while melting and crystallization enthalpies were measured from the areas of these peaks. Temperature ranges used in each of the studied systems are detailed in the corresponding chapters.

3.3.2 Dynamic Mechanical Thermal Analysis (DMTA)

Dynamic-mechanical tests are used for determining the moduli and mechanical losses of solid polymers as a function of temperature and in a wide range of frequencies. By means of tests carried out at fixed frequency and variable temperature, substantial information about the properties of polymeric materials is obtained. Among others, both the storage (E') and loss (E' ') modulus and the loss factor (tanδ) can be determined as a function of temperature. The three parameters are related by the following equation:

$$tan\delta = \frac{\mathrm{E}''}{\mathrm{E}'}$$

The glass transition temperature (Tg) is usually defined as the temperature corresponding to the maximum in tanδ vs. temperature plot, where most of the macromolecular movement begins. The use of the highly sensitive DMTA allows the glass transition to be properly studied even when it is not very intense. In the case of polymer blends, it is able to differentiate between two very close transitions and therefore to determine the degree of phase-miscibility. Secondary (T_β) transitions can be also studied by DMTA, often contributing to the knowledge of the phase behavior and miscibility of polymer blends.

The dynamic-mechanical analyses in this study were performed on a DMA Q800 machine of TA Instruments. The geometry of the tests was single cantilever in flexion, the fixed frequency was 1 Hz and the heating rate 4°C/min. Start and end temperatures of the scans varied depending on the systems studied and are specified in the corresponding chapters. When the analyses required starting crio-temperatures, a liquid-nitrogen cooling system was used.

3.3.3 Proton Magnetic Nuclear Resonance (^{1}H-RMN)

^{1}H-NMR analysis is very useful for detecting possible interactions or chemical reactions between polymers with very similar structures, for which the sensitivity of FTIR is insufficient. In the present work it was used to analyze PLA/PCL and PLA/PBAT reactions.

^{1}H-NMR spectra were performed at room temperature on a DPX300 Bruker ADVANCE at a frequency of 300.16 MHz and using tetramethylsilane (TMS) as a reference. In all cases 10 mg of sample were used, dissolved in 0.7 mL of deuterated chloroform ($CDCl_3$). A minimum of 3 samples were measured to make the determination.

3.3.4 Contact-angle measurements

Contact-angle measurements were used to calculate the interfacial tension values between all polymers and nanofillers in the present work. Interfacial tension values can be very useful to understand the morphology and structure in multiphase polymer systems, since they give information about the compatibility or chemical affinity between the different constituents[223].

The determination of interfacial tension was carried out using the harmonic equation of Wu[224]:

$$\gamma_{12} = \gamma_1 + \gamma_2 + \frac{4\gamma_1^d\gamma_2^d}{(\gamma_1^d+\gamma_2^d)} + \frac{4\gamma_1^p\gamma_2^p}{(\gamma_1^p+\gamma_2^p)}$$

in which subscripts 1 and 2 correspond to constituent 1 and constituent 2, respectively. Polar (γ^p), dispersive (γ^d) and total (γ) surface energies were determined from the corresponding contact angles with water and ethylene glycol. The determination of all contact-angles was performed using a CAM 100 goniometer (KSV). In the case of polymers, drops of each liquid were put on the surface of injection molded specimens and in the case of nanoparticles on the surface of mechanically compacted tablets. At least 10 drops were measured for each liquid.

3.3.5 X-Ray Diffraction (XRD)

XRD is a very useful technique to characterize the structure of polymer/clay nanocomposites simply and quickly. The technique is based on the Bragg-Brentano equation. An incident monochromatic X-ray beam penetrates under the material surface and is refracted out at an angle θ in phase with the incident radiation. By ascertating the incident and refracted angles the basal spacing between montmorillonite sheets can be calculated using the Bragg's law.

$$\lambda = 2 \text{ d sen}\theta$$

where:

λ: Wavelength of the incident radiation

d: Basal spacing between montmorillonite sheets

θ: Angle of incident or reflected radiation with the normal to the plane of the sample

XRD measurements were performed on a Philips PW 1729 GXRD diffractometer on 1.80 thick samples. The wavelength of the incident radiation (λ) was 0.15406 nm and in all cases the angle studied (θ) ranged from 2 to 10 °.

3.3.6 Rheological measurements

Thermoplastic polymers are viscoelastic materials combining elasticity (solid behavior) and viscosity (liquid behavior) at the same time. Therefore, their rheological analysis is essential to understand their properties. On the one hand, it allows studying the flow-characteristics of molten polymers, which is essential to optimize processing conditions such as the temperature and the shear forces employed. On the other hand, it can provide essential information about the structure, the properties and the melt-behavior of multiphase materials. The rheological analysis of polymer blends and nanocomposites provides precize information about their morphology and their nanostructure.

3.3.6.1 Melt flow behavior

In the present work two techniques were used to determine the melt flow behavior of pure polymers, polymer blends and nanocomposites. Capillary extrusion rheometry was used to determine the viscosity of molten materials at shear rates corresponding to injection molding and extrusion processes, respectively, and torque measurements to detect possible reactions occurred during the processing of polymer blends.

The capillary extrusion rheometry was performed in a Göttfert Rheo-Tester 1000 capillary rheometer with a 30/1 L/D ratio. Tests were carried out at 180ºC, in a strain rate range between 1000 s^{-1} and 20000 s^{-1}.

Torque measurements were carried out in a MICRO DSM 5 cc mini-extruder, which is equipped with two co-rotating screws and a recirculation system. The system measures the torque required to rotate the rotors at a fixed speed, which characterizes the flow resistance offered by the melt, and therefore gives an idea of its viscosity. Torque measurements were used to check possible ester interchange reactions during mixing in PLA/PCL and PLA/PBAT blends. Tests were carried out at 180ºC and 80 rpm.

3.3.6.2 Viscoelastic properties

The viscoelasticity relates the shear stress that is applied to a material (σ), the resulting deformation of the same (γ) and time. Rheological studies of multicomponent polymeric materials are usually carried out in the so-called linear viscoelastic region. Tests are performed under very low stresses and very small deformations, close to equilibrium, and consequently there is a linear relationship, which is independent of the magnitude of applied stress, between the stress applied to the material during testing (σ) and its resulting deformation (γ). The response of the material in the range of linear viscoelasticity is strongly linked to their chemical-physical structure, so these measurements are useful to characterize them.

G '(ω) and G' '(ω) are the storage modulus and the loss modulus, respectively. The storage modulus is related to the material elasticity, that is, with the ability the material shows to return to its original shape after being deformed. In contrast, the loss modulus reflects the viscous behavior of the material, in other words, its ability to flow under an irreversible deformation.

The viscoelastic behavior of thermoplastic polymers can be easily studied by representing the variation of storage G' and/or loss G" modulus against frequency, ω (or temperature). This study results in three different relaxation areas which depend on the viscoelastic nature of the materials. In the low frequency area, which was analyzed in the present work, the material is comparable to a viscous liquid and the viscous behavior is predominant over the elastic behavior. In the intermediate frequency area the material presents a rubbery nature and G' shows a plateau that is independent of the frequency applied. Finally, in the high frequency region the material exhibits glassy character and the storage modulus G' is related to the elastic modulus.

The viscoelastic tests conducted in this study were performed in an Anton Paar MCR 301 rheometer. Tests were carried out at a constant temperature of 180°C under an inert nitrogen atmosphere with compression molded specimens, with parallel plate geometry of 25 mm and 1 mm thickness. In a first step, the linear viscoelastic area was determined by varying the shear stress from 1 Pa to 1000 Pa at fixed frequencies of 1 rad/s and 100 rad/s for each studied material. In a second step, the viscoelastic parameters of the materials were determined by spectromechanical analysis conducted in the area of linear viscoelasticity. The samples were subjected to a variable frequency between 100 rad/s and 0.01 rad/s at the previously fixed shear stress.

To analyze the time-evolution of the materials under the action of temperature and stress in the linear viscoelastic range, a kinetic-follow was conducted at a fixed frequency of 100 rad/s to some specimens during 10 hours. This test provided information about possible degradations and/or changes in the phase structure that may have occurred in the material in the linear viscoelastic range during the determination of the viscoelastic parameters.

3.3.7 Morphology

Scanning electron, transmission electron and Atomic Force microscopy were employed to analyze the morphology of the blends and nanocomposites. As described below, the most appropriate technique was chosen in each case, as they provide different levels of information. The specimens submitted for observation also changed from one system to another, depending on the morphology-properties relationship under investigation.

3.3.7.1 Scanning Electron Microscopy (SEM)

SEM is a widely used technique in the field of polymeric materials. In multicomponent materials such as polymer blends, it can provide fundamental information to identify the processing, structure and properties relationship.

The microscope used was a Hitachi S-2700, at accelerating voltages between 10 kV and 15 kV. In this work, the surfaces of cryogenically fractured tensile or impact specimens were analyzed, but in certain cases fracture surfaces of tested specimens were also analyzed. Micrographs of the most representative morphologies were obtained, in all cases from the dominant inner part of the samples.

Prior to analyzing the morphology of the samples, they were coated with a thin gold layer. Coating minimized the damage produced by the radiation on the sample, providing a conductive surface which enables the elimination of electrical charges and encourages the reflection of electrons. Gold-coating was carried out in a Microscience Division SC500 Sputter Coater.

3.3.7.2 Transmission Electron Microscopy (TEM)

TEM is a very appropriate microscopic technique to study the morphology of polymer nanocomposites, as it provides good information about the dispersion of nanoparticles in polymers. Therefore, it is very useful to establish links between the nanostructure of nanocomposites with their final properties. The main disadvantage of TEM is related to the observed surface area, which only represents a very small region of the whole material. However, shooting at different magnifications and at different points of the sample allows for a fairly representative view of morphology and nanostructure.

The samples analyzed were obtained in all cases from the centre section of injected tensile specimens, and were embedded in an epoxy resin cured for 48 hours at 60ºC. All samples were machined with a shaper to obtain an inverted pyramid which was later microtomized using a LEICA Ultracut Cut. Ultramicrotom. In this way, samples for TEM observation with thicknesses ranging from 30 nm to 60 nm were obtained. In the case of PLA/oMMT and PLA/CNT nanocomposites the cut was made at room temperature, while all the other compositions were machined in cryogenic conditions (-60 ° C).

TEM micrographs were obtained in a Tecnai 20 transmission electron microscope using an acceleration voltage of 200 kV.

3.3.7.3 Atomic Force Microscopy (AFM)

AFM is a very useful technique for analyzing the surface morphology in polymeric materials. It is based on a tip that scans the surface of the material. The great advantage of AFM compared to the other techniques used in this work is that the scanning tip is sensitive to different signals discharged by the surface, such as the stiffness, the topology, the electrostatic dispersion and so on. Another advantage of AFM is that it is able to characterize the morphology of pure polymers, even to show their crystal structure.

In polymer blends, the efficiency of AFM is practically the same as that of SEM. However, in the case of nanocomposites it can be a complementary technique to TEM, which is the most popular of the two, nowadays. TEM is very useful to characterize nanocomposites but it only provides a bi-dimensional projection of a tri-dimensional morphology, while AFM gives us information about the real surface morphology of the materials.

AFM was used to analyze the morphology of CNT-containing binary and ternary nanocomposites. Analyzed surfaces were those of ultramicrotom-cutted specimens prepared for TEM analysis. The used microscope was a Bruker MM8 (MultiMode 8). It worked in Peak Force QNM (Quantitative Nanomechanical property Mapping) mode. Tips were Scan Asyst-Air, also purchased from Bruker.

3.3.8 Mechanical properties

The mechanical characterization of the different systems was performed by tensile tests, and it was one of the key parts of this research. From an academic point of view it allows the processing-structure-properties relationship in materials to be established, and thus, from a practical standpoint, it lends insight into their potential large-scale applications.

Tensile tests consist of subjecting an elongation to clamp-attached standard specimens at a constant rate until they break. The load applied to the material can be instantly monitored as a function of the elongation the tested specimen was subjected to. Therefore, load-displacement (stress-strain) representations are obtained. The most significant mechanical properties of polymeric materials are:

- Young’s modulus, E.
- Yield strength, σ_y.
- Elongation at break or ductility ε_r.

The Young’s modulus was obtained from the maximum slope of the tangent line in the initial linear region of the stress-strain curves.

The yield strength, σ_y, was calculated from force-displacement representations using the following expression:

$$\sigma_y = \frac{F_y}{A_0}$$

where F_y represents the value of the force at the maximum of the force-displacement plot, and A_0 the initial cross-section of the specimen.

The elongation at break was obtained from force-displacement representations provided by the machine using the following expression:

$$\varepsilon_r\ (\%) = \frac{\delta_r}{l_0}\ x\ 100$$

in which δ_r and l_0 represent the deformation of the material before breaking and the initial distance between clamps respectively.

Tensile tests were carried out on all the materials studied in the present work. They were all performed in a universal Instron 5569 tensile test machine, following the ASTM D-638 standard. A load cell of 5 kN was used and the initial distance between clamps was fixed at 64 mm in all cases. Young's modulus was determined using an extensometer and a crosshead-speed of 1 mm/min, while both yield strength and elongation at break values were determined using a crosshead-speed of 10 mm/min. At least five specimens were tested in each case.

3.3.9 Izod impact tests

Impact tests provide information about the toughness of the materials against impacts or shocks, by measuring the energy necessary to fracture a normalized specimen through impact, which takes place under high-speed deformations. The capacity of a material to absorb energy is a key parameter when identifying future applications.

Izod impact tests were performed using injection-molded impact specimens on an instrumentalized CEAST 6548/000 pendulum using a hammer of 4 J, following the ASTM D-256 standard. In order to study the performance of materials in the presence of a failure or a stress-concentrator, a standard notch (depth 2.54 mm, 0.25 mm radius and 45° angle) was machined in all specimens after injection molding. The value of the impact strength was calculated as the ratio between the energy lost by the pendulum during the collision and the thickness of the specimen. At least eight specimens of each composition were tested.

3.3.10 Measurements of oxygen permeability

The gas permeability of polymeric materials, particularly to oxygen molecules (O_2), is of great interest in applications targeted at the packaging industry. Oxygen can promote negative effects on different types of materials, such as degradation of foods, photo-oxidation, corrosion and oxidation phenomena, etc. Since the incorporation of MMT in polymers and polymer mixtures can produce improvements in their barrier behavior, it was considered of particular interest to determine the oxygen permeability of the clay-based nanocomposites. Films for permeability measurements were processed by compression molding as detailed in Chapter 3.2.3.2.

Permeability measurements were performed on a MOCON OX-TRAN model 2/21 permeator, which is designed to measure the flow of oxygen through the films by the action of a concentration gradient generated between both sides of the film. The measurement is carried out by passing a continuous flow of oxygen through one side of the film, so that the gas permeates through it and is collected in the other side by a carrier gas (a mixture of hydrogen and nitrogen) which subsequently passes to an O_2 sensor. The computer calculates the O_2 transmission rate (OTR), from which it can directly obtain the coefficient of permeability (P) of the material by the following equation:

$$OTR\left[\frac{cm^3}{m^2\ x\ day}\right] x\ l(mm) x\ \frac{0.29398}{p(mmHg)} = P(Barrer)$$

in which l is the thickness of the film, p is the pressure and 0.29398 a conversion factor.

The permeability of the films was determined in all cases at 23°C, at a pressure of 1 bar and at a relative humidity of 0% according to the ASTM D3985 standard. Measurements were taken on at least two films.

3.3.11 Electrical conductivity measurements

Pure polymers are mostly electrically insulating materials, and so, they are usually used for electrically isolating devices, machines or wires. However, the addition of conductive particles such as carbon black, carbon nanotubes or graphene can give semiconductivity to polymers, so that, they can be used in piezoelectric or electronic applications instead of typical inorganic silicon- or germanium-based semiconductors. In the present work, electrical conductivity measurements were carried out on all compositions containing carbon nanotubes.

The resistances of the materials were measured in a Keithley 6487 picoamperimeter and in a Keithley 2000 multimeter; the first device was used to measure resistances above 10^9 Ω and the second below 10^7 Ω. Both devices were connected to a Keithley 8009 test fixture.

Electrical conductivities of all materials were determined according to ASTM D 4496 and ASTM D 257 standards. The tested samples were sheets 70 mm in diameter and 1.25 mm thick, obtained by compression molding as detailed in Chapter 3.2.3.2. At least two samples of each composition were measured. The resistivity was calculated by the following equation:

$$\rho\ (ohm) = \frac{22.9}{thickness\ (cm)} . \left(\frac{V}{I}\right) (ohm. cm)$$

in which ρ is the resistivity of the material, V the voltage, I the current intensity and 22.9 a conversion factor. Resistivity is the specific electric resistance of the material, and conductivity (σ) is the inverse of resistivity (σ=1/ρ).

Chapter 4: PLA-based blends

CHAPTER 4: PLA-BASED BLENDS

PLA is a potentially very promising thermoplastic polymer, highly suitable for manufacturing many objects and goods in the near future. It combines thermoplasticity and good mechanical properties with unique environmentally friendly characteristics; it is both renewable and biodegradable. However, PLA shows intrinsic fragility against tensile and flexural stress, and also poor performance against impacts. Consequently, its current industrial application-range is quite limited. Ductile/tough polymers have been very efficient offsetting these disadvantages without impacting the stiffness and strength of PLA. PCL and PBAT are presented as two very interesting materials for this purpose, as they fulfill the aforementioned mechanical requirements and are also biodegradable.

In the present chapter, fully biodegradable PLA/PCL and PLA/PBAT blends are characterized. PLA-rich 90/10, 80/20, 70/30 and 60/40 compositions were obtained by melt-mixing, under the same processing conditions. The phase structures, morphology, rheological and mechanical properties of all compositions were characterized. This study analyzes and compares the characteristics of both blends and therefore offers insight into how PCL and PBAT can be used to modify PLA. In addition, the study also enables the most optimum PLA/PCL and PLA/PBAT compositions to be selected for subsequent modification with nanoparticles, as described in Chapter 6.

4.1 Poly(lactic acid)/Poly(ε-caprolactone) (PLA/PCL) blends

4.1.1 Phase structure

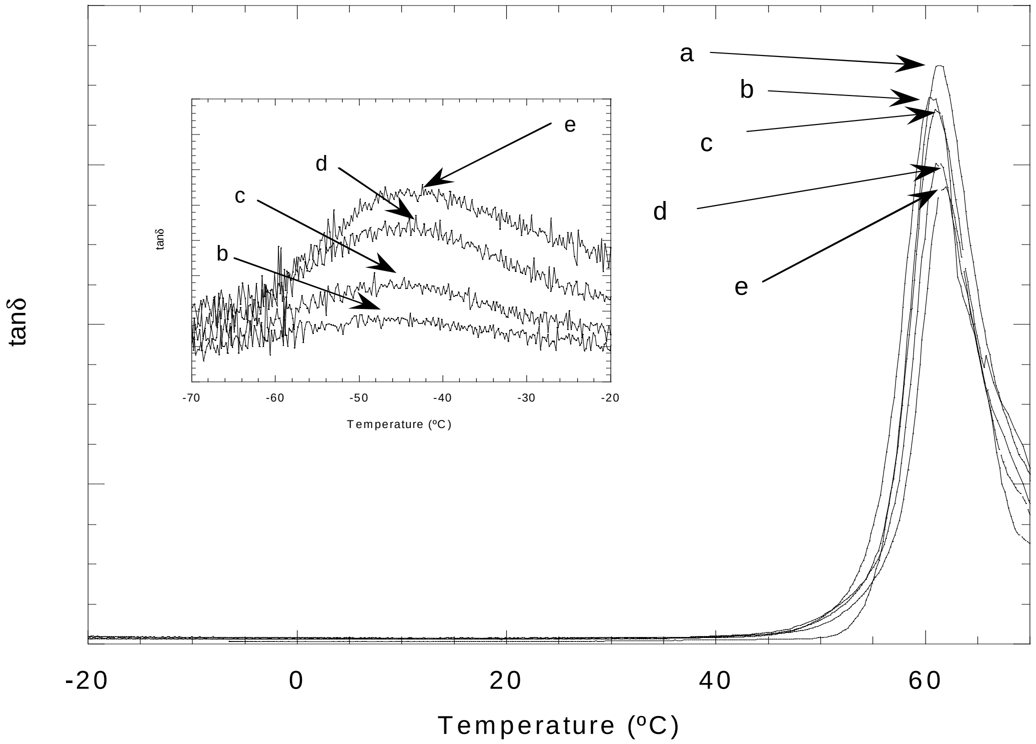

Figure 4.1.1: tanδ vs. temperature plots of pure PLA (a) and of 90/10 (b), 80/20 (c), 70/30 (d) and 60/40 (e) blends from -20ºC to 70ºC and from -70ºC to -20ºC.

Figure 4.1.1 shows tanδ vs. temperature plots of PLA and PLA/PCL blends. The glass transition temperature of neat PLA was 61.2ºC. The PCL was not processed in this study, but the DMTA-determined glass transition temperature of injection molded CAPA 6800 PCL has been reported to be centred at -45ºC[225]. Regarding the blends, two tanδ peaks were observed. The high temperature peak corresponds to the PLA phase, and the low temperature peak (in the amplified plot) to the PCL phase. The maxima of both tanδ peaks were almost unaltered in the different blend compositions (the corresponding temperatures were 61.2±0.4ºC and -45.0±0.3ºC), suggesting full immiscibility of the PLA with the PCL. This has been the general behavior reported for PLA/PCL blends. Only López-Rodriguez et al.[4] and Sakai et al.[42] reported partial miscibility between both polymers by applying the Fox equation[226]; and estimated that a very small amount of PCL was dissolved in PLA. Elsewhere, Takayama et al.[13] mentioned that the addition of LTI improved miscibility in the PLA/PCL 85/15 blend. However, this conclusion was based on the reduced size of PCL particles caused by the LTI; no parameters were calculated to determine the degree of miscibility.

The intensity of the PLA peaks in Figure 4.1.1 was clearly greater than that of the low temperature peaks even in the case of the 40% PCL containing blend. This has probably to do with the crystallinity levels of PLA and PCL in the blends. As we will see below, PCL is highly crystalline, while PLA is virtually amorphous or slightly crystalline. High crystallinity usually leads to low intensity of the glass transition due to the small fraction of the amorphous phase and the hindered mobility of the amorphous segments close to crystalline structures.

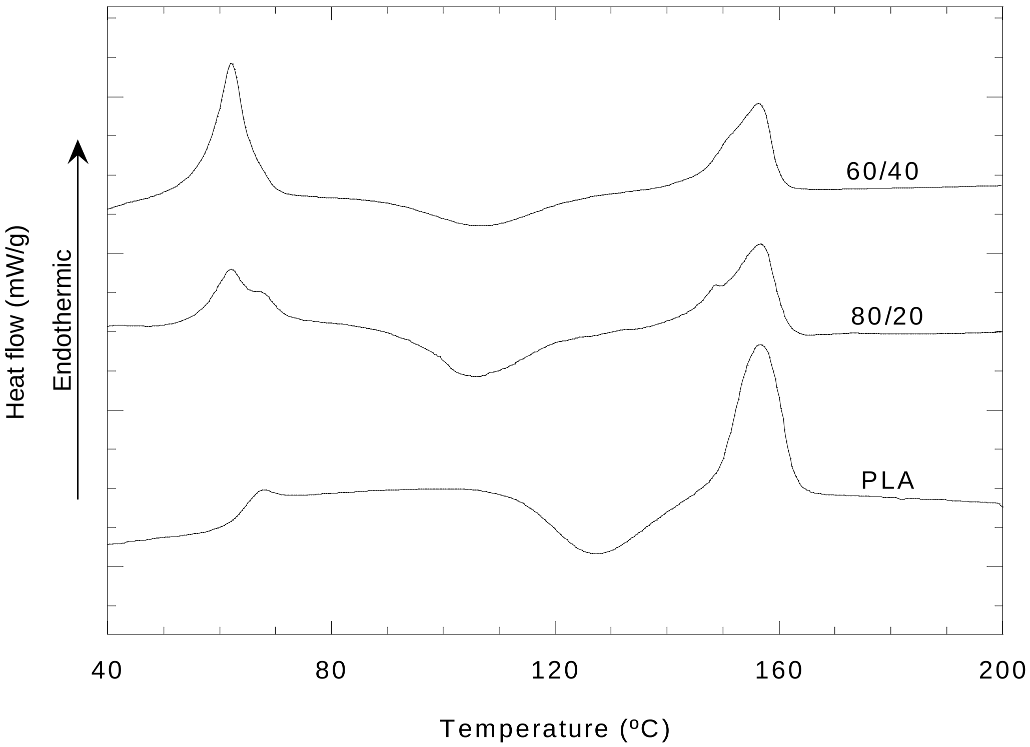

Figure 4.1.2: First DSC heating scans of pure PLA and of 80/20 and 60/40 blends.

Figure 4.1.2 shows the first DSC heating scans of neat PLA and 80/20 and 60/40 PLA/PCL blends. Due to its slow crystallization kinetics[8], PLA was unable to fully crystallize from the melt during cooling in the injection mold in any of the studied compositions, eventually crystallizing during the heating scan. The wide exotherms, centred at approximately 125ºC for PLA and at 105-110ºC for the blends, reflect these crystallization processes. Similarly, no PLA crystallization peak was observed on cooling at 20ºC/min in the calorimeter, with crystallization again occurring in the second heating scan. Regarding to PCL, its melting endotherm (Tm=64ºC for neat PCL) appeared close to the Tg of PLA, so that its level of crystallinity could not be accurately determined.

Table 4.1.1: Melting temperatures of PLA (Tm_{PLA}) and PCL (Tm_{PCL}) and, crystallization temperatures of PLA (Tc_{PLA}) and degrees of crystallinity (Xc) of PLA in the PLA/PCL blends.

Composition (PLA/PCL)	Tm_{PLA} (ºC)	Tm PCL (ºC)	Tc PLA (ºC)	Xc PLA (%)
100/0	155.1	-	125.1	0
90/10	158.1	61.7	110.7	9.2
80/20	156.7	62.0	104.7	4.7
70/30	155.4	61.1	104.7	3.4
60/40	156.3	62.0	107.7	3.4

Table 4.1.1 summarizes the calorimetric data obtained from the first heating scans. As shown, the presence of PCL led to a clear decrease in the crystallization temperature of PLA indicating, in keeping with previous studies[41,42,44,52,53], a nucleating effect of PCL. In any case, the crystallinity of PLA remained very low, close to 9% at most. Sarasua et al.[4] observed that dispersed PCL particles increased the crystallinity of PLA in a casted 80/20 PLA/PCL blend. The same authors compared the dynamic crystallization behavior of neat PLA with the 60/40 PLA/PCL blend with a heating rate of 10ºC/min. The blend showed two exothermic peaks, at 100ºC and just before the melting endotherm. This second peak was attributed to the possible recrystallization of imperfect PLA crystals into more perfect α crystals. In a separate study, Sakai et al. [42], having performed analyses at a heating rate of 20ºC/min, observed that PCL enhanced the nucleation of PLA at low temperatures, but had an insignificant effect on crystal growth, perhaps due to the low miscibility of the blend. Consequently, the enhanced cold crystallization was due to the increase in the number of nuclei generated at lower temperatures, induced by the presence of PCL.

Table 4.1.1 also shows that the melting temperature of PLA remained almost constant. In the case of the melting temperature of PCL, a scarcely significant 2ºC decrease was observed in all the blends with respect to that of neat PCL.

4.1.2 Morphology

Figure 4.1.3 shows micrographs reflecting the most representative inner (core) part of cryogenically fractured surfaces of 90/10, 80/20, 70/30 and 60/40 PLA/PCL tensile specimens. As it is seen, all the blends showed biphasic morphology regardless of the composition, confirming the immiscibility of PLA with PCL.

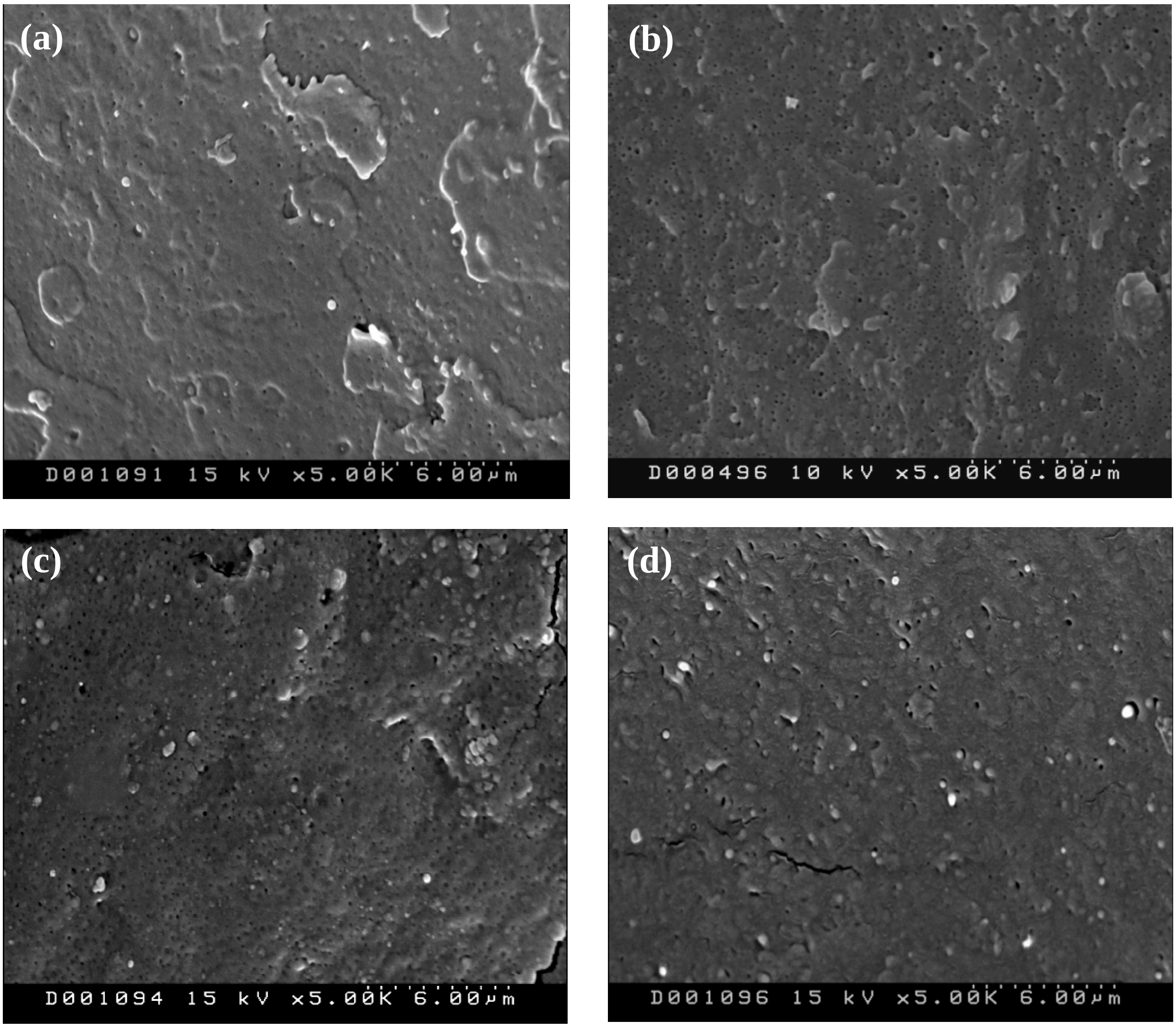

Figure 4.1.3: SEM micrographs of cryogenically fractured surfaces taken from tensile specimens of 90/10 (a), 80/20 (b), 70/30 (c) and 60/40 (d) PLA/PCL blends.

PCL particles were uniformly dispersed in the PLA matrix and the particle size was homogeneous and very small in all the compositions, with an average diameter of few hundred nanometers. The particle size seemed to increase slightly at higher PCL contents, but remained very small even in the 60/40 composition. This morphology is very different to that observed by other authors for unmodified PLA/PCL blends, where the average PCL particle size was clearly higher[43,44,59]. While some debonded particles were observed in Figure 4.1.3, the fractures showed a partially cohesive character, suggesting some interfacial adhesion between PLA and PCL in the solid state. Taking into account both observations, i.e. the small particle size and the fairly good interfacial adhesion, it seems that the blending conditions used in this study were more effective than those used in previous works on uncompatibilized PLA/PCL blends[45, 14, 15], even when compared with blends prepared using extruders with higher L/D ratios[45, 15].

With regard to the PCL phase morphology, Wu et al reported[59] that, in an uncompatibilized PLA/PCL system, it changed from spherical in the 80/20 composition to fibrillar in the 60/40 blend. In the blends in this study, the appearance of the PCL particles remained almost the same in all the compositions and very similar to that of compatibilized blends[48-50,52,53].

So, the morphology of the PLA/PCL blends in the present work suggests that, under the processing conditions used here, both polymers jointly form an immiscible but most likely compatible blend in the PLA-rich region. In contrast with previous works[7-13] it was not necessary to add a compatibilizing agent in order to obtain very small PCL particles and interfacial adhesion between both components.

The resulting interfacial tension for the PLA/PCL blends in this work was 1.55 mN/m. This value is comparable, although slightly higher, to those calculated respectively by Wu et al.[217] (0.9 mN/m) and Noorozi et al.[227] (1.206 mN/m). In agreement with previous works, this low interfacial tension accounts for the interfacial adhesion observed in PLA/PCL blends[228], and is also consistent[229,230] with the small size of the particles in Figure 4.1.3.

The viscosity ratio of PLA and PCL (η_{PLA}/η_{PCL}~0.95 in all the measured strain rate range) is another factor that tends to reduce the dispersed particle size[231,232]. It could be speculated that, despite the similar interfacial tension values, this viscosity effect is probably responsible for the different particle sizes observed in other studies. Thus, their combined effect could contribute to the small PCL particle size in PLA/PCL blends obtained in the present work.

4.1.3 Viscoelasticity

Figure 4.1.4 shows the storage modulus (G´) vs. angular frequency (ω) plots of pure PLA and PLA/PCL blends determined by measurements carried out at 180ºC using parallel-plate geometry and in the linear viscoelastic zone. As can be seen, G´ of the blends increased at low frequencies as the amount of PCL increased. These increases, also reported in bibliography[59,233], indicate that PCL improved the elastic melt behavior of PLA. Consequently, the melt strength of PLA was increased in the PLA/PCL blends. These results are very interesting from an applied point of view, since the low melt strength of PLA is one of the main drawbacks that it presents for melt-processing[4].

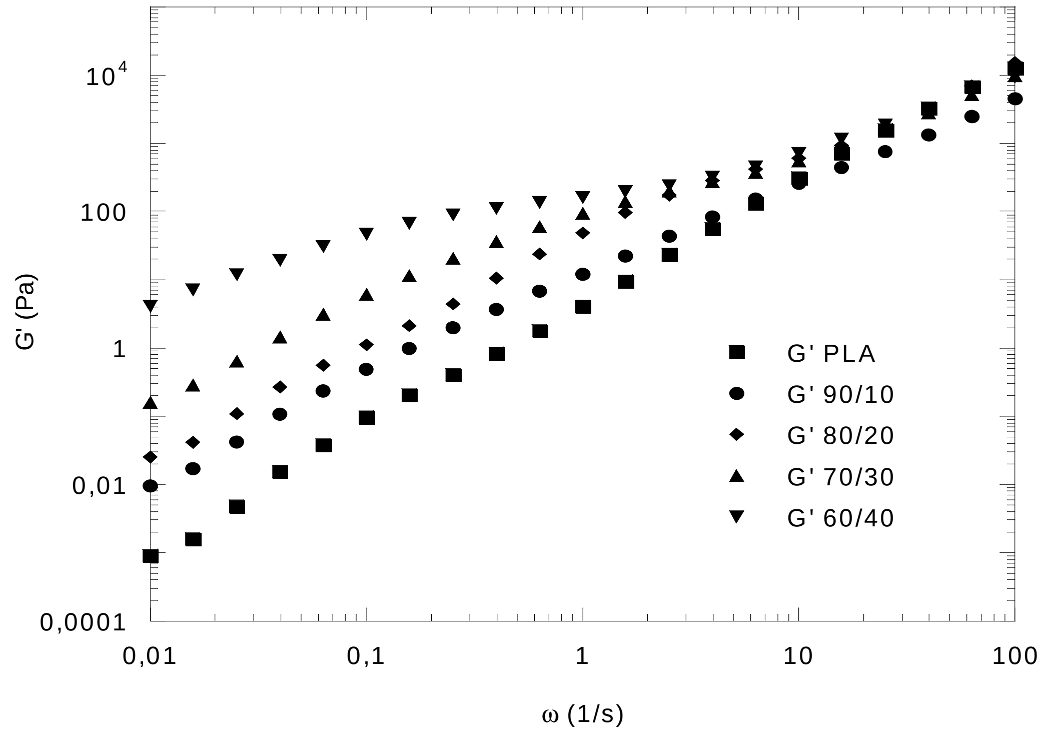

Figure 4.1.4: G´ vs. ω plots of pure PLA and of PLA/PCL blends.

4.1.4 Mechanical Properties

Figure 4.1.5 shows Young's modulus and the yield strength of neat PLA and the PLA/PCL blends as a function of composition. Both properties decreased as the PCL content increased, in agreement to that observed in previous works based on immiscible polymer blends consisting of a stiff matrix and soft dispersed particles[225,234]. Phase separated PCL droplets impaired both properties as a result of its low Young's modulus (410±20 MPa) and yield strength (14±0.2 MPa). In any case, thanks to the high modulus of PLA, the experimental values stayed well above 2000 MPa, even after 40% PCL was added. This is an important finding as it suggests that these blends will probably still be apt for use in most of the traditional applications of PLA. The decrease in the yield strength is considerably more significant, but it still remained close to 50 MPa at 40% PCL contents.

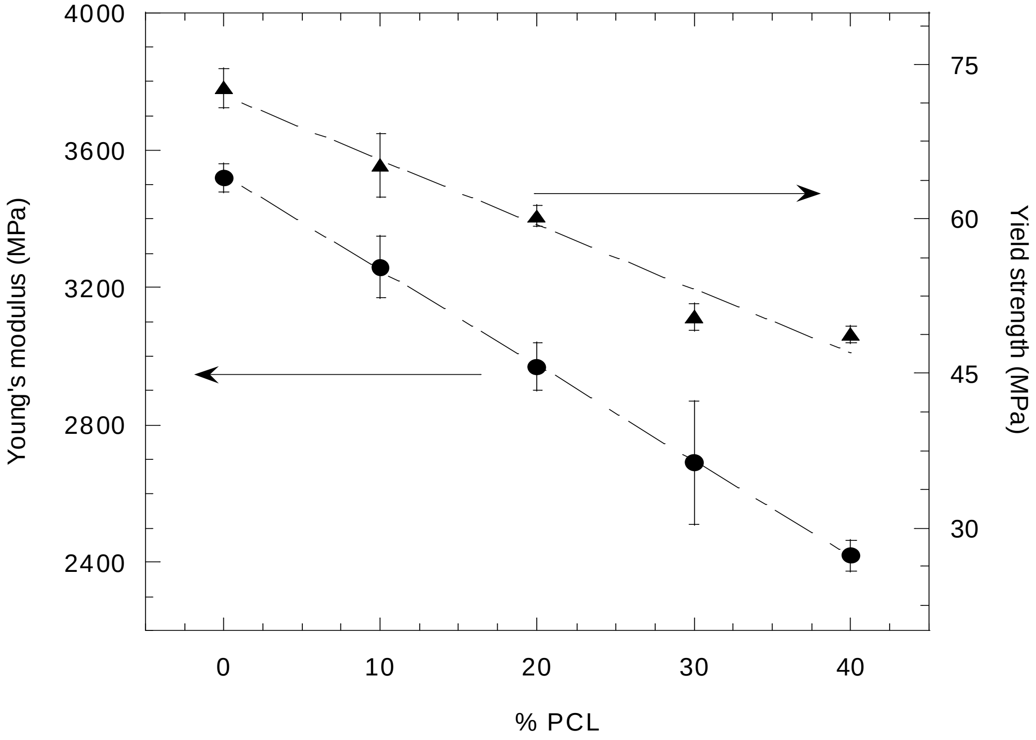

Figure 4.1.5: Young's modulus (●) and yield strength (▲) values of PLA/PCL blends with respect to the PCL content.

The elongation at break of PLA and the blends is shown against composition in Figure 4.1.6. PLA is known to be very brittle and appears so in Figure 4.1.6. By contrast, PCL is very ductile, with an elongation at break of 425±20%[225]. As it can be observed in Figure 4.1.6, the addition of only 10% PCL leads to a clear change in the fracture behavior of PLA, so that the 90/10 blend has an elongation at break of 140%, and remains virtually unchanged at higher PCL concentrations. Increased ductility of PLA in blends with PCL has been reported by other authors[44]. However, in these reported cases, and, with the exception of systems in which a compatibilizer was added during the blending process, the transition to ductility took place at PCL contents of over 30%[45,52,53,55]. In other works, while the presence of some interfacial adhesion between PLA and PCL was reported[41], ductility did not increase until the intermediate 50/50 composition was reached.

If we examine the reasons for the different elongation at break values presented in this study and in previous papers, it is known that the elongation at break of rigid polymers is affected by the testing rate, generally decreasing as the testing rate increases[235]. In several previous works on PLA/PCL blends[41,44,45,55,57], the elongation rate used in tensile tests was 50 mm/min, instead of 10 mm/min, which was used in this study. Thus, the elongation at break values in Figure 4.1.6 may have been partially affected by the testing rate. In fact, tensile tests carried out on the 80/20 blends in this study at 50 mm/min led to an elongation at break of 13.6 ± 2.7 %. Therefore, the differences between the data contained in Figure 4.1.6 and those in the literature are probably affected, at least partially, by the differences in the testing rate.

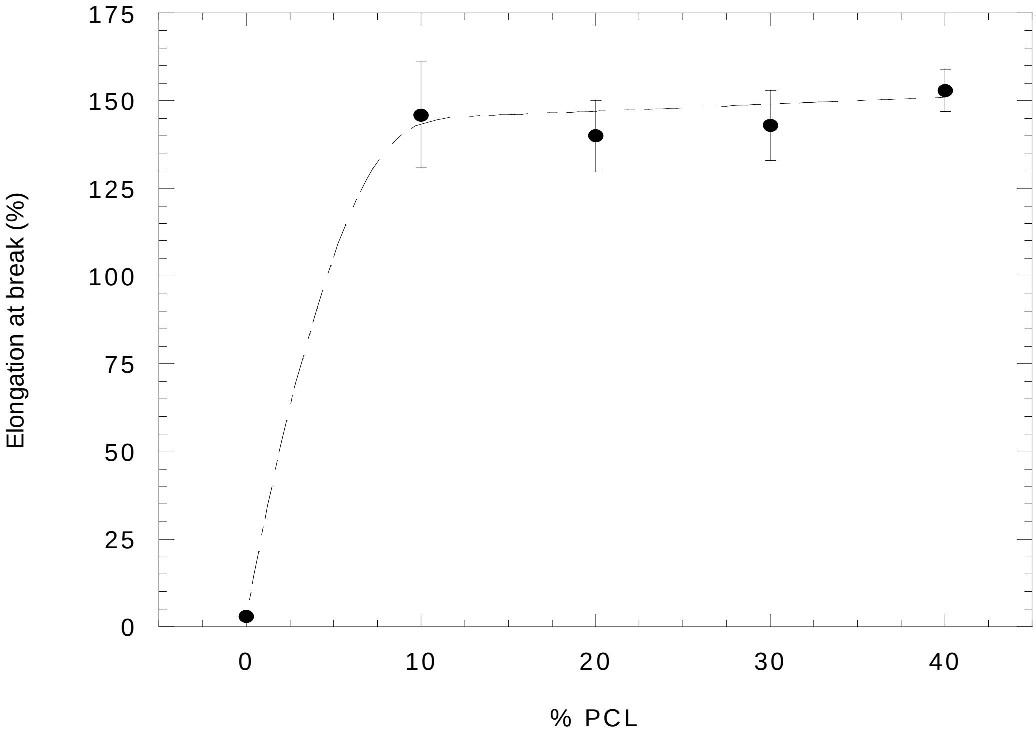

Figure 4.1.6: Elongation at break values of PLA/PCL blends with respect to the PCL content.

However, low elongation at break values have also been obtained in previous studies involving PLA/PCL blends, using elongation rates lower than 10 mm/min [43,46,47,52]. Furthermore, when the morphology of the PLA/PCL blends in Figure 4.1.3 is compared with that of previous studies, it is clear that the blends of this study resemble the morphology of compatibilized blends[49,50,52,53] more than they resemble uncompatibilized ones[41,43,44,53]. So, the morphology of the blends, which is characterized by a very small particle size[45,235,236], together with the existence of some interfacial adhesion[14,237] and the high elongation at break values shown in Figure 4.1.6 would all suggest that these PLA/PCL blends are mechanically compatible.

It has been reported[236] that fractionated crystallization of PCL can occur in blends with other polymers on cooling from the melt; therefore it is possible for some fraction of PCL to crystallize even at temperatures below room temperature. If this is true for the PLA/PCL blends in this study, some fraction of usually crystallized PCL could have remained in an amorphous state in the dispersed PCL particles, making these particles more deformable than expected, thus contributing to the improved ductility of the blends. Figure 4.1.7 shows DSC cooling scans from the melt of neat PCL and the PLA/PCL 80/20 blend.

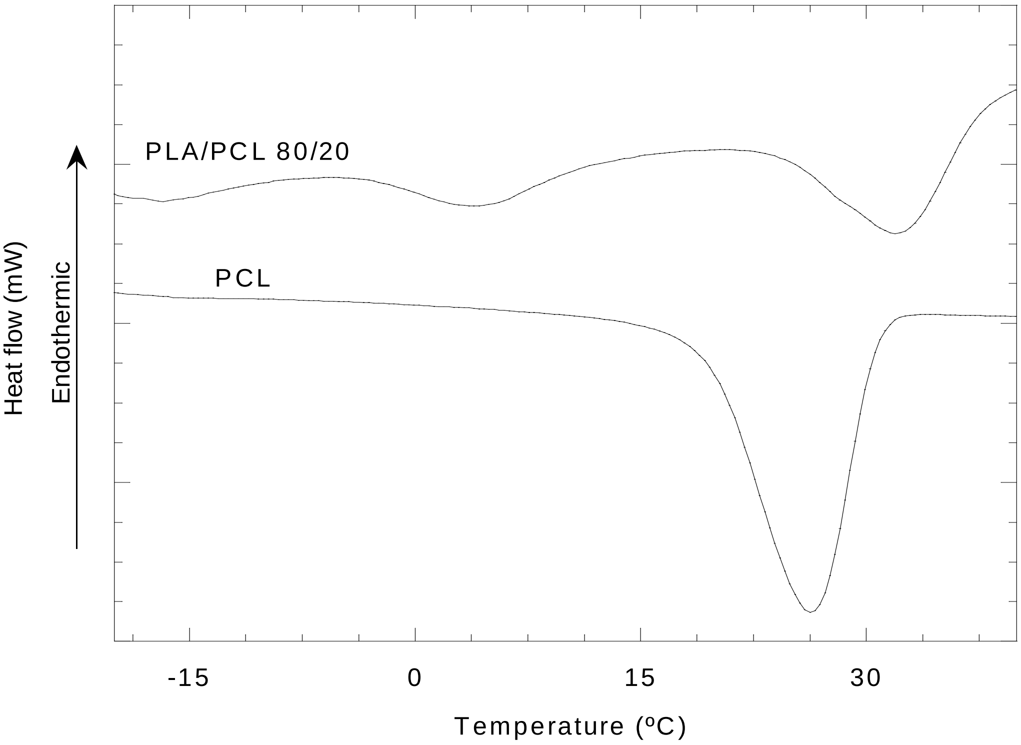

Figure 4.1.7: DSC cooling scans of pure PCL and of the 80/20 blend.

As the figure shows, fractionated crystallization occurred in the blend. In order to check whether this phenomenon affected the ductility values in Figure 4.1.6, some specimens of the PLA/PCL 80/20 blend were kept at a temperature of -40ºC for 24 hours for the PCL to crystallize completely. They were then tensile tested. The ductility value obtained was 167±10%, ruling out fractionated crystallization as the cause of the high ductility of the blends.

Another possible reason for the high ductility values in Figure 4.1.6 is the occurrence of interchange reactions between PLA and PCL during processing, which may have compatibilized the blends. As mentioned previously, the addition of compatibilizers DCP and LTI to PLA/PCL blends foments interchange reactions between both polymers, giving rise to ductile materials[45,52,53,55].

In order to check whether the interchange reactions also affected the compatibility observed in this study, ^{1}H-NMR analysis[57] and torque measurements[45,52] were carried out for different blend compositions. The representative signals of the LA-CL dyad (at 2.37 and 4.11 ppm)[237] did not appear in the NMR spectra of the blends and, furthermore, no viscosity peaks were appreciated in the torque-time plots up to a kneading time of 20 min, clearly higher than the residence time the blends spent in the melt state during extrusion and injection molding. Consequently, interchange reactions were ruled out as a possible explanation for the morphology and ductility of the blends.

To gain further insight into the morphology and mechanical behavior of PLA/PCL blends, the 90/10 and 80/20 compositions were prepared at the same temperature using three less effective processing methods (for comparison they will be called method 2, 3 and 4) than the standard procedure, which will be called method 1. Thus, processing was carried out by blending in a Collin twin-screw extruder-kneader at 80 rpm (Teachline, L/D ratio 18, screw diameter 25 mm) and injection molding under the same conditions as those of method 1 (method 2), and also directly by injection molding, without previous blending (method 3). In addition, pellets of the 80/20 PLA/PCL blend obtained using method 1 were compression molded at the same temperature in a Collin P-200-E compression molding machine (method 4).

In Figure 4.1.8, the morphology of the 80/20 blend processed by method 2 (low L/D extruder and ulterior injection molding) (Figure 4.1.8a) and method 3 (direct injection molding) (Figure 4.1.8b) is shown. Although the particles obtained using methods 2 and 3 are slightly bigger than those using more favorable method 1, they were still very small.

The mechanical properties were also very similar, as shown in table 4.1.2. The 90/10 composition produced similar results. So, irrespective of the procedure used, with and without previous blending, the morphology and mechanical properties, in particular the elongation at break of the blends, did not vary. This would strongly suggest that the injection molding process is the most important step for establishing them in our PLA/PCL blends. Given that the morphology and properties of these blends did not change during any of the processing methods used, and they remained stable when fractionated crystallization of PCL was avoided, it points to the small particle size and the interfacial adhesion as responsible for the high ductility of the blends.

This proposition was evaluated by processing the 80/20 blend prepared in the high L/D extruder by compression molding (method 4). This molding procedure involves a short and multidirectional flow, with a very low shear level. As the molding times are relatively long (5 min), there is a good chance of the particles coalescing. In Figure 4.1.8c the morphology obtained is shown. The particles are visibly larger than those obtained using methods 1-3 after injection molding, although there was still some adhesion.

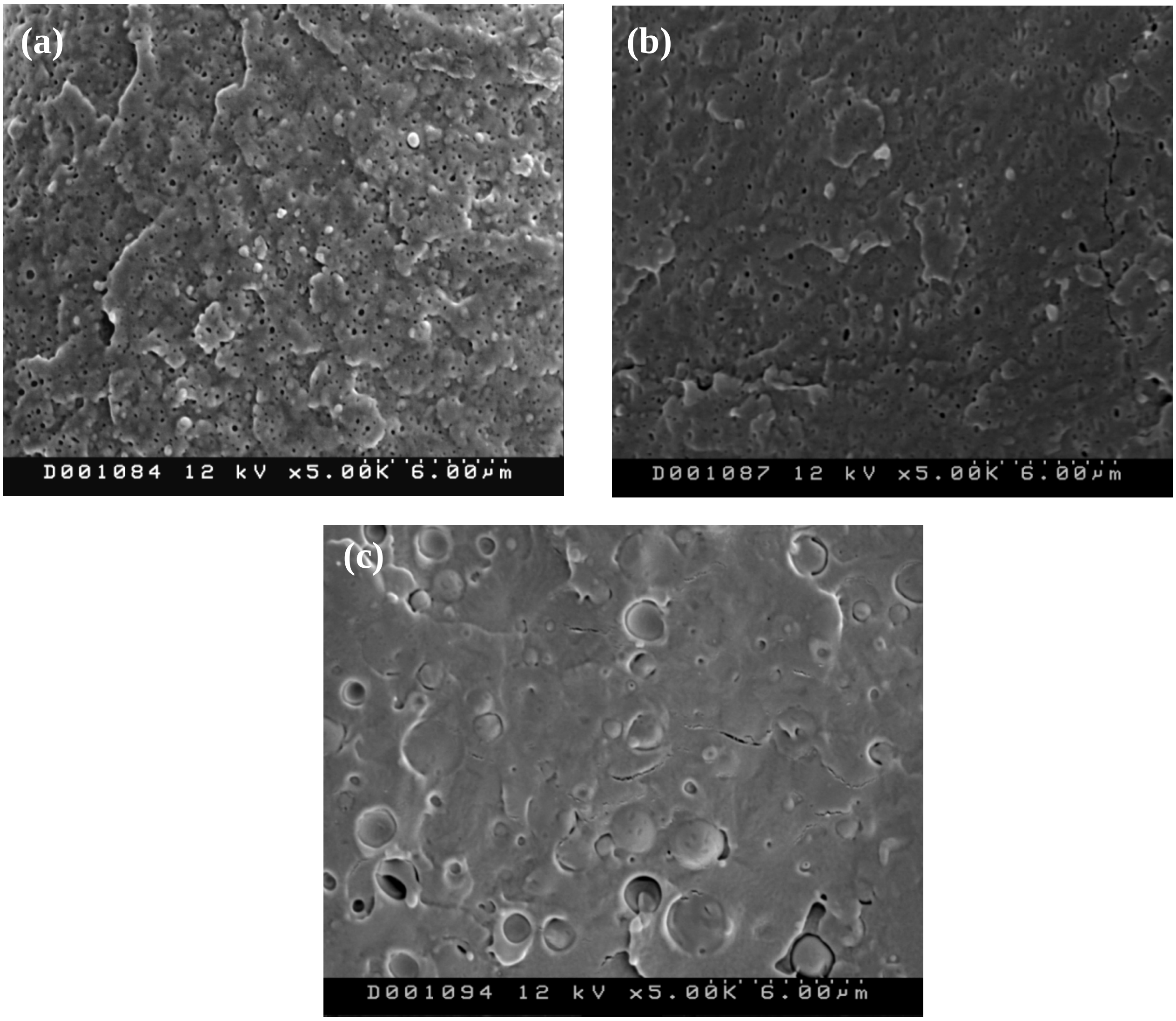

Figure 4.1.8: SEM micrographs of cryogenically fractured surfaces taken from tensile specimens of the 80/20 blend processed by methods 2 (a), 3(b) and 4(c).

The ductility was 50%, i.e. clearly lower. Taking into account the aforementioned particle size, it appears, as expected, that there is a relation between particle size and ductility: larger particles leading to less ductility. Therefore, the positive ductility values obtained for the blends processed with methods 1-3, involving injection molding, are attributed to the small size of the particles and the interfacial adhesion. This behavior is consistent with that shown by other PLA-based phase-separated blends[69,238].

Table 4.1.2: Young's modulus, yield strength and elongation at break values of the 80/20 blend processed by methods 1-4.

Method	Young's modulus (MPa)	Yield strength (MPa)	Elongation at break (%)
1	2970±70	60.3±1.0	140±10
2	2900±10	57.2±0.3	142±3
3	2900±40	54.8±1.2	136±5
4	2890±55	51.9±1.1	50.5±10.2

Regarding to the impact strength, Figure 4.1.9 shows that measured by means of the Izod test for the PLA/PCL blends as a function of composition. As previously mentioned, PLA is a brittle polymer, and consequently offers very poor impact strength[40]. By contrast, PCL offers good impact strength (400±50 J/m). Therefore, PCL could potentially improve the poor toughness of PLA. As the figure indicates, the addition of PCL led to a steady increase in impact strength. Although the absolute impact strength values remained relatively low, the relative increase was considerable (approximately 200% with 30% PCL and 350% with 40% PCL). The impact performance of the 40% PCL blend was comparable to that of some uncompatibilized PLA/elastomer 80/20 blends[239].

The behavior of the impact strength is clearly different to that of the ductility (Figure 4.1.6). The intrinsic differences between tensile and impact tests (strain rate, state of stress, notch presence-absence) probably account for this difference. In addition to this, the PCL particles in injection molded PLA/PCL blends, regardless of the blending method used (method 1 (Figure 4.1.3b), method 2 (Figure 4.1.8a) or method 3 (Figure 4.1.8b)), were too small to effectively improve the impact strength of PLA, taking into account recent results reported by Bai et al. [19]. They observed that, in the case of 80/20 amorphous PLA/PCL blends, the highest impact strength (corresponding to supertoughness) is obtained when the average PCL particle diameter is close to

0.9 μm. This is clearly larger than the particles in the 80/20 blends here, and could be the reason for the lower impact strength results in Figure 4.1.9.

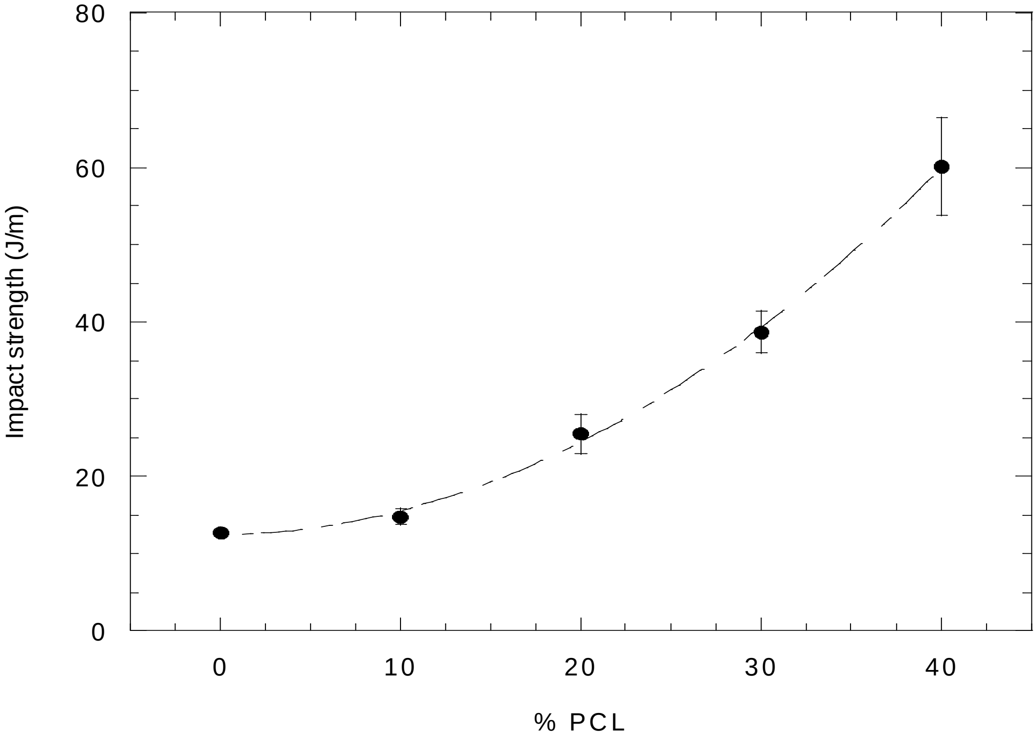

Figure 4.1.9: Impact strength values of PLA/PCL blends with respect to the PCL content.

4.2 Poly(lactic acid)/Poly(butylene adipate-co-terephthalate) (PLA/PBAT) blends

4.2.1 Phase structure

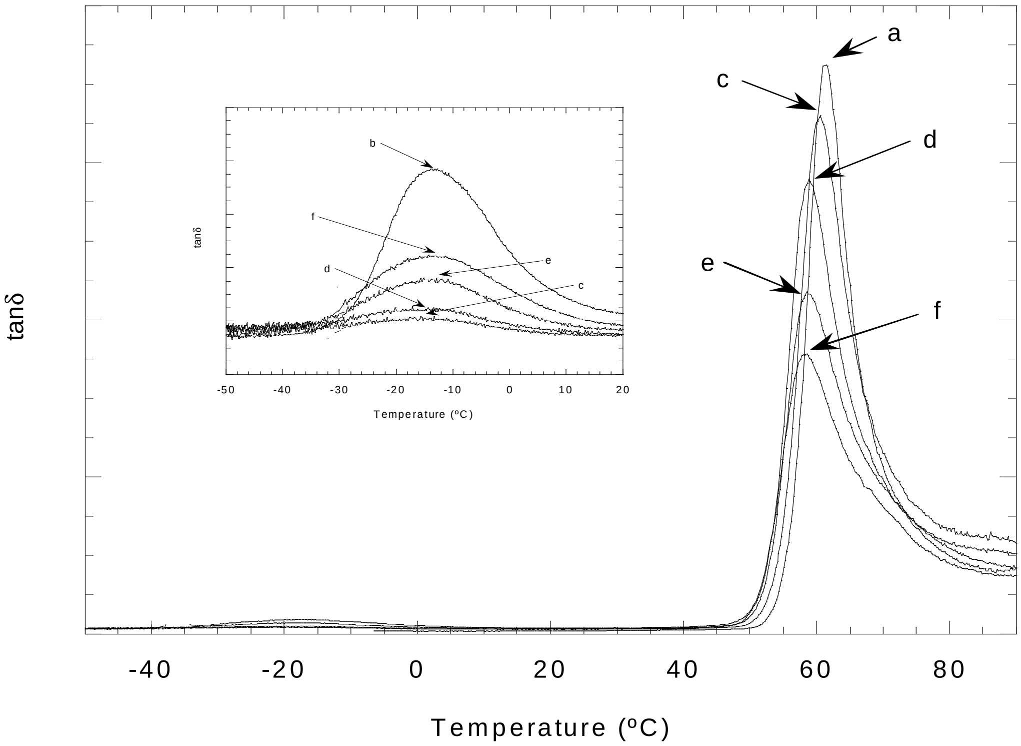

Figure 4.2.1: tanδ vs. temperature plots of pure PLA (a) and PBAT (b) and of 90/10 (c), 80/20 (d), 70/30 (e) and 60/40 (f) blends from -50ºC to 90ºC and from -50ºC to 20ºC.

Figure 4.2.1 shows tanδ vs. temperature plots of PLA, PBAT and PLA/PBAT blends obtained by DMTA. Pure PLA and pure PBAT presented glass transitions at 61.2ºC and -12ºC, respectively. In the PLA/PBAT blends, two tanδ signals were observed in all compositions, indicating phase-separation. The tanδ signals which appear at high temperatures correspond to the PLA phase and those appearing at low temperatures, and amplified in the insertion in Figure 4.2.1, to the PBAT phase. The latter remained close to -12ºC in all the PLA/PBAT blends, indicating that the presence of PLA did not affect the glass transition of the PBAT phase. However, and in contrast to that observed in PLA/PCL blends, the glass transition temperature of the PLA phase, decreased slightly but consistently at increasing PBAT contents.

This progressive decrease in the PLA transition, suggests some level of interaction between PLA and PBAT, consistent with findings reported by other authors[65,67,68]. In fact, some transesterification reactions between PLA and PBAT during melt-processing have been reported[64]. These reactions, involving the ester groups of both polymers, would lead to the creation of PLA-co-PBAT copolymers in-situ at the interphase between the two phases. This was examined in the present work by means of ^{1}H-NMR analysis and torque measurements.

^{1}H-NMR analysis did not show any signal additional to those of pure PLA and PBAT and the viscosity of the 80/20 and 60/40 PLA/PBAT compositions, followed by means of the kneading torque measured in a recirculating microextruder during 20 minutes (a time much longer than the residence time during processing), maintained or even decreased. Both results point to the absence of ester-exchange reactions in these PLA/PBAT blends, so they were ruled out as being the cause of the decrease in the transition corresponding to the PLA-phase.

Once interchange reactions were ruled out, the partial miscibilization of some PBAT in the PLA-rich phase appeared to be as the only alternative explanation. Theoretical diluted amounts for each blend composition were calculated using the Fox equation [240]:

$$\frac{1}{Tg_{blend}} = \left(\frac{w_{PLA}}{Tg_{PLA}}\right) + \left(\frac{1-w_{PLA}}{Tg_{PBAT}}\right)$$

where Tg_{blend} was the experimental Tg value of the PLA phase in the blend, Tg_{PLA} was the Tg value of neat PLA, Tg_{PBAT} was the Tg value of neat PBAT and w_{PLA} was the weight fraction of PLA in the main phase. The results obtained, along with the weight fraction of PBAT in the PLA phase (w_{PBAT}) and the calculated percentage of PBAT in the PLA phase with respect to the overall PBAT content of each composition (% PBAT in PLA phase) are shown in Table 4.2.1.

As can be seen, the w_{PBAT} was low in all the studied compositions, indicating that the miscibility of PBAT in PLA is very limited. The maximum w_{PBAT} was obtained for the 60/40 composition (3.3%). This is in agreement with the full miscibility obtained in PLA/PBAT blend with a low PBAT content (2.5%)[69]. However, when these w_{PBAT} fractions are compared with the overall PBAT content of the blend, albeit with slight variations among compositions, a 5-10% of the

PBAT was seen in the PLA-rich phase of the blend. Therefore, and as mentioned in previous works[65,67-69], PLA/PBAT blends can be considered partially miscible.

Table 4.2.1: Glass transition temperatures of the PLA phase, weight fractions of PLA (w_{PLA}) and PBAT (w_{PBAT}) in the PLA phase (calculated by the Fox equation) and, the percentages of PBAT dissolved in the PLA phase with respect to the overall PBAT contents.

Composition	**Tg of the PLA phase (ºC)**	**w_{PLA} (%)**	**w_{PBAT} (%)**	**Percentage of PBAT dissolved in PLA (%)**
100/0	61.2	100	0	0
90/10	60.4	99.1	0.9	8.2
80/20	59	97.6	2.4	9.8
70/30	58.7	97.2	2.8	6.7
60/40	58.1	96.7	3.3	5.1

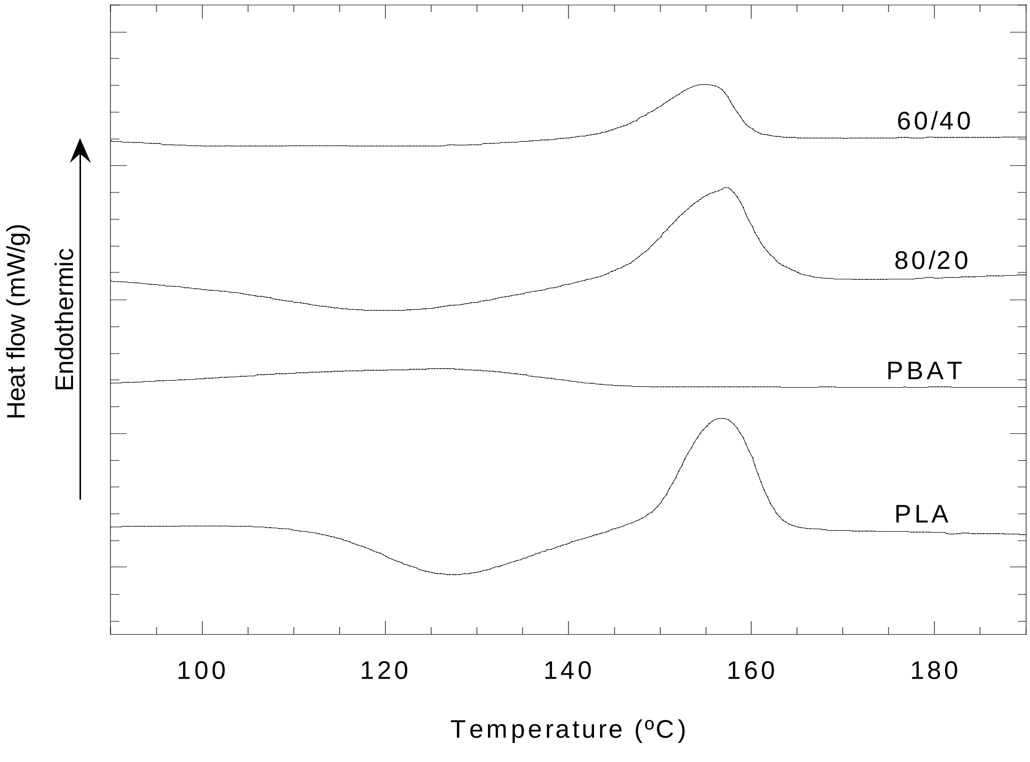

Figure 4.2.2: First DSC heating scans of pure PLA and pure PBAT and of 80/20 and 60/40 blends.

Figure 4.2.2 shows, as an example, the first heating scans of as-molded pure PLA and PBAT, PLA/PBAT 80/20 and 60/40 blends obtained by DSC. Table 4.2.2 shows the melting and crystallization (Tm and Tc) temperatures and enthalpies (ΔHm and ΔHc) and the ΔHm-ΔHc enthalpy of pure PLA and PLA/PBAT blends. As can be seen in Figure 4.2.2, as-molded PBAT presented a broad and diffuse melting endotherm between 100ºC and 140ºC, which in PLA/PBAT blends overlapped with the cold crystallization exotherm of PLA. According to previous data[241] the melting enthalpy of PBAT was negligible compared to the crystallization enthalpy of PLA, and therefore, both the melting enthalpy and the position of the maximum values of the exotherms were assumed to be those of the cold crystallization process of PLA.

Table 4.2.2: Melting (Tm) and cold crystallization (Tc) temperatures, melting (ΔHm), cold crystallization (ΔHc) and ΔHm-ΔHc enthalpies and, degrees of crystallinity (Xc) of PLA in PLA/PBAT blends.

Composition	Tm (ºC)	Tc (ºC)	ΔHm (J/g)	ΔHc (J/g)	ΔHm-ΔHc (J/g)	Xc PLA (%)
Pure PLA	155.1	125.1	20.7	-20.6	0.1	0
90/10	156.4	113.4	23.8	-17.9	5,9	7
80/20	156.7	117.7	25.1	-13.9	11,2	15
70/30	154.7	116.1	17.4	-11.6	5,8	12
60/40	155.1	117.1	14.6	-7.0	7,6	13,5

As shown in Figure 4.2.2. and Table 4.2.2, the cold crystallization temperature of PLA decreased 10-15ºC in PLA/PBAT blends with respect to that of pure PLA. In addition, the degree of crystallinity of PLA increased from almost 0 in pure PLA to 7-15% in PLA/PBAT blends. These results point to a nucleation effect of PBAT in the PLA/PBAT blends, allowing PLA to partially crystallize during cooling in the injection mold. The presence of PBAT molecules in the PLA phase due to the above mentioned partial miscibility may help to explain the nucleation effect of PBAT on PLA. Indeed, this effect has been widely reported in the literature[63,69,241-243].

The presence of PBAT modifies the spherulitic growth of PLA [241] and as a result the cold-crystallization temperature of PLA decreases[63,241]. The possible transference of impurities from the PBAT-rich phase to the PLA-rich phase has also been proposed as a possible explanation for the nucleation ability of PBAT in PLA/PBAT blends[241]. Small increases in the degree of crystallinity of PLA (from amorphous to 5% crystalline) have also been reported[241]. However, the nucleation effect did not seem to affect the structure or perfection of the grown crystals in the PLA/PBAT blends, since, as can also be seen in Table 4.2.2, the melting temperature of PLA in PLA/PBAT blends remained similar to that of pure PLA.

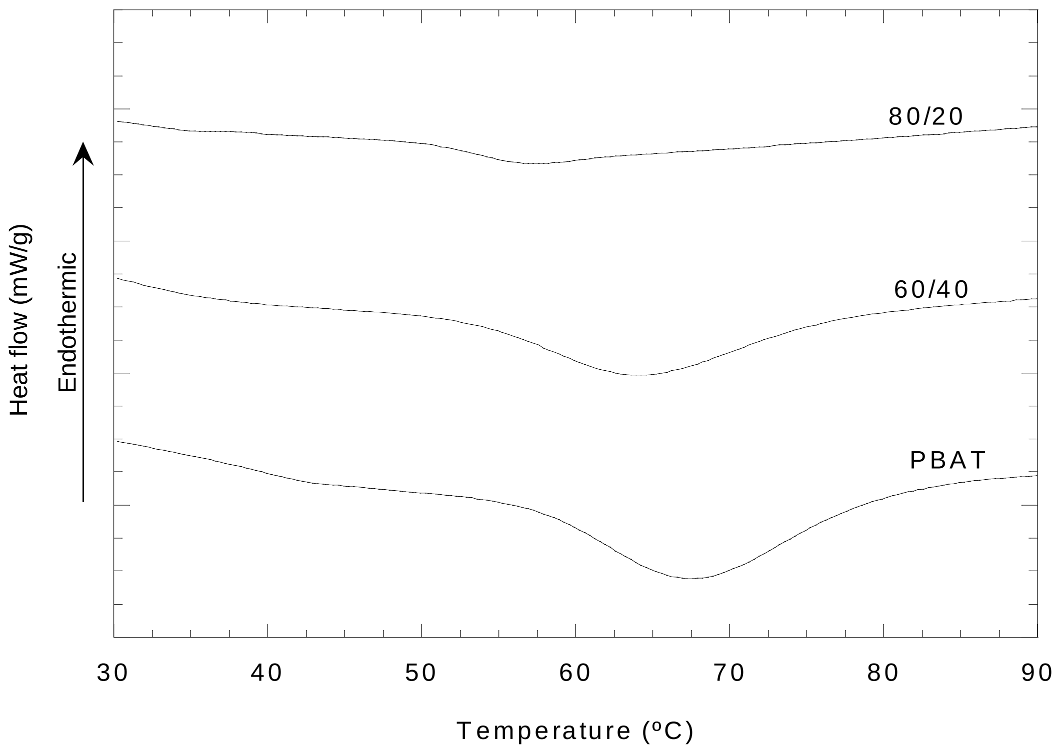

Figure 4.2.3: DSC cooling scans of pure PBAT and of 80/20 and 60/40 blends.

With respect to the PBAT phase, no relevant information was obtained from heating scans, as its melting peak overlapped with the cold crystallization peak of the PLA phase. This is why the behavior during cooling in the calorimeter was studied. Figure 4.2.3 shows cooling scans of pure PBAT and of 80/20 and 60/40 PLA/PBAT blends. Both the crystallization temperature and the crystallization enthalpy of PBAT became lower in the blend as the PLA content increased. As an example, the crystallization temperature of pure PBAT (67.9ºC) dropped to 63.6ºC with 60% PLA and to 57ºC with 80% PLA, respectively, while the degree of crystallinity was reduced by 30% and 70% with the same PLA contents. This indicates that the crystallization of PBAT was hindered in the PLA/PBAT blends, which could also be related to the migration of impurities from PBAT to PLA[241].

4.2.2 Morphology

Figure 4.2.4 shows SEM micrographs exhibiting representative morphologies of the 90/10 (a), 80/20 (b), 70/30 (c) and 60/40 (d) PLA/PBAT blends. As can be seen, 90/10, 80/20 and 70/30 compositions showed a clear matrix/dispersed phase morphology, in keeping with the DMTA results, which pointed to phase separation in PLA/PBAT blends. Nearly spherical PBAT particles were finely and homogeneously dispersed within the PLA matrix in 90/10 (a) and 80/20 (b) compositions. The observed sub-micron size of the dispersed particles (200-500 nm) is consistent with previous works[63,64], and was related to the good compatibility (the PLA/PBAT interfacial tension in the solid state, measured by the contact angle technique was 1.85 mN/m) and partial miscibility of PLA with PBAT.

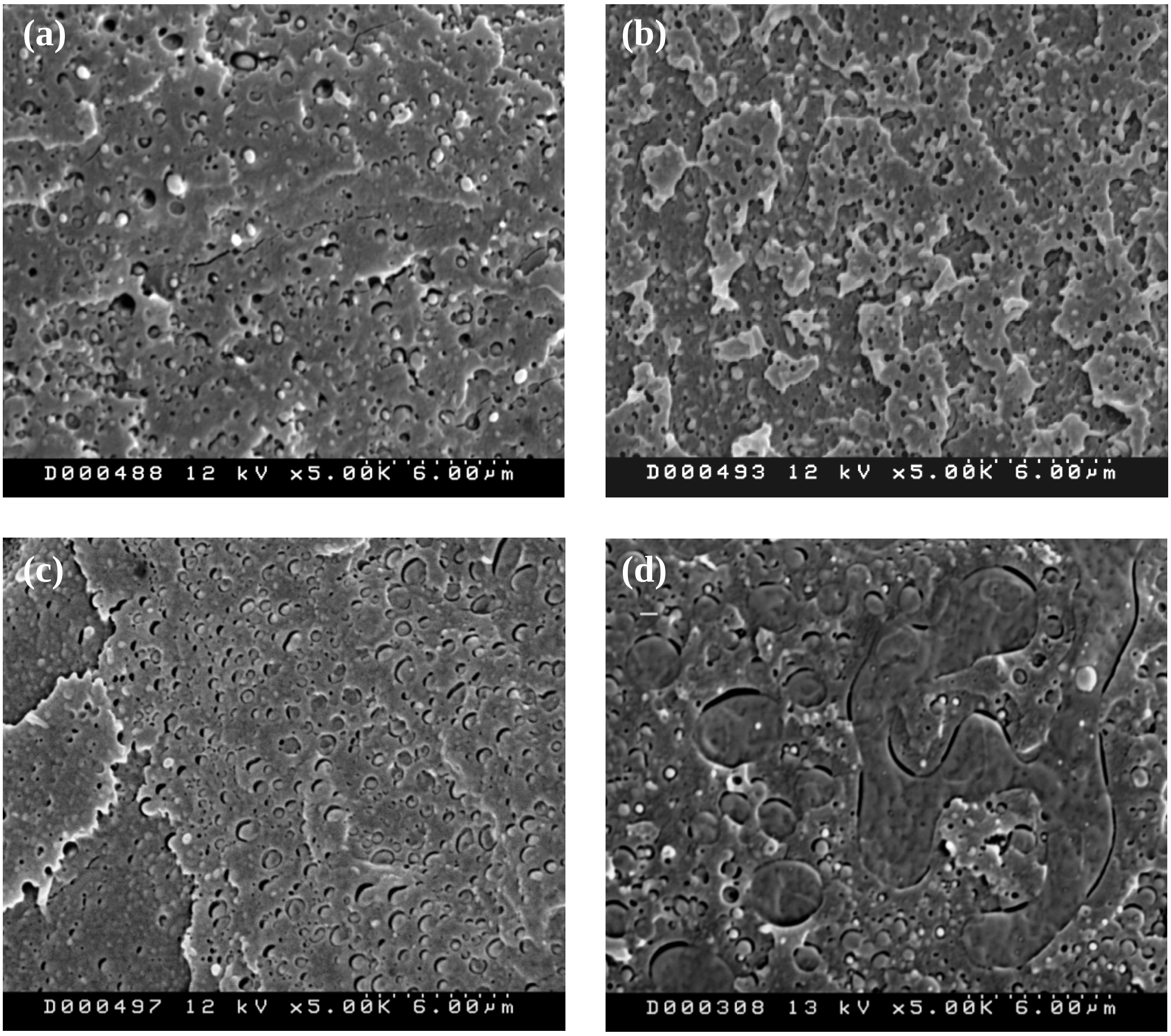

Figure 4.2.4: SEM micrographs of cryogenically fractured surfaces taken from tensile specimens of 90/10 (a), 80/20 (b), 70/30 (c) and 60/40 (d) blends.

In the 70/30 composition (4.2.4c), the PBAT particles were significantly bigger, probably due to the coalescence effects at this higher content. Indeed, the 60/40 composition (4.2.4d) showed the typical almost co-continuous morphology of a blend close to the phase inversion composition. The theoretical phase inversion concentration for these PLA/PBAT blends was estimated using the PLA/PBAT viscosity ratio and following the equation proposed by Utracki[244].

$$\frac{w_1}{w_2} = \frac{\eta_1}{\eta_2}$$

Where w_1 and w_2 are the weight fractions of polymer 1 and 2 at the phase inversion, respectively, and η_1 and η_2 are the corresponding melt viscosities.

The viscosity ratio between PLA and PBAT was estimated by capillary viscosimetry and stood at 1.30. Therefore, the phase-inversion concentration was estimated to be close to the 60/40 PLA/PBAT composition. The morphology of Figure 4.2.4d is completely consistent with this theoretical estimation. Although most of the dispersed particles shown in any of the compositions in Figure 4.2.4 appear debonded from the matrix, some of them look fractured, indicating that cohesive fracture is also present and that some level of interfacial adhesion between phases exists. The interactions between both polymers and their partial miscibility may account for this behavior.

4.2.3 Viscoelasticity

Figure 4.2.5 shows the storage modulus (G´) vs. angular frequency (ω) plots of pure PLA and PLA/PBAT blends. As Figure 4.2.5 shows, G´ of the blends increased at low frequencies as the PBAT content increased. These increases indicate that the presence of PBAT contributes to improving the elastic behavior of PLA, which is consistent with findings in previous works on PLA/PBAT blends[66,245,246], and has been related to the formation of entanglement structures in PLA/PBAT melts[66]. As a result, greater melt strength compared to that of pure PLA during melt processing is expected in PLA/PBAT blends. This improvement, as in the case of PLA/PCL blends of Chapter 4.1 and also mentioned by Jiang et al.[63], is a clear advantage for extrusion related processing techniques or blow-molding.

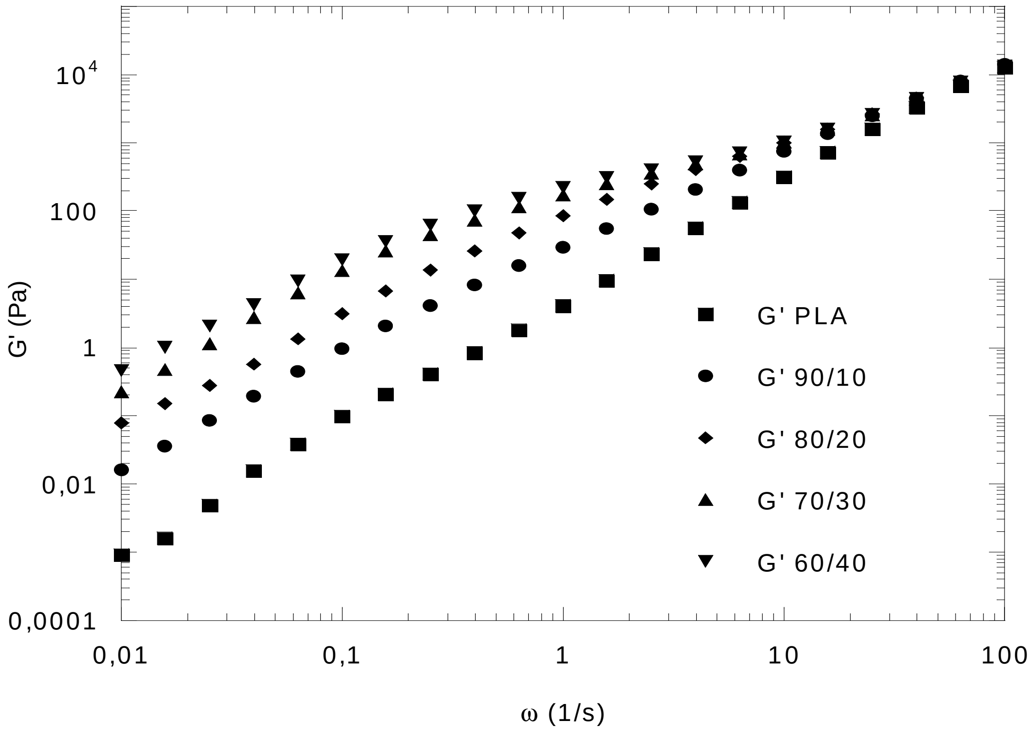

Figure 4.2.5: G´ vs. ω plots of pure PLA and of PLA/PBAT blends.

4.2.4 Mechanical properties

Figure 4.2.6 shows the stress-strain curves of pure PLA, and 80/20 and 60/40 compositions as an example of PLA/PBAT blends. The small insert in the right part of Figure 4.2.6 corresponds to the same curves between 0 and 4% strain. As can be seen and will be discussed below, increasing PBAT contents decreased both Young's modulus and yield strength and increased the ductility of PLA. This is consistent with the elastomeric nature of PBAT and coincides with the usual behavior described in previously studied PLA/PBAT blends[62,63,69] and similar to that of the PLA/PCL blends of Chapter 4.1.

Figure 4.2.7 shows Young's modulus and the yield strength values of PLA/PBAT blends as a function of the PBAT content. As shown in Figure 4.2.6, both low-deformation tensile properties decreased as the PBAT contents increased. This was caused by the much lower modulus and yield strength values of PBAT as compared to PLA (130±5 MPa and 1.7±0.6 MPa, respectively). Both decreases were linear and followed the rule of mixtures between pure polymers. However, the low-deformation mechanical properties of the composition with the highest PBAT content (40%) were still remarkable (Young's modulus: 2180 MPa and yield strength: 44 MPa).

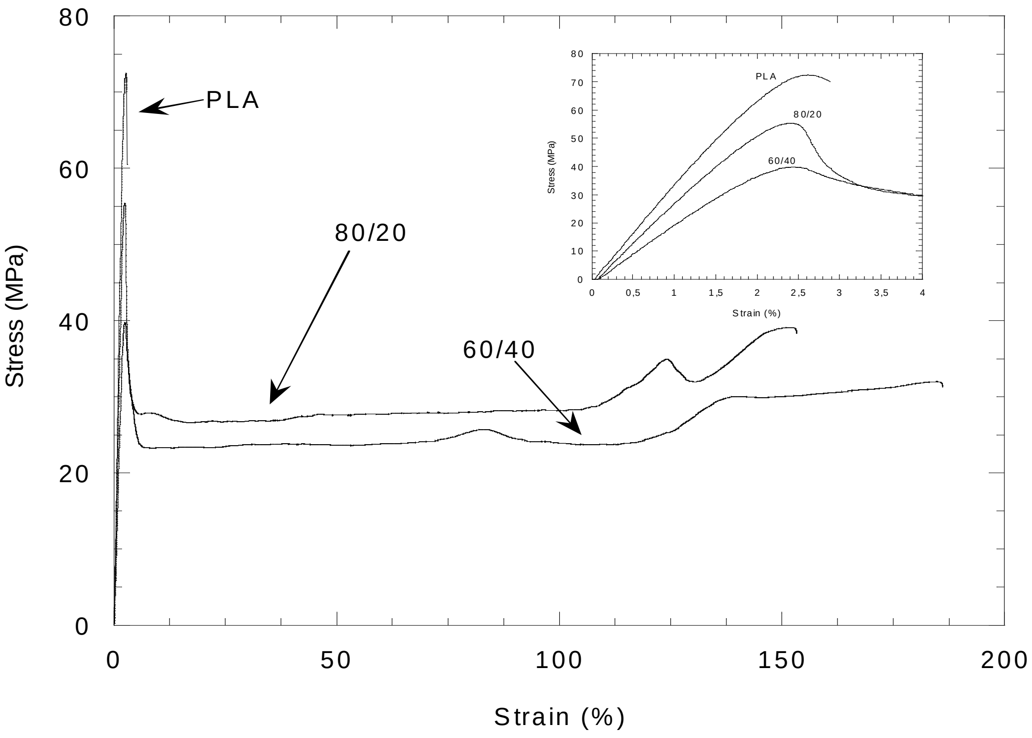

Figure 4.2.6: Stress-strain curves of pure PLA and of 80/20 and 60/40 blends. The small insert shows the same plots between 0 and 4% strain.

When the yield strength and the Young's modulus of the blends of this work were compared with those previously described in the literature on uncompatibilized PLA/PBAT blends[62,63], it is worth noting that the values in this study are significantly higher. As an example, the modulus decrease with respect to that of PLA in the 80/20 composition was 17% in this work compared to between 23-31% in the literature; and the yield strength decreased by 17% instead of 25-29%. Taking into account that in all cases the components are the same, the processing conditions and consequent morphology, increased crystallinity and good compatibility would be responsible for this behavior. These factors have produced positive behavior in the modulus and strength values of other polymer blends[247-249].

The yield strength and Young's modulus values of the PLA/PCL blends in Chapter 4.1 were slightly higher than those of the PLA/PBAT blends here. This is due to the superior properties of PCL as compared to PBAT (Young's modulus and yield strength 3 and 8 times higher, respectively).

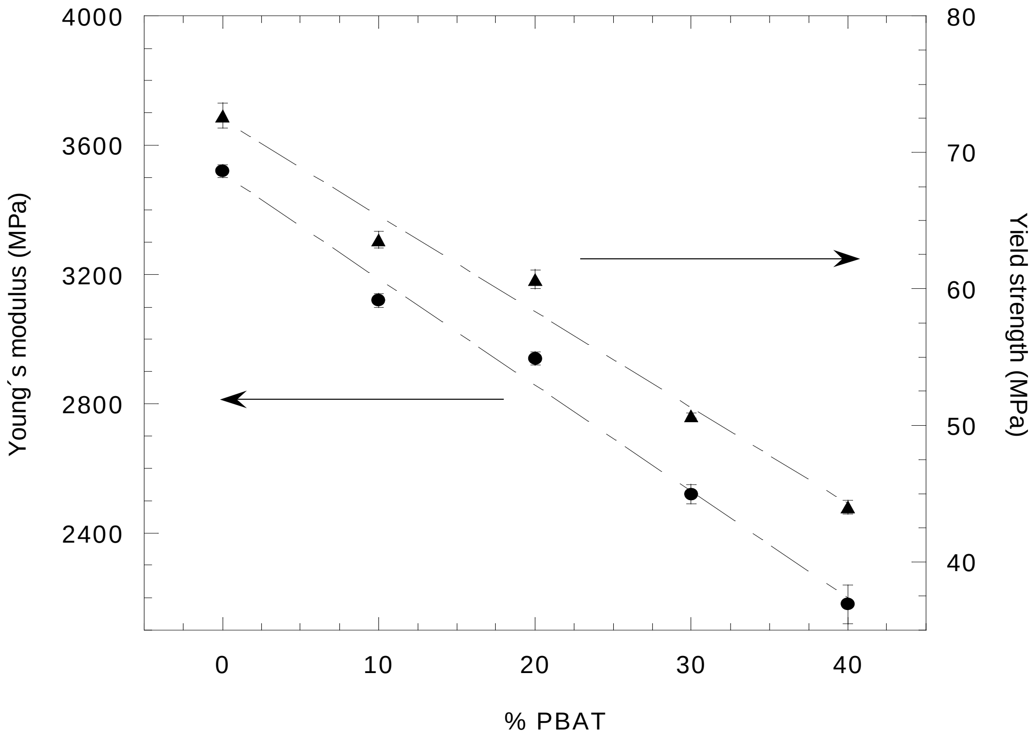

Figure 4.2.7: Young's modulus (●) and yield strength (▲) values of PLA/PBAT blends with respect to the PBAT content.

Figure 4.2.8 shows elongation at break and impact strength values of the PLA/PBAT blends. As can be observed, the low elongation at break of PLA improved considerably when PBAT was added, even at the lowest content (10%), as all PLA/PBAT blends elongated at least 140% before breaking. This behavior is decidedly synergistic. Pure PBAT breaks after being deformed 250±6%, so the elongation at break values for the 80/20 and 60/40 blends were 2.9 and 1.6 times higher than those calculated by means of the rule of mixtures. This indicates good stress-transmission between PLA and PBAT. Although the dispersion of ductility data for PLA/PBAT blends is high in the literature, the results of this study are consistent with those of previous works. Increases in ductility were obtained in all cases, ranging from 46% with a 20% PBAT content, which was the lowest[62] to 266% with 20% a PBAT content[69] or >100% with 10% PBAT content[63] as most. The size of the dispersed PBAT particles and the degree of interaction between phases are the factors which usually affect ductility, the results of which, in our study, were positive.

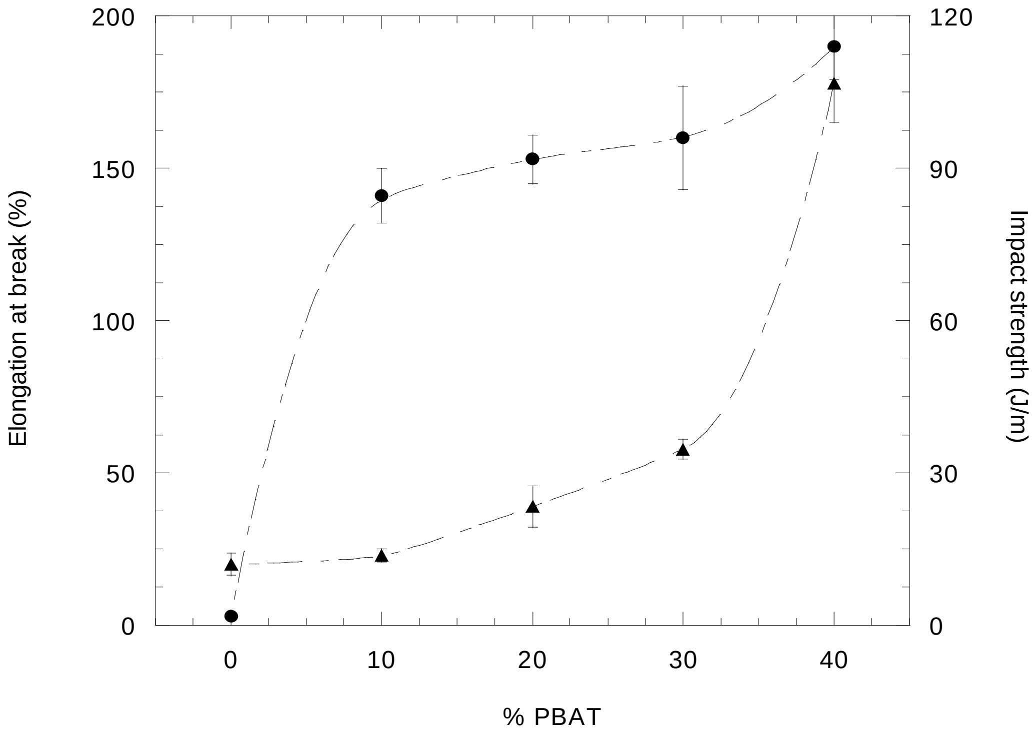

Figure 4.2.8: Elongation at break (●) and impact strength (▲) values of PLA/PBAT blends with respect to the PBAT content.

The ductility increases observed in PLA/PBAT blends are comparable to those of the PLA/PCL blends of Chapter 4.1 because, in both cases, the elongation at break increased significantly even at the lowest second polymer content levels. Although in the case of the PLA/PCL system partial miscibility was not observed, the reduced size of the dispersed phase and the good compatibility between phases were also the factors deemed responsible for this positive behavior.

As can be also seen in Figure 4.2.8, the behavior of the impact strength is significantly poorer than that of ductility. This is common behavior in phase-separated blends and was also observed in the PLA/PCL blends of Chapter 4.1. It is attributed to the fact that the less favorable conditions for plastic deformation of the impact test often lead to antisinergystic behaviors[60]. As can be observed in the figure, although the increases are significant with respect to pure PLA, low impact strength values were observed in 90/10, 80/20 and 70/30 compositions. This is consistent with reported behavior in previously studied uncompatibilized PLA/PBAT blends[63], however, more significant increases in the impact strength at these low PBAT contents have only been observed in compatibilized blends[65,67,70,71].

With respect to the 60/40 composition, a transition to toughness was observed. The value of impact strength for this composition was 8 times higher than that of pure PLA and indicated a change in the deformation mechanism of the blend. As previously described, the morphology of this composition clearly changed from a matrix/dispersed phase one to an almost co-continuous one, close to the phase inversion. This change in morphology must be related to the transition observed in the impact strength behavior, and is common behavior in phase-separated brittle/tough polymer blends[60].

Chapter 5: Nanocomposites based on PLA

CHAPTER 5: NANOCOMPOSITES BASED ON PLA

The usual advantage of adding nanoparticles to PLA, as in the case of most other polymers, is that it improves macroscopic thermal and mechanical properties and, depending on the nanoparticle selected, certain specific characteristics, such as fire resistance, low-permeability against gases, electric semiconductivity, and so on[72].

The literature states that the most useful and efficient nanoparticles for these purposes are oMMT nanolayers and CNTs[72]. The market offers a wide range of different oMMTs and CNTs, which vary mostly depending on the chemical modification of the surface of the particles. In a study carried out prior to that presented in Chapter 5, and consistent with findings described in the literature[87,136], different oMMTs and CNTs were melt-blended with PLA at different processing conditions in a twin screw extruder (COLLIN ZK 25L/D=30) at 180ºC. The nature of the nanoparticles and the processing method used are well known to be two key parameters which control the dispersion of the nanoparticles, and ultimately, the properties of the resulting polymer nanocomposites. This previous study identified the most suitable nanoparticles and processing conditions in order to obtain well-dispersed, well-balanced PLA/oMMT and PLA/CNT nanocomposites.

Three different commercially available oMMTs were studied, Cloisite15A, Cloisite20A (both modified with dimethyl, dehydrogenated tallow, quaternary ammonium) and Cloisite30B. In a first step, PLA with 3 and 5% oMMT contents was melt processed at a fix screw speed of 200 rpm and then injection molded. The nanocomposites containing the Cloisite30B nanoclay presented the best clay dispersion, in keeping with previous findings[87] and consequently the best mechanical properties. In a second step, PLA/Cloisite30B nanocomposites were processed at different screw-rotating velocities. A velocity-clay/dispersion relationship was observed, with the highest screw-rotating velocity (and consequent highest shear forces) producing the best oMMT dispersion. Thus, a screw speed of 320 rpm was selected for the preparation of PLA/Cloisite30B nanocomposites. oMMT contents of 1.5%, 3%, 5% and 7% were selected to be added to the PLA.

PLA/CNT nanocomposites have also been studied. As a previous tentative work, 2% and 4% pristine (pCNT) and carboxylated (COOH-CNT) carbon nanotubes were used. In a first step, PLA/CNT nanocomposites were melt-processed at 200 rpm and then injection molded and compression molded. The stiffness and electrical conductivity results obtained with pCNTs, were similar to those obtained with COOH-CNTs, therefore the surface modification of CNTs (grafted with 1.23% COOH content) was not seen to have any significant effect on their dispersion within the matrix and consequently on the final properties of the nanocomposites. Taking into account that PLA/pCNT nanocomposites have rarely been characterized[72], and the fact that functionalized nanotubes are much more expensive, pCNTs were selected for the PLA/CNT nanocomposites. In a second step, as for the PLA/oMMT nanocomposites, different screw-rotating velocities were used to process the PLA/CNT nanocomposites, and high-velocities, so shear forces, were again observed to be more efficient at dispersing CNTs within the PLA. Consequently, a screw-speed of 320 rpm was also selected for the PLA/CNT nanocomposites. CNT contents of 1%, 1.5%, 2%, 3%, 4%, 5% and 6% were selected to be added to PLA.

5.1 Poly (lactic acid)/organically modified montmorillonite (PLA/oMMT) nanocomposites

5.1.1 Nanostructure and morphology

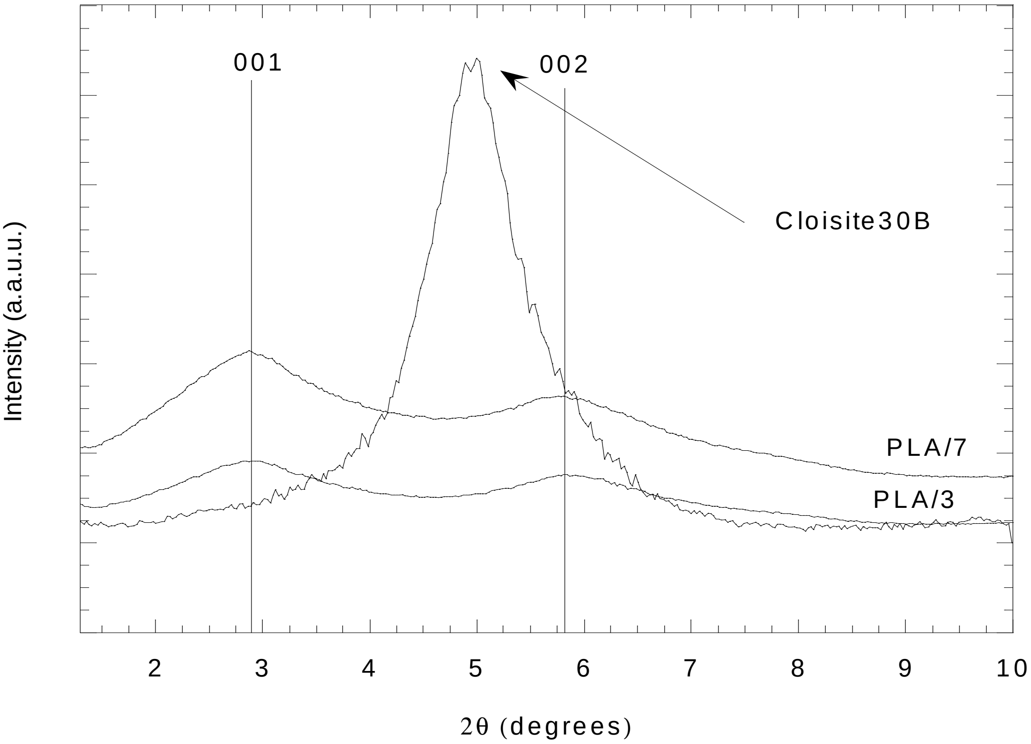

Figure 5.1.1: XRD diffractograms of pure Cloisite30B and of PLA/3 and PLA/7 nanocomposites. To facilitate the comparison between curves, that of pure Cloisite30B has been rescaled.

Figure 5.1.1 shows XRD patterns of pure Cloisite30B and PLA/oMMT nanocomposites with 3% (PLA/3) and 7% (PLA/7) nanoclay contents at increasing 2θ angles. The PLA/oMMT nanocomposites showed two diffraction peaks in the studied angle-range. The main peak, labelled 001, represents the oMMT interlaminar distance. Given its location at 5.8 degrees, the secondary peak, 002, was assumed to be a harmonic of the main peak. The 001 peak was centered at between 2.87 and 2.89 degrees for both nanocomposites, which, using Bragg's equation, gives a resulting d_{001} interlaminar distance of 3.15 nm. The position of the peak of pure oMMT, seen in Figure 5.1.1, is centered at higher angles, close to 4.9 degrees[250], which corresponds to an interlaminar distance of 1.86 nm[250]. The greater interlaminar distance in PLA/oMMT nanocomposites compared to pure oMMT (from 1.86 nm to 3.15 nm) clearly indicates the presence of intercalated nanoclay structures, and that the full exfoliation of the clay did not occur. The intercalation level is similar to that observed in previous PLA/Cloisite30B nanocomposites[95,102,251-253]. The intercalated nanostructure obtained in the present work is consistent with that generally observed in the literature on melt processed PLA/oMMT nanocomposites[72], in which fully exfoliated PLA/oMMT nanocomposites have rarely been reported[87-94].

Figure 5.1.1 also shows that the intensity of the main diffraction peak increased at increasing oMMT contents, but its position and shape did not change when the composition varied. This indicates that the number of intercalated structures increased with the oMMT content but the interlaminar distance between consecutive clay layers and thus, the intercalation level, was independent of the clay content.

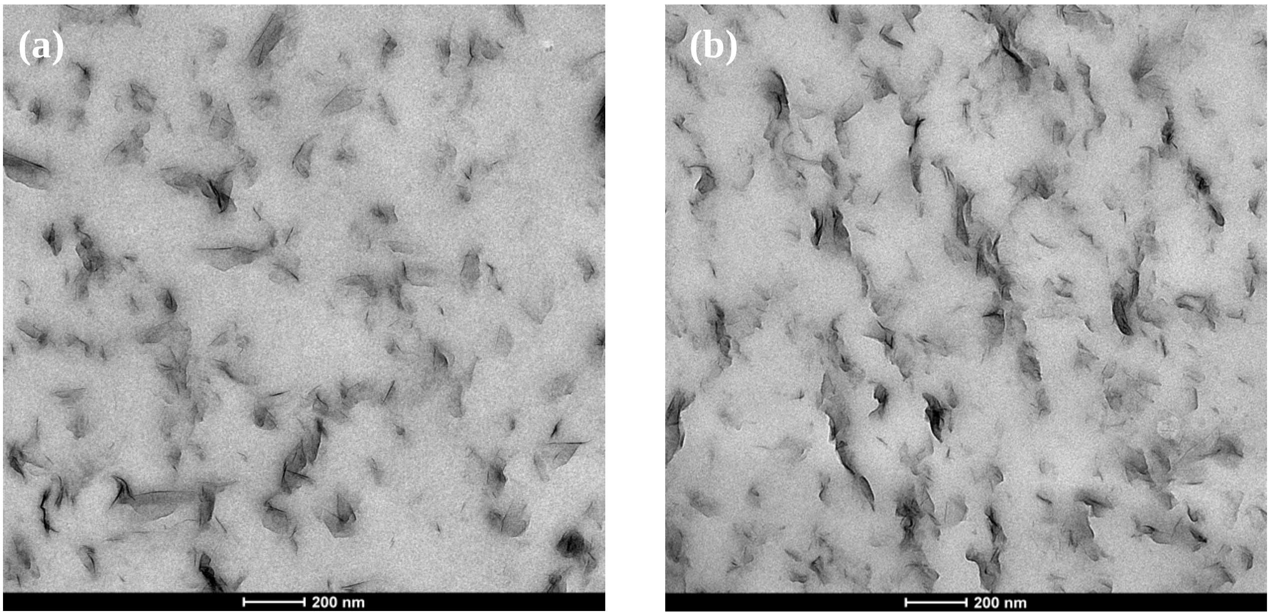

Figure 5.1.2: TEM micrographs of PLA/3 (a) and PLA/7 (b) nanocomposites.

Figure 5.1.2 shows TEM micrographs of the PLA/3 (a) and PLA/7 (b) nanocomposites. As micrographs show, the PLA/Cloisite30B nanocomposites presented well-distributed, mostly intercalated oMMT nanoparticles, few of which were fully exfoliated. Small clay stacks, which seemed to consist of between 2-4 layers, and some individual monolayers, appeared well-dispersed in the compositions with low oMMT contents. The number and size of the stacks increased at higher oMMT contents, but as shown in Figure 5.1.2b, the layers were well dispersed within the matrix even at 7% contents. The nanostructure of the nanocomposites is consistent with that predicted by the XRD results in Figure 5.1.1, and indicates, that, despite the fact that fully exfoliated nanocomposites were not obtained, the dispersion level of oMMT in PLA was quite good. The interfacial tension between PLA and oMMT was measured in the solid state using the contact angle technique. The result obtained (1.11 mN/m) suggests good compatibility. Moreover, nanocomposites were prepared under previously optimized processing conditions.

In addition, oMMT layers appeared mainly edge-positioned with respect to the image-caption direction in Figure 5.1.2, which corresponds to the injection molding-direction. Thus, a significant degree of orientation of the clay layers in the injection-molding direction, in other words, the tensile-test direction, was achieved.

5.1.2 Phase structure

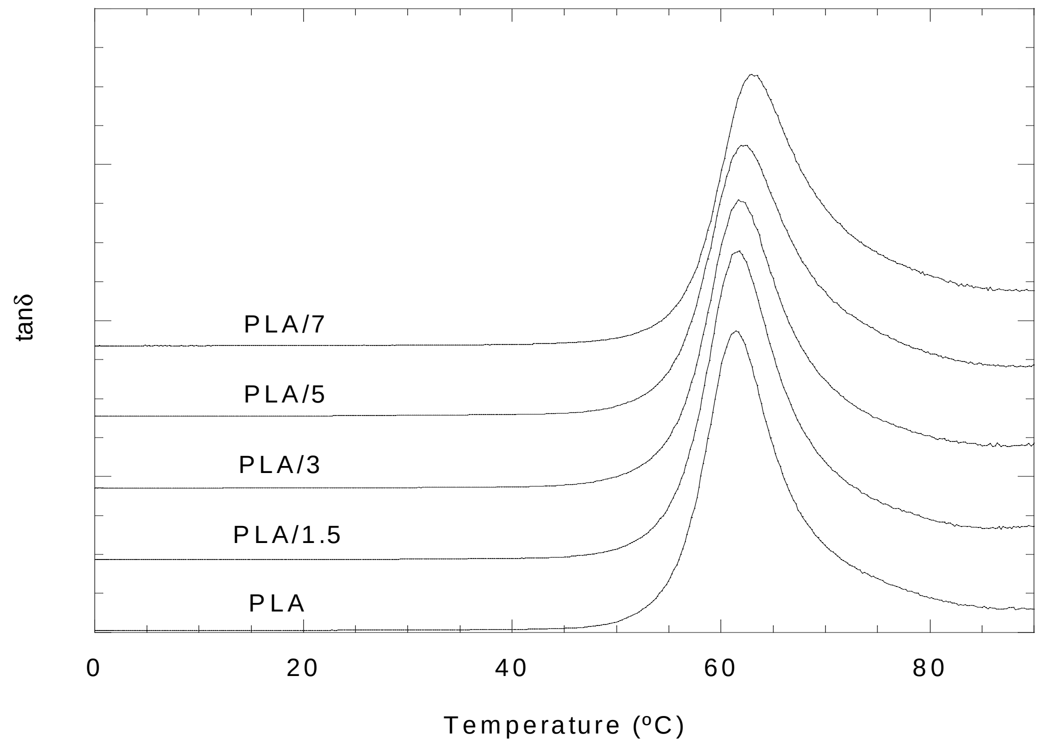

Figure 5.1.3: tanδ vs. temperature plots of pure PLA and of PLA/oMMT nanocomposites.

Figure 5.1.3 shows the tanδ vs. temperature curves obtained by DMTA for pure PLA and PLA/oMMT nanocomposites. As can be seen, a single peak, representing the α-transition of PLA was observed for all the nanocomposites. The position of the signal was independent of the oMMT content, and remained very close to that of pure PLA, 61.2ºC, in all cases. The small variations in temperature remained close to the experimental margin of error for measurements. This is consistent with the results obtained by Jiang et al.[106] and seems to indicate that the chain mobility of PLA was not affected by the presence of dispersed oMMT clay platelets. However, both decreases[95,251] and increases[102] in the glass transition temperature in PLA/oMMT nanocomposites have previously been reported and have been related to the plasticizing effect of the surfactant of the nanoclay which migrated to the polymeric matrix, and to the restricted mobility of the PLA chains caused by the nanoplatelets, respectively. The literature also shows that the effects of plasticization and restricted chain mobility can occur concurrently in polymer/oMMT nanocomposites without being reflected in the glass transition temperature of the matrix[254-256]. Therefore, the results shown in Figure 5.1.3 are not fully conclusive concerning the effects of Cloisite30B in PLA on plasticization or on chain mobility restriction.

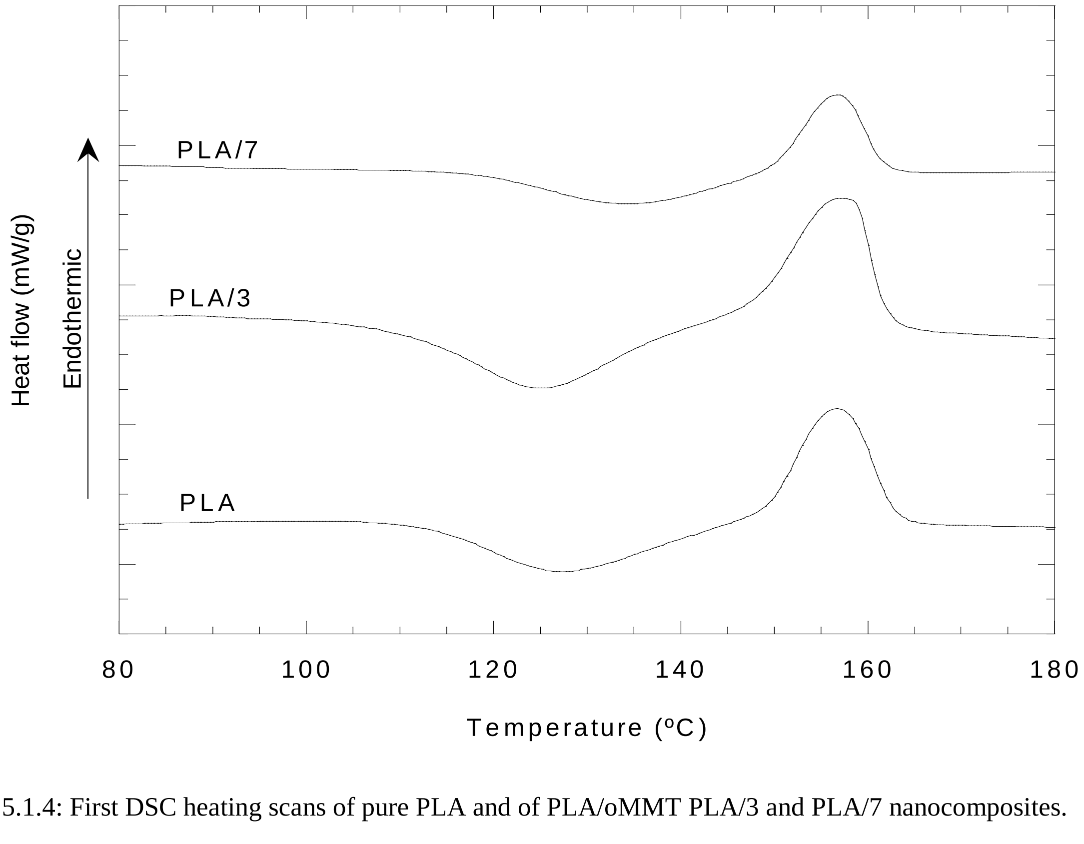

Figure 5.1.4: First DSC heating scans of pure PLA and of PLA/oMMT PLA/3 and PLA/7 nanocomposites.

Figure 5.1.4 shows DSC plots of the first heating scans of pure PLA, PLA/3 and PLA/7 nanocomposites, as an example. All the compositions showed the melting endotherm of PLA preceded by its cold crystallization exotherm, which indicated that PLA at least partially crystallized during the heating scan. Table 5.1.1 summarizes the calorimetric results for all the compositions. As can be seen, some relevant variations in the melting (ΔHm) and cold crystallization (ΔHc) enthalpies were observed depending on the oMMT content and are discussed below. Anyway, ΔHm-ΔHc enthalpies, and the resulting degree of crystallinity of the injection-molded samples was 0 in all cases. This indicates that the presence of oMMT influenced the cold crystallization process, and subsequent melting of the PLA/nanocomposites during the DSC heating scans, but did not during the cooling in the mold. Consequently, PLA remained completely amorphous in all cases.

Table 5.1.1: Melting (Tm) and cold crystallization (Tc) temperatures, melting (ΔHm), cold crystallization (ΔHc) and ΔHm-ΔHc enthalpies and, degrees of crystallinity (Xc) of PLA in PLA/oMMT nanocomposites.

Composition	Tm (ºC)	Tc (ºC)	ΔHm (J/g)	ΔHc (J/g)	ΔHm-ΔHc (J/g)	Xc PLA (%)
Pure PLA	155.1	125.1	20.7	-20.6	0.1	0
PLA/1.5	157.7	122.7	26.9	-26.7	0.2	0
PLA/3	157.4	122.2	25.1	-24.9	0.2	0
PLA/5	157.4	129.7	15.0	-14.9	0.1	0
PLA/7	156.7	134.3	11.2	-11.2	0	0

On examination of the behavior of the nanocomposites during the DSC heating scans (see Table 5.1.1), the cold crystallization enthalpy and consequent melting enthalpy were seen to increase slightly at low oMMT contents of up to 3%, and later decrease at higher oMMT contents (5 and 7%). The behavior of the cold crystallization temperature followed the opposite pattern. These results indicate that, while at low contents (1.5% and 3%) oMMT nanoparticles actuated as a nucleation agent for PLA, at high contents (5% and 7%) they hindered the crystallization process. The literature shows that oMMT platelets are effective nucleating agents for PLA[95,97,106,251,252], but also that at high contents they restrict the mobility of the surrounding polymer chains[257], thus hindering the crystallization process. The melting temperature of PLA remained constant in PLA/oMMT nanocomposites, pointing to similar PLA crystal-perfection in all compositions.

5.1.3 Viscoelasticity

Figure 5.1.5 shows the elastic modulus (G´) vs. the angular frequency (ω) plots of the PLA/oMMT nanocomposites. As can be observed, the behavior of pure PLA and the nanocomposites with 1.5%, 3% and 5% contents was qualitatively similar. G´ decreased at decreasing frequencies in the low angular frequency range, and the slope of the plots of the nanocomposites in this terminal flow zone was the same as that of pure PLA. In addition, all these nanocomposites showed increasing G´ values at increasing oMMT contents and broad relaxations starting close to 10 rad/s, which were related to their reinforcing ability and to the presence of oMMT structures[258], respectively. The amplitude of these relaxations increased at increasing oMMT contents, but their position remained constant. These results indicate that, despite the aforementioned reinforcing effect of the oMMT nanoparticles, the viscoelastic behavior of the PLA/oMMT nanocomposites was still dominated by the liquid-like behavior of PLA up to 5% oMMT contents[259].

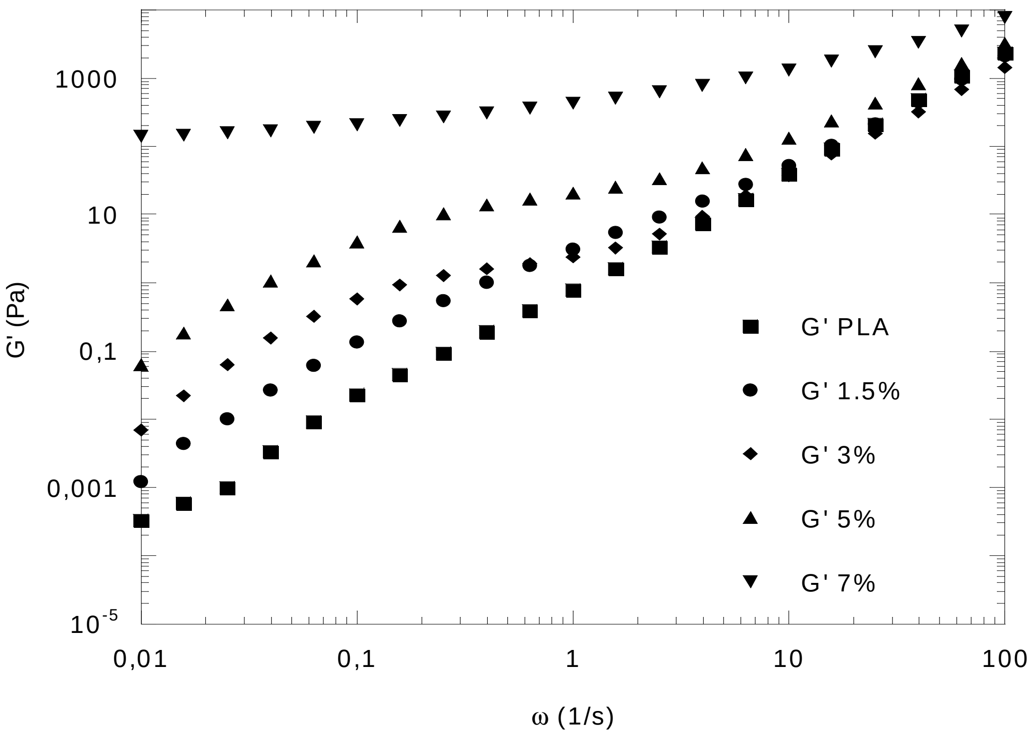

Figure 5.1.5: G´ vs. ω plots of pure PLA and of PLA/oMMT nanocomposites.

The PLA/7 composition, however, showed different qualitative behavior of G´ vs. ω than pure PLA and the rest of the nanocomposites. G´ did not decrease in the terminal flow zone (low frequencies) but remained constant irrespective of the frequency applied. This result points to a solid-like behavior, and indicates that structural percolation of the oMMT layers within the PLA matrix took place in this composition[128,260]. The nanostructure shown in Figure 5.1.2b, where oMMT layers appeared well dispersed and very close to each other in the PLA matrix, is consistent with the rheological percolation in this composition shown in Figure 5.1.5.

The percolation concentration of polymer nanocomposites is directly related to the degree of dispersion of the nanoparticles in the polymer matrix, taking place at lower contents of well-dispersed nanoparticles[261]. Thus, the percolation concentration for fully exfoliated PLA/oMMT nanocomposites has been reported at lower oMMT contents than the 7% content described in this study[91-93] and, on the contrary, poorly dispersed oMMT nanoparticles have not been able to percolate at 7% contents[91,92]. Therefore, the 7% oMMT content necessary for the rheological percolation of the PLA nanocomposites in this study is consistent with the partial exfoliation and good dispersion of intercalated nanoclays shown in Figure 5.1.2.

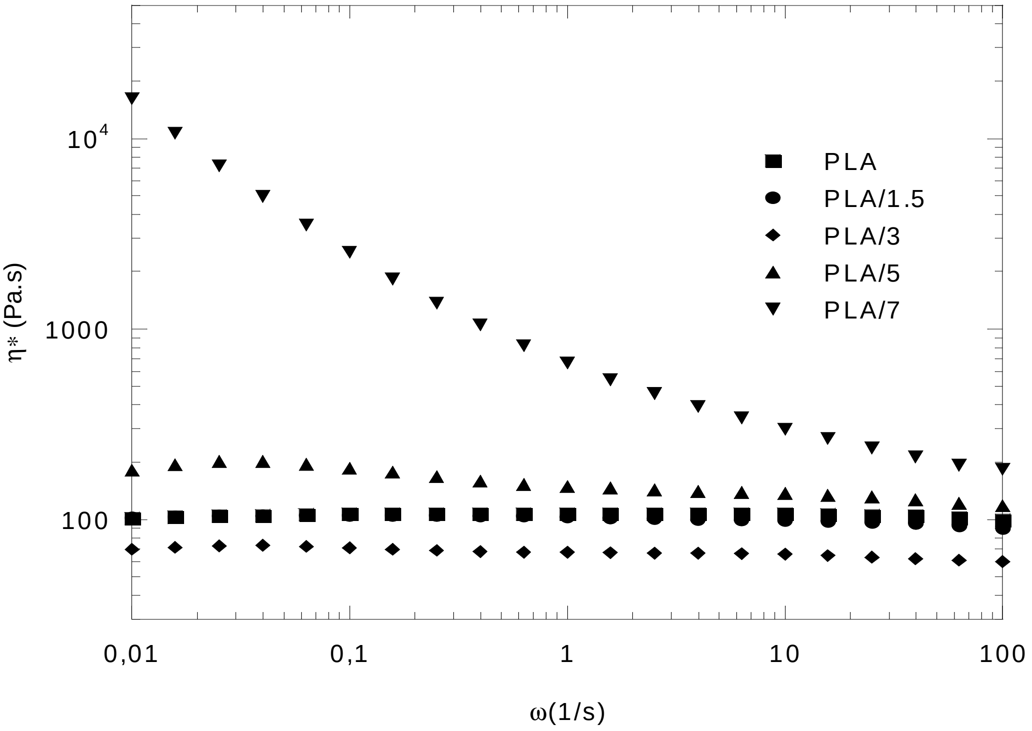

Figure 5.1.6: η* vs. ω plots of pure PLA and of PLA/oMMT nanocomposites.

Figure 5.1.6 shows the complex viscosity (η*) vs. angular frequency (ω) plots of pure PLA and PLA/oMMT nanocomposites. As can be observed, the complex viscosity of the PLA/7 nanocomposite, in contrast to pure PLA and the rest of nanocomposites, showed exponential behavior, consistent with the behavior of the G´ values described above. With respect to the nanocomposites with lower oMMT contents, the complex viscosity of PLA remained constant with 1.5%, decreasing slightly at 3%, and increasing once again at higher contents. The complex viscosity behavior is consistent with the aforementioned concurrent plasticizing/reinforcing oMMT-effect. Regarding Figure 5.1.6, at low oMMT contents, mainly 3%, the plasticization effect is greater than the reinforcing effect, while at higher oMMT contents, the reinforcing effect proves superior to the plasticization effect.

5.1.4 Mechanical properties

The addition of oMMT to PLA has rarely led to a mechanically well-balanced nanocomposite. First of all, the stiffening effect of the nanoclays gives rise to increases in Young's modulus and decreases in the ductility of the nanocomposites. This is why the PLA/oMMT nanocomposites simultaneously show good low-strain mechanical properties and poor high-strain mechanical properties, such as elongation at break or the related tensile strength[89,106]. This effect has been demonstrated to be more pronounced when the nanoclay is well-dispersed and/or fully exfoliated.

Secondly, a possible plasticizing effect on the mechanical behavior of PLA-based nanocomposites caused by the presence of oMMT has also been described[94,106]. This effect has been related to the migration of the chemical surfactant from the surface of the nanoclay to the polymeric matrix[262], to nucleation zones located at oMMT surfaces[106], and to the widespread contact between clay and matrix in fully exfoliated low-content PLA/oMMT nanocomposites[94]. Consequently, decreases (of up to 30%) in Young's modulus along with huge increases in ductility (up to 200%) have been reported for a fully exfoliated PLA nanocomposite with 1% oMMT[94].

Therefore, the development of a mechanically well-balanced PLA nanocomposite is a complex process, in which counteracting effects, i.e. stiffening and plasticization are in competition and are further affected by other factors, such as the amount and degree of dispersion of the nanoclay.

In the PLA/oMMT nanocomposites in this study, the viscoelastic properties suggested that some plasticization took place at low oMMT contents along with the usual reinforcing effect of the nanoclay. The influence of both effects on the mechanical properties will be discussed in this section.

Figure 5.1.7 shows Young's modulus values for PLA/oMMT nanocomposites vs. oMMT content. As the figure shows, the addition of oMMT improved the stiffness of PLA efficiently, with the modulus increasing with the oMMT content. As mentioned before, oMMT platelets are well known to be effective reinforcement nanoparticles for polymers because of their very high specific surface area (in the order of 800 m^2/g)[77] and stiffness. They are particularly effective in well dispersed nanocomposites and, the effect is further enhanced when layers are oriented in the tensile-test direction[263].

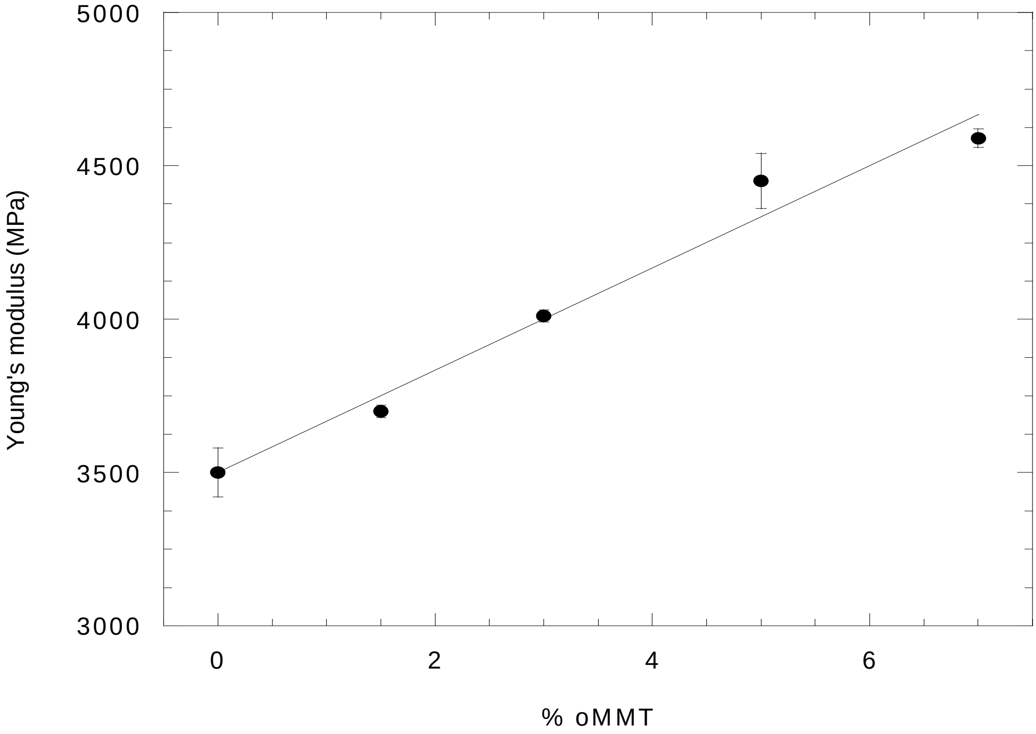

Figure 5.1.7: Young's modulus values of PLA/oMMT nanocomposites with respect to the oMMT content.

Figure 5.1.7 shows a linear increase in all the studied range and, as an example, the stiffness of the PLA/3 and PLA/7 nanocomposites was 14.5% and 31.1% higher than pure PLA, respectively. These increases in Young's modulus are lower than others described in the bibliography[89,106], probably because both reinforcing and plasticizing effects take place concurrently. However, the plasticization effect suggested by the rheological measurements in Figure 5.1.6 for the PLA/1.5 and PLA/3 compositions was not strong enough to cause decreases in modulus, such as those reported for a PLA/oMMT nanocomposite with 1% oMMT content[94], because full exfoliation of the nanoclay probably helped to augment the plasticization effect in the latter. As discussed below, the "non-optimized" low-strain mechanical behavior of the PLA/oMMT nanocomposites in this study will be balanced by the more favorable large-strain behavior.

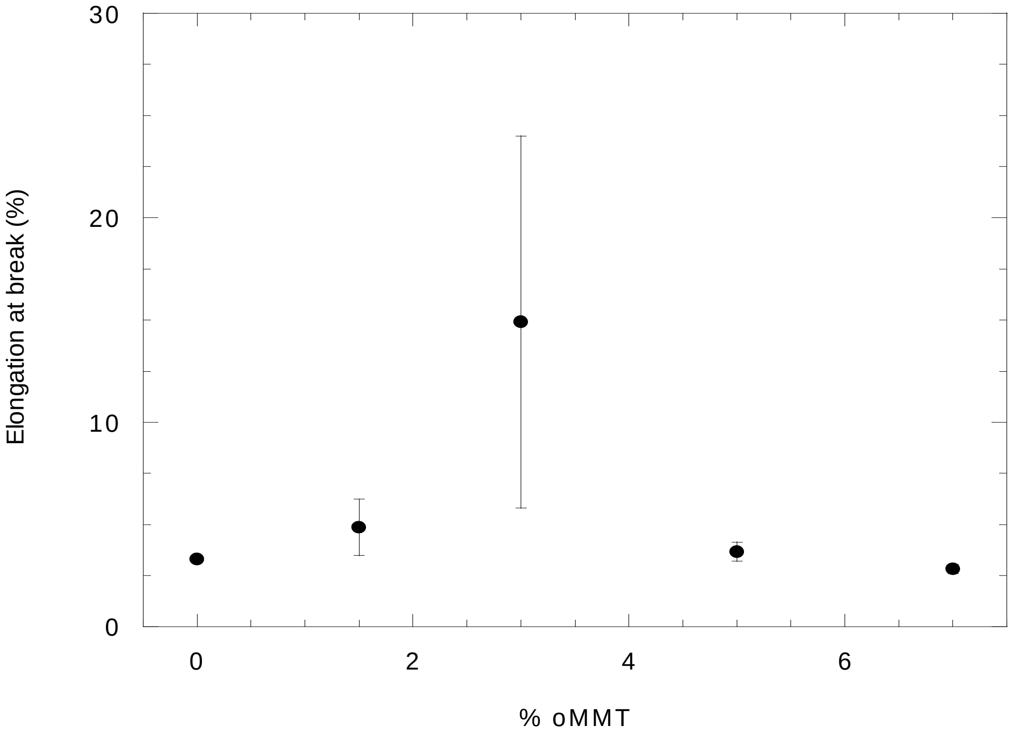

Figure 5.1.8: Elongation at break values of PLA/oMMT nanocomposites with respect to the oMMT content.

Figure 5.1.8 shows the elongation at break values of the PLA/oMMT nanocomposites. In all cases, break took place after yielding and the value of the yield strength of the nanocomposites stayed close to that of pure PLA (72.7 MPa). This is very positive behavior because the maximum tensile strength of these materials remained good and was not negatively affected by a reduced elongation at break. Therefore, the good strength and increased stiffness of the PLA/oMMT nanocomposites in this study allow them to be considered mechanically high-performance materials. The fully exfoliated nanocomposites mentioned above[89,106] originally seemed to be ideal candidates for improving strength, however, because the well-dispersed oMMT lowered the deformability of PLA, the strength of the nanocomposites were only the same[106] or even lower[89,106].

As can be also seen in Figure 5.1.8, ductility increased up to 3% content, decreasing again at higher oMMT contents. The elongation at break of the PLA/3 composition (14.9±9.1%) was significantly higher than for the rest of the nanocomposites. Taking into account the standard deviation of the results and that the specimens showed whitening after yielding, the PLA/3 composition seems to be close to a fragile/ductile transition. The increased ductility at low oMMT contents is consistent with both the literature[94,106], and the results shown in Figure 5.1.6, where the complex viscosity of this composition is lower than that of pure PLA due to plasticization. The ultimate decrease at higher oMMT contents has also been reported in the literature[94,106] and has been related to a premature material failure, which occurred before the shear yielding could start and was caused by the presence of more oMMT and stacks.

The low impact strength of pure PLA remained unchanged in PLA/oMMT nanocomposites, close to 15 J/m. The plasticization effect produced by oMMT in PLA partially modified the fracture mechanism of the PLA/3 composition in tensile tests as judged by the different fracture surfaces, where the latter showed a whitening behavior. However, it was not sufficient to increase the impact strength of the nanocomposite. The less favorable conditions for plastic deformation and the stress-concentrator behavior of oMMT in impact tests[77] impeded better results.

5.1.5 Oxygen permeability

From the point of view of applicability, an analysis of the mechanical behavior of any material is essential. This is because for every possible application, there is always some mechanical requirement. In the case of polymeric materials, and more specifically in polymer nanocomposites, the study of gas-permeability is of particular interest. This is because polymeric materials are often used in packaging and the addition of nanoparticles can improve their barrier properties considerably. In fact, the potential of biodegradable polymers, particularly PLA, for use in packaging applications is huge. This is why this section has been included in the study of PLA/oMMT nanocomposites.

Figure 5.1.9 shows the oxygen permeability of neat PLA and PLA/oMMT nanocomposites with 1.5% and 5% oMMT contents. The oxygen permeability of PLA decreased with increasing oMMT contents, in keeping with previous results[109,264]. The permeability of PLA decreased by 31% at 5% oMMT and by 7% at 1.5% oMMT, the latter being close to the experimental error of the measurement. oMMT layers are very good at reducing the permeability of polymers to different gases, as a result of the more tortuous path that they impose for the gaseous molecules[265]. The permeability of the PLA/5 nanocomposite is consistent with this. The poorer performance of the PLA/1.5 nanocomposite may be because there is not enough nanoclay present to hinder the permeation of the gas and/or may also be due to the aforementioned plasticizing effect of the oMMT at low contents. Plasticization may increase the free volume of the matrix, and consequently, facilitate the permeation of oxygen molecules throughout the PLA, thus counteracting the tortuosity produced by the oMMT layers.

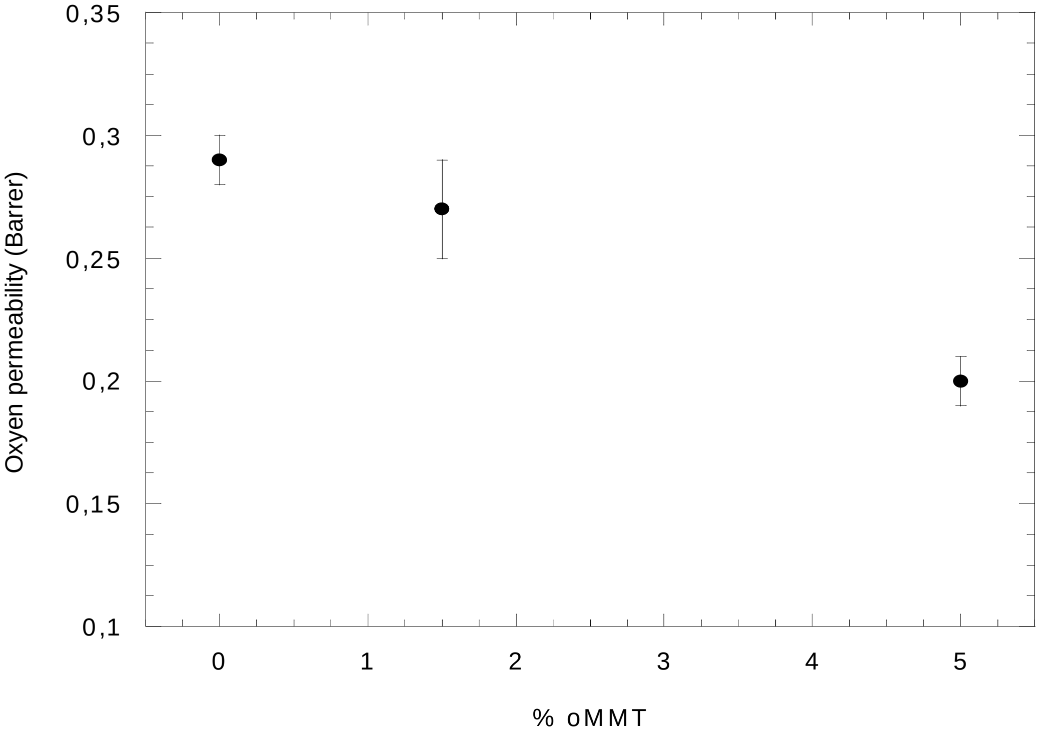

Figure 5.1.9: Oxygen permeability values of pure PLA, and of PLA/1.5 and PLA/5 nanocomposites.

5.2 Poly(lactic acid)/carbon nanotube (PLA/CNT) nanocomposites

5.2.1 Nanostructure and morphology

Figure 5.2.1 shows, as an example, TEM micrographs of PLA/CNT nanocomposites with 2% (PLA/2) and 4% (PLA/4) CNT taken at low (a, b) and high (c, d) magnifications. The light-colored matrix shows the PLA, and the black dispersed particles are the CNTs, easily observed at high magnification.

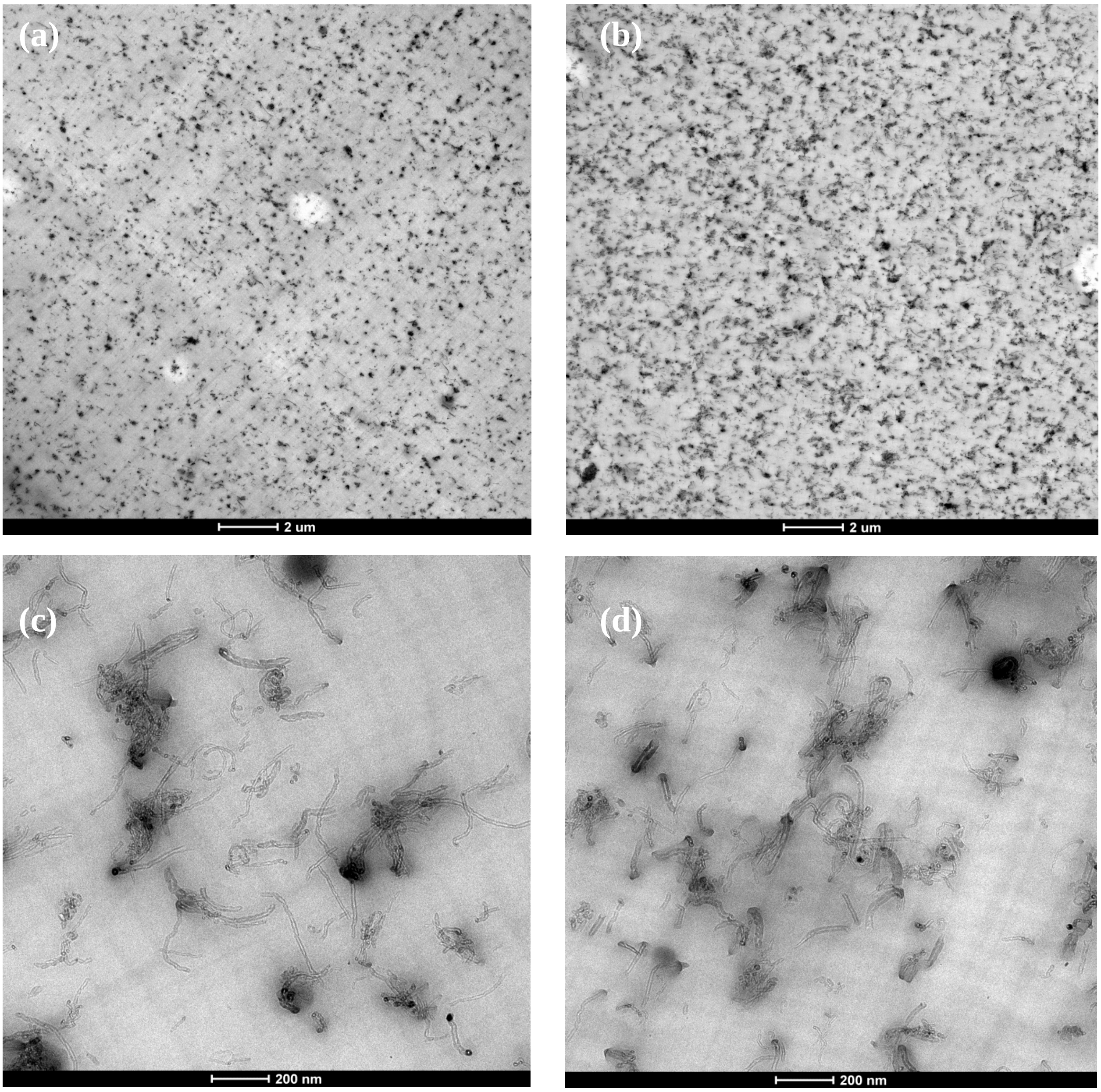

Figure 5.2.1: TEM micrographs of PLA/2 and PLA/4 nanocomposites taken at low (a, b) and high (c, d) magnifications.

In both cases, small CNT aggregates (100-300 nm size) were visible but, as shown in figures 5.2.1 c and d, a considerable number of CNTs were dispersed individually. As can be observed in figures 5.2.1a and b, the number of agglomerates increased with the CNT content, but even at the highest content levels the dispersion of CNTs within the PLA matrix was good. The nanostructure of the PLA/2 and PLA/4 compositions already suggested a percolated structure.

The PLA/CNT interfacial tension was measured in the solid state by the contact angle technique. The result was 6.35 mN/m, indicating a high degree of incompatibility between the PLA and CNTs. Given this incompatibility, the good dispersion level of the CNTs in the PLA matrix must be attributed to the processing method employed, which was based on high-screw speed, and therefore, high shear.

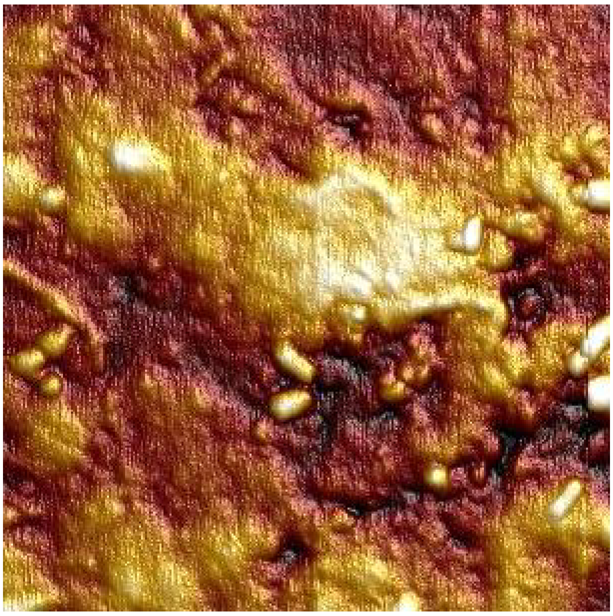

Figure 5.2.2: AFM micrograph of the PLA/4 nanocomposite.

AFM analysis provides information about the degree of orientation of CNTs in PLA/CNT nanocomposites. Figure 5.2.2 shows, as an example for the PLA/CNT nanocomposites, a representative 500x500 nm AFM micrograph of the PLA/4 composition measured as height signal. The white tubes and areas are the monodispersed or agglomerated CNTs, respectively, and the continuous dark phase is the PLA-matrix. The micrograph was taken perpendicular to the injection mold filling direction, i.e. to the tensile test direction. Therefore, non-oriented or slightly- oriented CNTs appear as long (horizontal) tubes while significantly or highly oriented CNTs appear as short tubes, small ellipses or circumferences, depending on the angle of orientation. Only a few long tubes (2-3) were observed, while mostly short tubes, ellipses or circumferences appeared, suggesting some level of orientation of CNTs in PLA/CNT nanocomposites. When the orientation level of these CNTs is compared to that of the oMMT shown in Figure 5.1.2 of Chapter 5.1, the nanoclay layers clearly appeared to be much more oriented in the injection molding direction than the CNTs.

5.2.2 Phase structure

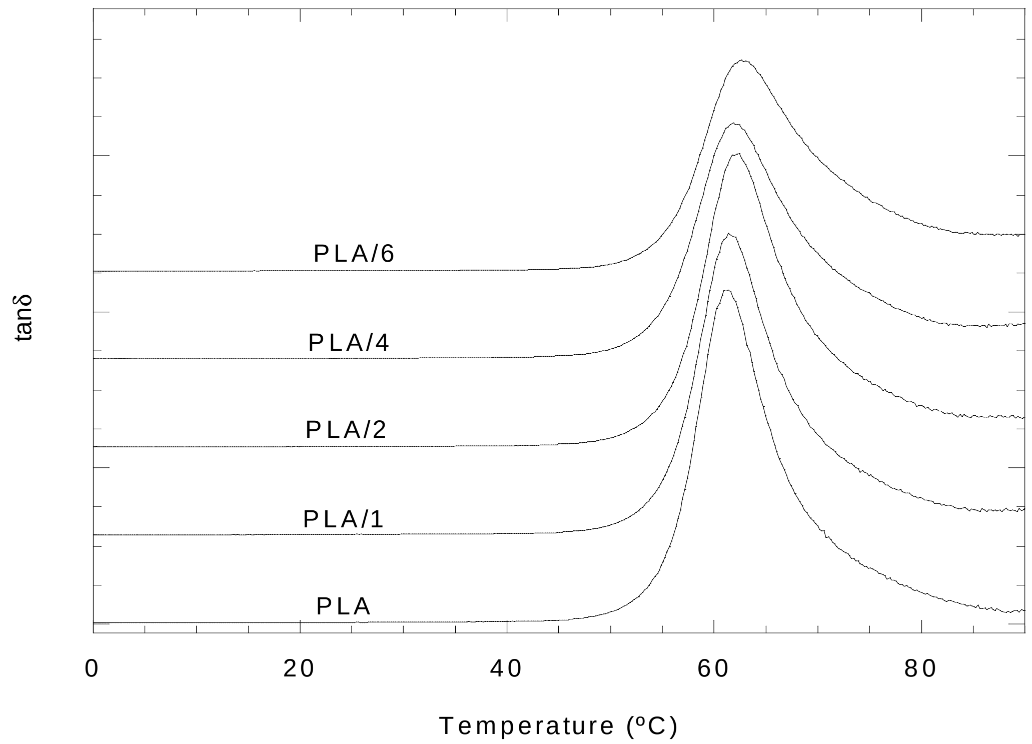

Figure 5.2.3: tanδ vs. temperature plots of pure PLA and of PLA/CNT nanocomposites.

Figure 5.2.3 shows tanδ vs. temperature plots of pure PLA and PLA/CNT nanocomposites at different CNT contents. As in the case of the PLA/oMMT nanocomposites of Chapter 5.1, all compositions showed a single peak, corresponding to the α-transition of PLA. In all cases the position of the peak remained close to that of pure PLA and was independent of the CNT content. The literature shows that the effect of CNTs on polymer chain mobility, and therefore, on its Tg, is difficult to predict. It has been demonstrated that when the interaction level between the matrix and the nanotubes is high, the Tg usually increases as a result of the immobilization of the polymer chains located close to CNT surfaces[126,266]. However, when the matrix-nanotube interactions is weak or non-existent, the Tg usually remains unchanged,[267,268] or it may even decrease[269]. In the present work, the aforementioned high interfacial tension between PLA and CNTs, probably a result of the unmodified chemical surface of the CNTs used, points to low compatibility and low interaction between the components. Thus, the mobility of the PLA chains did not appear to be affected by the presence of CNTs and the Tg of the nanocomposites remained constant.

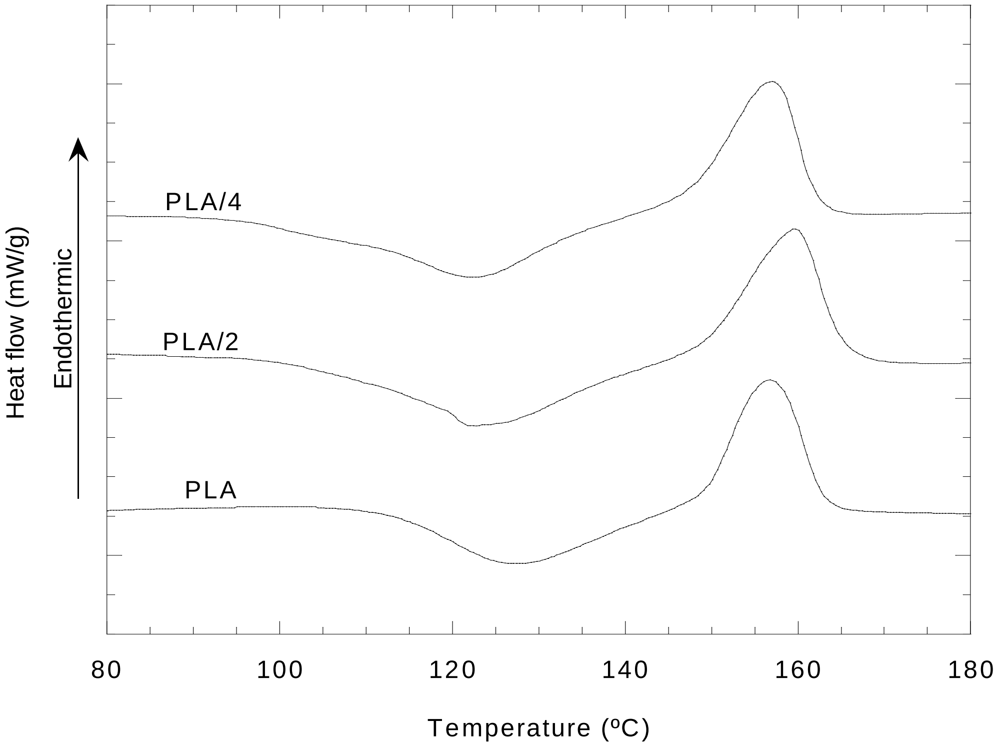

Figure 5.2.4: First DSC heating scans of pure PLA and of PLA/2 and PLA/4 nanocomposites.

Figure 5.2.4 shows the DSC plots of the first heating scan of as-molded PLA, PLA/2 and PLA/4 nanocomposites. Table 5.2.1 summarizes the calorimetric results. As in the case of pure PLA, the melting endotherm of PLA/CNT nanocomposites is preceded by its cold crystallization exotherm. As with the PLA/oMMT nanocomposites of Chapter 5.1, it is noteworthy that low or intermediate CNT contents effectively nucleated the crystallization of PLA in the nanocomposites, but only during the DSC heating scan. This will be explained below. As Figure 5.2.4 and Table 5.2.1 show, the cold crystallization temperature (Tc) dropped from 125ºC to

~119-120ºC and the corresponding crystallization enthalpy (ΔHc) increased from 20 J/g to ~26 J/g at low CNT contents. The ability of the CNTs to nucleate at low contents also influenced the melting enthalpy (ΔHm, again from 20 J/g to ~26 J/g). However, and similar to that observed in the PLA/oMMT nanocomposites of Chapter 5.1, this nucleation effect gradually disappeared at higher CNT contents, the Tm, Tc, ΔHm and ΔHc of the PLA/6 nanocomposite being similar to that of pure PLA.

Table 5.2.1: Melting (Tm) and cold crystallization (Tc) temperatures, melting (ΔHm), cold crystallization (ΔHc) and ΔHm-ΔHc enthalpies, and degrees of crystallinity (Xc) of PLA in PLA/CNT nanocomposites.

Composition	**Tm (ºC)**	**Tc (ºC)**	**ΔHm (J/g)**	**ΔHc (J/g)**	**ΔHm-ΔHc (J/g)**	**Xc PLA (%)**
Pure PLA	155.1	125.1	20.7	-20.6	0	0
PLA/1	155.7	119.3	26.5	-26.4	0.1	0
PLA/2	159.7	120.7	26.0	-26.0	0	0
PLA/4	157.0	122.3	24.8	-24.7	0.1	0
PLA/5	156.2	123.6	22.8	-22.7	0.1	0
PLA/6	156.7	125.1	21.8	-21.8	0	0

The literature shows that CNTs are well known nucleation agents for PLA[10,132,144,145,148]. However, the consequences of this characteristic are not clear. Most authors point to heterogeneous nucleation induced by nanotubes, which changes the amount and size of the spherulites[10,132,144,145,148], but this effect seems to be directly related to the degree of dispersion of the nanotubes[74]. In addition, due to the inferior dispersion of the CNTs obtained in melt-prepared nanocomposites, the nucleation ability under these conditions has been questioned[9]. In fact, counteracting effects of the presence of CNTs on the cold crystallization process have been reported[148], because CNTs favor nucleation thermodynamically but hinder the growth of the crystals dynamically [148]. The results of the PLA/CNT nanocomposites in this study support the latter. Here effective nucleation was observed at low CNT contents when the mobility of the PLA chains was still not restricted by the presence of the nanotubes, but it gradually disappeared at higher CNT contents, when dynamic restrictions overcome thermodynamic nucleation. Rheological percolation will be discussed in the next section but it is noteworthy that the nucleation effect increased up to the percolation CNT concentration, and decreased at higher contents, when solid-like behavior and thus, restricted chain mobility, predominated.

Finally, the close to 0 values of the ΔHm-ΔHc enthalpy of all the PLA/CNT nanocomposites, and consequently the degree of crystallinity, indicate that the nucleation ability of the CNTs at low contents was restricted to the heating scan in the DSC, and was not strong enough to cause the crystallization of PLA during cooling in the mold of the injection molding machine. So, from an application point of view of these nanocomposites, the nucleation induced by the CNTs was insignificant. Similar results were observed for the PLA/oMMT nanocomposites of Chapter 5.1. In fact, crystallization of PLA during injection molding processing has only been reported in one study[10], where both the nucleation effect of the nanotubes and the obtained orientation of the PLA chains contributed to increase the crystallization rate of PLA.

5.2.3 Viscoelasticity

Figure 5.2.5 shows storage modulus (G´) vs. angular frequency (ω) plots of pure PLA and PLA/CNT nanocomposites with 1%, 1.5%, 2% and 3% CNT contents. The behavior of the nanocomposites with higher CNT contents was similar to that of PLA/3 composition. As shown, the G´ value in the terminal flow zone increased considerably in the presence of CNTs, even at the lowest content. As can be also seen, the PLA/1 composition was the only composition that showed liquid-like behavior similar to that of pure PLA. Although it exhibited broad viscoelastic relaxation, attributed to the presence of well dispersed CNTs[270], the slope of the curve in the terminal flow zone was similar to that of pure PLA. At higher CNT contents, all PLA/CNT nanocomposites showed an almost frequency independent G´ value, which points to a solid-like behavior also in the terminal flow zone, with the PLA/1.5 composition showing an intermediate behavior. This result clearly indicates that CNTs were percolated within the PLA-matrix[128,260] at contents of over 1.5% CNT, as already pointed in Figure 5.2.1.

The rheological percolation concentration of CNTs in the present work is consistent with that reported by Wu et al. for High Aspect Ratio (HAR) COOH-CNTs[137]. In the case of Low Aspect Ratio (LAR) COOH-CNTs mixed at the same conditions, percolation took place at higher contents, namely 4%. The lower percolation concentration of HAR nanotubes was related to the structure created by the CNTs. At very low contents they were dispersed as self-entangled small flocs, and at intermediate contents these flocs combined together to create a compact and stable nanotube network within the PLA. In the case of LAR nanotubes, much higher CNT contents were necessary to create this network because of their lower aspect ratio. The CNTs used in the present work have an aspect ratio (1000-3000) similar to HAR nanotubes in the work by Wu et al. Therefore, the low percolation concentration obtained in the present work must be related to the CNT morphology and also to the efficient melt-processing method used to disperse them within the PLA.

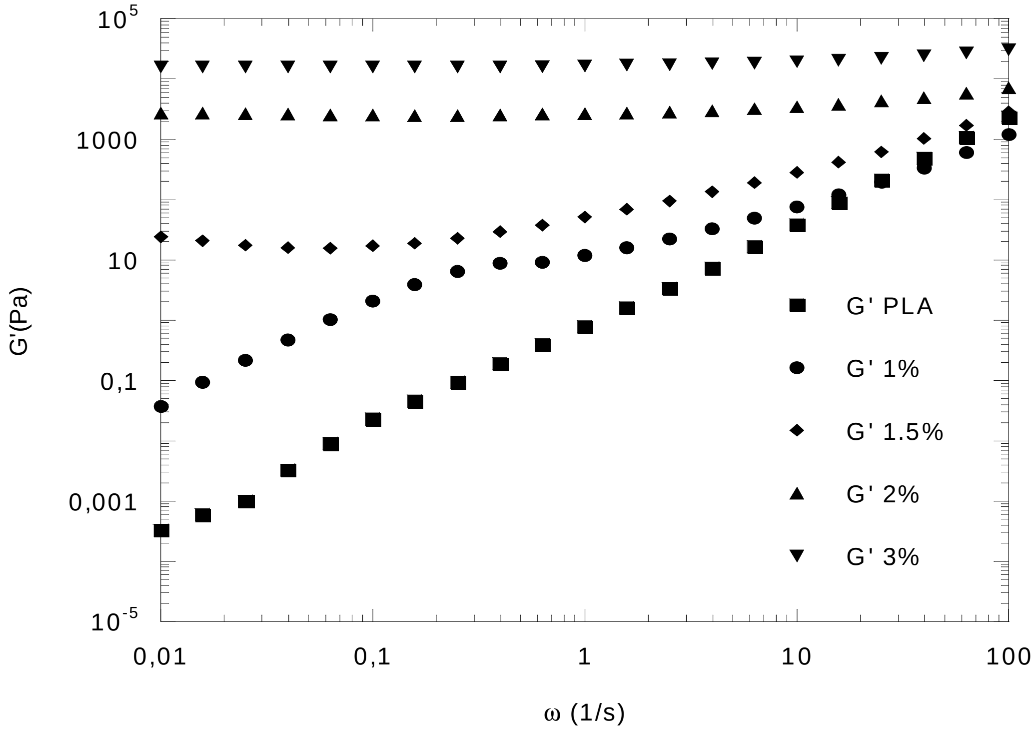

Figure 5.2.5: G´ vs. ω plots of pure PLA and of PLA/CNT nanocomposites.

When the rheological percolation concentration of these PLA/CNT nanocomposites is compared to that of the PLA/oMMT nanocomposites of Chapter 5.1, significantly lower values were obtained in the former. In both cases, nanoparticles were finely dispersed within the matrix of PLA but percolation concentrations were 1.5% and 7% for CNTs and oMMT, respectively. These results are consistent with the literature[271,272], and suggest that tubular nanoparticles are more effective at creating expanded networks within polymers than planar nanoparticles.

5.2.4 Mechanical properties

Figure 5.2.6 shows the Young’s modulus behavior of PLA/CNT nanocomposites with respect to the CNT content. The stiffness of PLA increased linearly in the presence of CNTs and, as an example, the modulus of PLA/2, PLA/4 and PLA/6 nanocomposites were 4%, 6.5% and 11%

higher than that of PLA, respectively. This linear increase points to a stiffening effect of the CNTs independent of the structural percolation discussed in the previous section. It is also consistent with the good dispersion level of the CNTs in all the nanocomposites, even at the highest CNT contents, in keeping with the TEM observation. In fact, previously studied melt-processed PLA/CNT nanocomposites[132] showed significant increases in Young’s modulus only at low CNT contents. At higher CNT contents Young’s modulus remained unchanged. This result was related to the increased number of CNT agglomerates, which affected the level of dispersion and thus their reinforcing capacity.

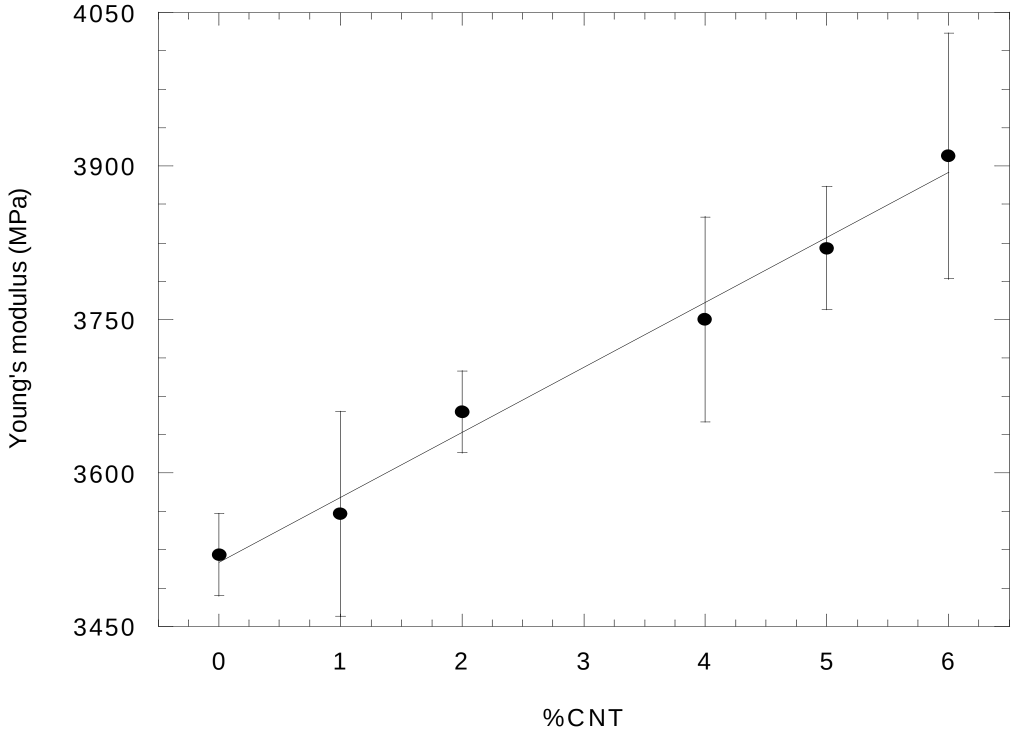

Figure 5.2.6: Young’s modulus values of PLA/CNT nanocomposites with respect to the CNT content.

When the mechanical properties of these PLA/CNT nanocomposites are compared with those of the PLA/oMMT nanocomposites in Chapter 5.1, it can be observed that oMMT layers were more effective than CNTs at improving the stiffness of PLA. In both cases, the stiffness increments were linear, 1.8%/CNT unit and 4.7%/oMMT unit, respectively, and as an example, 3% oMMT and 6% CNT containing nanocomposites presented almost the same Young’s modulus. This is a common finding when polymer/clay and polymer/CNT nanocomposites are compared. In addition, the development of percolated structures of any of the nanoparticles in the PLA matrix, which took place at 1.5-2% and 5-7% in PLA/CNT and PLA/oMMT nanocomposites, respectively, does not seem to play a significant role in the stiffening effect.

The yield strength values of the PLA/CNT nanocomposites were close to that of neat PLA, ~72MPa. The literature shows that increases in the yield strength of the nanocomposites have been observed in the presence of well dispersed CNTs [273-275] but, when the polymer-nanotube interfacial adhesion is insufficient for significant stress-transmission between components, such as that presumed for the nanocomposites in the present work, yield strength values of polymer/CNT nanocomposites remain close to that of the pure polymer or, even decrease[127,134,276]. These results suggest that a good level of dispersion of CNTs within the matrix does not ensure that its strength will be increased; it must be accompanied by a good compatibility between components. Similar conclusions were reported by Yoon et al. in PLA/CNT nanocomposites prepared using the solution-casting method[142].

The poor high-strain mechanical behavior of pure PLA did not change with the addition of CNTs. Ductility maintained low and the PLA/CNT nanocomposites broke just after yielding, with elongation at break values of 5% at most. In any case, elongation at break did not drop to values under than that of the yield strain, allowing the tensile strength of the nanocomposites to be maintained. This is positive behavior from a structural point of view, as it does not limit the potential applications of these new materials. The impact strength of the nanocomposites also remained at the low characteristic values of pure PLA (12-18 J/m) and did not change with the CNT content.

5.2.5 Electrical conductivity

Figure 5.2.7 shows volume conductivity values of the nanocomposites as a function of CNT content. As shown, pure PLA and the PLA/1 nanocomposite were electrically insulating materials, and both showed conductivity values close to 10^{-12} S/cm. The nanocomposites became semiconductive at CNT contents of 2% or higher and the electrical percolation threshold for PLA/CNT nanocomposites was located at between 1% and 2% CNT contents, close to the intermediate PLA/1.5 composition.

This electrical percolation threshold composition is consistent with the rheological percolation composition, as shown in Figure 5.2.5. In fact, the PLA/1.5 composition showed an intermediate behavior between the liquid-like of the PLA/1 composition and the solid-like behavior of the PLA/2 composition. It has been proposed that the CNT contents required to form rheologically percolated structures are generally lower than those required to allow semiconductivity in polymer/CNT nanocomposites[270], even when tunnel effects appeared[277]. This is because, in order to obtain electrical conductivity there must be a physical contact between nanotubes (or if not, they must be very close to each other[277]), but this is not necessary to form a rheologically percolated structure[270]. However, for most polymer/CNT systems[270], the differences, if any, between both percolation-compositions are usually small.

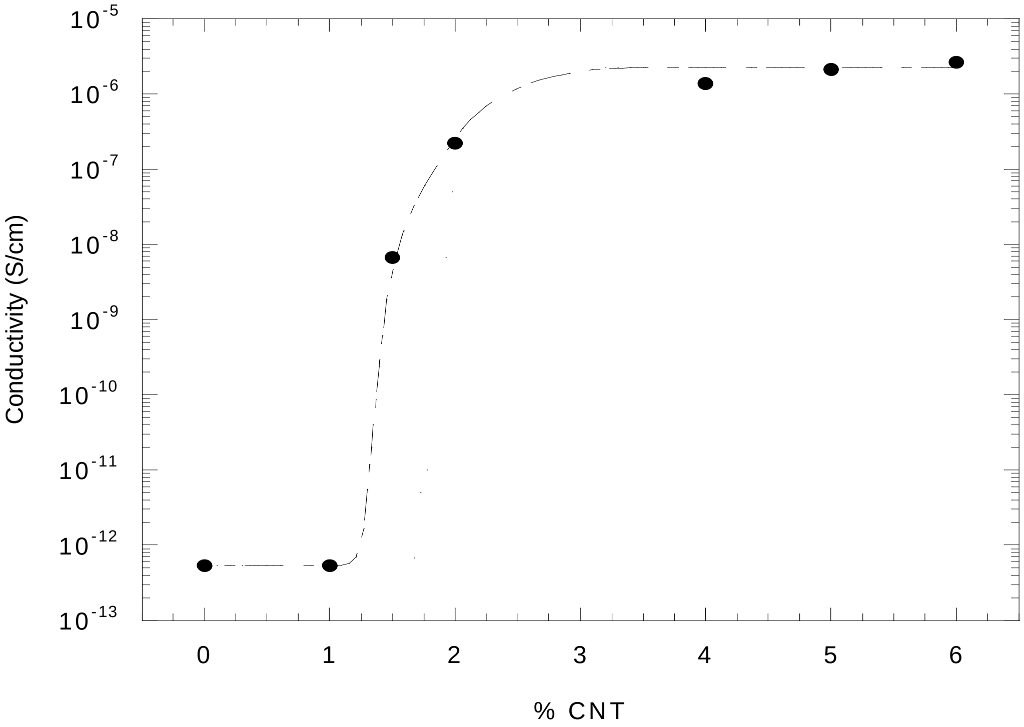

Figure 5.2.7: Volume conductivity values of PLA/CNT nanocomposites with respect to the CNT content.

The semiconductor nature of the PLA/CNT nanocomposites of the present work at CNT contents above 1.5% is consistent with the nanostructure shown in Figure 5.2.1, where an almost continuous CNT network was observed, even at the PLA/2 composition. Previous studies on electrical properties of PLA/CNT nanocomposites have shown that percolation was only obtained at lower CNT contents than the present work when high aspect ratio modified nanotubes (1% CNT content)[137] or special processing routes (0.5% CNT content, two extrusion steps and use of masterbatches)[74] were employed. When the aspect ratio of nanotubes decreased, despite being modified, the percolation threshold occurred at higher CNT contents (3%) [137].

Therefore, the PLA/CNT nanocomposites in this work combine acceptable mechanical performance with semiconductivity (obtained at low CNT contents). This performance is very interesting, especially if it is considered that unmodified nanotubes were used and the materials were obtained by a single extrusion process.

Chapter 6: Nanocomposites based on PLA/PCL and PLA/PBAT blends

CHAPTER 6: NANOCOMPOSITES BASED ON PLA/PCL AND PLA/PBAT BLENDS

PLA/PCL and PLA/PBAT blends in Chapter 4 and PLA/oMMT and PLA/CNT nanocomposites in Chapter 5 are high performance materials, with specific complementary properties which make them very interesting candidates for ternary nanocomposites. The addition of oMMT nanoplatelets and CNTs can further improve the already good mechanical properties of the PLA/PCL and PLA/PBAT blends and, provide them with particularly interesting additional properties such as improved gas-barrier performance and electric semiconductivity.

In a previous prospecting work, PLA/PCL/oMMT, PLA/PCL/CNT and PLA/PBAT/CNT nanocomposites were melt-processed using three different mixing routes. In the first process, they were all melt-mixed together, in the second one, the nanoparticles were added to previously melt-mixed blends and in the third one, PCL and PBAT were added to previously melt-processed PLA/oMMT and PLA/CNT nanocomposites. The melt-mixing conditions were the same as those used to prepare the reference binary blends and nanocomposites, i.e. a temperature of 180ºC and screw-speeds of 80 rpm (for adding the PCL and PBAT) and 320 rpm (for adding the nanoparticles). The aim of this pre-analysis was to establish the most efficient mixing route to obtain the best performing ternary nanocomposites. The stiffness, deformability and, electrical conductivity in nanocomposites containing CNT, were all taken into account. The mechanically most balanced 80/20 composition was selected for both the PLA/PCL and PLA/PBAT blends, and the nanoparticle content was kept at 3% for this prospecting work. In keeping with the aforementioned criteria, the most suitable method for mixing the PLA/PCL/oMMT nanocomposites was deemed to be pre-mixing PLA/PCL at 80 rpm and then adding oMMT in a second step at 320 rpm. However, it was decided that the best processing-route for both PLA/PCL/CNT and PLA/PBAT/CNT nanocomposites, was to pre-mix PLA/CNT at 320 rpm, and then add the PCL or PBAT at 80 rpm.

Once the most effective processing-route was established, the composition of the ternary blends was selected. 80/20 PLA/PCL and 80/20 and 60/40 PLA/PBAT compositions were set as reference blends. As in the case of the binary systems of Chapter 5, the nanoparticle content ranged from 1.5 to 7% Cloisite30B oMMT and from 1 to 6% CNT. The nanoparticle content was also fixed with respect to the PLA content, which explains why the real content refers to the overall polymeric matrix and is lower than that of Chapter 5. Table 6.1 shows all the compositions studied for each ternary system, along with the real nanoparticle weight content.

Table 6.1 (a): Compositions of PLA/PCL/oMMT nanocomposites.

Denomination	**PLA (%)**	**PCL (%)**	**Overall oMMT (%)**
PLA/PCL/1.5	80	20	1.2
PLA/PCL/3	80	20	2.4
PLA/PCL/5	80	20	4.2
PLA/PCL/7	80	20	5.8

Table 6.1 (b): Compositions of PLA/PCL/CNT nanocomposites.

Denomination	**PLA (%)**	**PCL (%)**	**Overall CNT (%)**
PLA/PCL/1	80	20	0.8
PLA/PCL/1.5	80	20	1.2
PLA/PCL/2	80	20	1.7
PLA/PCL/3	80	20	2.4
PLA/PCL/4	80	20	3.3
PLA/PCL/5	80	20	4.2
PLA/PCL/6	80	20	5

Table 6.1 (c): Compositions of PLA/PBAT/CNT nanocomposites.

Denomination	**PLA (%)**	**PBAT (%)**	**Overall CNT (%)**
80/20/1	80	20	0.8
80/20/2	80	20	1.7
80/20/3	80	20	2.4
80/20/4	80	20	3.3
80/20/5	80	20	4.2
60/40/1	60	40	0.6
60/40/2	60	40	1.2
60/40/3	60	40	1.8
60/40/4	60	40	2.3
60/40/5	60	40	2.9

6.1 Poly(lactic acid)/Poly(ε-caprolactone)/organically modified Montmorillonite (PLA/PCL/oMMT) nanocomposites

6.1.1 Nanostructure and morphology

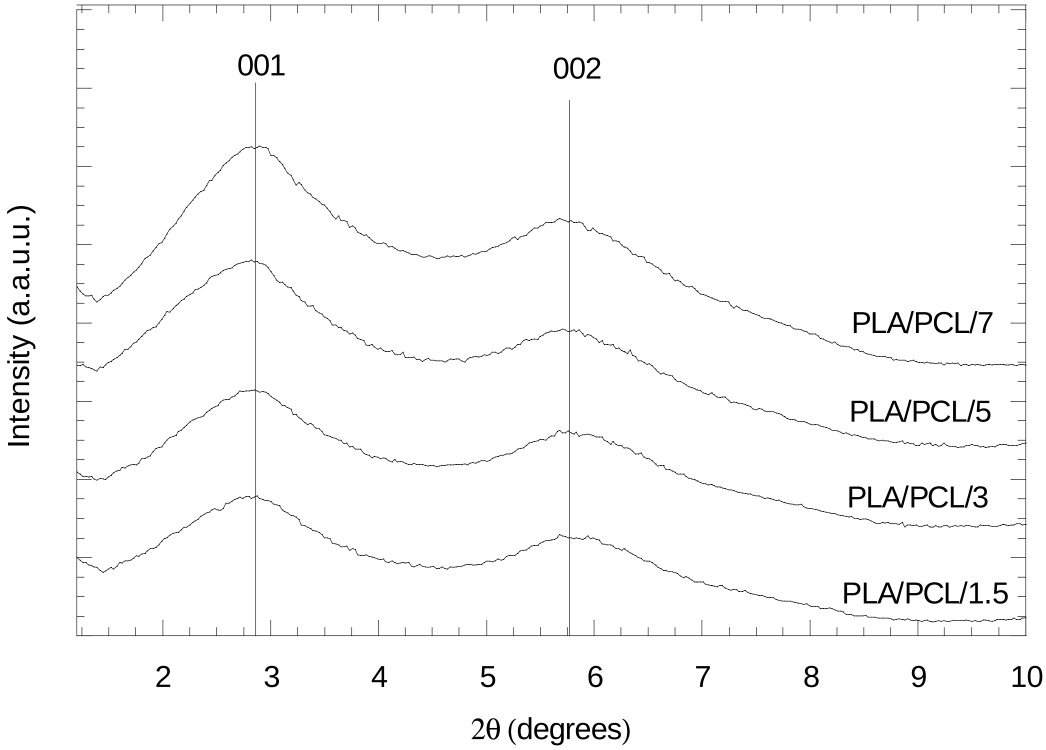

Figure 6.1.1: XRD diffractograms of PLA/PCL/oMMT nanocomposites.

Figure 6.1.1 shows the XRD patterns of PLA/PCL/oMMT nanocomposites. All the compositions showed two signals, a main 001 peak centered at between 2.86-2.89º, and a secondary 002 one, centered at approximately 5.89º. The latter peak was assumed to be a harmonic of the main 001 peak. The main peak represented the oMMT interlaminar distance, and appeared at lower 2theta angles than the main peak of pure Cloisite30B[250] (Figure 5.1.1), suggesting the presence of intercalated oMMT structures in these PLA/PCL/oMMT nanocomposites. The intensity of the main peak, and therefore, the number of intercalated structures, increased with increasing oMMT but its position, and therefore the interlaminar distance, remained constant. This indicates that the degree of intercalation is independent of the oMMT content in the range studied. The intergallery distance of oMMT in these PLA/PCL/oMMT nanocomposites was calculated from the position of the main peak using the Bragg equation and was close to 3.16 nm.

The interlaminar distance in these PLA/PCL/oMMT nanocomposites was the same as that calculated for the PLA/oMMT nanocomposites in Chapter 5.1 and points to one of the following two possibilities: 1) The PLA was intercalated in oMMT and was not affected by the PCL, in keeping with previously reported results for the same system[215] or, 2) irrespective of the location of the oMMT (in the PLA, in the PCL or at the interphase), the intercalation level of oMMT is similar to that shown in PLA.

In the PLA/PCL/oMMT systems studied to date, oMMT layers have been dispersed in the PLA-phase[214-216] or both in the PLA-phase and at the interphase[217]. This selective PLA-location of oMMT in PLA/PCL/oMMT nanocomposites has been related with a higher affinity of the clay to PLA than to PCL, which has been experimentally confirmed by calculating the interfacial tension between components[217] or by estimating the interaction parameters[214]. Table 6.1.1 shows the calculated solid-state interfacial tension values for PLA/oMMT and PCL/oMMT pairs. It can be concluded from the significantly lower interfacial tension value of the PLA/oMMT pair and, in keeping with previous works, that Cloisite30B nanoclay appears to be more compatible with PLA[97,214,215,217,278] than with PCL.

Table 6.1.1: PLA/oMMT and PCL/oMMT interfacial tension values measured in the solid-state.

Pair	**Interfacial tension (mN/m)**
PLA/oMMT	1.11
PCL/oMMT	2.9

So far, the results reported in the literature, along with the interfacial tension values contained in Table 6.1.1, point to the first of the aforementioned possibilities, i.e. to the oMMT being dispersed in the PLA/phase and the resulting intercalation occurring independently of the presence of PCL. However, the second possibility cannot be completely ruled out. Interlaminar distances of 3.2 nm, very similar to the 3.16 nm distances shown in this work, have also been reported for extruded PCL/Cloisite30B nanocomposites[114] and so, the location of the clay in the PCL phase must be considered as a possibility.

Figure 6.1.2 shows TEM micrographs of PLA/PCL/3 (a, c) and PLA/PCL/7 (b, d) nanocomposites taken at low (a, b) and high (c, d) magnifications. The light continuous phase is the PLA, the grey shows the PCL-phase, and the dark platelets are the oMMT nanolayers. As shown in Figures 6.1.2c and d, mainly intercalated but also some exfoliated oMMT nanoplatelets were well dispersed in the PLA/PCL blend. By comparing Figure 6.1.2a with Figure 6.1.2b, it can also be observed that as the oMMT content increased, the number and size of the agglomerates increased, but the overall dispersion of the oMMT remained good even at the highest oMMT content (Figure 6.1.2b and d).

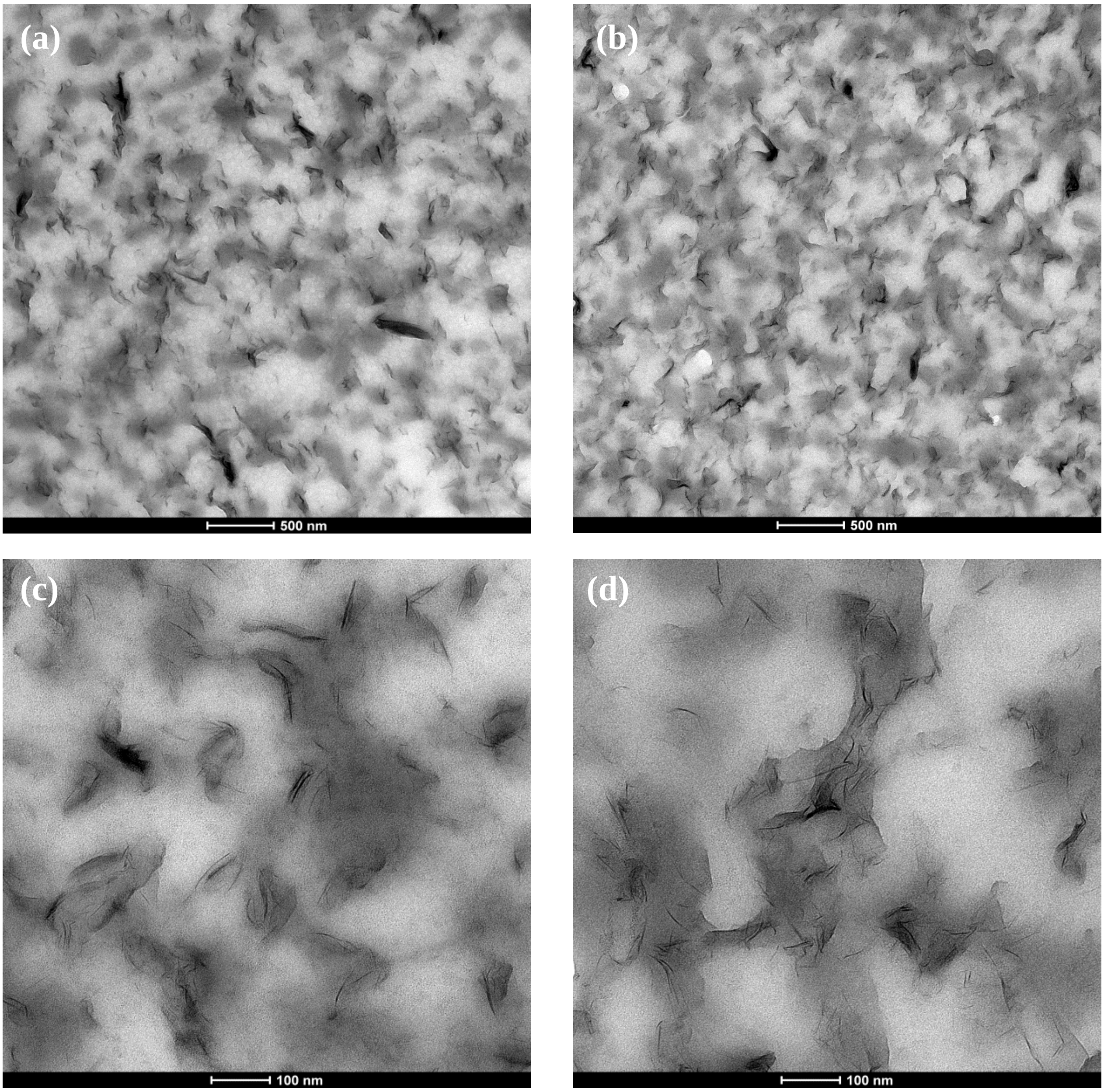

Figure 6.1.2: TEM micrographs of PLA/PCL/3 and PLA/PCL/7 nanocomposites taken at low (a, c) and high (b, d) magnifications.

More interestingly, as Figure 6.1.1c and d show, clay layers appeared preferentially located in the minor PCL phase, although some also appeared at the interphase between PLA and PCL. The amount of PLA-located clay was almost negligible. The location of oMMT in the PLA/PCL/oMMT nanocomposites in this work contrasts with previous findings reported in the literature[214-217], and also with the interfacial tension values of Table 6.1.1, i.e. with the established by thermodynamics.

The processing conditions for the melt-prepared PLA/PCL/oMMT nanocomposites of this work are based on high shear rates (screw-rotation speed: 320 rpm) and associated short residence times in the extruder (~30 seg). These conditions are far from thermodynamic equilibrium conditions, where the location of the nanoparticles is ruled by interactions[159]. In non-equilibrium processing conditions, such as those used here, kinetic effects, such as those promoted by the mixing procedure or the viscosity of the components, must be considered as factor which may affect the location of the nanoparticle in any of the separated polymer phases[159]. For example, the location of oMMT layers in PA66/SEBS-gMA/oMMT[279] and P6/mEPDM/EPDMgMA/oMMT[280] nanocomposites depended on the blending sequence employed.

With respect to the present processing route described in the introduction to this chapter, the oMMT was added in a second extrusion step to a previously melt-blended PLA/PCL 80/20 blend. Under these conditions, the oMMT initially makes contact with the PLA/PCL blend in the solid state. As the extrusion process progresses, and the material temperature rises, the PCL melts to render a liquid material at approximately the same temperature (~60-65ºC) that PLA softens to a rubbery state. Although PLA and PCL show similar melt viscosities at 180ºC (Chapter 4.1), at these initial stages of the extrusion process and consequent low temperatures, the rubbery PLA is much more viscous than completely melted PCL. This high viscosity ratio kinetically should favor the preferential location of the clay in the thermodynamically less favorable PCL phase. The short mixing times[158], resulting from the high screw-rotation speed, prevented the oMMT from migrating to the more compatible PLA-phase, and as a result, would remain in the less compatible PCL-phase at the end of processing.

To gain further insight into how the location of oMMT in the PCL-phase was the result of kinetic effects caused by the employed processing route, the extruded pellets of the PLA/PCL/3 composition were remixed in a microextruder at 180ºC and 80 rpm, operated in recirculation mode. Figure 6.1.3 shows TEM micrographs of the composition after remixed for 5 (a), 10 (b) and 15 (c) minutes. Changes can be seen in the location of the oMMT layers with respect to that shown in Figure 6.1.2c. As the mixing time increased, steadily increasing amounts of clay located in the light PLA phase or at the PLA/PCL interphase can be seen in Figures 6.1.3a to 6.1.3c.

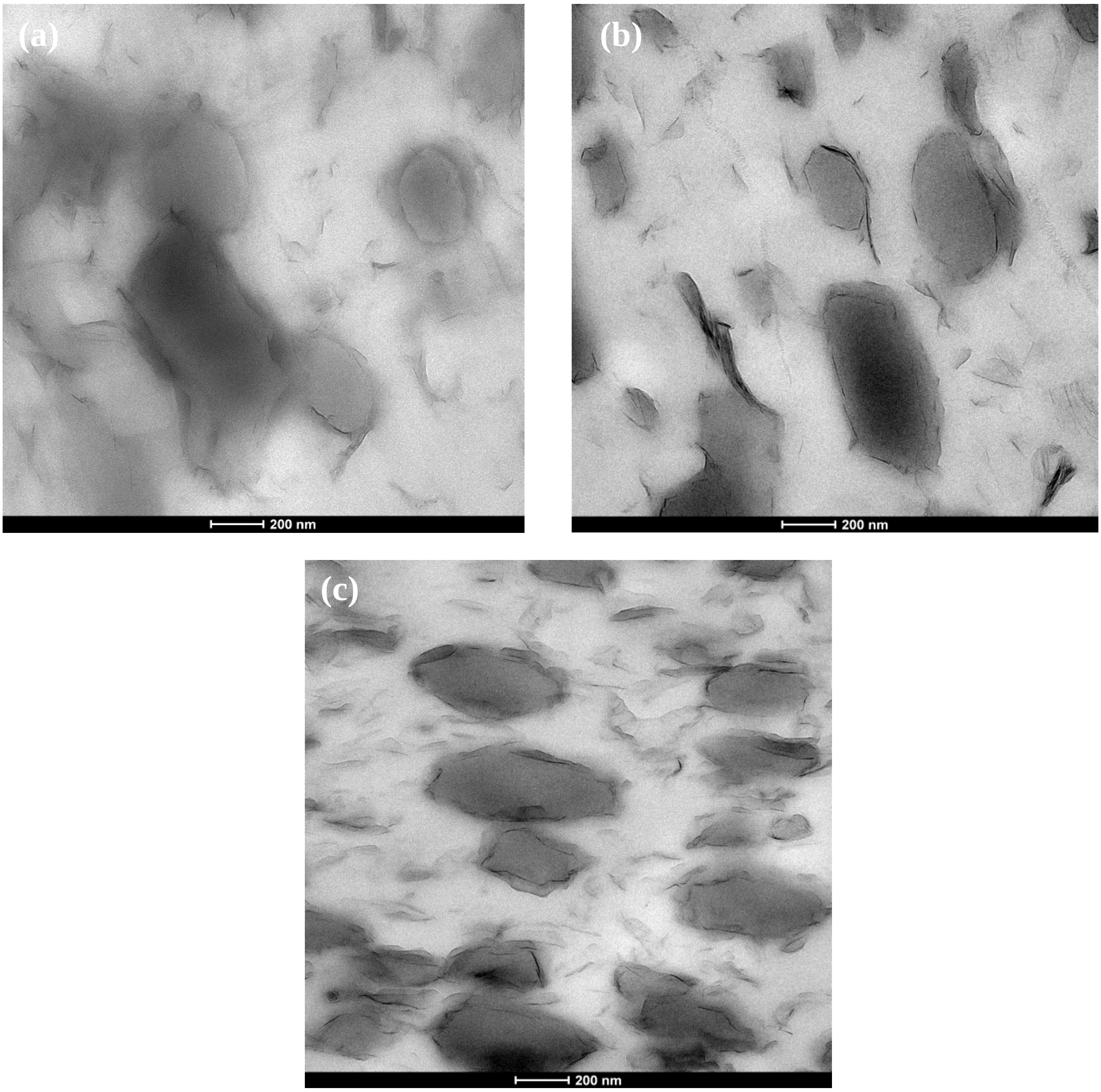

Figure 6.1.3: TEM micrographs of the PLA/PCL/3 nanocomposite after being remixed during 5 (a), 10 (b) and 15 (c) min in a recirculation microextruder.

This indicates that oMMT layers migrated from the PCL to PLA during the extra-mixing time in the micro-extruder, confirming the higher thermodynamic affinity of the clay with PLA than with PCL, and that the PCL-location of the original nanocomposites is related to the kinetic effects imposed by the processing method used. The resulting over-mixed morphology and oMMT dispersion and distribution is comparable to that observed by Wu et al.[217] in PLA/PCL/oMMT nanocomposites blended in an internal mixer for 6 min at 80 rpm.

Finally, when the morphology of the dispersed PCL phase of the 80/20 PLA/PCL composition of Chapter 4.1 and that of the PLA/PCL/oMMT nanocomposites in this chapter is compared, it can be observed that the finely dispersed sub-micron PCL particles in the PLA matrix of the PLA/PCL 80/20 composition (Figure 4.1.3b) presented an almost continuous or even co-continuous morphology depending on the oMMT content of the PLA/PCL/oMMT ternary nanocomposites (Figure 6.1.1). This indicates that the presence of oMMT significantly modified the morphology of the minor PCL phase in the 80/20 PLA/PCL blend. The ability of the nanoparticles to modify the morphology of phase-separated polymeric blends has been widely reported in the literature, and the factors affecting this have already been discussed in Chapter 2. In the case of these PLA/PCL/oMMT nanocomposites, the morphology of the PCL phase must be related to the dispersion mechanism of the oMMT during the extrusion process mentioned before. The preferential location of the oMMT nanoplatelets in the fully melted PCL phase led to a change in the shape of this phase, the PCL now surrounding and later intercalating between clay nanoparticles. The presence of the clay in the dispersed PCL phase should increase its viscosity[112] and so, the smaller mastication imposed by the PLA matrix could help only to deform and eventually elongate these PCL phases. In fact, it has been reported that the presence of nanoparticles in the minor dispersed phase can kinetically decrease its mobility, preventing the fracture of the dispersed particles during melt processing[184,205,206].

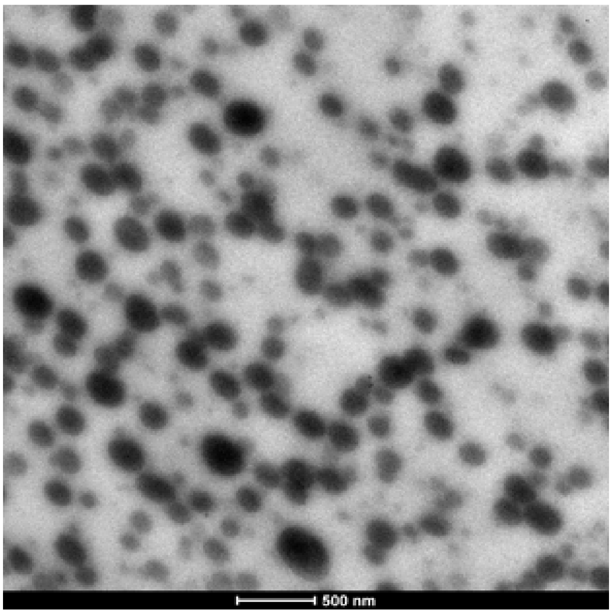

Figure 6.1.4: TEM micrograph of the PLA/PCL 80/20 blend

Figure 6.1.4 shows the morphology of the 80/20 PLA/PCL composition observed by TEM. It coincides with that observed by SEM and shown in Figure 4.1.3b. Consistent with the aforeproposed mechanism, the PCL (dark) particles in Figure 6.1.4 are deformed and eventually elongated, causing the coalescence of those particles and giving rise to the continuous morphology shown in Figure 6.1.1.

6.1.2 Phase structure

Figure 6.1.5 shows DMTA tanδ vs. temperature plots of the 80/20 PLA/PCL blend and those of the PLA/PCL/3 and PLA/PCL/7 nanocomposites. Two tanδ signals, corresponding to the α-transitions of PLA and PCL were observed in all the compositions. As can be seen in Figure 6.1.5, the positions of the peaks were very similar in all cases for PCL, close to -45ºC. The PLA peak increased slightly from 61.2ºC, suggesting that the PCL morphology development produced by oMMT hindered the chain mobility of the PLA phase. The small variations observed remained close to the experimental error of the measurement.

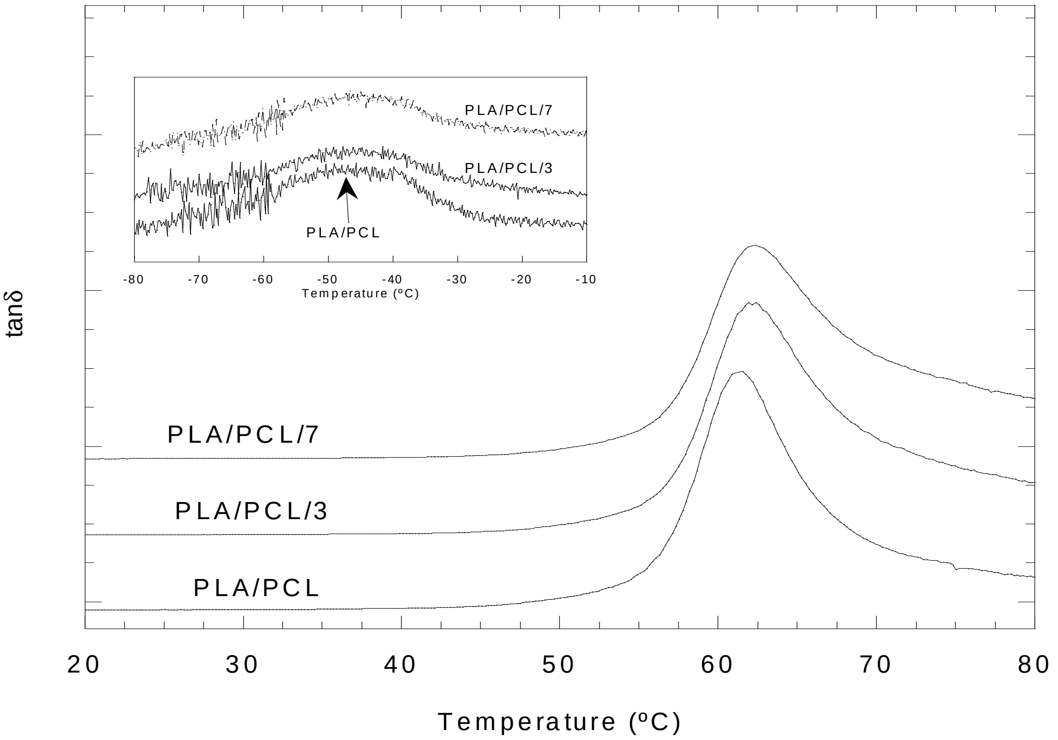

Figure 6.1.5: tanδ vs. temperature plots of PLA/PCL 80/20 blend and of PLA/PCL/3 and PLA/PCL/7 nanocomposites from 20ºC to 80ºC and from -80ºC to -10ºC.

These results indicate that the presence of oMMT did not modify the immiscibility of the PLA/PCL blend, as discussed in Chapter 4.1, in keeping previous findings on PLA/PCL/oMMT nanocomposites[214,217], and also in keeping with the general behavior of ternary nanocomposites. On some rare occasions, some interfacial-located nanoparticles have been found to partially[193,281-283] or even fully[282,283] miscibilize immiscible polymer blends.

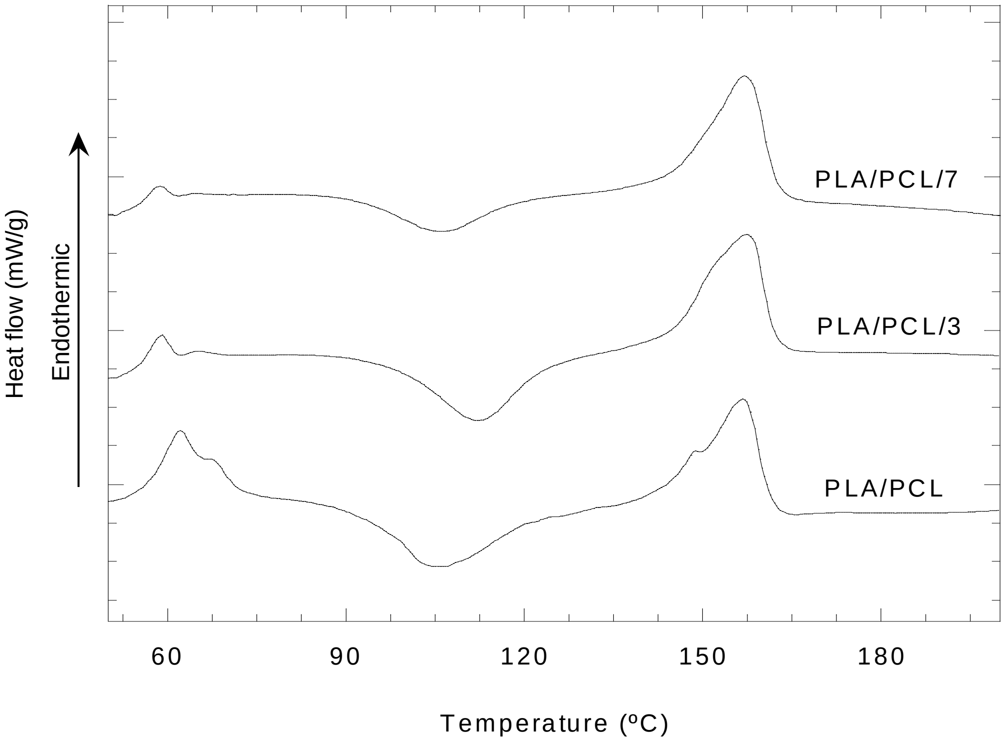

Figure 6.1.6: First DSC heating scans of the 80/20 PLA/PCL blend and of the PLA/PCL/3 and PLA/PCL/7 nanocomposites.

DSC plots of the first heating scans of the PLA/PCL blend and the PLA/PCL/3 and PLA/PCL/7 nanocomposites are shown in Figure 6.1.6. Two endothermic transitions and one exothermic transition were observed in all the compositions. The low temperature transition represents the melting peak of PCL, and the high temperature transition represents the melting peak of PLA. The exothermic transition represents the cold crystallization of PLA. Table 6.1.2 shows the melting temperatures of PCL and PLA, the cold crystallization temperature and the degree of crystallinity of PLA in all the compositions. Both the melting temperature and the degree of crystallinity of PLA remained unchanged in the presence of oMMT, and were similar to the initial values of the PLA/PCL blend. The small variations observed were hardly significant and, furthermore, did not show any clear trend.

The cold crystallization temperature of PLA varied depending on the oMMT content. It increased at low oMMT contents but regained the temperature of the unreinforced 80/20 composition at high oMMT contents. This suggests that the presence of small amounts of oMMT in PCL hindered the nucleation effect of PCL in PLA, while at high oMMT contents remained unchanged. This behavior was difficult to fully comprehend and no definitive cause is proposed here. However, the variations observed did not affect the melting behavior of PLA, indicating that the amount and the structure of the PLA-crystals created was similar in all cases.

Both the melting temperature and it would seem, the melting enthalpy of PCL, decreased at increasing oMMT contents. These results are consistent with the literature[284], and indicate that oMMT hindered the crystallization capacity of PCL.

Table 6.1.2: Melting temperatures of PLA (Tm_{PLA}) and PCL (Tm_{PCL}) and, cold crystallization temperatures (Tc_{PLA}) and degrees of crystallinity (Xc) of PLA in the PLA/PCL/CNT nanocomposites.

Composition	**Tm_{PLA} (ºC)**	**Tm_{PCL} (ºC)**	**Tc_{PLA} (ºC)**	**X_{cPLA} (%)**
PLA/PCL	156.7	62.0	104.7	4.8
PLA/PCL/1.5	159.4	61.7	116.1	4.6
PLA/PCL/3	158.7	59.4	112.1	7.5
PLA/PCL/5	157.4	58.7	112.1	4.9
PLA/PCL/7	157	58.3	106	9.8

6.1.3 Viscoelasticity

Figure 6.1.7 shows the storage modulus (G´) vs. angular frequency (ω) plots of the PLA/PCL/oMMT nanocomposites. As the figure shows, the behavior of the PLA/PCL blend and the nanocomposites was similar up to the PLA/PCL/5 composition. Broad relaxations starting from close to 10 rad/s and increasing G´ values with oMMT contents were observed in these compositions, as a result of the presence and reinforcing effect of the oMMT[258]. However, the viscoelastic behavior of the nanocomposites up to this composition was still dominated by the liquid-like behavior of the PLA/PCL blend[259]. This behavior changed in the PLA/PCL/7 composition. This is because it showed a significantly higher G´ value in the whole frequency range which remained constant in the terminal flow zone (low frequencies), irrespective of the applied frequency. This behavior indicates solid-like behavior and suggests structural percolation of the nanoclay.

The shape of the G´ vs. ω plots shown in Figure 6.1.7 is similar to those of the PLA/oMMT nanocomposites in Chapter 5.1.1 (Figure 5.1.5) and percolation was achieved at the same oMMT content. Moreover, the higher values of G´ shown in Figure 6.1.7 with respect to those of Figure 5.1.5 were only caused by the higher value of G´ in the PLA/PCL blend with respect to that of pure PLA. As stated in Chapter 5.1, the viscoelastic behavior of polymer nanocomposites is directly related to the dispersion level of the nanoparticles[261]. These results, together with the similar interlaminar distance of the PLA/oMMT (in Chapter 5.1.1) and PLA/PCL/oMMT (in this chapter) nanocomposites, points to a similar overall dispersion level of the oMMT layers in PLA and in PLA/PCL blends, regardless of their PLA and PCL location.

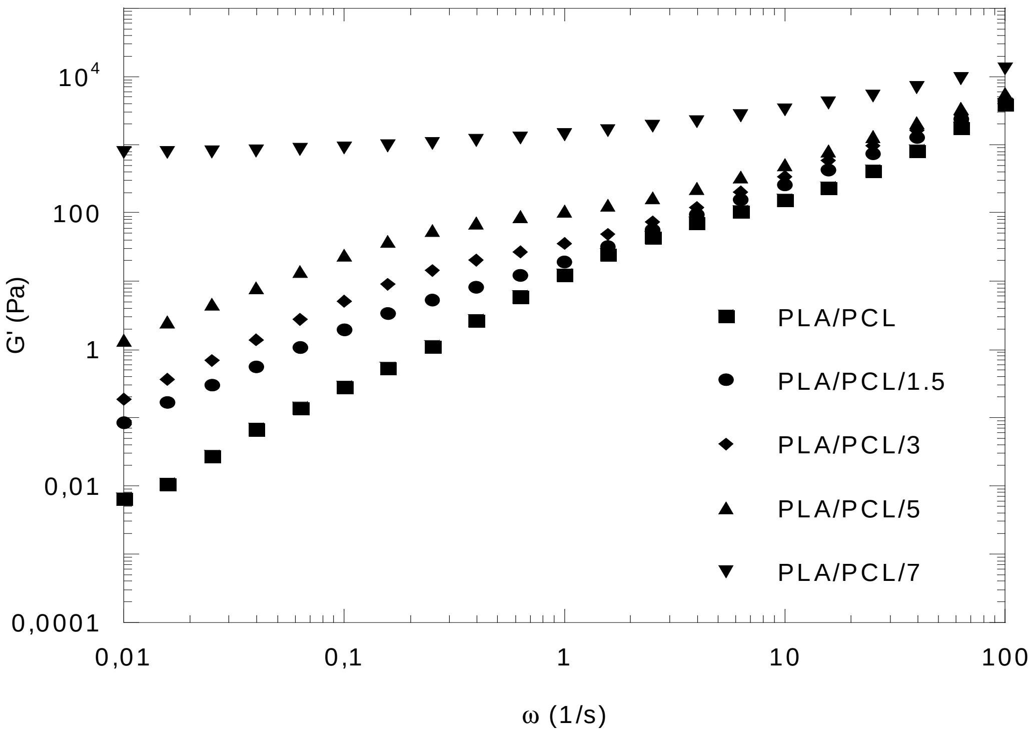

Figure 6.1.7: G´ vs. ω plots of the PLA/PCL 80/20 blend and of PLA/PCL/oMMT nanocomposites.

Figure 6.1.8 shows complex viscosity (η*) vs. angular frequency (ω) plots of the PLA/PCL blend and PLA/PCL/oMMT nanocomposites. The complex viscosity of the PLA/PCL blend increased progressively with the oMMT content. As can be observed, the behavior of the complex viscosity of the PLA/PCL/7 composition, unlike the rest of the compositions, became exponential as a result of aforementioned percolation. When these results are compared with those of the PLA/oMMT nanocomposites of Chapter 5.1, it can be seen that the plasticization effect of the organic surfactant of oMMT on the PLA in the binary nanocomposites was not observed in Figure 6.1.8, suggesting that oMMT did not plasticize the PCL phase in the ternary PLA/PCL/oMMT nanocomposites, unlike when it located in the PLA matrix of the binary nanocomposites.

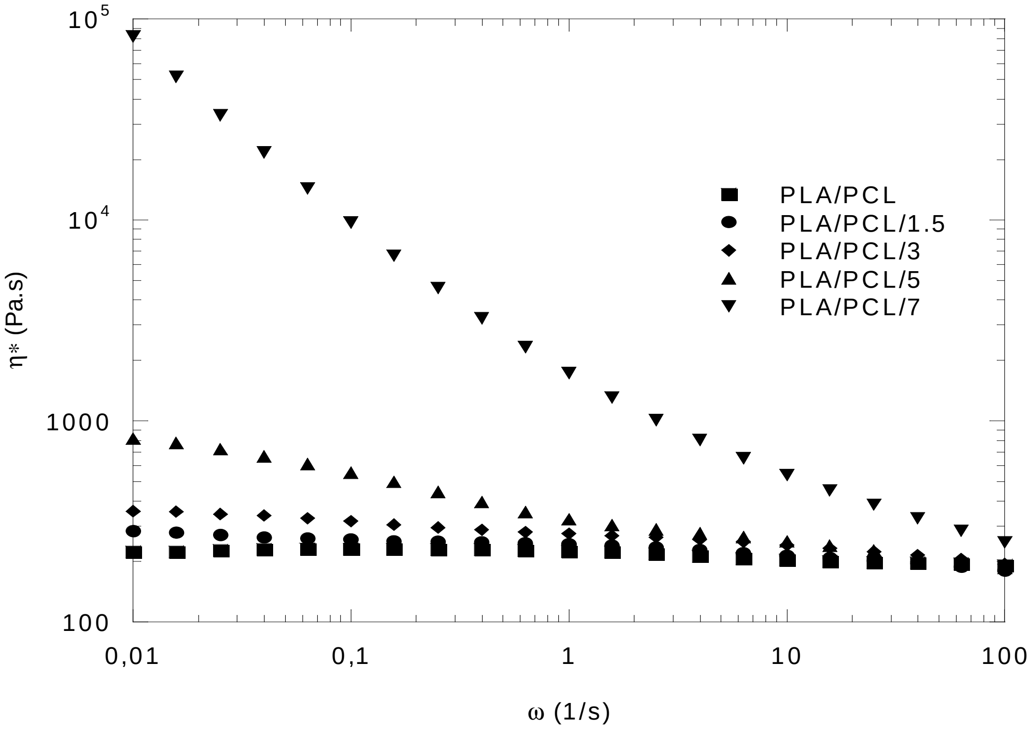

Figure 6.1.8: η* vs. ω plots of the PLA/PCL 80/20 blend and of PLA/PCL/oMMT nanocomposites.

6.1.4 Mechanical properties

Figure 6.1.9 shows the Young's modulus values for the PLA/PCL/oMMT nanocomposites vs. the real nanoclay content. As can be seen, the Young's modulus of the PLA/PCL blend increased with increasing amounts of oMMT as a result of the reinforcing effect produced by the nanoclay. The increase was linear in the studied oMMT content range. The addition of oMMT was very efficient and helped to recover the loss of stiffness (about 15.5%) produced by PCL in PLA (Chapter 4.1). The Young's modulus values of PLA/PCL/1.5 and PLA/PCL/3 nanocomposites were 3350±120 MPa and 3470±70 MPa, respectively, and were very similar to that of pure PLA, 3520±20 MPa. The maximum Young's modulus obtained, which was for the PLA/PCL/7 composition, was 3940±90 MPa, 12% higher than that of pure PLA and 29% higher than that of the reference 80/20 blend.

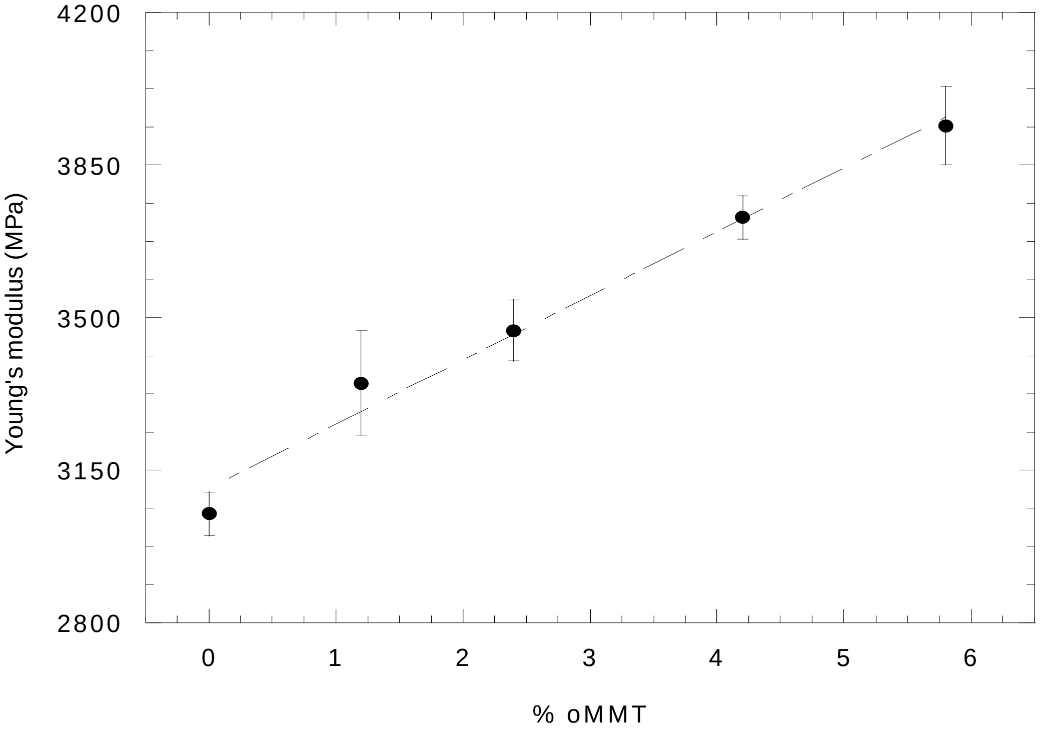

Figure 6.1.9: Young’s modulus values of PLA/PCL/oMMT nanocomposites with respect to the oMMT content.

The reinforcement effect produced by oMMT in the PLA/PCL blend is compared to that produced in neat PLA (Chapter 5.1) in table 6.1.3, where the relative modulus increases of the PLA/oMMT nanocomposites and the PLA/PCL/oMMT nanocomposites are shown. Bearing in mind that the real oMMT content is lower in the ternary nanocomposites, the increases in the relative modulus were very similar in both cases, suggesting that the reinforcing effect of oMMT in pure PLA and in the PLA/PCL blend was almost the same. These results indicate that the reinforcing ability of the oMMT in this study was similar regardless of whether it was located within the main matrix phase (binary system) or within the minor dispersed phase (ternary system). These findings are consistent with those shown in PA6/elastomer/oMMT nanocomposites[280], where the reinforcing effect of the nanoclay nanoparticles was also similar irrespective of their matrix- or dispersed phase-location. The good dispersion and similar intercalation level shown by the oMMT in both binary and ternary systems of this work is also consistent with these results.

Table 6.1.3: Relative modulus increases of PLA/oMMT (Chapter 5.1) and PLA/PCL/oMMT (Chapter 6.1) nanocomposites with respect to the oMMT content.

oMMT content (%)*	PLA/oMMT nanocomposites	PLA/PCL/oMMT nanocomposites
1.5 (1.2)	5.7%	9.8%
3 (2.4)	14.6%	13%
5 (4.2)	27%	22%
7 (6)	31%	29%

* The true oMMT contents in ternary PLA/PCL/oMMT nanocomposites appear between brackets.

Literature on the subject of the mechanical properties of ternary PLA/PCL/oMMT nanocomposites is scarce. Li et al.[218] studied the effect of adding Cloisite25A and modified Cloisite25A to a PLA/PCL blend, whose composition is not mentioned. It can be deduced that the PCL content must have been high, because the Young's modulus and yield strength values of the unreinforced PLA/PCL blend were very low (1120 MPa and 40 MPa, respectively). The Young's modulus increases were significant, even higher than those observed in this work (40% at 5% oMMT). Moreover, when the modified nanoclay was used, the results were even better (47% at the same oMMT content) but, given the very low initial value of the unreinforced PLA/PCL blend, the maximum value obtained was 50% lower than the maximum recorded in this study. In the work of Yu et al.[214], significant Young's modulus increases (19.5% and 23% with 1% and 3% oMMT contents, respectively) were followed by even greater decreases as the oMMT content increased (up to 10% oMMT content) when added to a 90/10 PLA/PCL blend. As in the work of Li et al.[218] the initial modulus value of unreinforced PLA/PCL blend was surprisingly low (1950 MPa).

The behavior of the tensile strength of the PLA/PCL/oMMT nanocomposites of this work was also favorable, because it remained similar to that of the unreinforced PLA/PCL blend (smaller variations than the standard deviation). Significant decreases in tensile strength have been observed at high oMMT contents in previously studied PLA/PCL/oMMT nanocomposites[214,216] and only marginal increases at low oMMT contents[214,216] or in the whole oMMT content range when the clay was modified[218] have been reported. The trend observed in PLA/PCL/oMMT nanocomposites was similar to that observed in the PLA/oMMT nanocomposites in Chapter 5.1. The dispersion of oMMT was comparable in the binary and the ternary nanpocomposites, and had a similar effect on the tensile strength of pure PLA and the PLA/PCL blend, based on the aforementioned Young's modulus values.

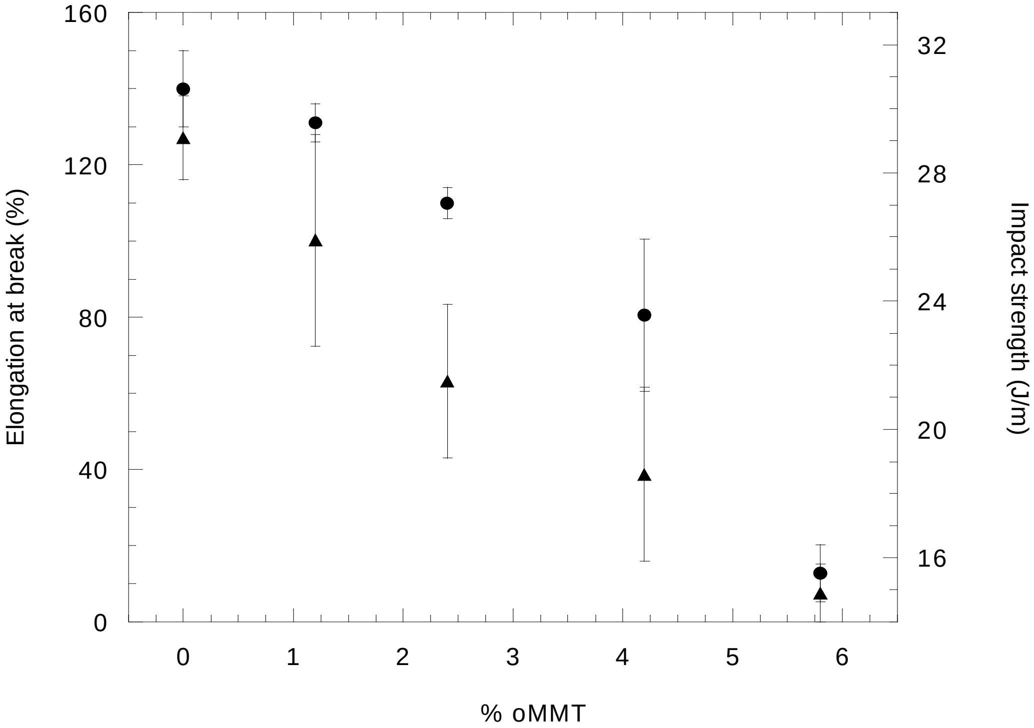

Figure 6.1.10: Elongation at break (●) and impact strength (▲) values of PLA/PCL/oMMT nanocomposites with respect to the oMMT content.

Figure 6.1.10 shows ductility and impact strength values with respect to the real content of oMMT in PLA/PCL/oMMT nanocomposites. As can be seen, the elongation at break of the PLA/PCL blend decreased with the nanoclay content. However, it was higher than 100% in PLA/PCL/1.5 and PLA/PCL/3 nanocomposites, and stayed close to 80% even at higher oMMT contents. Only the PLA/PCL/7 composition showed a close-to-brittle behavior, probably related to the structural percolation of the nanoclay proposed in the previous section. These results are better than those reported in previously mentioned PLA/PCL/oMMT nanocomposites, where the elongation at break decreased by 63% with 2% oMMT content and by 78% with 5% oMMT content, respectively, even in the most favorable case (modified oMMT)[218], or sharply decreased to brittle values, lower than that of the reference PLA/PCL blend[214].

The high ductility of the PLA/PCL/oMMT nanocomposites in this study indicates that, in the presence of oMMT, PCL partially maintained its ductile behavior in PLA/PCL/oMMT nanocomposites, at least up to the PLA/PCL/5 composition. This result is consistent with the bibliography[111], where highly deformable PCL/oMMT nanocomposites (elongation at break up to 500%) have been obtained at oMMT contents as high as 4%. Moreover, it has also been reported that efficient stress transfer between polymeric phases[166] is still possible when the interphase between them is not saturated by oMMT.

Figure 6.1.10 also shows how the impact strength of the PLA/PCL/oMMT nanocomposites decreased at increasing oMMT contents and was less positive than the ductility results. No literature data has been found in the literature on the impact strength of PLA/PCL/oMMT nanocomposites, except for a PLA/poly(ε-caprolactone-co-lactide) copolyester blend filled with silica nanoparticles where supertough materials were obtained at high filler contents, which was related to the favorable initial behavior of the unfilled blend and to the almost continuous morphology which developed in the presence of the nanoparticles[171].

6.1.5 Oxygen permeability

Figure 6.1.11 shows the oxygen permeability of PLA/PCL/oMMT nanocomposites with respect to the real oMMT content. The broken line shows the permeability of pure PLA. As can be seen, the permeability of the PLA/PCL 80/20 blend was significantly higher (0.37 Barrer) than that of pure PLA, as a result of the lower barrier property of PCL (0.90 Barrer).

Thanks to the morphology of this blend (Chapter 4.1, Figure 4.1.3), during permeation, O_2 molecules find finely and homogeneously distributed PCL dominions, thus facilitating easier and faster diffusion through the material. Figure 6.1.11 also shows that the permeability decreased with the addition of oMMT. The decrease was sharp at low oMMT contents and slower at higher oMMT contents. When this behavior is compared to that observed in the reference binary PLA/oMMT nanocomposites (Figure 5.1.9), it can be seen that the decreases in permeability of the PLA/PCL blend were significantly greater (21% and 35% with 1.5% and 5% oMMT, respectively) than in pure PLA (7% and 31%, respectively), even when the real overall oMMT content was lower in the former than in the latter.

Two factors need to be considered when analyzing the effect of adding oMMT to PLA/PCL: 1) the nanoplatelets themselves and 2) the preferential location of the nanoparticles in the PCL phase and the ensuing change in morphology. The presence of nanoplatelets is common to both the reference PLA/oMMT nanocomposites and the ternary PLA/PCL/oMMT nanocomposites, so the second factor must be responsible for the enhanced barrier behavior of the latter. This is because the preferential location of the nanoclay in the PCL phase counteracts the higher permeability of this material with respect to pure PLA, and, moreover, the transition to co-continuous morphologies caused by the oMMT would also help to prevent the O_2 molecules from finding a continuous path through the PLA matrix.

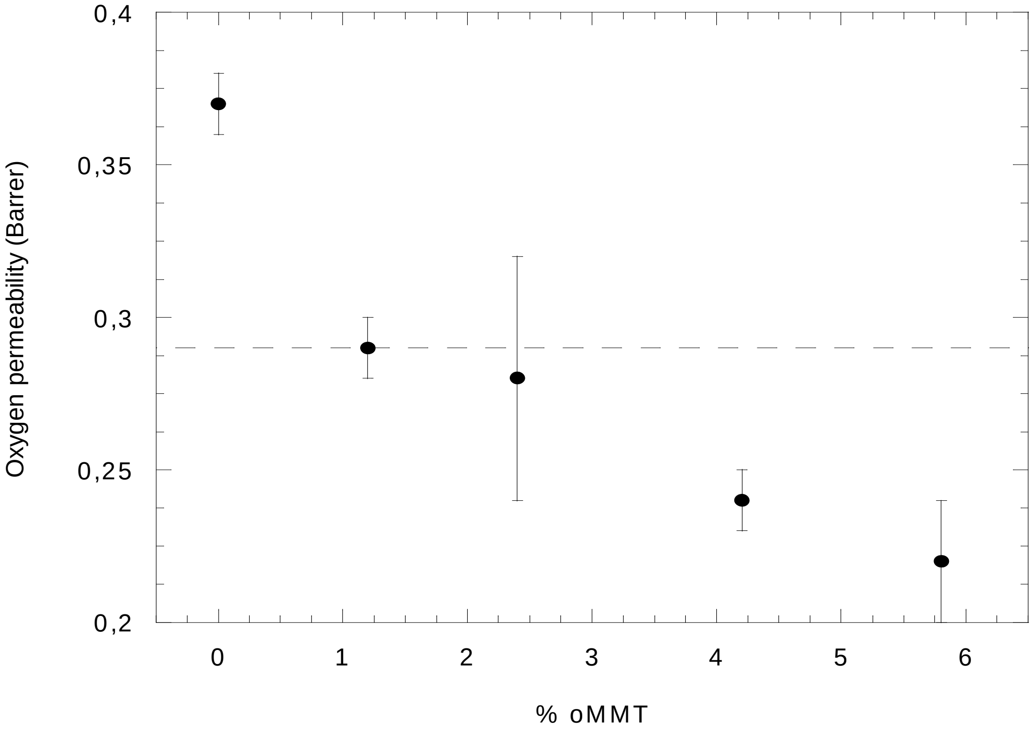

Figure 6.1.11: Oxygen permeability values of PLA/PCL/oMMT nanocomposites with respect to the oMMT content. The broken line indicates the oxygen permeability of pure PLA (Chapter 5.1).

Finally, and as can be seen in Figure 6.1.11, similar or even lower permeability values than for pure PLA can be obtained at intermediate oMMT contents. This behavior, along with the very favorable mechanical performance described in the previous section (Young’s modulus similar to that of pure PLA, high strength and ductility) makes these materials very interesting potential candidates for practical applications.

6.2 Poly(lactic acid)/Poly(ε-caprolactone)/carbon nanotube (PLA/PCL/CNT) nanocomposites

6.2.1 Nanostructure and morphology

The nanostructure and morphology of the PLA/PCL/CNT nanocomposites was analyzed by TEM and AFM techniques. Figure 6.2.1 shows representative TEM micrographs of the PLA/PCL/2 (a) and the PLA/PCL/3 (b) nanocomposites. The light and grey zones represent the PLA and the PCL phases, respectively, and the dark cylinders are the dispersed CNTs. As can be seen, small aggregates and monodispersed nanotubes appeared in both compositions. The size and the amount of aggregates increased with increasing CNT. However, the number of monodispersed CNTs was still significant even at high contents, pointing to a good dispersion level within the PLA/PCL blend in all the compositions. Figure 6.2.1 also shows that CNTs selectively located inside the PCL phase, and that both the PLA/PCL interphase and the PLA matrix appeared free of nanotubes.

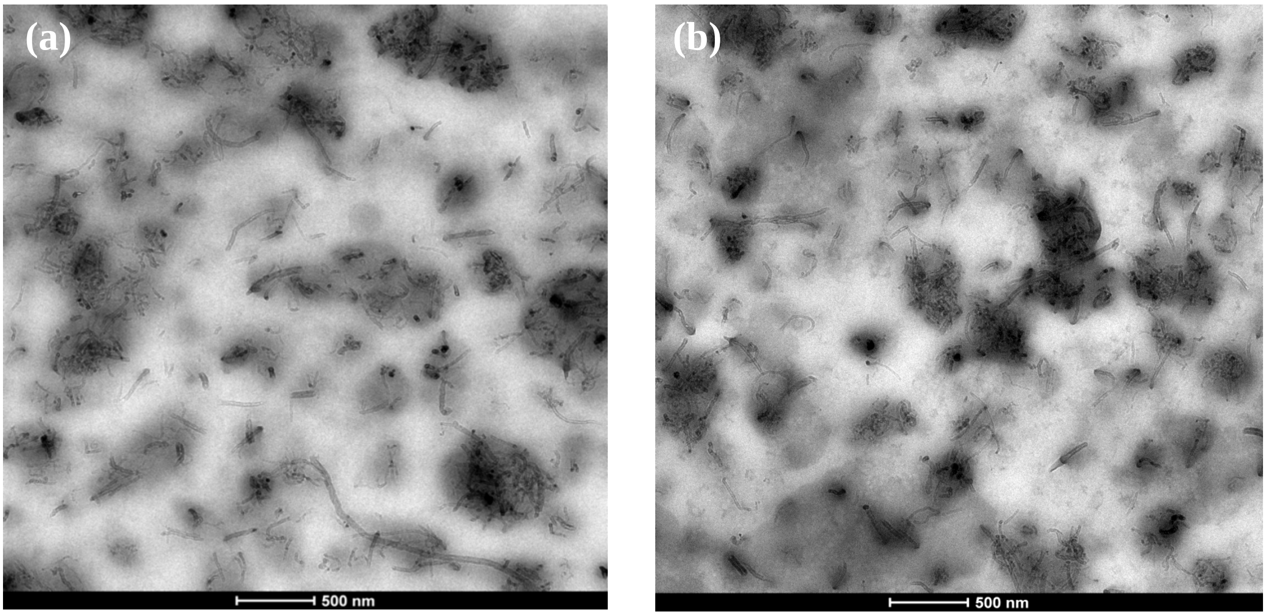

Figure 6.2.1: TEM micrographs of PLA/PCL/2 (a) and PLA/PCL/3 (b) nanocomposites.

Figure 6.2.2, shows a (2x2μm) representative AFM micrograph of the PLA/PCL/4 nanocomposite, taken as energy dissipation signal. As it is much stiffer than PCL, PLA disperses less mechanical energy and consequently, appears as the dark area in the figure, while the white area denotes the PCL phase. As can be seen, the preferential PCL-location of CNTs was confirmed by AFM and is consistent with that observed in previous PLA/PCL/pCNT[193] and PLA/PCL/COOH-CNT nanocomposites[193,217,219,220] where some nanotubes were also observed at the PLA/PCL interphase. However, as previously reported, this was not observed in the PLA/PCL/CNT nanocomposites of this work.

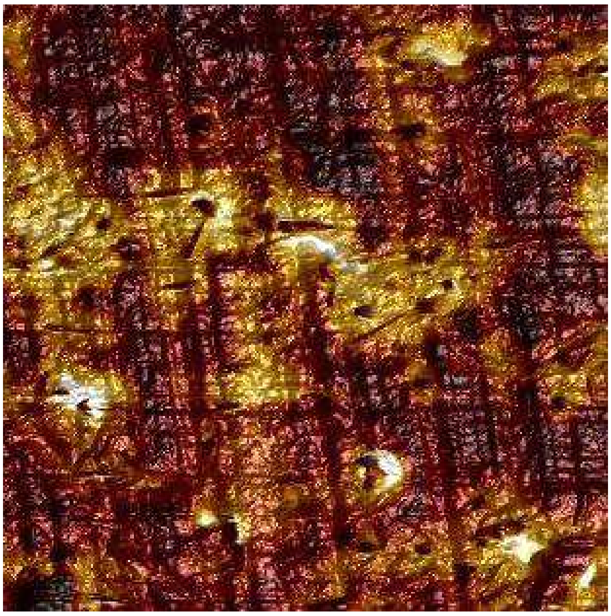

Figure 6.2.2: AFM micrograph of the PLA/PCL/4 nanocomposite.

Table 6.2.1 shows calculated solid-state interfacial tension values for PLA/CNT and PCL/CNT pairs. As can be seen, the PCL/CNT interfacial tension (2.65 mN/m) was lower than that of the PLA/CNT pair (6.35 mN/m) and, therefore, the PCL phase is expected to be more compatible with the CNTs. This is in agreement with the literature, where a higher affinity of the CNTs with the PCL phase than with the PLA phase has been reported[193,219,220]. However, these results contrast with the interfacial tension values reported by Wu et al.[217], where lower values were obtained for the PLA-CNT pair than for the PCL-CNT pair, but they are consistent with the preferential PCL-location of the CNTs also reported in the same work. Although the viscosity ratio was claimed as the main contributing factor, the authors did not fully explain the behavior and left the role of wetting parameters or interactions on the location of the nanoparticles open to discussion.

Taking into account the melt-mixing procedure followed for obtaining these PLA/PCL/CNT nanocomposites (PLA/CNT nanocomposites were obtained in a first extrusion step and PCL was added in a second extrusion step), the PCL-location of CNTs indicates that they migrated from the PLA phase to the PCL phase during the second step of processing. This was also observed by Huang et al. for PLA/PCL/COOH-CNT[169] nanocomposites. Given that both polymers showed similar viscosities at the processing temperature (ηPLA/ηPCL ~ 0.95), the higher compatibility with PCL and the long residence time in the extruder[285] (3 min. approximately), resulting from the low screw-rotating rate in this second step (80 rpm), favored and allowed, respectively, the migration process to take place.

Table 6.2.1: PLA/CNT and PCL/CNT interfacial tension values measured in the solid-state.

Pair	Interfacial tension (mN/m)
PLA/CNT	6.35
PCL/CNT	2.65

When the morphology of the PCL dispersed phase of these PLA/PCL/CNT nanocomposites shown in Figures 6.2.1 and 6.2.2 is compared with that of the reference PLA/PCL blend (Figure 6.1.4), it can be seen that the size and shape of the PCL particles changed significantly. In fact, as the CNT content increased, the PCL particles gradually became bigger and less spherical. This can be appreciated by comparing Figure 6.2.1a to 6.2.1b. Given the mixing procedure described in the previous paragraph and the nanostructure of the PLA/CNT nanocomposites in Chapter 5.2, the new morphology of these PLA/PCL/CNT nanocomposites points to the PCL melting during the extrusion process and locating preferentially around the well dispersed CNTs, giving rise to PCL particles that “follow” the nanostructure of the CNTs in the PLA matrix. So, a continuous structure of CNTs gradually developed as their content increased, eventually creating a similar structure to the PCL phase.

The “creation” of a new morphology of the dispersed phase, caused by the presence and dispersion of CNTs has been reported in the bibliography[210] and reproduced in Chapter 2. Figure 2.4.3, which is again reproduced here for clarity, showed how a “sea-island” morphology can turn into an almost co-continuous morphology when CNTs are present and when the compatibility of the minor phase with the CNTs is greater than the compatibility of the matrix.

Effect of the CNT dispersion (at low contents) on the morphology of the PPS/PA66 60/40 blend. Image obtained from reference 210.

As discussed below, the rheological percolation concentration as well as the electrical percolation in PLA/PCL/CNT nanocomposites was located at between 0.8% (PLA/PCL/1) and 1.7% (PLA/PCL/2) CNT contents, indicating that CNTs were physically interconnected from this last composition on. This points to the “so-called” double percolation effect in these PLA/PCL/CNT nanocomposites, and suggests that the PLA/PCL morphology was governed by the nanotubes dispersed in the PCL phase. These results agree with those reported in previous works[200,207,208,210,211], where the morphology of the system was mainly determined by the dispersion of the minor phase-located nanoparticles.

The efficiency of different nanoparticles, similar to that ones studied in this work (oMMT and CNTs) to promote changes in the morphology of the dispersed phase in ternary nanocomposites was compared in a PLA/PA11 70/30 blend by Nuzzo et al.[177]. They observed that morphological co-continuity of the dispersed phase coincided with the rheological percolation concentration of the filler in the case of oMMT, but filler contents higher than the percolation concentration were necessary in the case of the CNTs. This result was related to the ability of the oMMT to efficiently lower the interfacial tension between the filled dispersed PA11 phase and the continuous PLA matrix (from 13 to 4 mJ/m^2). Increased phase compatibility is well known to facilitate the formation of co-continuous morphologies in polymer blends[286]. The CNTs did not modify the PLA/PA11 interfacial tension, and therefore they did not improve the compatibility. In the case of the PLA/PCL blend in this study, Wu et al.[217] demonstrated that the PLA/PCL interfacial tension with PCL-located oMMT and CNTs was almost the same, 2.38 mJ/m^2 and 2.5 mJ/m^2, respectively. These results prove that the phase compatibility had no influence on the development of a co-continuous morphology of the dispersed phase in the PLA/PCL ternary nanocomposites of this work and help to explain the similar effect of both oMMT and CNT on the morphology of the PLA/PCL blend in Chapters 6.1 and 6.2.

6.2.2 Viscoelasticity

Figure 6.2.3 shows the storage modulus (G´) vs. angular frequency (ω) plots of PLA/PCL/CNT nanocomposites with 0-2.4% CNT contents. As can be seen, the storage modulus of the nanocomposites in the terminal flow zone (low frequencies) increased at increasing CNT contents. This is because PCL-located CNTs progressively reinforced the PLA/PCL melt. The behavior of the PLA/PCL/1 nanocomposite was similar to that of the PLA/PCL blend, where G´ continuously decreased as ω decreased. Therefore, the melt behavior of this PLA/PCL/CNT composition was mainly dominated by the liquid-like behavior of the PLA/PCL blend. However, the influence of the presence of CNT was significant, even at this low content and, as indicated in the Figure, the slope of the curve in the terminal flow-range was smaller in the nanocomposite than in the blend and the relaxation shown in the PLA/PCL blend disappeared in the nanocomposite. These differences indicate that dispersed PCL-CNT particles increased the melt-elasticity of PLA more than pure PCL and that PCL-located CNTs hindered the relaxation behavior of the PLA/PCL blend, respectively.

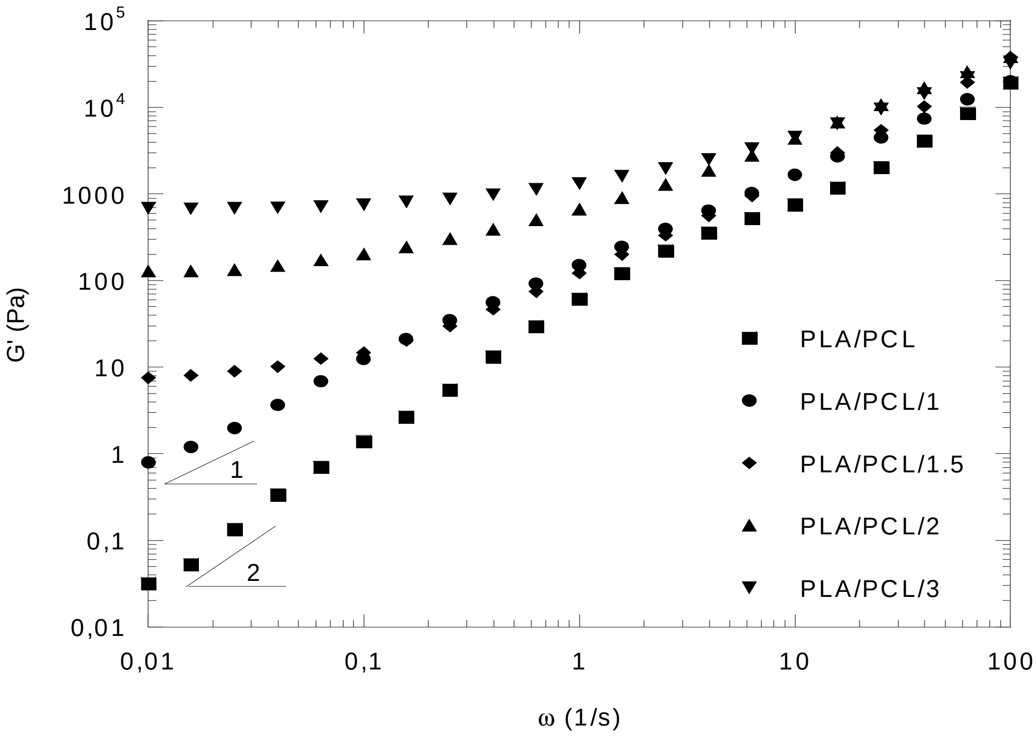

Figure 6.2.3: G´ vs. ω plots of the PLA/PCL 80/20 blend and of PLA/PCL/CNT nanocomposites.

As can also be seen in Figure 6.2.3, G´ showed a frequency-independent plateau behavior in the terminal flow zone at CNT contents higher than that of the PLA/PCL/1 composition. It was evident in the PLA/PCL/1.5 composition and more remarkable at higher CNT contents. This behavior points to solid-like behavior resulting from the development of fully percolated structures in these nanocomposites. Taking into account the PCL-location of CNTs and the continuity of PCL within PLA, the double-percolation phenomenon took place in PLA/PCL/CNT nanocomposites[155,169,193,207,219,220].

If the G´ vs. ω plots of Figure 6.2.3 are compared to those of Figure 5.2.5, it can be seen that the viscoelastic behavior of the PLA/PCL/CNT and PLA/CNT nanocomposites, respectively, was very similar. The only difference was the higher G´ values shown in the ternary nanocomposites, which were related to the higher G´ values of the PLA/PCL blend compared with those of pure PLA. As already mentioned, the viscoelastic properties of polymer nanocomposites are directly related to the dispersion level of the nanoparticles, so these results point to a similar CNT dispersion level in the ternary and in the binary nanocomposites, despite the preferential location of the CNTs in the dispersed PCL phase or the continuous PLA matrix, respectively. Similar results were obtained in the binary PLA/oMMT and ternary PLA/PCL/oMMT nanocomposites in Chapters 5.1 and 6.1.

6.2.2 Phase structure

Figure 6.2.4 shows tanδ vs. temperature plots obtained by DMTA of the PLA/PCL blend and PLA/PCL/CNT nanocomposites with 2% and 6% CNT contents, as an example. All compositions showed two peaks, reflecting the α-transition of the PLA phase (high temperature peak) and the PCL phase (low temperature peak). As can be seen, the position of both peaks did not change appreciably with the CNT content. These results indicate that the presence of CNT did not significantly affect the chain mobility of the PCL phase where they were dispersed, and also that the full immiscibility of the PLA/PCL blend was maintained in the PLA/PCL/CNT nanocomposites. This second result contrasts with that observed in COOH-CNT containing PLA/PCL/CNT nanocomposites[193], where the Tg's of PLA and PCL shifted to lower and higher temperatures, respectively, as a result of an emulsification effect produced by interphase-located nanotubes.

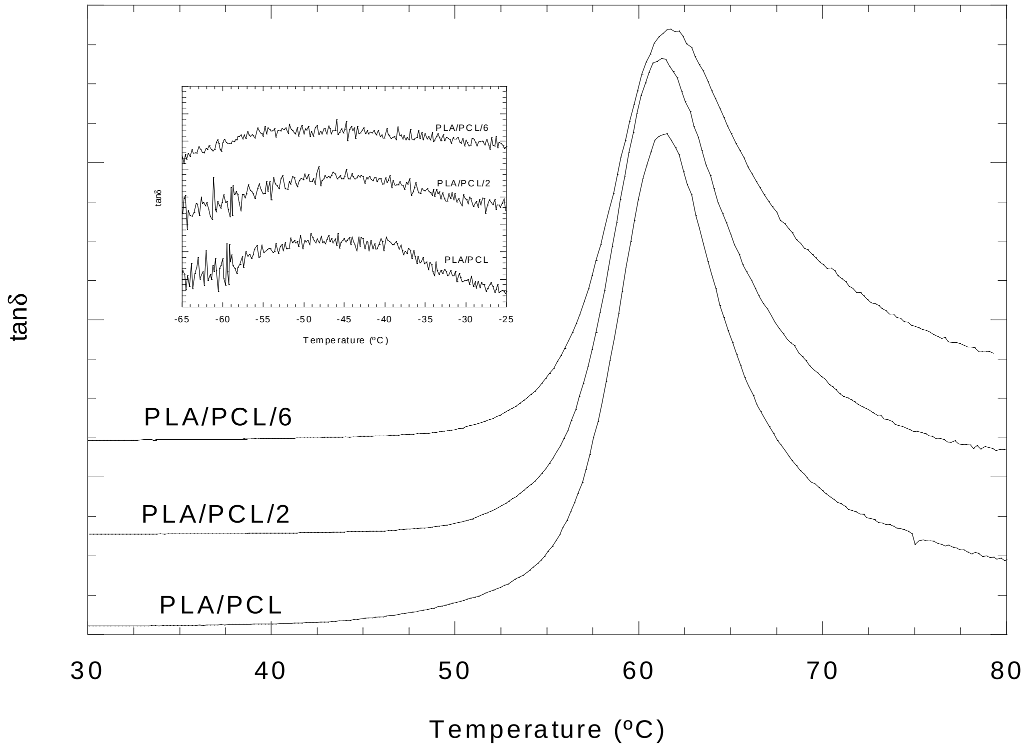

Figure 6.2.4: tanδ vs. temperature plots of the 80/20 PLA/PCL blend and of the PLA/PCL/2 and PLA/PCL/6 nanocomposites from 30ºC to 80ºC and from -65ºC to -25ºC.

Figure 6.2.5 shows the first DSC heating scans of the PLA/PCL blend, PLA/PCL/2 and PLA/PCL/4 nanocomposites, as an example. Two endothermic peaks and one exothermic peak can be observed in all the compositions, the low temperature endothermic peak shows the melting of the PCL crystalline phase and the high temperature endothermic peak indicates the melting of the PLA crystalline phase. The exothermic peak shows the cold crystallization of PLA. Table 6.2.2 summarizes the most relevant results obtained from these scans for all the PLA/PCL/CNT compositions.

As can be seen, the calorimetric behavior of PLA/PCL/CNT nanocomposites was very similar to that of the 80/20 PLA/PCL reference blend. In all the nanocomposites the melting temperatures of the PLA and PCL phases stayed similar to those of the PLA/PCL blend, 156.7ºC and 62.0ºC, respectively, indicating that the morphology of the PLA and PCL crystals did not change in the presence of CNTs. The only significant difference between the blend and the nanocomposites was the 6-10ºC increase observed in the cold crystallization temperature of the PLA phase. This would suggest that formation of crystals was hindered in the presence of CNTs, which was also reflected in the slight decrease in the degree of crystallinity shown in Table 6.2.2. However, from the point of view of the applicability of these materials, the observed differences are negligible.

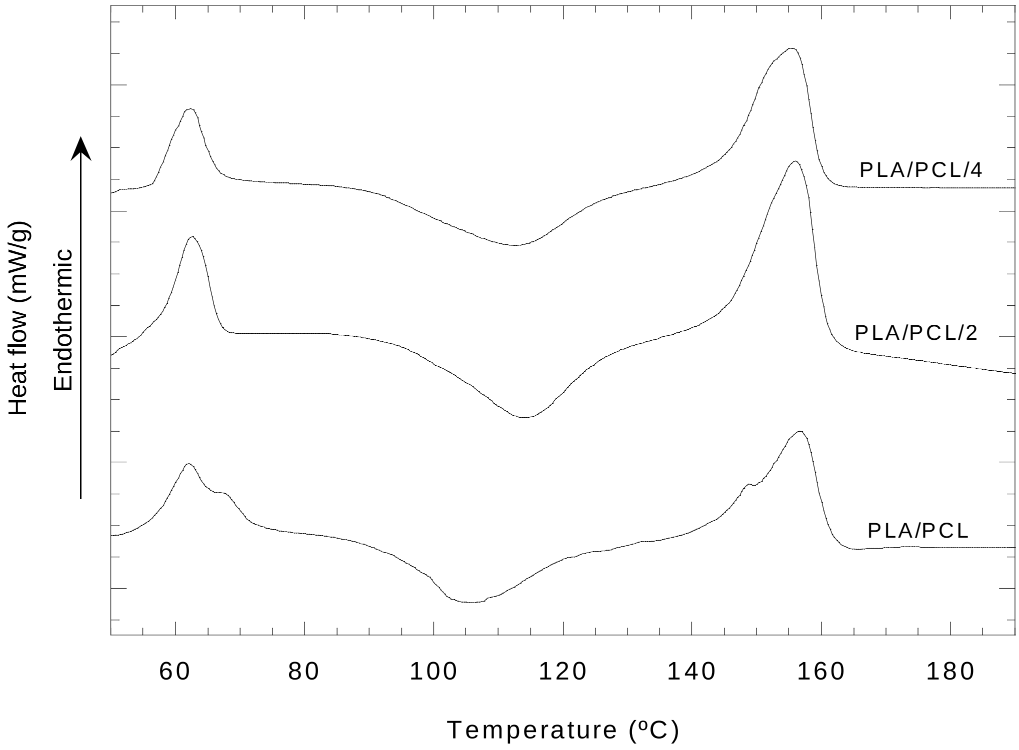

Figure 6.2.5: First DSC heating scans of the PLA/PCL 80/20 blend and of PLA/PCL/2 and PLA/PCL/4 nanocomposites.

Table 6.2.2: Melting temperatures of PLA (Tm_{PLA}) and PCL (Tm_{PCL}) and, cold crystallization temperatures (Tc_{PLA}), ΔHm-ΔHc and degrees of crystallinity (Xc) of PLA in the PLA/PCL/CNT nanocomposites.

Composition	**Tm_{PLA} (°C)**	**Tm_{PCL} (°C)**	**Tc_{PLA} (°C)**	**ΔHm-ΔHc (J/g)**	**Xc_{PLA} (%)**
PLA/PCL	156.7	62.0	104.7	3.6	4.8
PLA/PCL/1	155.7	62.7	110.0	1.3	1.8
PLA/PCL/2	156.0	62.3	114.0	1.6	2.2
PLA/PCL/3	155.7	62.7	113.6	1.2	1.6
PLA/PCL/4	155.4	62.4	112.4	2.2	3.0
PLA/PCL/6	157.4	62.1	112.4	2.1	3.0

The literature has shown that the presence of CNTs significantly affects the crystallization behavior of PCL[150,151]. In fact, CNTs are considered very efficient nucleation agents for PCL (supernucleation agents[150]) and have produced significant increases in the crystallization temperature from the melt (14-17ºC) or in the degree of crystallinity (65% increase). It has already been mentioned that the nucleation ability of CNT did not affect the melting temperature of the PCL phase in the PLA/PCL/CNT nanocomposites of this work. Moreover, the melting enthalpy of the PCL phase is not easy to analyze because it overlaps with the Tg-signal of the PLA amorphous phase which is why the crystallization of PCL during cooling in the calorimeter was studied.

Table 6.2.3 shows the crystallization temperatures of as molded PCL, and of the PCL phase in the 80/20 blend and in the different nanocomposites (cooling rate 20ºC/min). As can be seen, the crystallization temperature of PCL increased significantly from 26ºC in neat PCL and 32ºC in the PLA/PCL blend to approximately 60ºC in the PLA/PCL/CNT nanocomposites. These results confirm the aforementioned nucleation ability of the nanotubes, despite the unchanged melting behavior during the heating scan.

Table 6.2.3: Crystallization temperatures of pure PCL and of the PCL phase in the PLA/PCL blend and the PLA/PCL/CNT nanocomposites.

Composition	**Tc_{PCL} (ºC)**
Neat PCL	26.3
80/20	-16.7, 4.3, 32.3*
80/20/1	59.3
80/20/2	61.9
80/20/3	60.9
80/20/4	59.6
80/20/6	59.3

* Fractionated crystallization. The peak with the highest intensity is that centered at 32.3ºC.

6.2.4 Mechanical properties

Figure 6.2.6 shows the Young’s modulus of PLA/PCL/CNT nanocomposites vs. the true CNT content. As can be seen, the stiffness of the PLA/PCL 80/20 blend increased linearly with CNT content. For example, there were 3.7% and 7.1% increases in the PLA/PCL/2 and PLA/PCL/4 compositions, respectively. Thus, and as observed by Wu et al. for the PLA/PCL 30/70 blend[193], PCL-located nanotubes reinforced the system, counteracting the loss of stiffness produced by the presence of PCL on PLA, 15.5% at 20% contents (Chapter 4.1). None of the PLA/PCL/CNT nanocomposites in this study, even those with the highest CNT content, reached the modulus value of pure PLA, 3520±20 MPa but, even so, they showed values of over 3000 MPa, which is a favorable result from the point of their potential practical application.

Results shown in Figure 6.2.6 were compared with those reported for the binary PLA/CNT nanocomposites in Chapter 5.2 (Figure 5.2.6) and also with those reported for the ternary PLA/PCL/oMMT nanocomposites in Chapter 6.1 (Figure 6.1.9), in order to compare both the reinforcement effect of the CNTs in pure PLA and in the PLA/PCL blend, as well as the reinforcement effect produced by oMMTs and CNTs in the PLA/PCL blend, respectively.

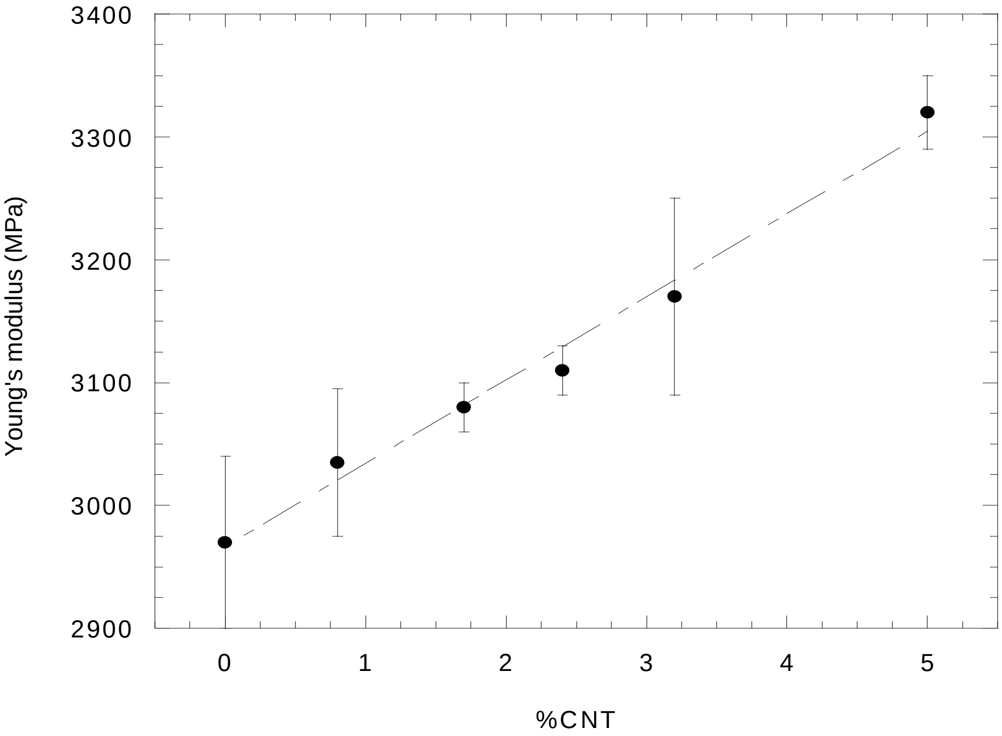

Figure 6.2.6: Young’s modulus values of PLA/PCL/CNT nanocomposites with respect to the CNT content.

Table 6.2.4 shows the increments in relative stiffness of the PLA/CNT nanocomposites in Chapter 5.2 and in the PLA/PCL/CNT nanocomposites in this chapter. As can be seen, the relative modulus increases were similar in both binary and ternary nanocomposites, eventually slightly higher in the ternary ones, given the lower true CNT content. This indicates that the reinforcing effect of the CNTs in pure PLA and in the PLA/PCL blend was similar despite the preferential PCL-location in the ternary system. This result agrees with that observed in the oMMT-containing PLA (Chapter 5.1) and PLA/PCL (Chapter 6.1) nanocomposites, and is consistent with the aforementioned similar nanoparticle dispersion in the binary and ternary systems. These results, together with those of Chapter 6.1 and those reported by Goitisolo et al. [287-289] confirm that well-dispersed minor phase located nanoparticles effectively improve the stiffness of polymer blends.

Table 6.2.4: Relative stiffness increases of PLA/CNT (Chapter 5.2) and PLA/PCL/CNT (Chapter 6.2) nanocomposites.

CNT content (%)*	PLA/CNT nanocomposites	PLA/PCL/CNT nanocomposites
1 (0.8)	1.1%	2.1%
2 (1.7)	4%	3.7%
4 (3.2)	6.5%	6.7%
6 (5)	11.1%	11.2%

*The real CNT contents in ternary PLA/PCL/CNT nanocomposites appear between brackets.

When the relative modulus increases produced by CNT and oMMT in the PLA/PCL blend are compared, the reinforcement ability of the oMMT nanoplatelets was seen to be higher than that of the CNTs. This result agrees with the findings when PLA/oMMT (Chapter 5.1) and PLA/CNT (Chapter 5.2) nanocomposites were compared and has been widely observed in the bibliography on PLA in particular[72] and on other polymers in general[290].

The yield strength values of PLA/PCL/CNT nanocomposites, whatever the CNT content, were similar to that of the reference PLA/PCL blend (~63 MPa). Therefore, in keeping with the findings on the PLA/PCL/oMMT nanocomposites of Chapter 6.1, the PCL-located nanoparticles did not increase the tensile strength of the PLA/PCL blend. The literature shows that the ability of the CNTs to improve the tensile strength of PLA/PCL blends seems to be related to the interfacial adhesion between phases and the consequent stress-transmission. This is because the presence of CNTs, not only in the PCL phase but also in the PLA/PCL interphase, leads to better stress-transmission and higher tensile strength values[193].

Figure 6.2.7 shows the elongation at break of the PLA/PCL/CNT nanocomposites vs. the real CNT content. The ductility of the PLA/PCL blend maintained in PLA/PCL/CNT nanocomposites and, as can be seen, all compositions elongated at least 130% before breaking. Given that the ductility of PCL maintains[291] or even increases in the presence of CNTs[292] and that no interfacial effects were expected in these PLA/PCL/CNT nanocomposites because no preferential location of the CNTs in the interphase was observed, the ductility of these ternary nanocomposites can be expected to present similar behavior to that of the reference PLA/PCL blend.

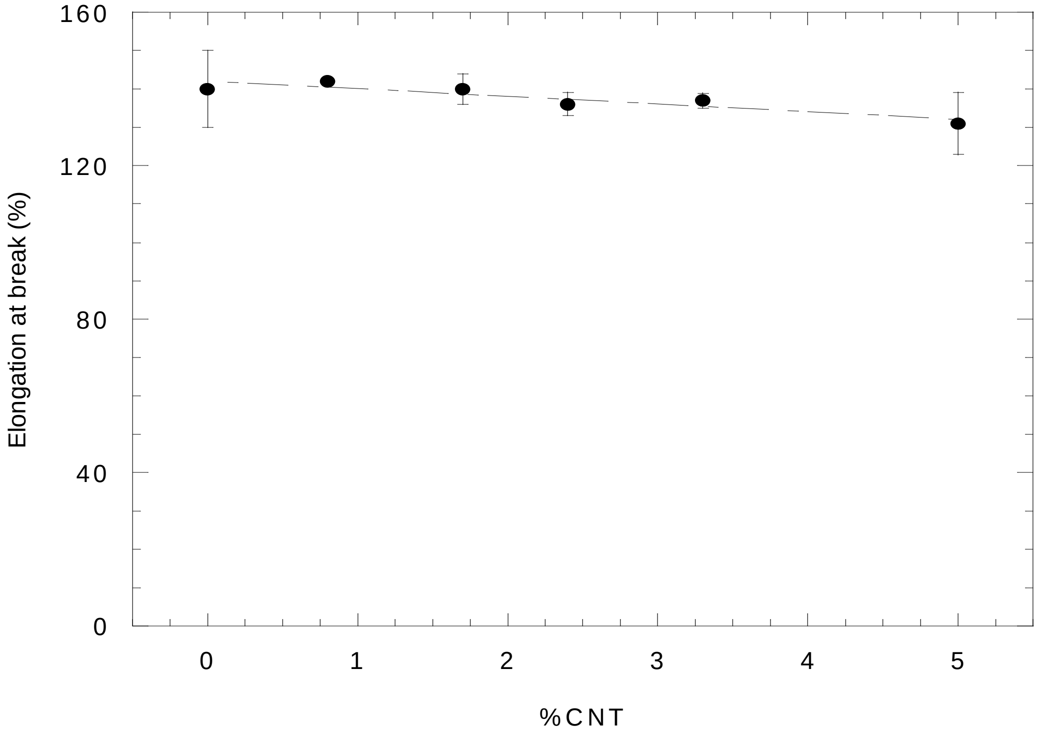

Figure 6.2.7: Elongation at break values of PLA/CNT nanocomposites with respect to the CNT content.

With respect to the impact strength and, as observed in all the PLA-based nanocomposites of the present work, the addition of CNTs to the reference PLA/PCL blend did not produce any positive effect. In fact, the impact strength of the PLA/PCL/CNT nanocomposites remained at low values (15-25 J/m) whatever the CNT content.

In summary, PLA/PCL/CNT nanocomposites show an interesting balance of mechanical properties, as they combine high deformability (>130%), with high stiffness (>3000 MPa) and strength (~63 MPa).

6.2.5 Electrical conductivity

Figure 6.2.8 shows the volume conductivity values of PLA/PCL/CNT nanocomposites vs. the real CNT content. As the figure shows, the PLA/PCL blend and PLA/PCL/1 nanocomposite were insulating materials and their conductivity was near 10^{-13} S/cm. A transition to semiconductivity was observed at higher CNT contents, with the PLA/PCL/1.5 composition showing intermediate behavior. The nanocomposites became semiconductive from the PLA/PCL/2 composition and their conductivity increased up to 10^{-5}-10^{-6} S/cm, so 10^{6}-10^{7} times higher than the insulating compositions.

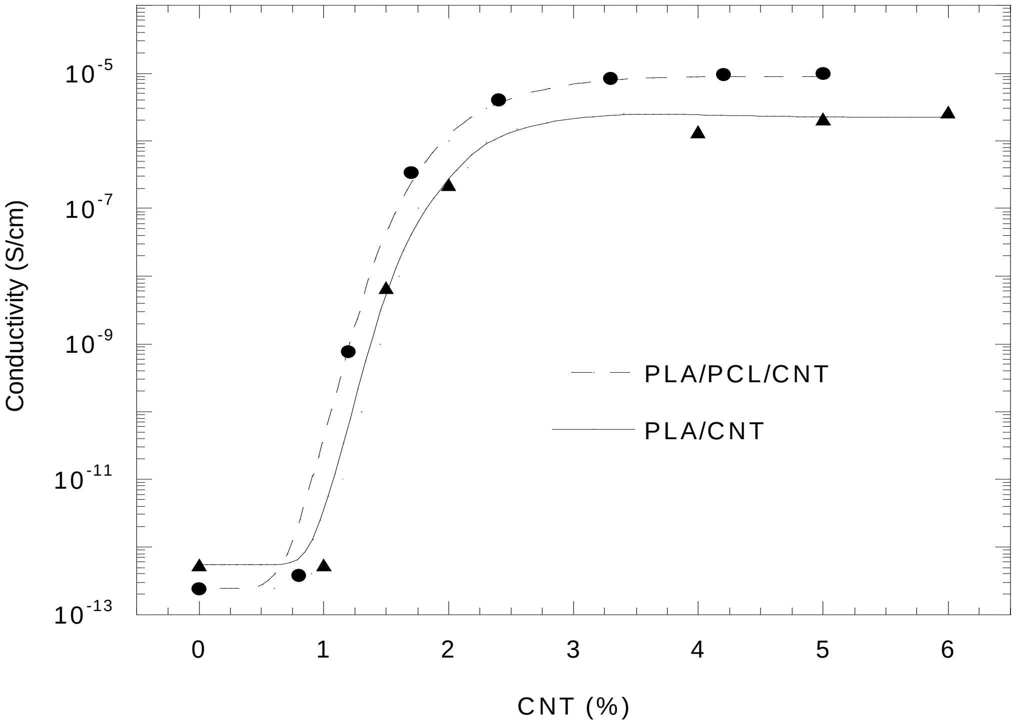

Figure 6.2.8: Volume conductivity values of PLA/PCL/CNT (●) and PLA/CNT (▲, Chapter 5.2) nanocomposites with respect to the CNT content.

The plot of conductivity vs. CNT content in Figure 6.2.8 is consistent with the G´ vs. ω behavior shown in Figure 6.2.3, where the existence of a fully percolated CNT network within the PLA/PCL blend was proposed for CNT contents of over 1.2% (the PLA/PCL/1.5 composition). TEM images of Figure 6.2.1 also pointed to this almost continuous CNT network for the PLA/PCL/2 composition and over.

Given that CNTs were selectively located in the PCL dispersed phase, the percolated structure of the nanofiller also points to an almost continuous morphology of the PCL within the PLA matrix, as has been discussed at length throughout the present chapter, and has also been shown in the TEM images of Figure 6.2.1. Again, this points to double percolation behavior[155,169,193,207,219,220] in the PLA/PCL/CNT nanocomposites.

The double percolation phenomenon has also been reported by Wu et al.[193,219] in nanocomposites based on the 30/70 PLA/PCL blend, where COOH-CNTs were located in the PCL phase and at the interphase simultaneously. Interphase-located CNTs compatibilized the blend and, therefore, increased the surface contact area between PLA and PCL and allowed a direct path for electron conductivity. Given that a PCL-rich composition was studied instead of a PLA-rich composition as in the present work, the electrical percolation threshold, 0.98%, was estimated at lower CNT contents than those observed in the present PLA/PCL/CNT nanocomposites. However, the conductivity value of $3.5x10^{-6}$ obtained at 2% CNT contents was similar to that observed in Figure 6.2.8 for the equivalent composition. Xu et al[220] analyzed the effect of the PLA/PCL ratio on the conductivity of the 1% CNT nanocomposites. All the compositions located close to the co-continuity (60/40-30/70) showed semiconductive behavior, but the PLA-rich ones (which offered the best mechanical performance) remained insulating. The extremely low CNT-content (0.025%) reported to achieve semiconductivity in a PLA/PCL 50/50 blend by Huang et al.[169] was a very interesting result and it was related to the exclusive CNT location at the interphase between components. This allowed a continuous CNT network to develop within the polymeric material with the aforementioned extremely low CNT content.

When the electrical behavior of the PLA/CNT nanocomposites of Chapter 5.2 is compared to that of the PLA/PCL/CNT nanocomposites of this chapter, similar conductivity values were observed in the semiconductive compositions. Moreover, given the lower real CNT content of the PLA/PCL-based nanocomposites with respect to the PLA-based ones, the electrical percolation threshold took place at lower CNT contents in the former. This result can be observed in Figure 6.2.8, where the curve correspondent to PLA/CNT nanocomposites has also been included for comparison purposes.

6.3 Poly(lactic acid)/Poly(butylene adipate-co-terephthalate)/Carbon nanotube (PLA/PBAT/CNT) nanocomposites

6.3.1 Nanostructure and morphology

Figure 6.3.1 shows representative TEM micrographs of PLA/PBAT 80/20 (a) and 60/40 (b) blends, and of PLA/PBAT/CNT 80/20/3 (c) and 60/40/3 (d) nanocomposites. Light and dark zones represent the PLA and PBAT phases, respectively. Figure 6.3.2 shows a 2x2 µm AFM micrograph of the 80/20/4 nanocomposite taken as an energy dissipation signal. Because of the greater stiffness of PLA as compared to PBAT, the dark area indicates the former and the light area the latter.

As can be seen in Figures 6.3.1 and 6.3.2, CNTs were located in the minor PBAT phase in the PLA/PBAT/CNT nanocomposites. This preferential location agrees with that reported by Ko et al. in previously studied PLA/PBAT/pCNT nanocomposites[221,222]. In these works, a higher affinity of CNTs to PBAT than to PLA was concluded due to this preferential location and was related to the presence of aromatic groups in the main chain of PBAT. However, this higher affinity was not experimentally tested. Table 6.3.1 shows the solid-state interfacial tension values for PLA/CNT and PBAT/CNT pairs obtained by the contact angle technique. As the table shows, the PBAT/CNT interfacial tension (3.20 mN/m) was significantly lower than that of the PLA/CNT pair (6.35 mN/m) supporting the PBAT preferential location of the CNTs in these and other previously studied PLA/PBAT blends[221,222].

Given the mixing procedure used to obtain these PLA/PBAT/CNT nanocomposites (first, extrusion to obtain the PLA/CNT binary system followed by the addition of PBAT in a second extrusion step), as in the case of the PLA/PCL/CNT nanocomposites (Chapter 6.2), the preferential location of the CNTs indicates that they migrated from the PLA phase to the PBAT phase during the second extrusion step of the melt mixing procedure. The aforementioned higher affinity of CNTs to PBAT, the higher diffusivity of CNTs through PBAT due to the favorable viscosity ratio[222] (ηPLA/ηPCL ~ 1.3) and the sufficient residence time[285] during the second extrusion step (approximately 3 min.), promoted and favored this migration process.

The level of dispersion of the CNTs in the PBAT phase appears to be related to the PLA/PBAT ratio, as can be seen in Figure 6.3.1. In the 80/20/CNT nanocomposites (6.3.1c), the CNTs appeared mainly aggregated while in the 60/40/CNT nanocomposites (6.3.1d), a significant amount of individual CNTs along with some small aggregates were observed whatever the CNT content.

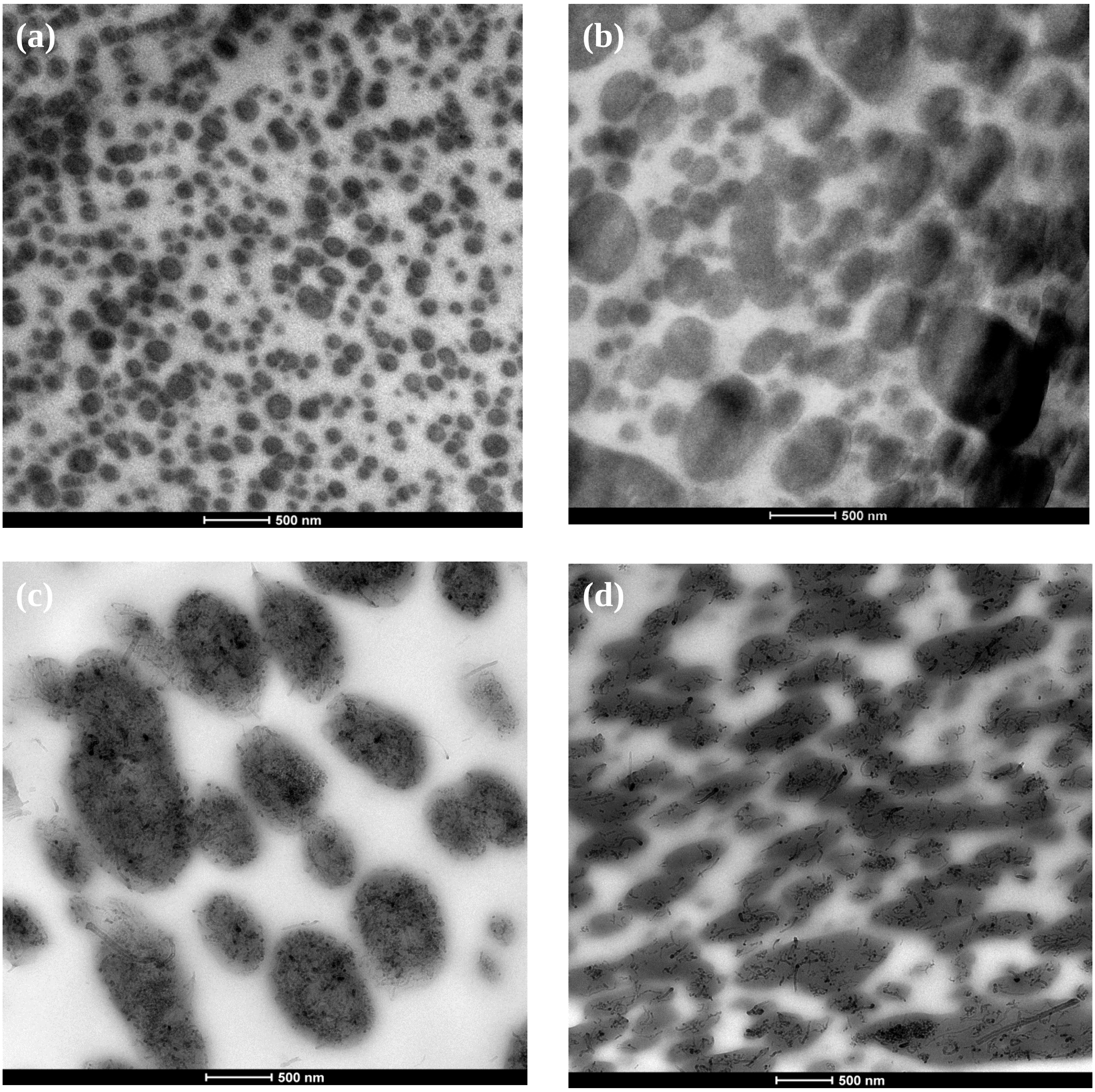

Figure 6.3.1: TEM micrographs of 80/20 (a) and 60/40 (b) blends and of 80/20/3 (c) and 60/40/3 (d) nanocomposites.

This blend composition-dependence of the dispersion level of the CNTs has also been observed in PLA/PCL/CNT nanocomposites[220] and has been related to the increased volume fraction of the CNT-preferred polymer in the blend. When the dispersion level of CNTs in these PLA/PBAT blends is compared to that of the PLA/PCL blends in Chapter 6.2, it can be inferred from Figures 6.3.1c and d that dispersion is poorer in the former than in the latter. This indicates a lower affinity of CNTs to PBAT than to PCL, which is in agreement with the interfacial tension values measured in the solid state for the PBAT/CNT and PCL/CNT pairs (3.20 mN/m and 2.65 mN/m, respectively), taken from Tables 6.3.1 and 6.2.1.

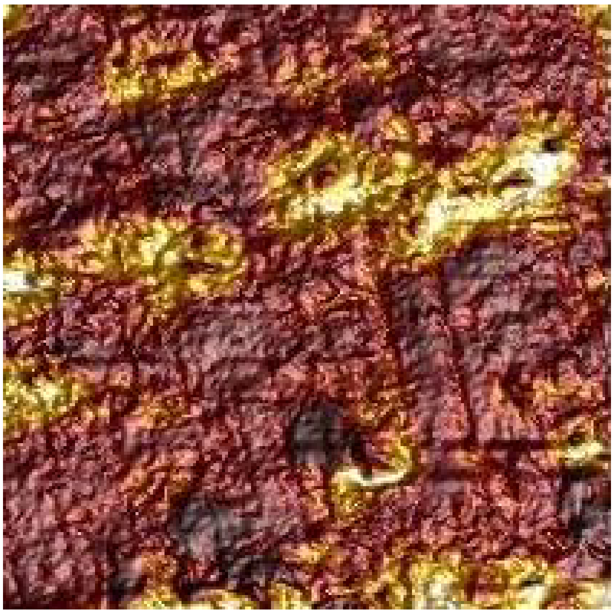

Figure 6.3.2: AFM micrograph of the 80/20/4 nanocomposite.

Figure 6.3.1 also shows that the CNT changed the morphology of the starting PLA/PBAT blend, whatever the composition. In the case of the 80/20 composition, there was a clear increase in the size of the CNT-filled PBAT dispersed particles, indicating that the increased melt viscosity of the minor phase hindered mastication by the major phase. In addition, the shape of the particles changed from almost spherical to elongated ones. These two morphological changes took place regardless of CNT content but were more pronounced at increasing CNT contents. In fact 6.3.1 shows how the 80/20/3 composition presented an almost continuous dispersed phase morphology, which will later be related to the viscoelastic and electrical behavior. This morphological change in the PLA/PBAT blend caused by the presence of CNT is similar to that described in Chapter 6.3.2 for the 80/20 PLA/PCL blend.

With respect to the 60/40 PLA/PBAT composition, the CNT-free reference blend was already close to the phase inversion composition. This is reflected in Figure 6.3.1b and was seen previously in Chapter 4.2 (Figure 4.2.4). Figure 6.3.1d shows how the presence of CNT assisted the development of full continuity of the PBAT phase in the 60/40/3 composition. This also happened in the ternary 60/40/CNT nanocomposites containing any other amount of CNT.

Table 6.3.1: PLA/CNT and PBAT/CNT interfacial tension values measured in the solid-state.

Pair	**Interfacial tension (mN/m)**
PLA/CNT	6.35
PBAT/CNT	3.20

6.3.2 Viscoelasticity

Figure 6.3.3 shows the storage modulus (G´) vs. angular frequency (ω) plots for the 80/20/CNT (6.3.3a) and 60/40/CNT (6.3.3b) nanocomposites with different CNT contents. When the behavior of each composition is individually studied, the storage modulus is seen to increase as the CNT content increases. This is caused by the melt reinforcement effect of the nanofiller and is also reported for both the pure PLA in Chapter 5.2 and the 80/20 PLA/PCL blend in Chapter 6.2.

When the 80/20 and 60/40 compositions are compared, it is noteworthy that solid-like behavior (plateau at the terminal flow zone) was observed in both cases for the equivalent PLA/PBAT/3 composition. This result corresponds to a lower true content of CNT in the 60/40 composition (1.8%) than in the 80/20 composition (2.4%). The rheological percolation of the filler took place at these CNT contents. However, Figure 6.3.3 also shows how, at lower CNT contents, the relative increase in G´ in the terminal flow zone was significantly higher in the 60/40 composition than in the 80/20 composition, even when the initial value of the unfilled composition was also higher and the real content of CNT was lower in the 60/40 composition. This enhanced reinforcement ability of the nanofiller at these low CNT contents should be related to the only structural difference between both compositions, i.e. the morphology of the dispersed phase, where the CNTs are preferentially located, which is co-continuous in the 60/40/CNT nanocomposites but “sea-island” type in the 80/20/CNT nanocomposites at these CNT contents[286].

The results shown in Figure 6.3.3b also indicate that the development of a continuous morphology of the minor phase within the major one, even when the CNTs are preferentially located in the former, is not enough to obtain rheological (and most likely electrical) percolation. This is beacuse the 60/40/1 and 60/40/2 compositions showed co-continuous morphologies but still liquid-like rheological behavior.

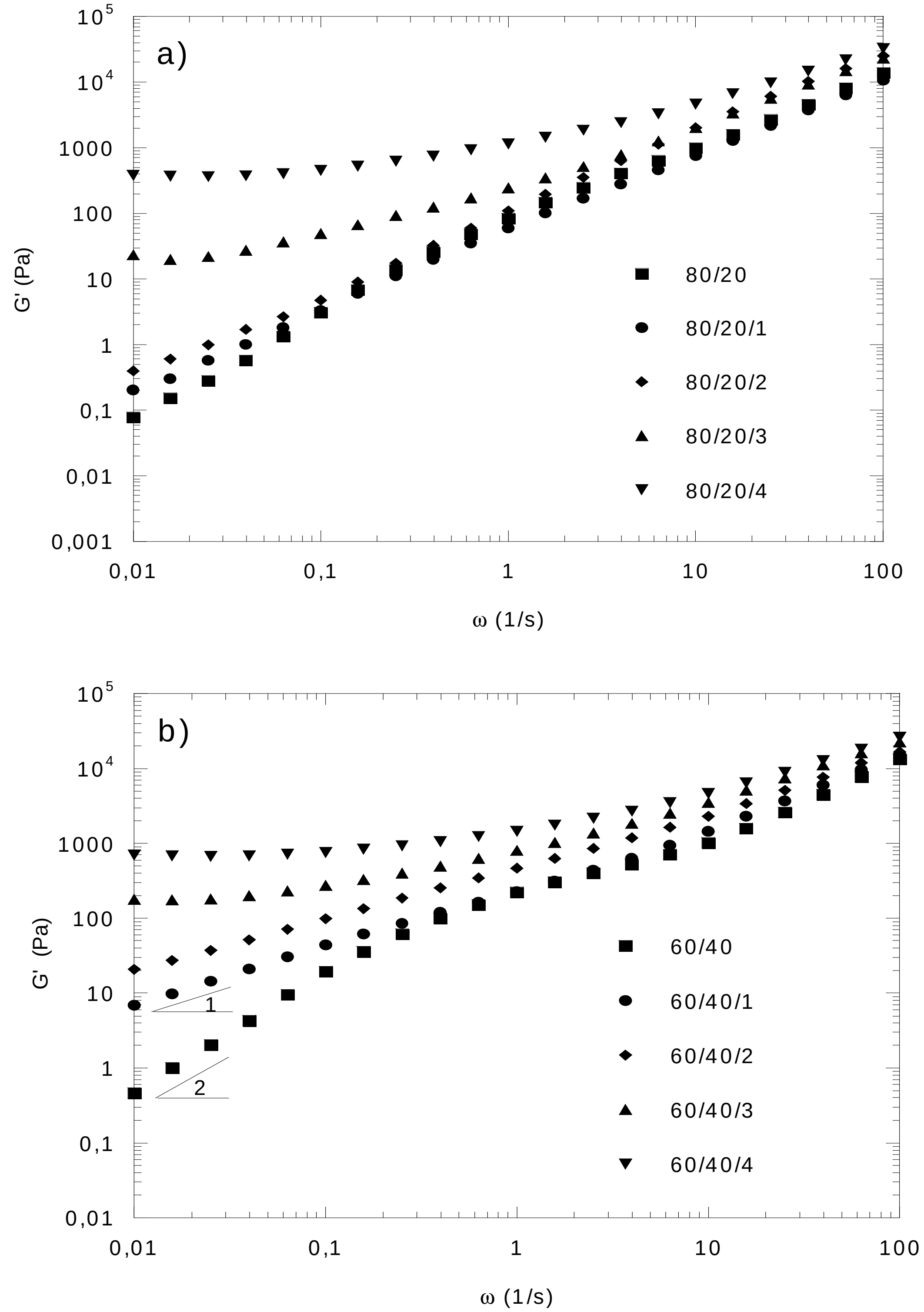

Figure 6.3.3: G´ vs. ω plots of 80/20 and 60/40 blends and of 80/20/CNT (a) and 60/40/CNT (b) nanocomposites.

However, in the 80/20/CNT nanocomposites, the minimum CNT content necessary to create a continuous dispersed phase was enough to achieve percolation of the filler (Figure 6.3.3a), so the development of a continuous morphology simultaneously gave rise to the solid-like behavior.

When the viscoelastic behavior of PLA(80)/PBAT(20)/CNT (in the present chapter) and that of the PLA/PCL/CNT (in Chapter 6.2) nanocomposites is compared, G´ increases in the terminal flow zone of the non-percolated nanocomposites are less significant in this chapter, and the percolation concentration takes place at higher CNT contents (2.4% with PBAT vs. 1.7% with PCL). This suggests a poorer dispersion of the CNTs in the PLA/PBAT blend than in the PLA/PCL blend, as discussed in the previous section.

6.3.3 Phase structure

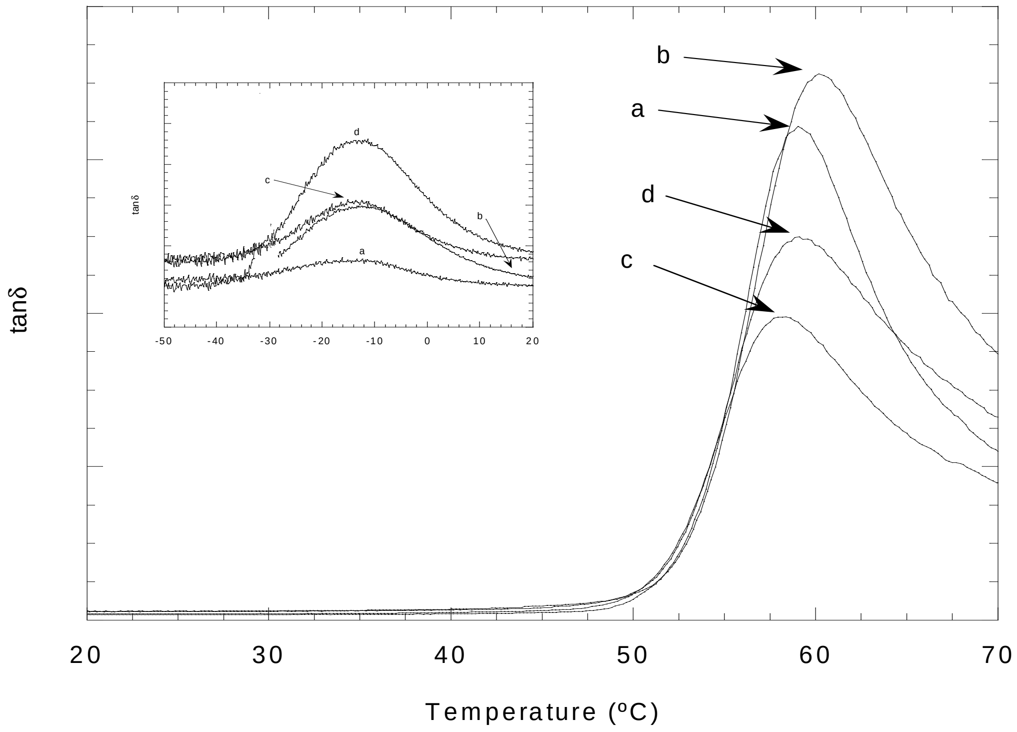

Figure 6.3.4: tanδ vs. temperature plots of the 80/20 (a) and 60/40 (c) blends and of the 80/20/5 (b) and 60/40/5 (d) nanocomposites from 0ºC to 80ºC and from -50ºC to 20ºC.

Figure 6.3.4 shows the tanδ vs. temperature plots of the 80/20 (a) and 60/40 (c) PLA/PBAT blends, and 80/20/5 (b) and 60/40/5 (d) PLA/PBAT/CNT nanocomposites, as an example. All the compositions showed two tanδ signals, marking the α-transitions of the PLA phase (high temperature peak) and the PBAT phase (low temperature peak). The position of the latter did not change in the nanocomposites with respect to the PLA/PBAT reference blends, indicating that the presence of CNTs did not influence the mobility of this phase.

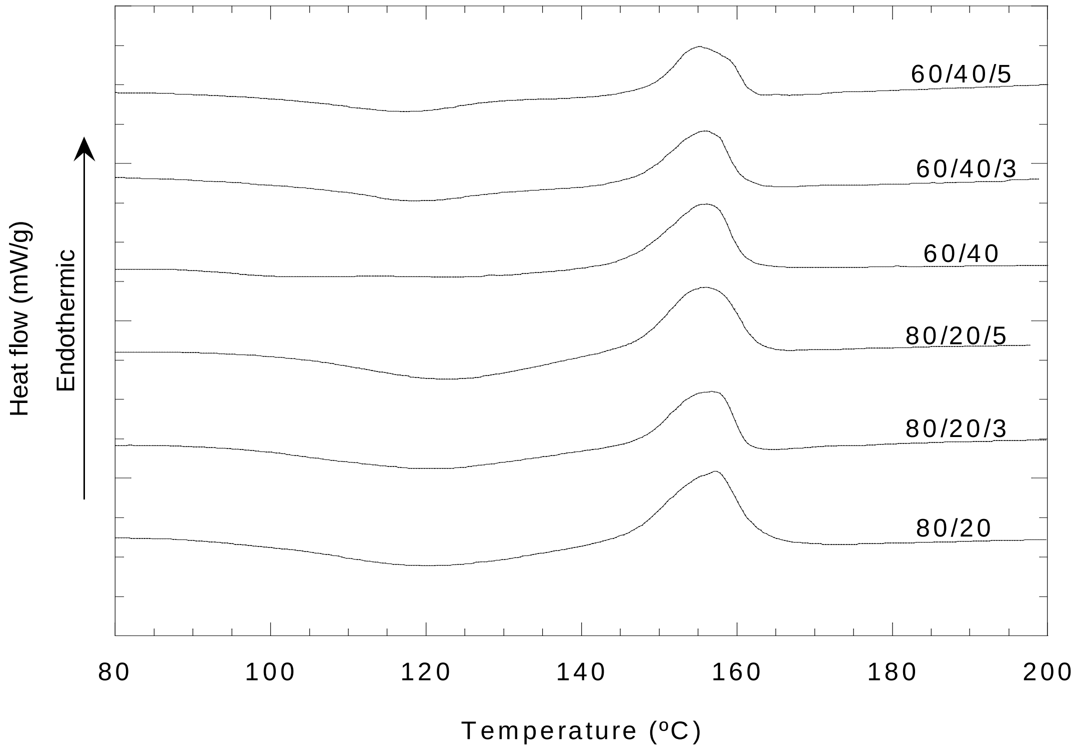

Figure 6.3.5: First DSC heating scans of 80/20 and 60/40 blends and of 80/20/3, 80/20/5, 60/40/3 and 60/40/5 nanocomposites.

The PLA-phase related peak located approximately at the position of pure PLA and its position shifted to slightly higher temperatures in the PLA/PBAT/CNT nanocomposites. This indicates that the partial miscibility of PBAT in PLA that led to a decrease in the temperature of the PLA peak was either counteracted by a second effect or simply disappeared in the presence of CNTs. Given that these Tg shifts were 1-2ºC, no further investigation was followed in this direction but, taking into account the affinity of PBAT to nanotubes and the coarsening of the morphology of the PBAT phase, full immiscibility between PLA and PBAT in the presence of nanotubes is proposed. In addition, Figure 6.3.4 shows that the intensities of the PLA-corresponding peaks increased from PLA/PBAT blends to PLA/PBAT/CNT nanocomposites, pointing to a decrease in the crystallinity of PLA when the PBAT phase contains nanotubes. This effect was further investigated by DSC.

Figure 6.3.5 shows calorimetric plots corresponding to the first heating scans of the 80/20 and 60/40 PLA/PBAT blends, and 80/20/3, 80/20/5, 60/40/3 and 60/40/5 PLA/PBAT/CNT nanocomposites. One endothermic peak, indicating the melting temperature of the crystalline PLA phase, and one exothermic peak, showing its cold crystallization process were observed. The melting peak of PBAT overlapped with the cold crystallization exotherm of PLA but, due to its low intensity and as reported in Chapter 4.2, the position and the area under the peak of the exotherm were taken to be the cold crystallization of PLA. Table 6.3.2 summarizes results of the melting temperature and degree of crystallinity taken from the first heating scans for all compositions. As can be seen, the melting temperature remained constant whatever the CNT content in both the 80/20 and 60/40-based nanocomposites, indicating that the presence of CNTs in the PBAT phase, or the morphological change they caused, did not modify the crystalline perfection of PLA.

Table 6.3.2: Melting (Tm) temperatures and degrees of crystallinity (Xc) of PLA in 80/20 and 60/40 PLA/PBAT blends and in PLA/PBAT/CNT nanocomposites.

Composition	**Tm (ºC)**	**Xc PLA (%)**	**Composition**	**Tm (ºC)**	**Xc PLA (%)**
80/20	156.7	15	60/40	155.1	13.5
80/20/1	155.7	6.7	60/40/1	158.1	6.2
80/20/2	157.1	6.4	60/40/2	156.7	3.5
80/20/3	156.7	2.2	60/40/3	156.7	3.1
80/20/4	156.7	1.1	60/40/4	155.7	4.4
80/20/5	158.0	1.3	60/40/5	155.1	3.8

Table 6.3.2 also shows how, even at the lowest CNT contents, the degree of crystallinity of the PLA phase decreased sharply from the reference blends to the ternary nanocomposites, while, at increasing CNT contents, the decrease was more gradual. This indicates that the presence of CNTs somehow counteracted the nucleation ability of the PBAT dispersed phase on the crystallization of PLA, as stated in Chapter 4.2 for unfilled PLA/PBAT blends. Given the preferential PBAT location of the CNTs and the fact that the crystallization of the PLA phase may not be affected, this effect could be related either to the absence of PBAT in the PLA phase,

due to the previously proposed full immiscibility of PLA and PBAT in the ternary nanocomposites or the change in the morphology induced by the CNTs. The very finely dispersed "sea-island" morphology of the 80/20 composition seen in Figures 4.2.4b and 6.3.1a evolved into the coarse and elongated almost continuous morphology of the 80/20/3 composition in Figure 6.3.1c.

6.3.4 Mechanical properties

Table 6.3.3 shows the Young's modulus, yield strength and elongation at break values of the 80/20 and 60/40 PLA/PBAT blends and of the 80/20/3, 80/20/5, 60/40/3 and 60/40/5 nanocomposites, as an example.

The table reflects how the stiffness of the PLA/PBAT blends barely increased whatever the CNT content. Although usually not as efficient as oMMT nanoparticles, CNTs have been known to significantly reinforce polymeric matrices (see previous chapters) thanks to their high anisotropy and contact area. However, when dispersion level of the nanotubes is poor, the reinforcement effect of CNTs can be drastically reduced, as demonstrated in HDPE/PE-g-SWCNT[293] and PMMA/MWCNT[294] nanocomposites. The dispersion level of CNTs in the PLA/PBAT/CNT nanocomposites, as previously stated by means of viscoelastic measurements, is poorer than in both the PLA/CNT nanocomposites (Chapter 5.2) and also than in PLA/PCL/CNT nanocomposites (Chapter 6.2), where modulus increases of up to 10% with the highest CNT content were recorded. In addition, the significant decrease in the degree of crystallinity of the PLA phase from the PLA/PBAT blends to the PLA/PBAT/CNT nanocomposites could also help to explain the lower reinforcement observed[295,296].

Unlike the PLA/CNT and PLA/PCL/CNT nanocomposites in Chapters 5.2 and 6.2, where the yield strength remained similar to that of the unfilled matrix, the yield strength of these PLA/PBAT/CNT nanocomposites decreased considerably in both the 80/20 and the 60/40-based nanocomposites, as Table 6.3.3 shows. The relative decreases reached approximately 20% for the nanocomposite with most CNT. The literature generally states that the factors affecting Young's modulus can also explain the behavior of the yield strength[297] and it is indeed true that poor dispersion of the CNTs and a lower degree of crystallinity in the major phase should worsen the yield strength values of the PLA/PBAT/CNT nanocomposites. However, the morphological change caused by the CNT could also help to explain this unfavorable behavior. This is because, at the strain values at which yielding happens, the presence of an almost continuous rubber phase could allow the whole material to yield at significantly lower strengths than the material with a “sea-island” morphology, and consequent continuous stiff matrix[297].

Finally, with respect to the ductility of PLA/PBAT/CNT nanocomposites, Table 6.3.3 shows how the high elongation at break of the 80/20 and 60/40 PLA/PBAT blends maintained and all the compositions elongated more than 150% before breaking. This behavior, similar to that observed for the PLA/PCL/CNT nanocomposites in Chapter 6.2, is related to the selective location of nanotubes in the PBAT phase. The ductile behavior of pure PBAT must have maintained in the presence of CNTs[153] and, the lack of interphase-located CNTs still allowed an effective stress-transfer between the PLA and PBAT/CNT phases.

Table 6.3.3: Young’s modulus, yield strength and elongation at break values for the 80/20 and 60/40 blends and the 80/20/3, 80/20/5, 60/40/3 and 60/40/5 nanocomposites.

Composition	Young’s modulus (MPa)	Yield strength (MPa)	Elongation at break (%)
80/20/0	2940±20	60.7±0.7	153±8
80/20/3	2950±40	49.3±1.3	153±8
80/20/5	2980±70	48.8±1.1	156±11
60/40/0	2180±60	44±0.5	190±11
60/40/3	2200±20	37.1±1.3	156±8
60/40/5	2210±50	35.0±0.9	153±11

Figure 6.3.6 shows the impact strength of 80/20/CNT and 60/40/CNT nanocomposites with respect to the CNT content. As can be seen, the impact strength of the 80/20 and 60/40 PLA/PBAT reference blends, 23.4±4 J/m and 106.7±7.6 J/m, respectively, increased in the presence of CNT. In the case of the 80/20/CNT nanocomposites, the maximum value obtained was 65.8±3.8 J/m for the 80/20/5 composition. This increase involved an improvement of 180% with respect to the PLA/PBAT blend and was more than 400% better than the pure PLA. However, the most noteworthy results were those of the 60/40/CNT nanocomposites. The impact strength of the 60/40 blend increased to at least 195±20 J/m in the 60/40/3 composition, and a maximum value of 270±13 J/m was obtained in the 60/40/5 composition. Although still far from supertoughness, this impact strength was 2.5 times higher than the 60/40 PLA/PBAT blend and 22 times higher the pure PLA.

To gain further insight into these positive impact strength results, cryogenically fractured impact specimens of 80/20 (a) and 60/40 (b) PLA/PBAT blends and 80/20/5 (c) and 60/40/5 (d) nanocomposites were observed by SEM. Representative micrographs are shown in Figure 6.3.7. In all cases, the phase separation between PLA and PBAT can be seen and the presence of CNTs in PBAT in the 80/20/5 (6.3.7c) and 60/40/5 (6.3.7d) compositions can also be clearly observed. Moreover, as previously shown by TEM (Figure 6.3.1) and AFM (Figure 6.3.2) and widely discussed in this chapter, the micrographs show how the sea-island type morphology of the 80/20 composition (6.3.7a) and the close to phase inversion of the 60/40 composition (6.3.7b) became almost co-continuous in the presence of PBAT-located CNTs.

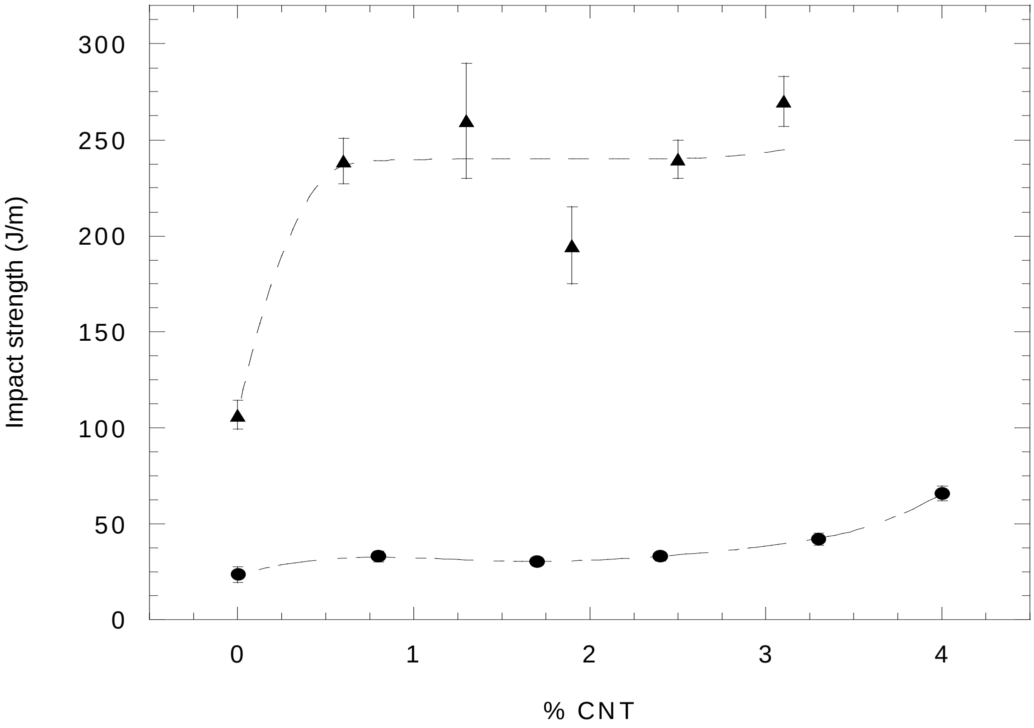

Figure 6.3.6: Impact strength values of 80/20/CNT (●) and of the 60/40/CNT (▲) nanocomposites with respect to the CNT content.

These morphological changes could explain the impact strength behavior observed in Figure 6.3.6, according to previous results obtained by Odent et al. for 90/10 PLA/(PCL-co-PLA) blends modified with silica nanoparticles[171] and by Xiu et al. for 85/15 PLA/PU blends modified with carbon black[209] and hydrophilic silica nanoparticles[175]. In these three studies, nanoparticles also modified the morphology of the minor elastomeric phase from discrete particles to a continuous phase, and as a result, the impact strength of the blends increased dramatically. Odent et al.[171] mentioned that the resulting “infinite” networks afford a more efficient toughening mechanism compared to the individually dispersed nodules. Xiu et al., meanwhile, suggested that the PU continuous network could act as a path for the propagation of the plastic deformation required for effective energy dissipation[175] and/or that shear banding of PLA at the interphase was favored[209], as a result of the greater volume fraction of filled PU.

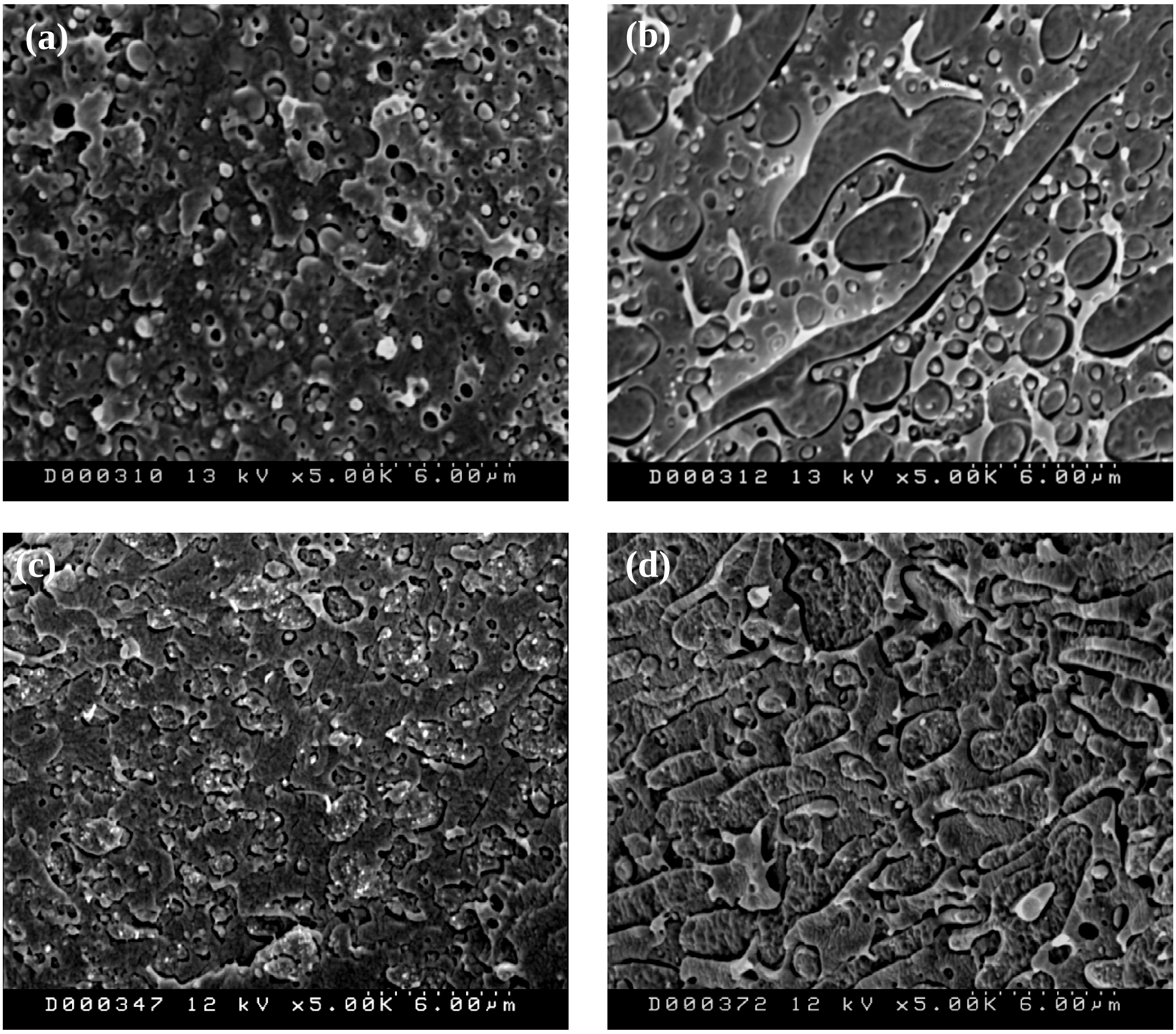

Figure 6.3.7: SEM micrographs of cryogenically fractured surfaces of impact specimens of 80/20 (a) and 60/40 (b) blends and of 80/20/5 (c) and 60/40/5 (d) nanocomposites.

The more favorable behavior of the 60/40/CNT nanocomposites when compared to the 80/20/CNT nanocomposites is probably related to the proximity of the reference 60/40 PLA/PBAT blend to the phase inversion, which already favors co-continuity, and to the initial impact strength value of this composition, not far from the fragile-ductile transition, where any parameter affecting toughness can give rise to large increases in impact strength[60].

In summary, the poor low-deformation mechanical behavior of these PLA/PBAT/CNT nanocomposites was at least compensated by high deformability. Moreover, the impact strength of the nanocomposites, unlike that observed in the PLA/PCL/oMMT (Chapter 6.1) and PLA/PCL/CNT (Chapter 6.2) nanocomposites, showed remarkable improvements when CNTs were added, particularly in the case of the 60/40/CNT nanocomposites.

6.3.5 Electrical conductivity

Figure 6.3.8 shows the volume conductivity values of the 80/20/CNT and 60/40/CNT nanocomposites vs. CNT content. Unfilled PLA/PBAT blends and the 80/20/1 and 60/40/1 nanocomposites were insulating materials. A transition to semiconductivity was observed at higher CNT contents, with the 80/20/2 and 60/40/2 (1.7% and 1.2% real CNT content) showing intermediate behavior. From the 80/20/3 and 60/40/3 (2.4% and 1.8% real CNT content) to higher CNT content levels, conductivity values similar to the PLA/CNT nanocomposites (Chapter 5.2) were observed, independent of the PLA/PBAT composition.

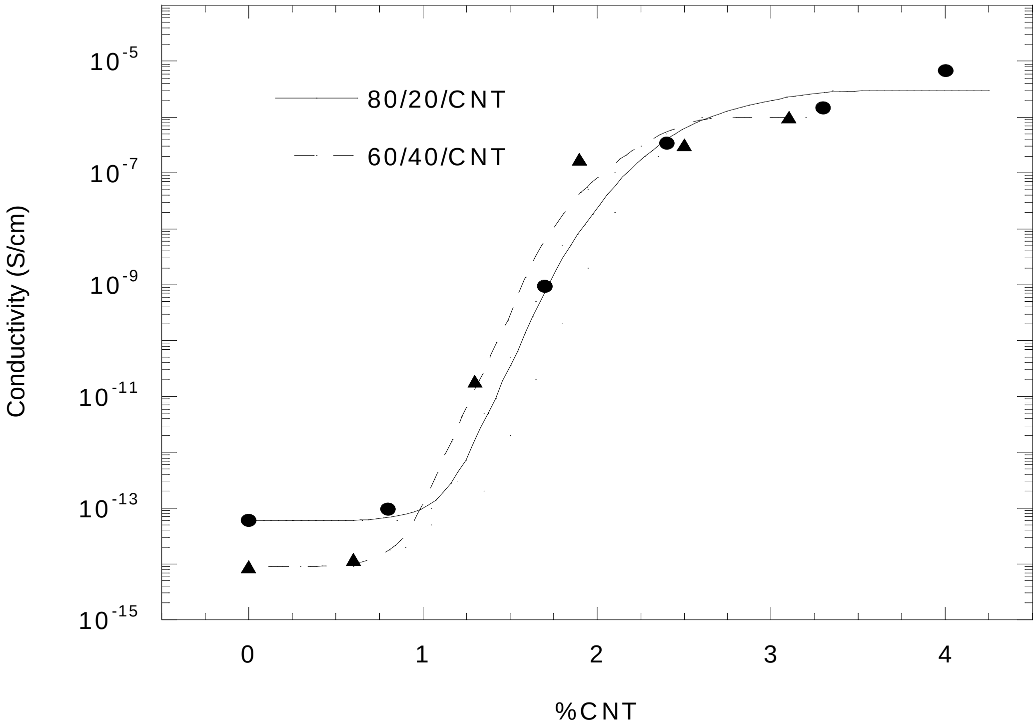

Figure 6.3.8: Volume conductivity values of the 80/20/CNT (●) and 60/40/CNT (▲) nanocomposites with respect to the CNT content.

This electrical behavior is consistent with the viscoelastic properties shown in Chapter 6.3.2. This is because the solid-like behavior in the terminal flow zone, which is related to the percolation of the filler, was observed from the 80/20/3 and the 60/40/3 composition on to higher CNT contents (Figure 6.3.3). Since the true CNT content is not the same for both compositions, the curve of the 60/40/CNT nanocomposites showed a slightly lower electrical percolation threshold than that of the 80/20/CNT system. The development of a continuous PBAT morphology, where CNTs are located within the PLA matrix appears to be the key to turning PLA/PBAT/CNT nanocomposites into semiconductive materials, as in the case of PLA/PCL/CNT nanocomposites in Chapter 6.2. When this behavior is compared with that of the binary PLA/CNT nanocomposites in Chapter 5.2, the transition to conductivity is seen to have taken place at similar CNT contents and when this comparison is extended to the ternary PLA/PCL/CNT system in Chapter 6.2, it is noteworthy that, due to the double percolation effect described there, the recorded decrease in the minimum CNT content necessary to achieve semiconductivity was not observed here in either the 80/20/CNT or in the 60/40/CNT nanocomposites. This is probably due to the dispersion level of the nanotubes in these PLA/PBAT nanocomposites, which is poorer than in the PLA/PCL ones, as suggested by TEM and confirmed by the viscoelastic properties.

Chapter 7: Conclusions

CHAPTER 7: CONCLUSIONS

1) The balance of properties in today's most promising biopolymer, PLA, was further enhanced by the addition of a second polymer and/or nanoparticle, without harming the bionature of the system in any way. The all-important mechanical behavior and/or other specific properties were modified in different ways depending on the second/third component added:

a) Mechanical behavior: The addition of PCL or PBAT to PLA produced either fully immiscible or very limited partially miscible, compatible blends. The low-strain mechanical properties were slightly poorer but maintained significantly high values while the deformation at break increased considerably, even at low PCL or PBAT contents, with the PLA being brittle and the blends highly deformable.

b) Mechanical behavior + gas barrier behavior: The addition of oMMT nanoparticles to both pure PLA and PLA/PCL blends produced new materials with enhanced mechanical and barrier properties. Young's modulus increased and permeability to oxygen decreased with respect to the reference material and even to pure PLA in the case of the PLA/PCL/oMMT nanocomposites. The presence of the oMMT particles worsened the deformability of the material but, in the case of the PLA/PCL-based nanocomposites the ductility maintained over 80% at 5% oMMT contents.

c) Mechanical behavior + electrical behavior: The addition of CNTs to pure PLA and both PLA/PCL and PLA/PBAT blends produced new materials showing interesting mechanical balance and semiconductivity. The PLA showed increases in Young's modulus and semiconductivity from 2% CNT on, while large-strain mechanical properties deteriorated. In PLA/PCL blends the addition of CNTs helped to compensate the decrease in rigidity caused by the presence of PCL. It also made the blend semiconductive at lower CNT contents than pure PLA and did not hinder the high ductility of the reference material. In the case of PLA/PBAT blends, the increases in Young's modulus were lower and the yield strength decreased, but the ductility remained the same and the impact strength increased.

2) The addition of two different nanoparticles to pure PLA and to binary PLA/PCL and PLA/PBAT blends has helped to better understand their different behavior and, in the case of ternary nanocomposites their preferent location and the morphology changes that they produce:

a) When both are equally well dispersed, CNTs show lower rheological percolation concentration than oMMTs, indicating the superior network ability of the CNTs over oMMTs. However, oMMT nanoplatelets are much more efficient from a mechanical point of view.

b) Low residence times during melt-mixing and favorable kinetic conditions can lead to a nanoparticle location in contravention of the rules of thermodynamics. This effect was observed in the PLA/PCL/oMMT nanocomposites. However, extended residence times favor the migration of the nanoparticles to the thermodynamically favored phase, as observed in the case of the PLA/PCL/CNT and PLA/PBAT/CNT nanocomposites. This points to the melt-mixing procedure as a design-parameter to be taken into consideration when aiming to develop a specific nanostructure.

c) Morphological changes with respect to the reference binary blends, from sea-island to almost co-continuous, and double percolation effects have been observed in PLA/PCL/oMMT, PLA/PCL/CNT and PLA/PBAT/CNT nanocomposites. With oMMT, the minor phase became continuous at lower contents than the nanoclay percolation concentration. With CNTs, the phase development depended on the blend composition. At low minor polymeric phase contents (20%), continuity was ruled by the dispersion of CNTs, and both the filler and the dispersed phase percolated at the same CNT content. Since the reference blend was already close to the phase inversion composition, at higher minor polymeric phase contents (40%), the minor phase became continuous at lower contents than the CNT percolation concentration.

d) The performance of ternary nanocomposites with minor phase located CNTs is directly related to the dispersion of the nanoparticles. The better the dispersion, the easier it is for continuous dispersed phase morphologies and CNT percolation to be obtained. In addition, better dispersed CNTs produce larger increments in stiffness.

Chapter 8: Bibliography

CHAPTER 8: BIBLIOGRAPHY

1. Garlotta, D., Journal of Polymers and the Environment *9*, 63 (**2001**).
2. Mehta, R.; Kumar, V.; Bhunia, H.; Upadhyay, S. N., Journal of Macromolecular Science-Polymer Reviews *C45*, 325 (**2005**).
3. Tokiwa, Y.; Calabia, B. P., Applied Microbiology and Biotechnology *72*, 244 (**2006**).
4. Lim, L. T.; Auras, R.; Rubino, M., Progress in Polymer Science *33*, 820 (**2008**).
5. Gupta, A. P.; Kumar, V., European Polymer Journal *43*, 4053 (**2007**).
6. Rasal, R. M.; Janorkar, A. V.; Hirt, D. E., Progress in Polymer Science *35*, 338 (**2010**).
7. Nampoothiri, K. M.; Nair, N. R.; John, R. P., Bioresource Technology *101*, 8493 (**2010**).
8. Harris, A. M.; Lee, E. C., Journal of Applied Polymer Science *107*, 2246 (**2008**).
9. Saeidlou, S.; Huneault, M. A.; Li, H.; Park, C. B., Progress in Polymer Science *37*, 1657 (**2012**).
10. Tang, H.; Chen, J. B.; Wang, Y.; Xu, J. Z.; Hsiao, B. S.; Zhong, G. J.; Li, Z. M., Biomacromolecules *13*, 3858 (**2012**).
11. Odent, J.; Leclere, P.; Raquez, J.-M.; Dubois, P., European Polymer Journal *49*, 914 (**2013**).
12. Xiao, H.; Lu, W.; Yeh, J.-T., Journal of Applied Polymer Science *113*, 112 (**2009**).
13. Li, H.; Huneault, M. A., Polymer *48*, 6855 (**2007**).
14. Anderson, K. S.; Schreck, K. M.; Hillmyer, M. A., Polymer Reviews *48*, 85 (**2008**).
15. G. Kfoury, J.-M. R., F. Hassouna, J. Odent, V. Toniazzo, D. Ruch, P. Dubois, Frontiers in Chemistry *1*, 1 (**2013**).
16. Di Lorenzo, M. L.; Rubino, P.; Cocca, M., European Polymer Journal *49*, 3309 (**2013**).
17. Wang, Y.; Chiao, S. M.; Hung, T. F.; Yang, S. Y., Journal of Applied Polymer Science *125*, 402 (**2012**).
18. Vu Thanh, P.; Coltelli, M.-B.; Cinelli, P.; Cifelli, M.; Verstichel, S.; Lazzeri, A., Polymer *55*, 4498 (**2014**).
19. Harris, A. M.; Lee, E. C., Journal of Applied Polymer Science *128*, 2136 (**2013**).
20. Feng, F.; Ye, L., Journal of Macromolecular Science Part B-Physics *49*, 1117 (**2010**).
21. Zhang, W.; Chen, L.; Zhang, Y., Polymer *50*, 1311 (**2009**).
22. Zhang, W.; Liu, S.; Liu, J.; Zhang, Y., 2008 International Symposium on Fiber Based Scaffolds for Tissue Engineering, Proceedings, 165 (**2008**).
23. Oyama, H. I., Polymer *50*, 747 (**2009**).
24. Jiang, J.; Su, L.; Zhang, K.; Wu, G., Journal of Applied Polymer Science *128*, 3993 (**2013**).
25. Anderson, K. S.; Lim, S. H.; Hillmyer, M. A., Journal of Applied Polymer Science *89*, 3757 (**2003**).
26. Hashima, K.; Nishitsuji, S.; Inoue, T., Polymer *51*, 3934 (**2010**).
27. Li, D. D.; Shentu, B. X.; Weng, Z. X., Journal of Macromolecular Science Part B-Physics *50*, 2050 (**2011**).
28. Pai, F. C.; Chu, H. H.; Lai, S. M., Journal of Polymer Engineering *31*, 463 (**2011**).
29. Ho, C. H.; Wang, C. H.; Lin, C. I.; Lee, Y. D., Polymer *49*, 3902 (**2008**).
30. Feng, Y. L.; Yin, J. H.; Jiang, W.; Zhao, G. Y., Chemical Journal of Chinese Universities-Chinese *33*, 400 (**2012**).
31. Feng, Y.; Hu, Y.; Yin, J.; Zhao, G.; Jiang, W., Polymer Engineering and Science *53*, 389 (**2013**).

32. Vroman, I.; Tighzert, L., Materials *2*, 307 (**2009**).
33. Babu, R.; O'Connor, K.; Seeram, R., Progress in Biomaterials *2*, 1 (**2013**).
34. Huneault, M. A.; Li, H., Polymer *48*, 270 (**2007**).
35. Wang, N.; Yu, J.; Ma, X., Polymer Composites *29*, 551 (**2008**).
36. Stoclet, G.; Seguela, R.; Lefebvre, J. M., Polymer *52*, 1417 (**2011**).
37. Pai, F.-C.; Lai, S.-M.; Chu, H.-H., Journal of Applied Polymer Science *130*, 2563 (**2013**).
38. Patel, R.; Ruehle, D. A.; Dorgan, J. R.; Halley, P.; Martin, D., Polymer Engineering and Science *54*, 1523 (**2014**).
39. Bitinis, N.; Verdejo, R.; Cassagnau, P.; Lopez-Manchado, M. A., Materials Chemistry and Physics *129*, 823 (**2011**).
40. Yuan, D.; Xu, C.; Chen, Z.; Chen, Y., Polymer Testing *38*, 73 (**2014**).
41. Lopez-Rodriguez, N.; Lopez-Arraiza, A.; Meaurio, E.; Sarasua, J. R., Polymer Engineering and Science *46*, 1299 (**2006**).
42. Sakai, F.; Nishikawa, K.; Inoue, Y.; Yazawa, K., Macromolecules *42*, 8335 (**2009**).
43. Broz, M. E.; VanderHart, D. L.; Washburn, N. R., Biomaterials *24*, 4181 (**2003**).
44. Simões, C. L.; Viana, J. C.; Cunha, A. M., Journal of Applied Polymer Science *112*, 345 (**2009**).
45. Semba, T.; Kitagawa, K.; Ishiaku, U. S.; Hamada, H., Journal of Applied Polymer Science *101*, 1816 (**2006**).
46. Maglio, G.; Migliozzi, A.; Palumbo, R.; Immirzi, B.; Volpe, M. G., Macromolecular Rapid Communications *20*, 236 (**1999**).
47. Na, Y. H.; He, Y.; Shuai, X.; Kikkawa, Y.; Doi, Y.; Inoue, Y., Biomacromolecules *3*, 1179 (**2002**).
48. Li, S. M.; Liu, L. J.; Garreau, H.; Vert, M., Biomacromolecules *4*, 372 (**2003**).
49. Takayama, T.; Todo, M.; Tsuji, H.; Arakawa, K., Journal of Materials Science *41*, 6501 (**2006**).
50. Takayama, T.; Todo, M., Journal of Materials Science *41*, 4989 (**2006**).
51. Takayama, T.; Todo, M.; Tsuji, H., Journal of the Mechanical Behavior of Biomedical Materials *4*, 255 (**2011**).
52. Harada, M.; Iida, K.; Okamoto, K.; Hayashi, H.; Hirano, K., Polymer Engineering and Science *48*, 1359 (**2008**).
53. Tuba, F.; Olah, L.; Nagy, P., Engineering Fracture Mechanics *78*, 3123 (**2011**).
54. Bartczak, Z.; Galeski, A.; Krasnikova, N. P., Polymer *28*, 1627 (**1987**).
55. Semba, T.; Kitagawa, K.; Ishiaku, U. S.; Kotaki, M.; Hamada, H., Journal of Applied Polymer Science *103*, 1066 (**2007**).
56. Semba, T.; Kitagawa, K.; Kotaki, M.; Hamada, H., Journal of Applied Polymer Science *108*, 256 (**2008**).
57. Wang, L.; Ma, W.; Gross, R. A.; McCarthy, S. P., Polymer Degradation and Stability *59*, 161 (**1998**).
58. Bai, H.; Huang, C.; Xiu, H.; Gao, Y.; Zhang, Q.; Fu, Q., Polymer *54*, 5257 (**2013**).
59. Wu, D.; Zhang, Y.; Zhang, M.; Zhou, W., European Polymer Journal *44*, 2171 (**2008**).
60. Gaymans, R. J., Polymer Blends, Volume 2: Performance, John Wiley and Sons (**2000**), 177-224 (Toughening of Semicrystalline Thermoplastics).
61. Bai, H.; Xiu, H.; Gao, J.; Deng, H.; Zhang, Q.; Yang, M.; Fu, Q., Acs Applied Materials & Interfaces *4*, 897 (**2012**).
62. Farsetti, S.; Cioni, B.; Lazzeri, A., Eurofillers *301*, 82 (**2011**).
63. Jiang, L.; Wolcott, M. P.; Zhang, J. W., Biomacromolecules *7*, 199 (**2006**).
64. Signori, F.; Coltelli, M.-B.; Bronco, S., Polymer Degradation and Stability *94*, 74 (**2009**).
65. Naiwen, Z.; Qinfeng, W.; Jie, R.; Liang, W., Journal of Materials Science *44*, 250 (**2009**).

66. Gu, S.-Y.; Zhang, K.; Ren, J.; Zhan, H., Carbohydrate Polymers *74*, 79 (**2008**).
67. Kumar, M.; Mohanty, S.; Nayak, S. K.; Parvaiz, M. R., Bioresource Technology *101*, 8406 (**2010**).
68. Sangmook, L.; Youngjoo, L.; Jae Wook, L., Macromolecular Research *15*, 44 (**2007**).
69. Jen-Taut, Y.; Chi-Hui, T.; Chi-Yuan, H.; Kan-Nan, C.; Chin-San, W.; Wan-Lan, C., Journal of Applied Polymer Science *116*, 680 (**2010**).
70. Zhang, N.; Zeng, C.; Wang, L.; Ren, J., Journal of Polymers and the Environment *21*, 286 (**2013**).
71. Al-Itry, R.; Lamnawar, K.; Maazouz, A., Polymer Degradation and Stability *97*, 1898 (**2012**).
72. Raquez, J.-M.; Habibi, Y.; Murariu, M.; Dubois, P., Progress in Polymer Science *38*, 1504 (**2013**).
73. Murariu, M.; Dechief, A. L.; Bonnaud, L.; Paint, Y.; Gallos, A.; Fontaine, G.; Bourbigot, S.; Dubois, P., Polymer Degradation and Stability *95*, 889 (**2010**).
74. Villmow, T.; Pötschke, P.; Pegel, S.; Haussler, L.; Kretzschmar, B., Polymer *49*, 3500 (**2008**).
75. Rhim, J.-W.; Park, H.-M.; Ha, C.-S., Progress in Polymer Science *38*, 1629 (**2013**).
76. Utracki, L. A., Clay-Containing Polymeric Nanocomposites, Volume 1, Rapra technology, (**2004**).
77. Pavlidou, S.; Papaspyrides, C. D., Progress in Polymer Science *33*, 1119 (**2008**).
78. Maiti, P.; Yamada, K.; Okamoto, M.; Ueda, K.; Okamoto, K., Chemistry of Materials *14*, 4654 (**2002**).
79. Ray, S. S.; Maiti, P.; Okamoto, M.; Yamada, K.; Ueda, K., Macromolecules *35*, 3104 (**2002**).
80. Ray, S. S.; Yamada, K.; Okamoto, M.; Ueda, K., Polymer *44*, 857 (**2003**).
81. Ray, S. S.; Yamada, K.; Okamoto, M.; Ogami, A.; Ueda, K., Chemistry of materials *15*, 1456 (**2003**).
82. Ray, S. S.; Yamada, K.; Okamoto, M.; Ogami, A.; Ueda, K., Composite Interfaces *10*, 435 (**2003**).
83. Ray, S. S.; Yamada, K.; Okamoto, M.; Fujimoto, Y.; Ogami, A.; Ueda, K., Polymer *44*, 6633 (**2003**).
84. Ray, S. S.; Yamada, K.; Okamoto, M.; Ueda, K., Journal of Nanoscience and Nanotechnology *3*, 503 (**2003**).
85. Ray, S. S.; Okamoto, M., Macromolecular Materials and Engineering *288*, 936 (**2003**).
86. Krikorian, V.; Pochan, D. J., Chemistry of Materials *15*, 4317 (**2003**).
87. Krishnamachari, P.; Zhang, J.; Lou, J. Z.; Yan, J. Z.; Uitenham, L., International Journal of Polymer Analysis and Characterization *14*, 336 (**2009**).
88. Krishnamachari, P.; Zhang, J.; Yan, J. Z.; Shahbazi, A.; Uitenham, L.; Lou, J. Z., Proceedings of the 2007 National Conference on Environmental Science and Technology, 219 (**2009**).
89. Zaidi, L.; Bruzaud, S.; Bourmaud, A.; Mederic, P.; Kaci, M.; Grohens, Y., Journal of Applied Polymer Science *116*, 1357 (**2010**).
90. Krikorian, V.; Pochan, D. J., Macromolecules *38*, 6520 (**2005**).
91. Pogodina, N. V.; Cercle, C.; Averous, L.; Thomann, R.; Bouquey, M.; Muller, R., Rheologica Acta *47*, 543 (**2008**).
92. Wang, B.; Wan, T.; Zeng, W., Journal of Applied Polymer Science *121*, 1032 (**2011**).
93. Wang, B.; Wan, T.; Zeng, W., Journal of Applied Polymer Science *125*, E364 (**2012**).
94. Lai, S.-M.; Wu, S.-H.; Lin, G.-G.; Don, T.-M., European Polymer Journal *52*, 193 (**2014**).
95. Pluta, M., Journal of Polymer Science Part B-Polymer Physics *44*, 3392 (**2006**).
96. Filippi, S.; Paci, M.; Polacco, G.; Dintcheva, N. T.; Magagnini, P., Polymer Degradation and Stability *96*, 823 (**2011**).
97. Fukushima, K.; Tabuani, D.; Camino, G., Materials Science & Engineering, Part C: Biomimetic and Supramolecular Systems *29*, 1433 (**2009**).
98. Wu, D. F.; Wu, L. A.; Wu, L. F.; Zhang, M., Polymer Degradation and Stability *91*, 3149 (**2006**).
99. Bocchini, S.; Fukushima, K.; Di Blasio, A.; Fina, A.; Frache, A.; Geobaldo, F., Biomacromolecules *11*, 2919 (**2010**).

100. Zaidi, L.; Kaci, M.; Bruzaud, S.; Bourmaud, A.; Grohens, Y., Polymer Degradation and Stability *95*, 1751 (**2010**)

101. Fukushima, K.; Abbate, C.; Tabuani, D.; Gennari, M.; Camino, G., Polymer Degradation and Stability *94*, 1646 (**2009**).

102. Ozkoc, G.; Kemaloglu, S., Journal of Applied Polymer Science *114*, 2481 (**2009**).

103. Li, S. M.; McCarthy, S., Macromolecules *32*, 4454 (**1999**).

104. Pluta, M.; Paul, M. A.; Alexandre, M.; Dubois, P., Journal of Polymer Science, Part B: Polymer Physics *44*, 299 (**2006**).

105. Pluta, M.; Paul, M. A.; Alexandre, M.; Dubois, P., Journal of Polymer Science, Part B: Polymer Physics *44*, 312 (**2006**).

106. Jiang, L.; Zhang, J. W.; Wolcott, M. P., Polymer *48*, 7632 (**2007**).

107. Messersmith, P. B.; Giannelis, E. P., Chemistry of Materials *5*, 1064 (**1993**).

108. Ojijo, V.; Ray, S. S., Progress in Polymer Science *38*, 1543 (**2013**).

109. Bordes, P.; Pollet, E.; Averous, L., Progress in Polymer Science *34*, 125 (**2009**).

110. Ojijo, V.; Ray, S. S., Progress in Materials Science *62*, 1 (**2014**).

111. Pantoustier, N.; Lepoittevin, B.; Alexandre, M.; Kubies, D.; Calberg, C.; Jerome, R.; Dubois, P., Polymer Engineering and Science *42*, 1928 (**2002**).

112. Di, Y. W.; Iannace, S.; Di Maio, E.; Nicolais, L., Journal of Polymer Science Part B-Polymer Physics *41*, 670 (**2003**).

113. Gain, O.; Espuche, E.; Pollet, E.; Alexandre, M.; Dubois, P., Journal of Polymer Science, Part B: Polymer Physics *43*, 205 (**2005**).

114. Labidi, S.; Azema, N.; Perrin, D.; Lopez-Cuesta, J.-M., Polymer Degradation and Stability *95*, 382 (**2010**).

115. Ludueña, L. N.; Kenny, J. M.; Vazquez, A.; Alvarez, V. A., Materials Science and Engineering, A: Structural Materials Properties Microstructure and Processing *529*, 215 (**2011**).

116. Ludueña, L. N.; Vazquez, A.; Alvarez, V. A., Journal of Applied Polymer Science *128*, 2648 (**2013**).

117. Breuer, O.; Sundararaj, U., Polymer Composites *25*, 630 (**2004**).

118. Xie, X. L.; Mai, Y. W.; Zhou, X. P., Materials Science & Engineering, R: Reports *49*, 89 (**2005**).

119. Moniruzzaman, M.; Winey, K. I., Macromolecules *39*, 5194 (**2006**).

120. Coleman, J. N.; Khan, U.; Blau, W. J.; Gun'ko, Y. K., Carbon *44*, 1624 (**2006**).

121. Spitalsky, Z.; Tasis, D.; Papagelis, K.; Galiotis, C., Progress in Polymer Science 35, 357 2010.

122. Alig, I.; Poetschke, P.; Lellinger, D.; Skipa, T.; Pegel, S.; Kasaliwal, G. R.; Villmow, T., Polymer *53*, 4 (**2012**).

123. Sun, Y. P.; Fu, K. F.; Lin, Y.; Huang, W. J., Accounts of Chemical Research *35*, 1096 (**2002**).

124. Ma, P.-C.; Siddiqui, N. A.; Marom, G.; Kim, J.-K., Composites Part a-Applied Science and Manufacturing *41*, 1345 (**2010**).

125. Bauhofer, W.; Kovacs, J. Z., Composites Science and Technology *69*, 1486 (**2009**).

126. Du, F. M.; Scogna, R. C.; Zhou, W.; Brand, S.; Fischer, J. E.; Winey, K. I., Macromolecules *37*, 9048 (**2004**).

127. McNally, T.; Potschke, P.; Halley, P.; Murphy, M.; Martin, D.; Bell, S. E. J.; Brennan, G. P.; Bein, D.; Lemoine, P.; Quinn, J. P., Polymer *46*, 8222 (**2005**).

128. Potschke, P.; Fornes, T. D.; Paul, D. R., Polymer *43*, 3247 (**2002**).

129. Andrews, R.; Jacques, D.; Minot, M.; Rantell, T., Macromolecular Materials and Engineering *287*, 395 (**2002**).

130. Song, Y. S.; Youn, J. R., Carbon *43*, 1378 (**2005**).

131. Barrau, S.; Vanmansart, C.; Moreau, M.; Addad, A.; Stoclet, G.; Lefebvre, J. M.; Seguela, R., Macromolecules *44*, 6496 (**2011**).
132. Park, S. H.; Lee, S. G.; Kim, S. H., Composites Part a-Applied Science and Manufacturing *46*, 11 (**2013**).
133. Chiu, W.-M.; Chang, Y.-A.; Kuo, H.-Y.; Lin, M.-H.; Wen, H.-C., Journal of Applied Polymer Science *108*, 3024 (**2008**).
134. Chrissafis, K.; Paraskevopoulos, K. M.; Jannakoudakis, A.; Beslikas, T.; Bikiaris, D., Journal of Applied Polymer Science *118*, 2712 (**2010**).
135. Laredo, E.; Bello, A.; Diaz, J.; Grimau, M.; Martinez-Tong, D.; Wu, D.; Wu, L., Polymer Composites *34*, 67 (**2013**).
136. Wu, D. F.; Wu, L.; Zhang, M.; Zhao, Y. L., Polymer Degradation and Stability *93*, 1577 (**2008**).
137. Wu, D. F.; Wu, L.; Zhou, W. D.; Sun, Y. R.; Zhang, M., Journal of Polymer Science, Part B: Polymer Physics *48*, 479 (**2010**).
138. Wu, C.-S.; Liao, H.-T., Polymer *48*, 4449 (**2007**).
139. Chen, G. X.; Kim, H. S.; Park, B. H.; Yoon, J. S., Journal of Physical Chemistry B *109*, 22237 (**2005**).
140. Song, W.; Zheng, Z.; Tang, W.; Wang, X., Polymer *48*, 3658 (**2007**).
141. Rizvi, R.; Kim, J.-K.; Naguib, H., Smart Materials & Structures *19*, 094003 (**2010**).
142. Yoon, J. T.; Jeong, Y. G.; Lee, S. C.; Min, B. G., Polymers for Advanced Technologies *20*, 631 (**2009**).
143. Yoon, J. T.; Lee, S. C.; Jeong, Y. G., Composites Science and Technology *70*, 776 (**2010**).
144. Ramontja, J.; Ray, S. S.; Pillai, S. K.; Luvt, A. S. 5th International Symposium on Nanostructured Materials and Nanotechnology, 53 (**2011**).
145. Ramontja, J.; Ray, S. S.; Pillai, S. K.; Luyt, A. S., Macromolecular Materials and Engineering *294*, 839 (**2009**).
146. Sobkowicz, M. J.; Sosa, R.; Dorgan, J. R., Journal of Applied Polymer Science *121*, 2029 (**2011**).
147. Kuan, C.-F.; Kuan, H.-C.; Ma, C.-C. M.; Chen, C.-H., Journal of Physics and Chemistry of Solids *69*, 1395 (**2008**).
148. Wu, D.; Wu, L.; Zhou, W.; Zhang, M.; Yang, T., Polymer Engineering and Science *50*, 1721 (**2010**).
149. Villmow, T.; Kretzschmar, B.; Poetschke, P., Composites Science and Technology *70*, 2045 (**2010**).
150. Trujillo, M.; Luisa Arnal, M.; Mueller, A. J.; Mujica, M. A.; Urbina de Navarro, C.; Ruelle, B.; Dubois, P., Polymer *53*, 832 (**2012**).
151. Chin, S. J.; Vempati, S.; Dawson, P.; Knite, M.; Linarts, A.; Ozols, K.; McNally, T., Polymer *58*, 209 (**2015**).
152. Yeh, J.-T.; Yang, M.-C.; Wu, C.-J.; Wu, C.-S., Journal of Applied Polymer Science *112*, 660 (**2009**).
153. Hong, S. Y.; Ko, S. W.; Choi, H. J.; Lee, J. H., Journal of Macromolecular Science Part B-Physics *51*, 125 (**2012**).
154. Wu, C.-S., Carbon *47*, 3091 (**2009**).
155. Gonzalez, I.; Ignacio Eguiazabal, J.; Nazabal, J., Composites Part a-Applied Science and Manufacturing *43*, 1482 (**2012**).
156. Dasari, A.; Yu, Z.-Z.; Mai, Y.-W., Polymer *50*, 4112 (**2009**).
157. Ojijo, V.; Ray, S. S.; Sadiku, R., Macromolecular Materials and Engineering *299*, 596 (**2014**).
158. Fenouillot, F.; Cassagnau, P.; Majeste, J. C., Polymer *50*, 1333 (**2009**).
159. Taguet, A.; Cassagnau, P.; Lopez-Cuesta, J. M., Progress in Polymer Science *39*, 1526 (**2014**).
160. Anastasiadis, S. H., Polymer Thermodynamics: Liquid Polymer-Containing Mixtures *238*, 179 (**2011**).

161. Kamal, M. R.; Calderon, J. U.; Lennox, R. B., Journal of Adhesion Science and Technology *23*, 663 (**2009**).
162. Mirzadeh, A.; Lafleur, P. G.; Kamal, M. R.; Dubois, C., Polymer Engineering and Science *50*, 2131 (**2010**).
163. Liebscher, M.; Blais, M.-O.; Poetschke, P.; Heinrich, G., Polymer *54*, 5875 (**2013**).
164. Goeldel, A.; Marmur, A.; Kasaliwal, G. R.; Poetschke, P.; Heinrich, G., Macromolecules *44*, 6094 (**2011**).
165. Göldel, A.; Kasaliwal, G. R.; Poetschke, P.; Heinrich, G., Polymer *53*, 411 (**2012**).
166. Goitisolo, I.; Gonzalez, I.; Eguiazabal, J. I., Polymers for Advanced Technologies *24*, 357 (**2013**).
167. Ray, S. S.; Pouliot, S.; Bousmina, M.; Utracki, L. A., Polymer *45*, 8403 (**2004**).
168. Chang, L.; Xinhui, H.; Jiaxi, W.; Xiaoning, H., Advanced Materials Research *557-559*, 654 (**2012**).
169. Huang, J.; Mao, C.; Zhu, Y.; Jiang, W.; Yang, X., Carbon *73*, 267 (**2014**).
170. Scaffaro, R.; Botta, L., Nanostructured Polymer Blends, 133 (**2014**).
171. Odent, J.; Habibi, Y.; Raquez, J.-M.; Dubois, P., Composites Science and Technology *84*, 86 (**2013**).
172. Tiwari, R. R.; Paul, D. R., Polymer *52*, 5595 (**2011**).
173. Tiwari, R. R.; Paul, D. R., Polymer *53*, 823 (**2012**).
174. Tiwari, R. R.; Hunter, D. L.; Paul, D. R., Journal of Polymer Science, Part B: Polymer Physics *50*, 1577 (**2012**).
175. Xiu, H.; Huang, C.; Bai, H.; Jiang, J.; Chen, F.; Deng, H.; Wang, K.; Zhang, Q.; Fu, Q., Polymer *55*, 1593 (**2014**).
176. Gao, C.; Zhang, S.; Han, B.; Sun, H.; Wang, G.; Jiang, Z., Rsc Advances *4*, 42175 (**2014**).
177. Nuzzo, A.; Bilotti, E.; Peijs, T.; Aciern, D.; Filippone, G., Polymer *55*, 4908 (**2014**).
178. Naderi, G.; Lafleur, P. G.; Dubois, C., Polymer Composites *29*, 1301 (**2008**).
179. Li, Y. J.; Shimizu, H., Polymer *45*, 7381 (**2004**).
180. Tiwari, R. R.; Paul, D. R., Polymer *52*, 1141 (**2011**).
181. Tiwari, R. R.; Paul, D. R., Polymer *52*, 4955 (**2011**).
182. Mishra, J. K.; Chang, Y. W.; Choi, N. S., Polymer Engineering and Science *47*, 863 (**2007**).
183. Khatua, B. B.; Lee, D. J.; Kim, H. Y.; Kim, J. K., Macromolecules *37*, 2454 (**2004**).
184. Filippone, G.; Dintcheva, N. T.; La Mantia, F. P.; Acierno, D., Polymer *51*, 3956 (**2010**).
185. Ha, M.; Atallah, A.; Krishnamoorti, R., Polymer *52*, 5890 (**2011**).
186. Tao, F.; Auhl, D.; Baudouin, A.-C.; Stadler, F. J.; Bailly, C., Macromolecular Chemistry and Physics *214*, 350 (**2013**).
187. Baudouin, A.-C.; Auhl, D.; Tao, F.; Devaux, J.; Bailly, C., Polymer *52*, 149 (**2011**).
188. Huitric, J.; Ville, J.; Mederic, P.; Moan, M.; Aubry, T., Journal of Rheology *53*, 1101 (**2009**).
189. Elias, L.; Fenouillot, F.; Majeste, J. C.; Cassagnau, P., Polymer *48*, 6029 (**2007**).
190. Laoutid, F.; Francois, D.; Paint, Y.; Bonnaud, L.; Dubois, P., Macromolecular Symposia *321-322*, 90 (**2012**).
191. Fang, Z.; Harrats, C.; Moussaif, N.; Groeninckx, G., Journal of Applied Polymer Science *106*, 3125 (**2007**).
192. Hong, J. S.; Kim, Y. K.; Ahn, K. H.; Lee, S. J.; Kim, C., Rheologica Acta *46*, 469 (**2007**).
193. Wu, D.; Zhang, Y.; Zhang, M.; Yu, W., Biomacromolecules *10*, 417 (**2009**).
194. Wu, D. F.; Sun, Y. R.; Lin, D. P.; Zhou, W. D.; Zhang, M.; Yuan, L. J., Macromolecular Chemistry and Physics *212*, 1700 (**2011**).
195. Elias, L.; Fenouillot, F.; Majeste, J. C.; Alcouffe, P.; Cassagnau, P., Polymer *49*, 4378 (**2008**).

196. Entezam, M.; Khonakdar, H. A.; Yousefi, A. A.; Jafari, S. H.; Wagenknecht, U.; Heinrich, G., Materials & Design *45*, 110 (**2013**).

197. Zou, H.; Ning, N.; Su, R.; Zhang, Q.; Fu, Q., Journal of Applied Polymer Science *106*, 2238 (**2007**).

198. Filippone, G.; Idintcheva, N. T.; La Mantia, F. P.; Acierno, D., Journal of Polymer Science, Part B: Polymer Physics *48*, 600 (**2010**).

199. Dhibar, A. K.; Kim, J. K.; Khatua, B. B., Journal of Applied Polymer Science *119*, 3080 (**2011**).

200. Filippone, G.; Dintcheva, N. T.; Acierno, D.; La Mantia, F. P., Polymer *49*, 1312 (**2008**).

201. Wang, L.; Guo, Z.-X.; Yu, J., Journal of Applied Polymer Science *123*, 1218 (**2012**).

202. Wang, L.; Shi, C.; Guo, Z.-X.; Yu, J., Journal of Industrial and Engineering Chemistry *20*, 259 (**2014**).

203. Kong, M.; Huang, Y.; Chen, G.; Yang, Q.; Li, G., Polymer *52*, 5231 (**2011**).

204. Kontopoulou, M.; Liu, Y.; Austin, J. R.; Parent, J. S., Polymer *48*, 4520 (**2007**).

205. Steinmann, S.; Gronski, W.; Friedrich, C., Polymer *43*, 4467 (**2002**).

206. Li, L.; Miesch, C.; Sudeep, P. K.; Balazs, A. C.; Emrick, T.; Russell, T. P.; Hayward, R. C., Nano Letters *11*, 1997 (**2011**).

207. Xiang, F.; Shi, Y.; Li, X.; Huang, T.; Chen, C.; Peng, Y.; Wang, Y., European Polymer Journal *48*, 350 (**2012**).

208. Cai, X.; Li, B.; Pan, Y.; Wu, G., Polymer *53*, 259 (**2012**).

209. Xiu, H.; Zhou, Y.; Dai, J.; Huang, C.; Bai, H.; Zhang, Q.; Fu, Q., Rsc Advances *4*, 37193 (**2014**).

210. Zou, H.; Wang, K.; Zhang, Q.; Fu, Q., Polymer *47*, 7821 (**2006**).

211. Wu, G.; Li, B.; Jiang, J., Polymer *51*, 2077 (**2010**).

212. Peng, G. W.; Qiu, F.; Ginzburg, V. V.; Jasnow, D.; Balazs, A. C., Science *288*, 1802 (**2000**).

213. Nuzzo, A.; Coiai, S.; Carroccio, S. C.; Dintcheva, N. T.; Gambarotti, C.; Filippone, G., Macromolecular Materials and Engineering *299*, 31 (**2014**).

214. Yu, Z.; Yin, J.; Yan, S.; Xie, Y.; Ma, J.; Chen, X., Polymer *48*, 6439 (**2007**).

215. Ren, J.; Yu, T.; Li, H.; Ren, T.; Yang, S., Polymer Composites *29*, 1145 (**2008**).

216. Hoidy, W. H.; Al-Mulla, E. A. J.; Al-Janabi, K. W., Journal of Polymers and the Environment *18*, 608 (**2010**).

217. Wu, D.; Lin, D.; Zhang, J.; Zhou, W.; Zhang, M.; Zhang, Y.; Wang, D.; Lin, B., Macromolecular Chemistry and Physics *212*, 613 (**2011**).

218. Li, Q.; Yoon, J.-S.; Chen, G.-X., Journal of Polymers and the Environment *19*, 59 (**2011**).

219. Laredo, E.; Grimau, M.; Bello, A.; Wu, D. F.; Zhang, Y. S.; Lin, D. P., Biomacromolecules *11*, 1339 (**2010**).

220. Xu, Z.; Zhang, Y.; Wang, Z.; Sun, N.; Li, H., Acs Applied Materials & Interfaces *3*, 4858 (**2011**).

221. Ko, S. W.; Hong, M. K.; Park, B. J.; Gupta, R. K.; Choi, H. J.; Bhattacharya, S. N., Polymer Bulletin *63*, 125 (**2009**).

222. Ko, S. W.; Gupta, R. K.; Bhattacharya, S. N.; Choi, H. J., Macromolecular Materials and Engineering *295*, 320 (**2010**).

223. Guerrica-Echevarria, G.; Eguiazabal, J. I.; Nazabal, J., Polymer Testing *19*, 849 (**2000**).

224. Souheng, W., Journal of Colloid and Interface Science *71*, 605 (**1979**).

225. Granado, A.; Eguiazábal, J. I.; Nazábal, J., Journal of Applied Polymer Science 109, 3892 (**2008**).

226. Avramova, N., Polymer *36*, 801 (**1995**).

227. Noroozi, N.; Schafer, L. L.; Hatzikiriakos, S. G., Polymer Engineering and Science *52*, 2348 (**2012**).

228. Jose, S.; Nair, S. V.; Thomas, S.; Karger-Kocsis, J., Journal of Applied Polymer Science *99*, 2640 (**2006**).

229. Souza, A. M. C.; Demarquette, N. R., Polymer *43*, 3959 (**2002**).

230. Minkova, L.; Yordanov, H.; Filippi, S.; Grizzuti, N., Polymer *44*, 7925 (**2003**).
231. Shariatpanahi, H.; Nazokdast, H.; Hemmati, M., Journal of Elastomers and Plastics *35*, 115 (**2003**).
232. Wu, S. H., Polymer Engineering and Science *27*, 335 (**1987**).
233. Wu, D.; Zhang, Y.; Yuan, L.; Zhang, M.; Zhou, W., Journal of Polymer Science, Part B: Polymer Physics *48*, 756 (**2010**).
234. Arostegui, A.; Nazabal, J., Journal of Polymer Science, Part B: Polymer Physics *41*, 2236 (**2003**).
235. Kawai, T.; Rahman, N.; Matsuba, G.; Nishida, K.; Kanaya, T.; Nakano, M.; Okamoto, H.; Kawada, J.; Usuki, A.; Honma, N.; Nakajima, K.; Matsuda, M., Macromolecules *40*, 9463 (**2007**).
236. Lovera, D.; Marquez, L.; Balsamo, V.; Taddei, A.; Castelli, C.; Muller, A. J., Macromolecular Chemistry and Physics *208*, 924 (**2007**).
237. Fernandez, J.; Etxeberria, A.; Sarasua, J.-R., Journal of the Mechanical Behavior of Biomedical Materials *9*, 100 (**2012**).
238. Jen-Taut, Y.; Tsou, C.-H.; Lu, W.; Li, Y.-M.; Xiao, H. W.; Huang, C.-Y.; Chen, K.-N.; Wu, C.-S.; Chai, W.-L., Journal of Polymer Science, Part B: Polymer Physics *48*, 913 (**2010**).
239. Balakrishnan, H.; Hassan, A.; Wahit, M. U., Journal of Elastomers and Plastics *42*, 223 (**2010**).
240. Marin, N.; Favis, B. D., Polymer *43*, 4723 (**2002**).
241. Quero, E.; Mueller, A. J.; Signori, F.; Coltelli, M.-B.; Bronco, S., Macromolecular Chemistry and Physics *213*, 36 (**2012**).
242. Coltelli, M.-B.; Della Maggiore, I.; Bertold, M.; Signori, F.; Bronco, S.; Ciardelli, F., Journal of Applied Polymer Science *110*, 1250 (**2008**).
243. Xiao, H.; Lu, W.; Yeh, J.-T., Journal of Applied Polymer Science *112*, 3754 (**2009**).
244. Utracki, L. A., Journal of Rheology *35*, 1615 (**1991**).
245. Al-Itry, R.; Lamnawar, K.; Maazouz, A., Rheologica Acta *53*, 501 (**2014**).
246. M. Nofar, A. M., H. Sojoudi, M. C. Heuzey, P. J. Carreau, Journal of Rheology *59*, 317 (**2015**).
247. Li, Y.; Liu, L.; Shi, Y.; Xiang, F.; Huang, T.; Wang, Y.; Zhou, Z., Journal of Applied Polymer Science *121*, 2688 (**2011**).
248. de Souza, P.; Baird, D. G., Polymer *37*, 1985 (**1996**).
249. Kolarik, J., Journal of Macromolecular Science: Physics *55*, B39 (**2000**).
250. Paul, M. A.; Alexandre, M.; Degee, P.; Henrist, C.; Rulmont, A.; Dubois, P., Polymer 44, 443 (**2003**).
251. Pluta, M.; Jeszka, J. K.; Boiteux, G., European Polymer Journal *43*, 2819 (**2007**).
252. Katiyar, V.; Gerds, N.; Koch, C. B.; Risbo, J.; Hansen, H. C. B.; Plackett, D., Journal of Applied Polymer Science *122*, 112 (**2011**).
253. Najafi, N.; Heuzey, M. C.; Carreau, P. J., Composites Science and Technology *72*, 608 (**2012**).
254. Gurmendi, U.; Eguiazabal, J. I.; Nazabal, J., Polymer International *55*, 399 (**2006**).
255. Gonzalez, I.; Eguiazabal, J. I.; Nazabal, J., Macromolecular Materials and Engineering *293*, 781 (**2008**).
256. Santamaria, P.; Eguiazabal, J. I., Polymers for Advanced Technologies 24, 300 (**2013**).
257. Di, Y. W.; Iannace, S.; Di Maio, E.; Nicolais, L., Journal of Polymer Science, Part B: Polymer Physics *43*, 689 (**2005**).
258. Hassanabadi, H. M.; Wilhelm, M.; Rodrigue, D., Rheologica Acta *53*, 869 (**2014**).
259. Chafidz, A.; Ali, M. A.-h.; Elleithy, R., Journal of Materials Science *46*, 6075 (**2011**).
260. Guehenec, M.; Tishkova, V.; Dagreou, S.; Leonardi, F.; Derail, C.; Puech, P.; Pons, F.; Gauthier, B.; Cadaux, P. H.; Bacsa, W., Journal of Applied Polymer Science *129*, 2527 (**2013**).
261. Ray, S. S.; Okamoto, M., Progress in Polymer Science *28*, 1539 (**2003**).

262. Gurmendi, U.; Eguiazabal, J. I.; Nazabal, J., Composites Science and Technology *66*, 1221 (**2006**).

263. Tarawneh, M. a. A.; Ahmad, S. H.; Bahri, S. A. R.; Jiun, Y. L., Solid State Science and Technology *501*, 194 (**2012**).

264. Choudalakis, G.; Gotsis, A. D., European Polymer Journal *45*, 967 (**2009**).

265. Nielsen, L. E., Journal of Macromolecular Science, Part A: Chemistry *1*, 929 (**1967**).

266. Diez-Pascual, A. M.; Naffakh, M.; Gomez, M. A.; Marco, C.; Ellis, G.; Martinez, M. T.; Anson, A.; Gonzalez-Dominguez, J. M.; Martinez-Rubi, Y.; Simard, B., Carbon *47*, 3079 (**2009**).

267. Atieh, M. A., Journal of Thermoplastic Composite Materials *24*, 613 (**2011**).

268. Meng, Z. X.; Zheng, W.; Ding, M. H.; Zhou, H. M.; Chen, X. Q.; Chen, J. C.; Liu, M. K.; Zheng, Y. F., Journal of Nanoscience and Nanotechnology *11*, 3126 (**2011**).

269. Zhang, D.; Kandadai, M. A.; Cech, J.; Roth, S.; Curran, S. A., Journal of Physical Chemistry B *110*, 12910 (**2006**).

270. Nobile, M. R., Polymer–carbon nanotube composites: Preparation, properties and applications;, McNally, T.; Pötschke, P., (**2011**), 428 (Rheology of polymer–carbon nanotube composites melts).

271. Lebovka, N. I.; Lysenkov, E. A.; Goncharuk, A. I.; Gomza, Y. P.; Klepko, V. V.; Boiko, Y. P., Journal of Composite Materials *45*, 2555 (**2011**).

272. Marini, J.; Suman Bretas, R. E., Polymer Engineering and Science *53*, 1512 (**2013**).

273. Wong, M.; Paramsothy, M.; Xu, X. J.; Ren, Y.; Li, S.; Liao, K., Polymer *44*, 7757 (**2003**).

274. Li, Z.; Xu, S.; Liu, W.; He, S.; Zhu, C., Journal of Applied Polymer Science *113*, 2805 (**2009**).

275. Blond, D.; Barron, V.; Ruether, M.; Ryan, K. P.; Nicolosi, V.; Blau, W. J.; Coleman, J. N., Advanced Functional Materials *16*, 1608 (**2006**).

276. Koval'chuk, A. A.; Shchegolikhin, A. N.; Shevchenko, V. G.; Nedorezova, P. M.; Klyamkina, A. N.; Aladyshev, A. M., Macromolecules *41*, 3149 (**2008**).

277. Feller, J. F.; Castro, M.; Kumar, B., Polymer-carbon nanotube composites. Preparation, properties and applications (**2011**).

278. Sabet, S. S.; Katbab, A. A., Journal of Applied Polymer Science *111*, 1954 (**2009**).

279. Dasari, A.; Yu, Z. Z.; Mai, Y. W., Polymer *46*, 5986 (**2005**).

280. Gallego, R.; García-López, D.; López-Quintana, S.; Gobernado-Mitre, I.; Merino, J. C.; Pastor, J. M., Journal of Applied Polymer Science *109*, 1556 (**2008**).

281. DePolo, W. S.; Baird, D. G., Polymer Composites *30*, 200 (**2009**).

282. Ray, S. S.; Bousmina, M.; Maazouz, A., Polymer Engineering and Science *46*, 1121 (**2006**).

283. Voulgaris, D.; Petridis, D., Polymer *43*, 2213 (**2002**).

284. Lepoittevin, B.; Devalckenaere, M.; Pantoustier, N.; Alexandre, M.; Kubies, D.; Calberg, C.; Jeome, R.; Dubois, P., Polymer *43*, 4017 (**2002**).

285. Gueltner, M.; Goeldel, A.; Poetschke, P., Composites Science and Technology *72*, 41 (**2011**).

286. Potschke, P.; Paul, D. R., Journal of Macromolecular Science-Polymer Reviews *C43*, 87 (**2003**).

287. Goitisolo, I.; Eguiazabal, J. I.; Nazabal, J., European Polymer Journal *44*, 1978 (**2008**).

288. Goitisolo, I.; Eguiazabal, J. I.; Nazabal, J., Composites Science and Technology *70*, 873 (**2010**).

289. Goitisolo, I.; Ignacio Eguiazabal, J.; Nazabal, J., Macromolecular Materials and Engineering *295*, 233 (**2010**).

290. Tjong, S. C., Materials Science & Engineering R-Reports *53*, 73 (**2006**).

291. Dottori, M.; Armentano, I.; Fortunati, E.; Kenny, J. M., Journal of Applied Polymer Science *119*, 3544 (**2011**).

292. Khan, R. A.; Dussault, D.; Salmieri, S.; Safrany, A.; Lacroix, M., Journal of Applied Polymer Science *127*, 3962 (**2013**).
293. Xin, T.; Chang, L.; Cheng, H. M.; Zhao, H. C.; Feng, Y.; Zhang, X. Q., Journal of Applied Polymer Science *92*, 3697 (**2004**).
294. Gorga, R. E.; Cohen, R. E., Journal of Polymer Science Part B-Polymer Physics *42*, 2690 (**2004**).
295. Cocca, M.; Di Lorenzo, M. L.; Malinconico, M.; Frezza, V., European Polymer Journal *47*, 1073 (**2011**).
296. Perego, G.; Cella, G. D.; Bastioli, C., Journal of Applied Polymer Science *59*, 37 (**1996**).
297. Kolarik, J., Polymer Engineering and Science *36*, 2518 (**1996**).

Annexes

GLOSSARY

^{1}H-RMN	Proton magnetic nuclear resonance
A_0	Initial cross-section of a tensile specimen
AA	Acrylic acid
ABS	Acrylonitrile butadiene styrene
AFM	Atomic force microscopy
Al	Aluminium
ASTM	*American Society for Testing and Materials*
$CDCl_3$	Deuterated chloroform
CdS	Cadmium sulfide
CL	Caprolactone
CNT	Carbon nanotube
COOH	Carboxyl
d	Basal spacing between montmorillonite sheets (XRD)
D	Diameter
DCP	Dodecadecyl amine
DMODA	Dimethyl octadecylamine
DMTA	Dynamic mechanical nuclear resonance
DSC	Scanning electron calorimetry
E	Young's modulus
E´	Solid state storage modulus
E´´	Solid state loss modulus
EGMA	Poly(ethylene-glycidyl methacrylate)
EPDM	Ethylene propylene diene monomer rubber
EPDMgMA	Ethylene propylene diene monomer rubber-grafted maleic anhidride
FTIR	Fourier transmission infrared microscopy

F_y	Force at the maximum of the force-displacement plot
G´	Melt state storage modulus
G´´	Melt stage loss modulus
GMA	Glycidyl methacrylate
H_2O	Water
HAR	High aspect ratio
HDA	Hexadecyl amine
HDPE	High density polyethylene
HDT	Heat deflection temperature
I	Current intensity
L	Length
l	Thickness of the film (measurements for oxygen permeability, electrical conductivity measurements)
l_0	Initial distance between clamps (tensile tests)
LA	Lactic acid
LAR	Low aspect ratio
LTI	Lysine triisocyanate
MA	Maleic anhidride
mEPDM	Maleated ethylene propylene diene monomer rubber
MFI	Melt flow index
MFR	Melt flow ratio
Mg	Magnesium
MMT	Montmorillonite
MWCNT	Multi-walled carbon nanotube
Na	Sodium
O	Oxygen
O_2	Oxygen molecule
OH	Hidroxyl
oMMT	Organically modified montmorillonite

OTR	O_2 transmission rate
P	Permeability
p	Pressure
P:	Electric percolation
PA	Polyamide
PA11	Polyamide 11
PA6	Polyamide 6
PA66	Polyamide 66
PAE	Polyamide elastomer
PBAT	Poly(butylene adipate-co-terephthalate)
PBT	Poly(butylene terephthalate)
PC	Polycarbonate
PCL	Poly(ε-caprolactone)
pCNT	pristine CNT
PEG	Poly(ethylene glycol)
PLA	Poly(lactic acid)
PLLA	Poly(L-lactic acid)
p-MWCNT	pristine multi walled carbon nanotube
PP	Polypropylene
PPS	Poly(p-phenylene sulfide)
PS	Polystyrene
PU	Polyurethane
PVME	Poly(vinyl methyl ether)
SEM	Scanning electron microscopy
Si	Silicon
SWCNT	Single-walled carbon nanotube
tanδ	Loss factor
Tc	Crystallization temperature

TEM	Transmission electron microscopy
Tg	Glass transition temperature
Tg_{blend}	Experimental Tg value of the PLA phase
T-GMA	Random terpolymer of ethylene, acrylic ester and GMA
Tg_{PBAT}	Tg value of neat PBAT
Tg_{PCL}	Tg value of neat PCL
Tg_{PLA}	Tg value of neat PLA
Tm	Melting temperature
TMC-328	N,N′,N″-tricyclohexyl-1,3,5-benzene-tricarboxylamide
TMODA	Trimethyl octadecylamine
Tm_{PBAT}	Tm of PBAT
Tm_{PCL}	Tm of PCL
Tm_{PLA}	Tm of PLA
TMS	Tetramethylsilane
TPP	Triphenyl phosphate
T_β	Secondary transition temperature
V	Voltage
w_1	Weight fraction of phase 1
w_2	Weight fraction of phase 2
WAXD	Wide-angle X-ray scattering
w_{PBAT}	Weight fraction of PBAT in the PLA phase
w_{PLA}	Weight fraction of PLA in the main phase
Xc	Degree of crystallinity
XRD	X-ray diffraction
γ	Deformation (Viscoelastic properties)
γ	Total surface energy (contact angle measurements)
γ^d	Dispersive surface energy (contact angle measurements)
γ^p	Polar surface energy (contact angle measurements)

ΔHc	Crystallization enthalpy
ΔHm	Melting enthalpy
δ_r	Deformation of the material before breaking
ε_r	Elongation at break or ductility
η	Melt viscosity
η^*	Complex viscosity
η_1	Melt viscosity of phase 1
η_2	Melt viscosity of phase 2
θ	Angle of incident or reflected radiation with the normal to the plane of the sample (XRD)
λ	Wavelength of the incident radiation (XRD)
ρ	Resistivity
σ	Shear stress (Viscoelastic properties)
σ_y	Yield strength
ω	Angular frequency